AGARD-R-785

AGARD

ADVISORY GROUP FOR AEROSPACE RESEARCH & DEVELOPMENT
7 RUE ANCELLE 92200 NEUILLY SUR SEINE FRANCE

AGARD REPORT 785

The Utilization of Advanced Composites in Military Aircraft

(L'Emploi des Matériaux Composites de Pointe pour les Avions Militaires)

Papers presented at the 73rd Meeting of the AGARD Structures and Materials P[illegible] held in San Diego, CA, United States, 7th—11th October 1991.

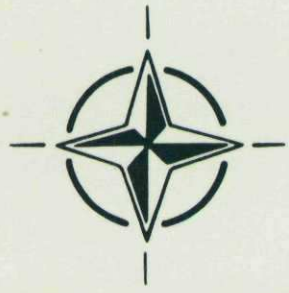

NORTH ATLANTIC TREATY ORGANIZATION

Published April 1992

Distribution and Availability on Back Cover

AGARD
ADVISORY GROUP FOR AEROSPACE RESEARCH & DEVELOPMENT
7 RUE ANCELLE 92200 NEUILLY SUR SEINE FRANCE

AGARD REPORT 785

The Utilization of Advanced Composites in Military Aircraft

(L'Emploi des Matériaux Composites de Pointe pour les Avions Militaires)

Papers presented at the 73rd Meeting of the AGARD Structures and Materials Panel, held in San Diego, CA, United States from 7th—11th October 1991.

North Atlantic Treaty Organization
Organisation du Traité de l'Atlantique Nord

The Mission of AGARD

According to its Charter, the mission of AGARD is to bring together the leading personalities of the NATO nations in the fields of science and technology relating to aerospace for the following purposes:

- Recommending effective ways for the member nations to use their research and development capabilities for the common benefit of the NATO community;
- Providing scientific and technical advice and assistance to the Military Committee in the field of aerospace research and development (with particular regard to its military application);
- Continuously stimulating advances in the aerospace sciences relevant to strengthening the common defence posture;
- Improving the co-operation among member nations in aerospace research and development;
- Exchange of scientific and technical information;
- Providing assistance to member nations for the purpose of increasing their scientific and technical potential;
- Rendering scientific and technical assistance, as requested, to other NATO bodies and to member nations in connection with research and development problems in the aerospace field.

The highest authority within AGARD is the National Delegates Board consisting of officially appointed senior representatives from each member nation. The mission of AGARD is carried out through the Panels which are composed of experts appointed by the National Delegates, the Consultant and Exchange Programme and the Aerospace Applications Studies Programme. The results of AGARD work are reported to the member nations and the NATO Authorities through the AGARD series of publications of which this is one.

Participation in AGARD activities is by invitation only and is normally limited to citizens of the NATO nations.

Published April 1992

ISBN 92-835-0666-9

Printed by Specialised Printing Services Limited
40 Chigwell Lane, Loughton, Essex IG10 3TZ

Preface

At its 73rd meeting in the fall of 1991, the Structures and Materials Panel held a Workshop to address compression loading and fluid effects in composite materials, two important topics related to the technology development of these materials. The purpose of the Workshop was to identify the current state-of-the-art in key issues related to these subjects that were of common interest between participating nations.

Papers presented revealed some areas of common concern. In the area of compression loading there was considerable concern over the quite different results obtained from various test methods. It was agreed that the failure modes produced by the various test methods along with a better fundamental understanding of compression failure were key issues in the development of compression test methods. In the area of fluid effects, a lack of a comprehensive data base hampers identification of key mechanisms leading to fluid degradation. This is further complicated by the fact that interactions depend on the fluid and the composite under consideration. For example, the effect of moisture is often different than the effect of jet fuel for a given composite system.

It is hoped that the Workshop, bringing together the various experiences of industry, government, and universities, has served in achieving the goal of identifying key issues related to compression loading and fluid effects in composite materials.

Préface

Lors de sa 73éme réunion, au printemps 1991, le Panel AGARD des Structures et Matériaux a organisé un atelier sur les charges de compression et les effets fluidiques dans les matériaux composites: deux questions importantes pour le développement technologique de ces matériaux. L'atelier a eu pour objectif de définir l'état de l'art dans les domaines clés connexes d'intérêt commun aux pays participant.

Les communications ont fait état d'un certain nombre domaines d'intérêt commun. En ce qui concerne les charges de compression, les participants ont fait part de leurs inquiétudes devant l'importance des écarts entre les resultats obtenus par les différentes méthodes d'essai. Ils ont été unanimes pour reconnaître que les modes de rupture engendrés par les différentes méthodes d'essai représentaient des éléments clés pour le développement des méthodes d'essais de compression.

Dans le domaine des effets fluidiques, le manque d'une base de données complète entrave l'identification des mécanismes clés conduisant à la dégradation des fluides. La situation est aggravée davantage par le fait que les interactions dépendent du fluide et du matériau composite en question. Par exemple, les effets de l'humidité sont souvent très différents des effets d'un carburant réacteur pour un système de matériaux composites donné.

Il est à espérer que l'atelier, qui a réuni des experts de l'Industrie, de l'Administration et des Universités, a contribué à l'identification des questions clés relatives aux charges de compression et aux effets fluidiques dans les materiaux composites.

James M. WHITNEY
WL/MLBM
Wright-Patterson AFB
United States

Structures and Materials Panel

Chairman: Mr Samuel L. Venneri
Director, Materials & Structures
Division (Code RM)
Office of Aeronautics & Space Technology
NASA Hq
Washington DC 20546
United States

Deputy Chairman: Mr Roger Labourdette
Directeur Scientifique des Structures
ONERA
29 ave de la Division Leclerc
92322 Châtillon
France

SUB-COMMITTEE MEMBERS

Chairman: Dr M.L. Minges
Director, Non-Metallic Materials Division
Wright Laboratory/MLB
Wright-Patterson AFB
OH 45433-6533
United States

Members

T. Akyurek	TU	G. Papakonstantinou	GR
D. Chaumette	FR	B.F. Peters	CA
P. Costa	FR	R. Potter	UK
D. Coutsouradis	BE	T. Ronald	US
G. Cunningham	UK	M. Rother	GE
M. Doruk	TU	A. Salvetti	IT
W. Elber	US	M. Scolaris	IT
L. Grabowski	UK	O. Sensburg	GE
G. Grüninger	GE	S. Signoretti	IT
A. Güemes	SP	S.L. Venneri	US
R. Labourdette	FR	J. Waldman	US
A. Looije	NL	W. Wallace	CA
G. Oddone	IT	A.P. Ward	UK
J. Odorico	FR	H. Zocher	GE
S. Paipetis	GR		

PANEL EXECUTIVE

Major William D. Lyle, CAF
(Acting SMP Executive)

Mail from Europe:
AGARD-OTAN
7, rue Ancelle
92200 Neuilly sur Seine
France

Mail from US and Canada:
AGARD-NATO/SMP
Unit 21551
APO AE 09777

Telephone: (1) 4738 5790 & 5792
Telex: 610176 (France)
Telefax: (1) 4738 5799

Contents

	Page
Preface/Préface	iii
Structures and Materials Panel	iv
	Reference
SESSION I – COMPRESSION PHENOMENA	
Issues in Compression Loading of Composite Structures by J.M. Whitney	1
Behaviour of Composite Structures under Compressive Loading by J. Starnes and M. Shuart	2†
A New Test Method to Determine the Compressive Strength of Fiber-Reinforced Composites by A.S. Crasto, R.Y. Kim and J.M. Whitney	3
Aspects of Compression in Aerospace Composites – Future Requirements by S. Green	4
Three-Dimensional Elasticity Analysis of Buckling of Laminated Plates by A.J.M. Spencer	5
A Review of RAE Sponsored Work on the Compressive Behaviour of Composite Materials by P.T. Curtis	6
Influence of Edge Effect on Compression-Tension Fatigue of Toughened Graphite/Epoxy Laminates by J.P. Komorowski, J.B.R. Heath, D. Lefebvre, C. Roy and R. Masmoudi	7
Damage Progression under Compressive Loading in Composite Laminates Containing an Open Hole by C. Poon, N.C. Bellinger, R.W. Gould and M.D. Raizenne	8
Propagation d'un Délaminage dans un Panneau Composite Soumis à un Chargement de Compression par R. Girard	9
GARTEUR Compression Behaviour of Advanced CFRP by W.G.J. 't Hart et al.	10
Innovative Constituents Requirements to Improve Composites Compressive Strength by L. Anquez and P. Vautey	11
CFRP Stiffened Panels under Compression by A. Bucci and U. Mercurio	12
SESSION II – FLUID EFFECTS	
An Overview of Concerns Relating to Fluid Effects on Composites by G.A. Wright	13
Effects of Fuel on Hercules AS-4/8552 Composite Material by A.T. Rodriguez, A. Lavia, I. Fernandez and E. Redondo	14

† Not available at time of printing.

	Reference
Environmental Degradation of High Temperature Composites by R.C. Cochran, T.M. Donnellan, R.E. Trabocco and J. Thompson	15
Prise en Compte des Effets de l'Environnement sur le Comportement en Service des Structures Primaires d'Avions en Matériau Composite — Historique et Situation Actuelle par J. Rouchon	16
Fluid Effects: Thermoset and Thermoplastic Matrix Composites by D.B. Curliss	17
Paper 18 withdrawn	
Jet Fuel Absorption and Dynamic Mechanical Analysis of Carbon Fibre Composites by S.A. Paipetis and V. Kostopoulos	19
Fracture Surface Characteristics of Compressive Failures in Carbon Fibre Reinforced Epoxy Laminate Subjected to Hot/Wet Conditioning by S. Lee, P.C. Gaudert and R.F. Scott	20
The Effect of Heat Treatment on the Properties of PEEK and APC-2 by A. Ankara, M.J. Folkes and G. Kalay	21
Environmental Resistance of Amorphous Bonded Thermoplastic Joints by C. Voto and M. Iannone	22
Flight Service Environmental Effects on Composite Materials and Structures by H.B. Dexter and D.J. Baker	23

ISSUES IN COMPRESSION LOADING OF COMPOSITE STRUCTURES

James M. Whitney
University of Dayton
300 College Park
Dayton, Ohio 45469-0240, USA

SUMMARY

Compression loading causes difficulty in the development of test methods and failure criteria. Compression testing has produced considerable controversy with a number of different experimental methods being considered. Each method, however, often produces different values of apparent compression strength. The failure mode is the key issue, as each test method may produce a different failure mode. In addition, the failure modes often depend on fiber and matrix properties and on laminate geometry. When data is reported the failure mode is often ignored. In analyzing failure modes one must consider how relevant the test geometry and load introduction is to the actual application for which the data is being generated. Development of failure criteria also creates difficulty because of the various possible failure modes. This paper considers these issues in detail.

1. INTRODUCTION

Advancements in carbon fiber technology have given rise to considerable weight-savings potential in composite structures. Improvements in fiber tensile strength and stiffness have not, however, been matched by improvements in compressive strength. To understand the reasons for this problem, considerable research is being done in the field of compression testing. The objective is to study the behavior of composite components under compression loading and to relate their behavior and failure modes to the intrinsic properties of the materials. The final goal then is to develop a reliable method for testing the compressive strength of composites as related to design requirements.

The need to critically evaluate composite material test methods has increased in recent years due to the complex nature of data required for design considerations. The heterogeneous, anisotropic nature of fiber reinforced composites has required careful scrutiny of any test method or proposed test method from an applied mechanics point of view. Thus, a number of papers have appeared in the technical literature which addressed test methods from a theoretical standpoint. Although the importance of analysis in the development of experimental techniques is well recognized, recent attention has been concentrated in the area of failure modes associated with certain test methods [Ref. 1]. In particular, the failure mode assumed in conjunction with a given data reduction scheme may not be attained in practice. The possibility of multiple failure modes also makes it difficult to develop failure criteria for compression loading.

In the present paper test methods and failure criteria associated with compression loading of fiber reinforced composites are scrutinized.

2. COMPRESSION FAILURE MODES

Compression failure models have traditionally been based on fiber micro-buckling as the dominant failure mode. Such a model was originally suggested by Rosen [Ref. 2] and involves the buckling of individual fibers in the matrix. The lowest compression strength is obtained with the anti-symmetric mode as shown in Fig. 1. The compression strength for this failure mode

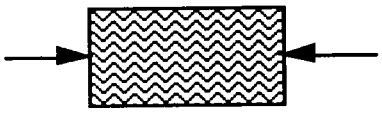

Fig. 1 Microbuckling

is given by the relationship

$$S_{LC} = \frac{G_m}{(1 - V_f)} \qquad (1)$$

where S_{LC}, G_m, and V_f are the longitudinal compression strength, matrix shear modulus, and volume fraction of fiber, respectively. For current engineering composites eq. (1) predicts a compression strength far above experimentally measured values. Lower compression strength can be predicted in conjunction with microbuckling if one considers imperfections in the form of initial curvature of the fiber [Ref. 3] or initial fiber misalignment [Ref. 4]. In these models the imperfections are assumed to be uniform. In actuality fiber curvature and misalignment are likely to be rather random. The models are valuable, however, in demonstrating the effect of these initial imperfections on compression strength if failure is due to fiber microbuckling. Fiber microbuckling as illustrated in Fig. 1 is not observed in practice as a primary failure mode. Current state-of-the-art matrix materials are stiff enough (at least at room temperature) to provide sufficient support for the fiber. If longitudinal splitting (see Fig. 2) occurs first, however, the fiber loses support and can buckle as a column. Longitudinal splitting can be initiated by transverse stresses. Such stresses can be initiated even in compression loading of a unidirectional composite due to a mismatch of Poisson's ratios between the fiber and the matrix.

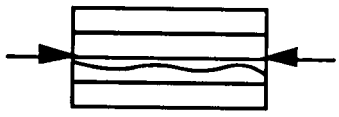

Fig. 2 Longitudinal Splitting

Another failure mode which has been discussed in detail by Hahn and Williams [Ref. 3] involves local bending or buckling of a fiber. This local fiber instability can lead to the buckling of adjacent fibers and the formation of a "kink-band" which then leads to shear crippling. A kink-band is illustrated in Fig. 3. The formation of kink-bands can be initiated in regions of voids or where the fiber.matrix interface is locally disbonded.

Fig. 3 Kink-band

The final failure mode observed in a unidirectional composite under compression loading is shear failure of the fiber (see Fig. 4). This failure mode is commonly observed in pitch base graphite fiber composites and under certain conditions can also be produced in pan base graphite fiber composites.

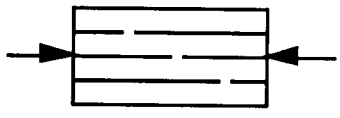

Fig. 4 Fiber Failure

The problem in characterizing composite compression strength arises from the fact that these failure modes are all possible under various circumstances. Load introduction, free-edge effects, and specimen alignment are some of the factors which may influence the failure mode. In some cases the observed failure mode is secondary to other events such as delamination.

For multidirectional laminates the 0° plies will be under biaxial loading which creates an interesting challenge relative to failure criteria. In particular consider the three loading conditions shown in Fig. 5. One would anticipate a higher compression strength in the presence of transverse compression loading (Fig. 5b) compared to pure compression (Fig. 5a). However, if the transverse load is tension (5c), one would anticipate a lower longitudinal compression strength. We envision that transverse compression would provide additional stability to the longitudinal compression loading, while transverse tension would have the opposite effect. In addition transverse tension could possibly induce longitudinal splitting followed by fiber microbuckling.

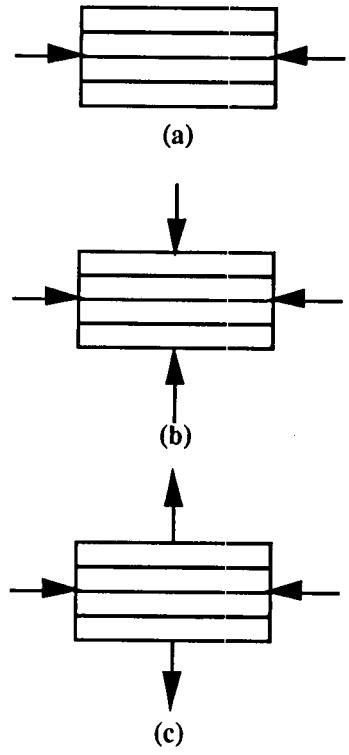

Fig. 5 Biaxial Loading

The anticipated difference in longitudinal compression strength between the loadings shown in Fig. 5 are not predictable with conventional failure criteria. Maximum stress and maximum strain do not recognize coupling between longitudinal and transverse normal stresses. For criteria which recognize coupling between stress components, such as the quadratic interaction criterion introduced by Tsai and Wu [Ref. 5], there are also problems which we will now consider. This criterion is of the form

$$\frac{\sigma_L^2}{S_{LT}\,S_{LC}} + \frac{\sigma_T^2}{S_{TT}\,S_{TC}} - \frac{\sigma_L\,\sigma_T}{2\sqrt{S_{LT}\,S_{LC}\,S_{TT}\,S_{TC}}} + \frac{\tau_{LT}^2}{T_{LT}^2} + \left(\frac{1}{S_{LT}} - \frac{1}{S_{LC}}\right)\sigma_L + \left(\frac{1}{S_{TT}} - \frac{1}{S_{TC}}\right)\sigma_T = 1 \qquad (2)$$

where σ_L, σ_T, and τ_{LT}, are the normal stresses parallel to the fibers, transverse to the fibers, and inplane shear stress, respectively. The strength parameters S_{LT}, S_{LC}, S_{TT}, S_{TC}, and T_{LT}, denote tensile strength and compression strength parallel to the fibers, tensile and compression strength transverse to the fibers, and the inplane shear strength, respectively.

The linear terms and the interaction term between σ_L, and σ_T govern the loading conditions shown in Fig. 5b and 5c. In particular, let us consider the two inplane loading conditions

$$\sigma_L = -\sigma_0, \sigma_T = \pm R\sigma_0 \qquad \sigma_0, R > 0 \tag{3}$$

Under these loading conditions eq. (2) reduces to the form

$$a\sigma_0^2 + b\sigma_0 - 1 = 0 \tag{4}$$

where

$$a = \left(\frac{1}{S_{LT}S_{LC}} + \frac{R^2}{S_{TT}S_{TC}} \pm \frac{R}{2\sqrt{S_{LT}S_{LC}S_{TT}S_{TC}}}\right)$$

$$b = \left[\frac{1}{S_{LC}} - \frac{1}{S_{LT}} \pm R\left(\frac{1}{S_{TT}} - \frac{1}{S_{TC}}\right)\right]$$

As an example, let us consider the case where R = ± 0.02 in conjunction with a unidirectional composite having the following strength properties:

$$S_{LT} = S_{LC} = 36 \text{ MPa} \qquad S_{TT} = 1 \text{ MPa}, S_{TC} = 3 \text{ MPa} \tag{5}$$

These strength values are typical of state-of-the-art graphite/epoxy materials. Substituting these strength numbers into eq. (2) we find that failure would occur at σ_0 = 46.7 MPa for the case of transverse compression loading (R=-0.02). Thus, the longitudinal compression strength is enhanced by the presence of the transverse compression loading. If we reverse the transverse load to tension (R=+0.02), then failure occurs when σ_0 = 25.0 MPa, indicating that the transverse tension load reduces the longitudinal compression strength. Now let us consider the case where transverse compression and tension are equal, i.e.

$$S_{LC} = S_{LT} = S_L = 36 \text{ MPa} \qquad S_{TC} = S_{TT} = S_T = 1 \text{ MPa} \tag{6}$$

Equation (4) now reduces to

$$\sigma_0 = \frac{2S_LS_T}{\sqrt{2\left[2S_T^2 + RS_L\left(2RS_L \pm S_T\right)\right]}} \tag{7}$$

For the case of transverse compression (R=-0.02), failure occurs at σ_0 = 33.4 MPa and for transverse tension (R=+0.02), failure occurs at σ_0 = 26.3 MPa. Thus, we obtain a lower strength by applying transverse compression in conjunction with longitudinal compression. It should be noted that the transverse stress at failure is below S_T in both cases. If we raise the transverse strength such that

$$S_{TT} = S_{TC} = S_T = 3 \text{ MPa} \tag{8}$$

then we obtain a failure stress σ_0 = 37.2 MPa for transverse compression and σ_0 = 33.2 MPa for transverse tension.

These numerical results do not make physical sense. In particular, an increase in longitudinal compression strength in the presence of transverse compression should not depend on a difference between S_{TT} and S_{TC}, assuming that $\sigma_T < S_{TC}$ at failure. In a similar manner, the sensitivity of the longitudinal compression strength to transverse compression load should not depend on S_{TC}, as long as $\sigma_T < S_{TC}$ at failure. In addition, a cursory examination of eq. (7) reveals that the value of σ_0 at failure would be identical for biaxial tension and biaxial compression. In the case of biaxial tension, one would anticipate that transverse tensile load would be detrimental or have no effect on longitudinal tension failure provided $\sigma_T < S_{TT}$ at failure. Thus, there are difficulties associated with using a quadratic interaction criterion in conjunction with the 0° unidirectional ply loading as illustrated in Fig. 5. New approaches to failure prediction for this type of loading are required.

3. COMPRESSION TESTING

In order to illustrate difficulties associated with compression test methods, we will consider two configurations of the IITRI compression test (ASTM D-3410) which produce entirely different apparent compression strength and failure modes. The conventional IITRI specimen produces apparent compression strengths and failure modes which are typical of current state-of-the-art compression test methods. The second configuration of the IITRI test involves a mini-sandwich beam consisting of composite face sheets co-cured with a core material constructed of the same matrix contained in the face sheet [Ref. 6]. The mini-sandwich beam produces fiber failure, while a very complex failure mode is associated with the standard IITRI specimen. Unidirectional data in conjunction with AS-4/3501-6 graphite/epoxy are discussed. Consideration is also given to the relationship between coupon compression data and needs of the designer.

3.1 Conventional IITRI Specimen

The conventional IITRI specimen is an option to the Celanese compression test method as described in ASTM D 3410. For the present investigation data is considered in conjunction with $[0°]_{24}$, AS-4/3501-6 composites [Ref. 7]. The specimen is a straight-sided coupon with a length of 127 mm and a width of 6.35 mm. An unsupported gage length of 12.7 mm is utilized in this test method. Specimens are gripped through tapered glass/epoxy end tabs. Compression strengths as measured from the conventional IITRI specimen are shown in Table 1. Failure was initiated near or in the end tab region with delamination being the primary mode of failure.

3.2 The Mini-Sandwich Beam

A mini-sandwich beam has been introduced by Crasto

and Kim [Ref. 6] as an alternate configuration to the conventional IITRI specimen. The original sandwich beam consisted of a composite face sheet and a metal face sheet bonded to a honeycomb core. Load was introduced through four-point bending with the composite face sheet on the compression side. This specimen is large, expensive to fabricate, and requires a large volume of material for a single specimen. In addition, premature failure often occurs in the form of crushing of the composite skin under the load nose. In the mini-sandwich beam the honeycomb core is replaced by solid resin of the same material as the matrix of the composite being tested. Composite prepreg is placed on both sides of the resin core and the unit is co-cured (or co-consolidated), eliminating the conventional adhesive layer. The specimen is then loaded in compression, using a standard IITRI fixture rather than the four-point loading configuration of the conventional sandwich beam. Back-to-back strain gages indicate that macro-buckling does not occur in the mini-sandwich specimen.

TABLE 1 Conventional IITRI Data [Ref. 7]

Geometry	Strength (MPa)
$[0°]_{24}$	1028
$V_f = 62\%$	1097
	1176
	1174
	1163
AVG	1128

Sandwich beam data obtained from Ref. 6 are shown in Table 2. The face sheets are $[0°]_2$ unidirectional composites. Typical failure modes obtained with unidirectional face sheets are shown in Fig. 6. Unlike the conventional IITRI specimen fiber fracture is the primary mode of failure. The angle of the fracture path is at approximately 75° to the specimen axis.

TABLE 2 Mini-Sandwich Data (Ref. 6)

Face Sheet Geometry	Strength (MPa)
$[0°]_2$	2105
$V_f = 65\%$	2070
	2084
AVG	2086

4. DISCUSSION

It is apparent from the data presented in Tables 1 and 2 that the ultimate composite compressive stresses obtained with the mini-sandwich beam greatly exceed those obtained with the conventional IITRI specimen. The key to this difference is the failure mode. As shown by Tan [Ref. 8], large interlaminar stresses are present under the tab region in the conventional unidirectional IITRI specimen making the specimen prone to delamination. The large loads required to fail the fiber in compression accentuate the tendency to delaminate.

From a design perspective one needs to question the relevance of the high compression strengths observed in the mini-sandwich beam. It is possible in structural applications, just as in the case of the conventional IITRI specimen, that initial failure may be in the form of delamination which will cause catastrophic failure due to fiber buckling. However, in any design situation it is important that the failure modes and processes are well understood if an intelligent design is to be performed. It is of little consequence that a structure is able to withstand its design load if the failure mode is not the one designed for. From a materials standpoint it does not make sense to attempt to improve the compression strength of the fiber if the failure process involves modes which do not invoke fiber failure. Thus, it is important to be able to measure the intrinsic compression strength and to understand the failure processes that occur under compression loading. In addition, the complex failure processes may cause considerable difficulty in developing failure criteria, as illustrated when a quadratic failure criterion was utilized in conjunction with the loading conditions shown in Fig. 5.

5. CONCLUSIONS

Experimental data reviewed in this paper indicates that the intrinsic compression strength of high performance composites may be much higher than indicated from data obtained with state-of-the-art compression tests such as the conventional IITRI method. In these specimens premature failure is often induced by large interlaminar stresses under the end tabs. Although the intrinsic compression strength may be difficult to achieve in structural applications due to other failure modes initiating the failure process, it is of practical importance to be able to determine this number. Complex failure modes and processes make it difficult to develop failure criteria for compression loading.

REFERENCES

1. J. M. Whitney, "Reflection on Development of Test Methods for Advanced Composites," *Composite Materials: Testing and Design (10th Conference)*, ASTM STP, Edited by G. Grimes, American Society for Testing and Materials, Philadelphia, 1991, in press.

2. Rosen, B. W., *Mechanics of Composite Strengthening in Fiber Composite Materials*,

American Society for Metals, 1956, Chapter 3, pp. 37-75.

3 Hahn, H. T. and Williams, J. G., "Compression Failure Mechanisms in Unidirectional Composites," *Composite Materials: Testing and Design (7th Conference)*, Edited by ASTM STP 893, Edited by J. M. Whitney, American Society for Testing and Materials, Philadelphia, 1986, pp. 115-139.

4. Wisnom, M. R., "The Effect of Fiber Misalignment on the Compressive Strength of Unidirectional Carbon Fibre/Epoxy," *Composites*, Vol. 21, No. 5, September, 1990, pp. 403-407.

5. Tsai, S. W. and Hahn, H. T. *Introduction to Composite Materials*, Technomic Publishing Co., Lancaster, PA, 1980.

6. Crasto, A. S. and Kim, R. Y., "Compression Strengths of Advanced Composites from A Novel Mini-Sandwich Beam," *Proceedings of the 22nd SAMPE Technical Conference*, Society for Advanced Manufacturing and Processing Engineers, Covina, CA, 1990, pp. 264-277.

7. Whitney, J. M. and Guihard, S. K., "Failure Modes in Compression Testing of Composite Materials", *Proceedings of the 36th International SAMPE Symposium and & Exhibition*, Society for Advanced Manufacturing and Processing Engineers, Covina, CA, 1991, pp. 1069-1073.

8. Tan, S. C. "Stress Analysis and the Evaluation of Celanese and IITRI Compression Test Specimens," *Proceedings of the American Society for Composites Fifth Technical Conference*, Technomic Publishing Co., Lancaster, PA, 1990, pp. 827-838.

A NEW TEST METHOD TO DETERMINE THE COMPRESSIVE STRENGTH OF FIBER-REINFORCED COMPOSITES

A. S. Crasto and R. Y. Kim
University of Dayton Research Institute
300 College Park, Dayton, OH 45469-0168, USA

and

J. M. Whitney
WL/MLBM
WPAFB, OH, USA

1. SUMMARY

The measured compression strength of advanced composites is sensitive to specimen inhomogeneities, loading geometry, and test conditions. Consequently, the reported "strength" is not an intrinsic material property, but simply the "failure stress under compression loading," and varies widely for a given composite system. To obtain a more accurate measure of the material property, premature failure must be avoided, and a specimen was specifically designed for this purpose. The specimen is a miniature sandwich beam with identical composite skins on either side of a neat resin core, and can be tested in axial compression as well as four-point flexure. The axial compressive properties of epoxy composites reinforced with carbon, glass, and boron filaments, and composites of carbon fibers in a polyetheretherketone (PEEK) matrix have been evaluated with this specimen in an IITRI test fixture. Failure occurred predominantly in the gage section for unidirectional composites at composite stresses and strains substantially higher than those observed with all-composite test coupons and with substantially less variation in the data. Multidirectional laminates also displayed higher strengths with the sandwich specimen.

2. INTRODUCTION

Improvements in the strength and stiffness of reinforcing fibers have promoted similar improvements in most composite properties, an exception being composite "compression strength." This "property" has either remained the same, or deteriorated, promoting extensive studies to characterize the response of a composite to compressive loading. A key requirement in the measurement of true compression strength is that the composite fail in compression, and not as a consequence of eccentric loading and/or poor specimen design or quality. Hahn and Williams [1] have defined three modes of failure for unidirectional composites under compression loading, with true compressive failure precipitated by shear failure of the fibers. While this failure mode is commonly observed in composites of low compression strength (such as those reinforced with high-modulus pitch-based carbon fibers), it has never been reported in composites of low or intermediate-modulus PAN-based carbon fibers (such as AS4 and IM8). What is generally observed in careful testing of composites of these fibers is failure via fiber microbuckling, which implies that the full compressive potential of the reinforcing fiber has not been realized.

Over the years a number of compression tests have been devised for composite materials, where specimens are directly end-loaded, loaded through shear, or loaded in four-point flexure. Specimen shapes have also varied from straight-sided coupons to tubes, rings, and sandwich structures. The most popular test method is the shear loading of a straight-sided coupon through bonded tabs in an IITRI or Celanese test fixture [2]. Refinements to this technique have included variation of the specimen gage length [3], tabs of different materials and end taper angles, both bonded and unbonded [4], and modifications to the test fixtures themselves [5]. The success of any refinement is generally measured by the increase in "compression strength" for a given composite. Implied in this belief is that "compression strength" as conventionally reported is not an intrinsic material property, but simply put, the "failure stress under compressive loading." This failure stress is determined by the failure mode, which in turn may be dependent partly on composite variables such as the strength of the interface bond or the shear stiffness of the matrix, and partly on the specimen geometry and test method. If this measured "compression strength" is not an intrinsic material property but dependent rather on specimen design and test conditions, the usefulness of this data in the design of structures subjected to compression loading is debatable. However, in an effort to evaluate the compressive properties of fibers and composites, it is necessary to develop a test technique which precludes premature failure and thereby provides a better comparison of true compressive strengths. With this in mind we have developed a miniature sandwich specimen which is a variation of the traditional honeycomb sandwich specimen.

3. DESIGN RATIONALE

There are two keys to obtaining accurate, reliable composite compression strengths. The first is related to good composite quality (minimum variations in fiber alignment and fiber volume fraction) and precise specimen

alignment with the loading axis, and with sufficient care, these can be satisfied; the second encompasses specimen design. An ideal design should minimize stress concentrations at the ends of the gage section and allow the specimen to fail in compression before the critical buckling load is reached. A sandwich structure, in which composite skins are separated by a material of lower modulus, satisfies the latter requirement: the specimen fails at a lower load (since it has fewer composite plies than a conventional specimen) and the geometry provides greater stability against buckling. Sandwich specimens have been proposed in the past [6], and a four-point flex test method which employs a sandwich specimen is also incorporated in ASTM D-3410. These specimens are large and expensive to fabricate and have therefore seen limited use. In addition a mismatch of Poisson's ratios between composite skin and core (usually an aluminum honeycomb) can cause premature debonding between the two under an applied load and artificially lower strengths. Furthermore, when tested in flexure, local crushing of the composite skin beneath the loading pins also occurs frequently, with consequent premature failure. In spite of these drawbacks sandwich specimens, in general, yield higher "compression strengths" than other specimen geometries.

To overcome the problems described above, (a) specimen size should be reduced to where it can be tested on conventional test fixtures in axial compression, (b) material and fabrication costs should be reduced, and (c) Poisson's ratios of core and skin should be better matched. Accordingly, a miniature sandwich specimen was designed to address these issues. The length and width of this sandwich specimen is the same as for conventional compression test coupons, while the volume of composite material is reduced by 67%. The aluminum honeycomb core is replaced with a slab of neat resin, and skin and core are bonded *in-situ* during composite cure eliminating the need for an intermediate adhesive layer. Furthermore, Poisson's ratios of the resin core and unidirectional composite skin are better matched than in traditional sandwich specimens. In comparison to conventional test coupons, these miniature sandwich specimens have significantly lower stress concentrations over their gage length under axial loading, as determined from finite element modeling. The longitudinal stress σ_x is maximum at the end of the gage section with a stress concentration factor of 1.4 for conventional coupons and only 1.2 for the miniature sandwich specimen [7]. These modifications should allow a more realistic and reliable estimation of composite compression strength.

4. EXPERIMENTAL

4.1 Materials

The cores of the miniature sandwich specimens were fabricated from neat epoxy resins, either 3501-6 (a 177°C-cure epoxy system from Hercules, Inc.) or Epon 828 (an epoxy resin from Shell Chemical Co.) cured with Jeffamine D-230 (a polyetheramine from Texaco Inc.), and polyetheretherketone (PEEK), which was obtained as a 0.125 mm thick film (Stabar K from ICI Americas, Inc.). The composite skins were fabricated from the following prepreg tapes: AS4/3501-6, IM8/3501-6 (Hercules, Inc.), S-Glass/1034 (Fiberite), AS4/APC-2 (ICI/Fiberite), and boron/epoxy 5505/4 (Textron, Inc.). AS4 and IM8 are intermediate-modulus PAN-based carbon fibers, and the matrices 1034 and 5505 are epoxy systems with cure cycles similar to 3501-6.

4.2 Fabrication of thermoset sandwich panels

4.2.1 Elevated-temperature cured core

A mold was constructed from two square glass plates (25.4 cm x 25.4 cm) separated by a uniform metal spacer (3.18 mm thick) along three sides. This assembly was clamped firmly together to produce a rectangular cavity approximately 22.8 cm x 20.3 cm x 3.18 mm, open at one end. The plates and the spacer were liberally coated with a release agent (Frekote 40) prior to assembly. Approximately 180 g of 3501-6 epoxy resin were melted and debulked under vacuum at 120°C for 1 hour to remove entrapped and dissolved air. The molten resin was then cast in the heated mold, heated at 120°C for another 3 hours, and cooled slowly to room temperature to yield a solid rectangular casting. A 15.3 cm x 15.3 cm square was cut from this plate, and both faces were lightly sanded and rinsed with acetone to remove residual release agent. An equal number of unidirectional fiber/epoxy plies were placed on either side of this partially cured plate, and the assembly was co-cured in an autoclave with the standard composite cure cycle. The product was a symmetric miniature sandwich panel with excellent bonding between composite skin and resin core.

4.2.2 Room-temperature cured core

In an alternative technique, symmetric multidirectional laminate face sheets were first fabricated with the standard cure cycle, lightly sanded, and then used to form the mold (replacing the glass plates in the assembly detailed above). Epon 828 (with 32 phr Jeffamine D-230) was then cast in this mold and allowed to cure at room temperature for 2 days. The result was a symmetric miniature sandwich panel with good bonding between face sheets and core.

4.3 Fabrication of thermoplastic sandwich panels

An assembly consisting of an equal number of unidirectional AS4/APC-2 plies on either side of 25 sheets of PEEK film was consolidated in a 22.9 cm x 15.2 cm closed mold under heat and pressure in a thermal press. Under an initial pressure of 70 KPa, the temperature was ramped up to 370°C in 1 hour. The pressure was then slowly increased to 350 KPa (at temperature) over 15 minutes, held constant, and the panel cooled. Flash was minimal and the sandwich panels obtained were free of warpage and displayed excellent consolidation and skin-to-core adhesion.

4.4 Testing of sandwich panels

After assuring laminate quality by ultrasonic C-scans, tensile, compressive, and four-point flex tests were

performed on specimens cut from these sandwich panels. Specimen sizes were in accordance with ASTM standards for conventional laminates, and tests were also conducted under similar conditions. Four-point flex tests were run with quarter-point loading on 12.7 mm wide sandwich beams with a span-to-depth ratio of 20:1 and a loading rate of 1.25 mm/min, and strains were measured on both composite skins (undergoing tension and compression). To prevent premature failure from local crushing under the line loading of the contact pins, thin rubber pads were placed between these pins and the specimen. Axial compression testing was performed in an IITRI fixture on specimens 127 mm long, and 6.4 mm wide. Specimens were gripped through bonded tapered glass/epoxy tabs with a gage length of 12.7 mm. Strain gages were bonded to both faces of each specimen to monitor any bending or buckling resulting from eccentric loading. An additional strain gage was bonded to the side of selected specimens to simultaneously measure axial strain in the core. Tensile tests were also performed on specimens from these panels. Failed specimens were examined in an optical microscope and also in a JEOL JSM 840 scanning electron microscope.

5. RESULTS AND DISCUSSION

By simultaneously consolidating or curing the components in a miniature sandwich panel, excellent adhesion is obtained between skin and core without the necessity of an intermediate adhesive layer. From an optical examination of sandwich cross-sections in Figure 1, it can be seen that the matrix material is continuous from skin to core with no discernible interface between the two. This is not unexpected in the thermoplastic sandwich where core and prepreg resin fuse together during panel consolidation. The continuity in the epoxy sandwich is due to the fact that the starting resin core is gelled (at 120°C) and not fully cured. This partially-cured core softens during final cure in the autoclave (at 177°C) - as determined from a measurement of dynamic shear modulus as a function of temperature - and blends with the matrix of the prepreg.

When a symmetric sandwich specimen is subjected to direct axial compression, the compressive stress (σ_S) on the composite skin can be calculated from the rule of mixtures and is written as:

$$\sigma_S = (\sigma_t - \varepsilon_t E_c V_c) / V_S \qquad (1)$$

where ε, E and V are the compressive strain, compressive modulus and volume fraction, respectively, and the subscripts t, s, and c refer to the total specimen, skin (composite), and core (resin), respectively. This expression assumes perfect skin-core bonding with identical axial strains (ε_t) throughout the specimen. Axial compression of the neat resin core revealed nonlinear stress-strain behavior for both PEEK and 3501-6 with the modulus decreasing with increasing stress. Figure 2 shows average stress-strain curves for neat 3501-6 and PEEK specimens up to the strains at which they buckle (as determined from the divergence of back-to-back strain gages). An epoxy specimen with a reduced gage length (7.6 mm) gives essentially the same curve but extends out to about 3.5% strain before buckling. The data for both PEEK and epoxy cores can be fit by quadratic equations, and differentiation of these lead to linear expressions for the compression modulus as a function of strain. These variable core moduli (E_c) were used in the above equation (1) to calculate composite compressive stresses.

Composite compressive stresses (σ_S) in the four-point flex test (at quarter-point loading) were calculated from the following expression [8]:

$$\sigma_S = PL / 8bh\,(t + h) \qquad (2)$$

where P is the load, L is the span, b is the specimen width, and t and h are the thicknesses of the core and skin, respectively.

To verify the validity of the results obtained with these specimens, miniature sandwich beams were also tested in tension. Calculated composite tensile strengths and moduli were identical to those obtained from conventional composite coupons. Furthermore, the measured strains in the skins and core were identical when these beams were loaded in either tension or compression, verifying the assumption underlying equation (1). The results of the axial compression and four-point flex tests on these miniature sandwich specimens are summarized in Table 1. Also included in this table are the average compression strengths obtained for all-composite coupons tested under similar conditions.

5.1 Compression of Unidirectional Graphite/Epoxy Composites

AS4/3501-6 unidirectional composite coupons tested in axial compression usually fail prematurely, either via global specimen buckling or from stress concentrations in the gripped region. Figure 3 illustrates one such case, where stress concentrations result in intralaminar splitting originating under the tab. As a result of premature failure, reported compressive strengths for this composite system are in the neighborhood of 1300 to 1500 MPa which is considerably lower than the value obtained from the miniature sandwich specimen. Figure 4 shows a typical composite stress-strain curve from a sandwich specimen with unidirectional 2-ply skins. The strains are the average from back-to-back strain gages, while the stresses are calculated from equation 1. What stands out in this plot is the nonlinear behavior of this material in compression and the relatively high failure stress and strain compared to conventional composite specimens. This softening in compression is attributed to a reversible reduction in fiber stiffness with increasing strain. Examination of failed specimens revealed fracture of the skin in the gage section with the fracture path at an angle of approximately 75 degrees to the specimen axis (Figure 5). This fracture was accompanied by delamination and core cracking.

Specimens with unidirectional 4-ply skins displayed composite stress-strain curves similar to those of

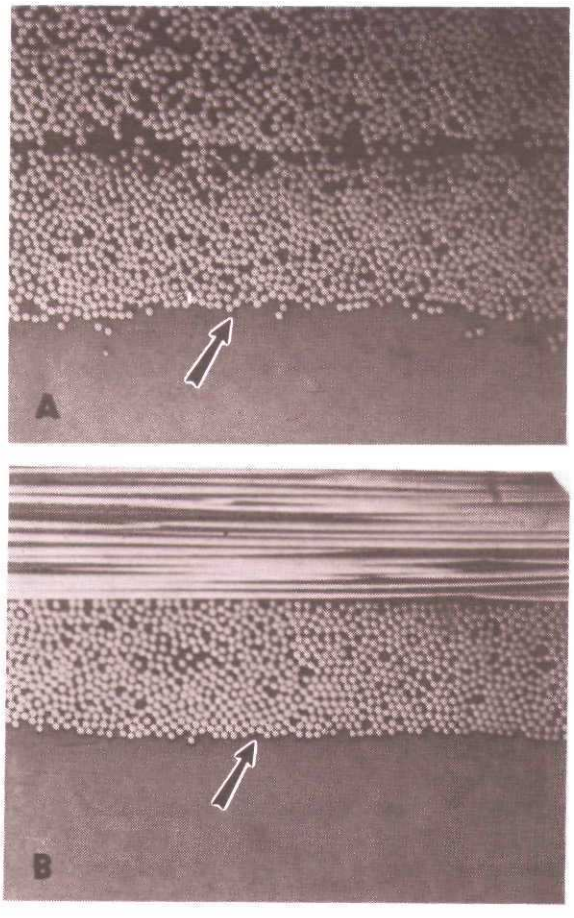

FIGURE 1. Photomicrographs of cross-sections of (A) (02/±30) AS4/APC-2 and (B) (0/902/0) AS4/3501-6 sandwich panels, displaying excellent adhesion between skin and core. (Arrows show skin/core interface region).

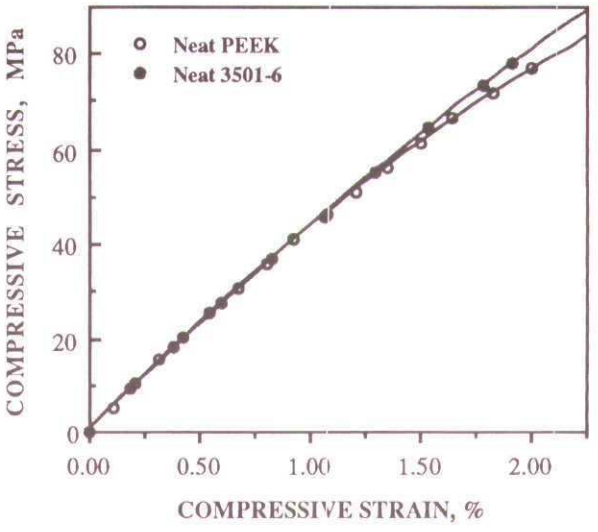

FIGURE 2. Average compressive stress-strain curves for neat PEEK and epoxy (3501-6) resins.

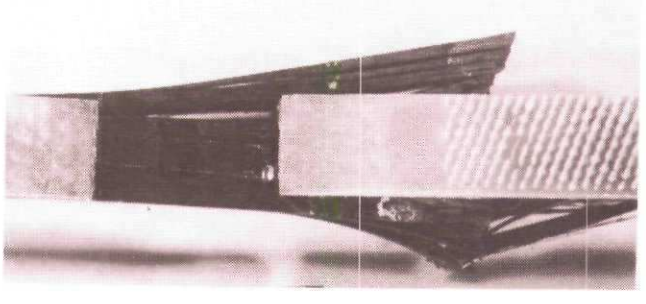

FIGURE 3. Intralaminar fracture (originating under the tab) of a 24-ply unidirectional AS4/3501-6 composite specimen tested in compression.
(Specimen width:6.35 mm)

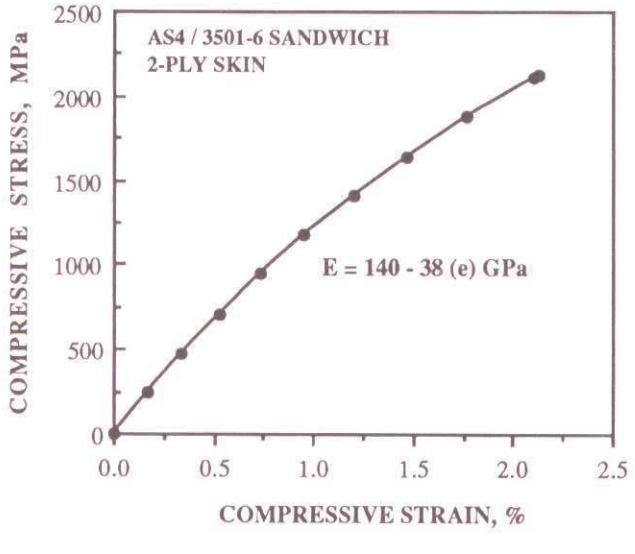

FIGURE 4. Stress-strain curve for the 2-ply composite skin of a unidirectional AS4/3501-6 sandwich specimen tested in axial compression.

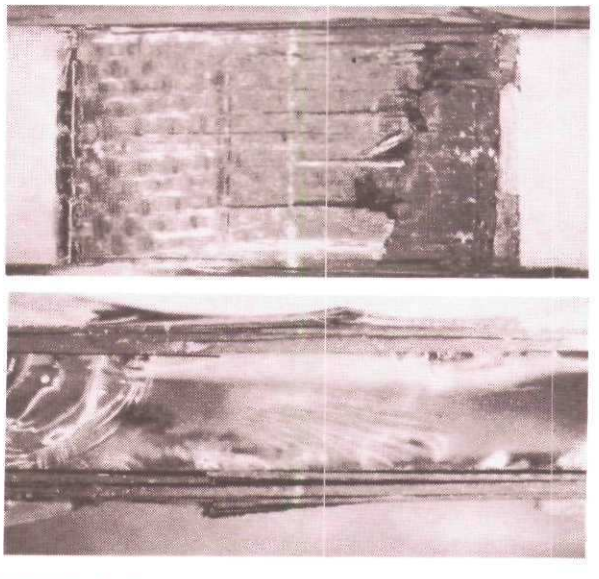

FIGURE 5. Flat and side views of the gage section of a failed 2-ply unidirectional AS4/3501-6 sandwich specimen tested in axial compression. (Specimen width : 6.35 mm)

specimens with 2-ply skins. Two such compression stress-strain curves are shown in Figure 6 for the same specimen. This specimen was initially loaded to a strain of 1.5%, unloaded to zero, and then loaded again to failure. The second stress-strain curve is almost identical to the first, demonstrating the reversible nonlinear behavior of this composite in compression. The plotted data follow a quadratic fit, and hence the compression modulus varies linearly with strain, dropping from an initial value of 144 GPa to 100 GPa at a strain of 1%. This is in contrast to the tensile stress-strain behavior of these composites, where a stiffening is noted with increasing strain [9]. The magnitude of the skin failure stress for some of these sandwich specimens (~ 2140 MPa) is of the same order as the composite tensile strength, implying that this composite is at least as strong in compression as it is in tension.

The 4-ply sandwich specimens also failed in the gage section (Figure 7) in a manner similar to that observed in the 2-ply specimens. A microscopic examination of the skin fracture surface revealed fiber fracture morphology uncharacteristic of microbuckling near the outer surface of the composite skin. A section of this surface is shown in Figure 8. The hackles across the fiber cross-sections, all oriented the same way, suggest a shearing of the fibers induced by the compressive loading. In the absence of any published micrographs on the compression fracture morphology of AS4, it is suggested that these fracture features reflect true compressive failure of the fibers. On the same composite fracture surface, but closer to the core, there was evidence of failure via fiber buckling. In this case each fiber cross-section exhibited a dual tensile and compressive fracture morphology with a distinct neutral axis and with the neutral axes of all fibers aligned in the same direction. These observations suggest that the initial compressive failure on the outer surface of a skin produces an eccentricity in the applied stress, promoting instantaneous buckling and catastrophic global failure. With an increase in each composite skin thickness to 6 (unidirectional) plies, the considerably higher applied loads promoted global buckling of the specimen and premature failure, though at composite stresses still significantly higher than observed for all-composite coupons. For the core thickness employed in this study (3.18 mm), therefore, a skin consisting of 2 to 4 plies is recommended.

IM8/3501-6 unidirectional composites displayed a similar response to axial compressive loading as AS4/3501-6. Typical stress-strain curves for all-composite and 2-ply sandwich specimens are shown in Figure 9. Both curves demonstrate a pronounced nonlinearity, and the difference in slopes is due to differences in fiber volume fractions. The average ultimate compression strength for this composite system is 2300 MPa, which is almost 10% greater than the corresponding value for AS4/3501-6. This result was unexpected, since in general an inverse correlation is observed between carbon fiber stiffness and composite compression strength. (Moduli of AS4 and IM8 are 225 and 310 GPa, respectively.)

In the four-point flex testing of these miniature sandwich specimens, failure initiated in the brittle epoxy core, presumably in that section of the core in tension. The crack then bridged the two composite skins followed by skin/core delamination in the gage section. These premature failures resulted in lower ultimate skin stresses than observed for the same panel in axial compression, although these failure stresses and strains still significantly exceed the corresponding values for all-composite coupons tested similarly (see Table 1). Successful testing in flexure may require a core material less sensitive to flaws.

5.2 Compression of Unidirectional AS4/APC-2 Composites

AS4/APC-2 miniature sandwich panels were fabricated with unidirectional 2-ply skins on either side of a PEEK core. In direct axial compression of these specimens, failure occurred at composite stresses lower than obtained with the corresponding epoxy sandwich, although substantially greater than obtained with similar (24-ply) all-composite coupons (see Table 1). The composite stress-strain curve also exhibits reversible nonlinearity similar to that seen with AS4/3501-6, but failure occurs at significantly lower strains (Figure 10). Some specimens failed in the gage section with the skin fractured at approximately 75 degrees to the specimen axis (Figure 11). Under SEM examination some fibers had a shear fracture morphology similar to that seen in AS4/3501-6 sandwich panels (see Figure 8), while others displayed the dual tensile/compressive fracture morphology typical of fiber buckling. In other specimens the composite skin buckled at a number of locations below the tab. Differences in compressive strengths between thermoplastic and thermoset composites reinforced by the same carbon fiber have been noted before. In our tests the difference in compressive strengths between AS4/3501-6 and AS4/APC-2 (normalized to the same fiber volume fraction) is less than 15%. At least part of this difference may be attributed to the significantly higher residual stresses in the thermoplastic composite.

These sandwich specimens were also tested in four-point flexure, and typical stress-strain curves for the skins in tension and compression are shown in Figure 12. The divergent curves emphasize the stiffening of the composite in tension and softening in compression. Initial failure occurred via fracture of the composite skin between the loading pins on the surface in compression at an angle of approximately 75 degrees to the specimen axis (Figure 13A). This was accompanied by interlaminar failure between the two skin plies. No other specimen damage was evident. SEM examinations of the composite fracture surfaces revealed fiber shear as the primary failure mode with skin buckling evident at some distance from this failure site (Figure 13B). The sheared faces rubbed against each other following fracture, and not much information could be gleaned from their examination. Because of the toughness of this core material and its lower sensitivity to crack propagation than the brittle epoxy, the core did not fracture prematurely in this test. Compressive strengths

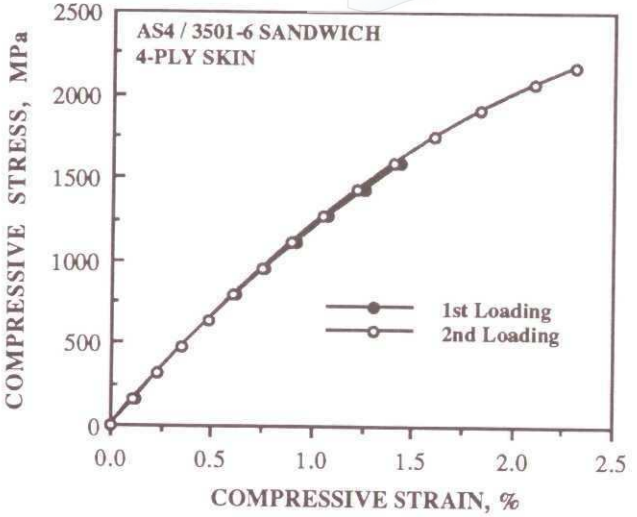

FIGURE 6. Stress-strain curve for the 4-ply skin of a unidirectional AS4/3501-6 sandwich specimen tested in axial compression.

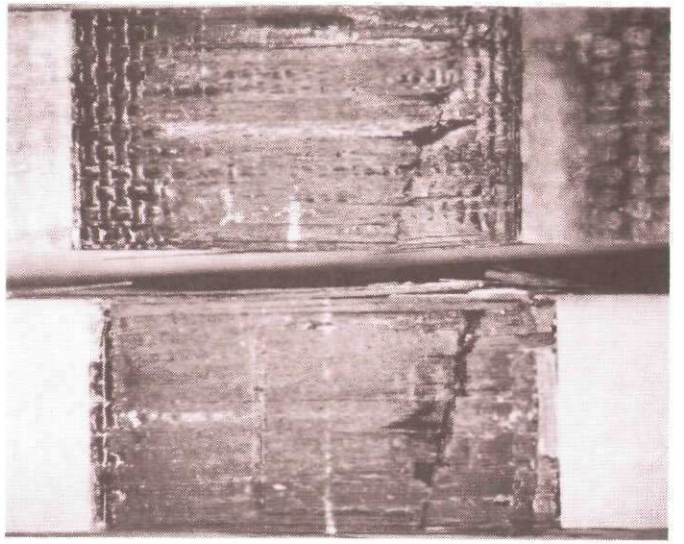

FIGURE 7. Flat views of the gage section of failed 4-ply unidirectional AS4/3501-6 sandwich specimens tested in axial compression. (Specimen width : 6.35 mm)

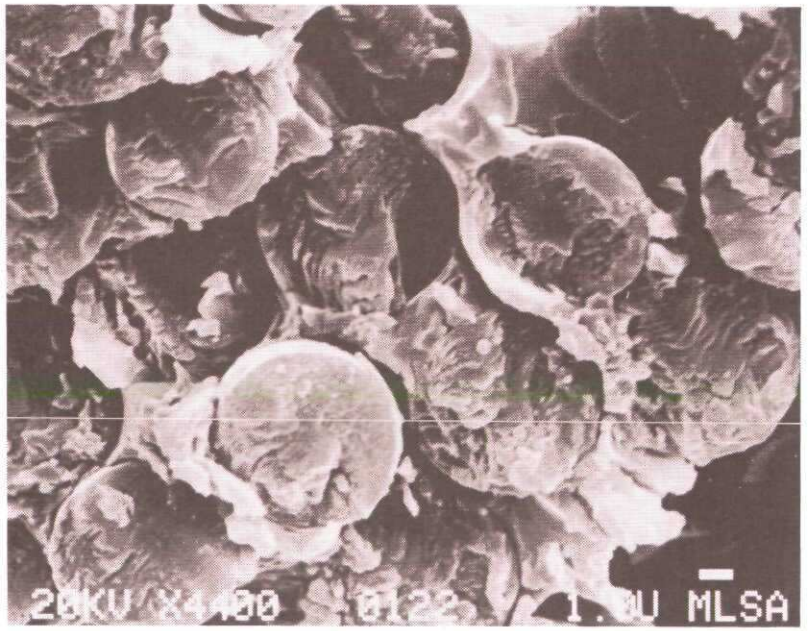

FIGURE 8. SEM micrograph of the fracture surface of the 4-ply composite skin of a unidirectional AS4/3501-6 sandwich specimen failed in axial compression.

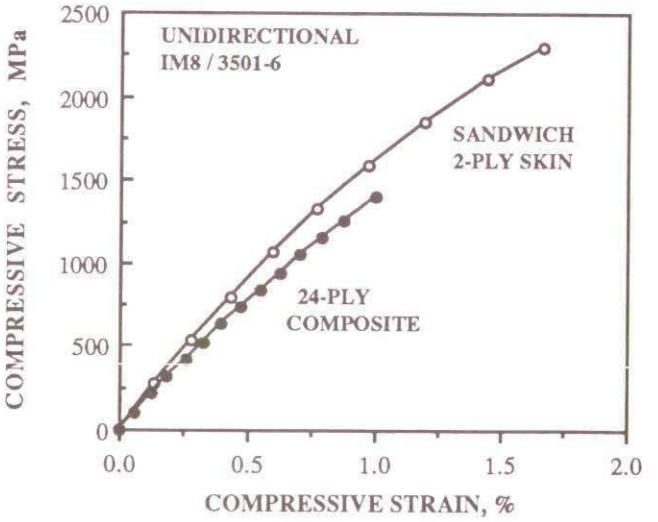

FIGURE 9. Stress-strain curves for a unidirectional IM8/3501-6 composite tested in a miniature sandwich specimen and as an all-composite 24-ply coupon.

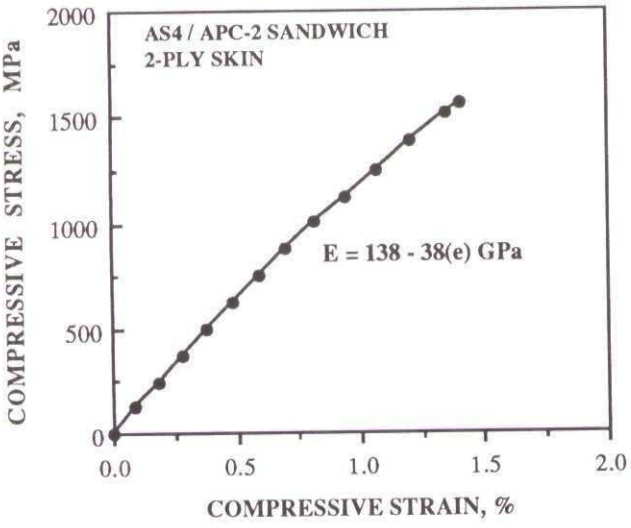

FIGURE 10. Stress-strain curve for the 2-ply skin of of a unidirectional AS4/APC-2 sandwich specimen tested in axial compression.

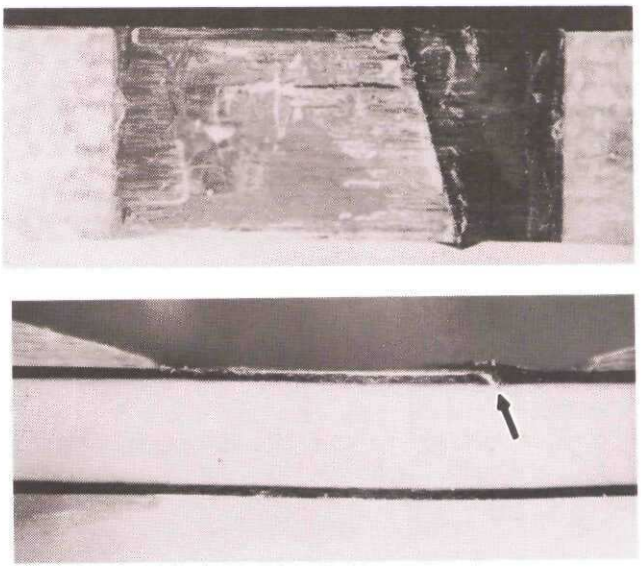

FIGURE 11. Flat and side views of the gage section of a failed 2-ply unidirectional AS4/APC-2 sandwich specimen tested in axial compression.
(Specimen width : 6.35 mm)

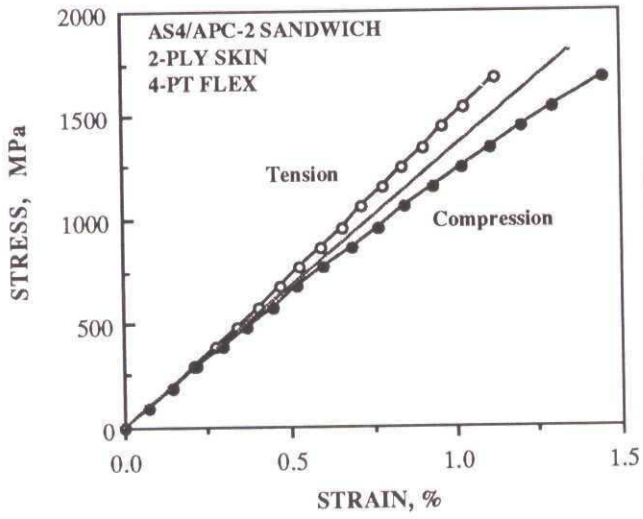

FIGURE 12. Stress-strain curves for the composite skins of a 2-ply unidirectional AS4/APC-2 sandwich specimen tested in four-point flexure.

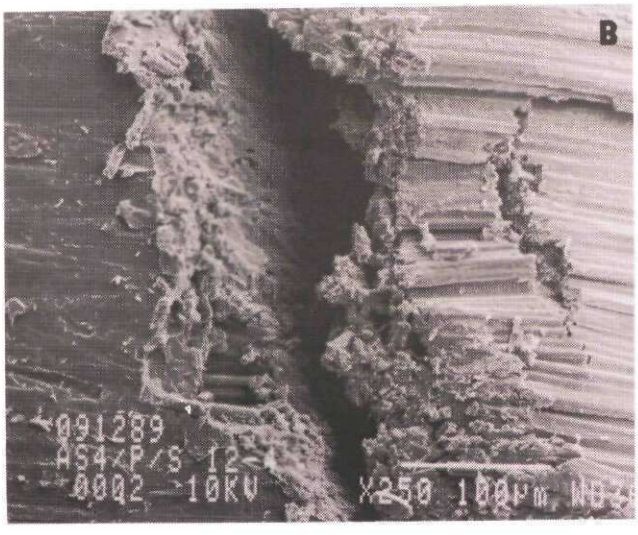

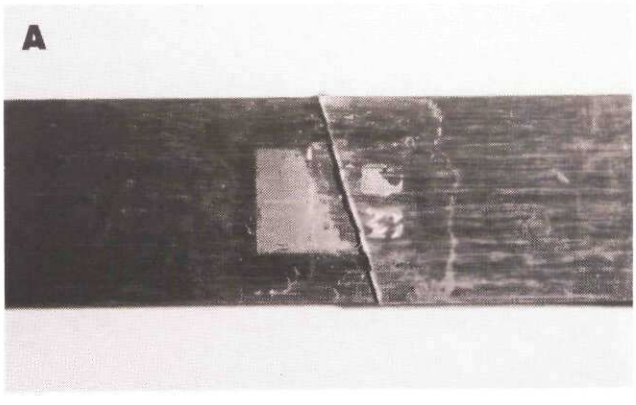

FIGURE 13. **(A)** Flat view of the gage section of a unidirectional AS4/APC-2 sandwich specimen failed in four-point flexure, showing the surface in compression. (Specimen width : 12.7 mm)
(B) SEM micrograph of the composite fracture surface of the specimen in (A).

from this test therefore match those obtained from the axial compression test (Table 1) and are in fact slightly higher.

5.3 Compression of Unidirectional S-Glass/1034 Composites

Miniature sandwich panels were fabricated with 4-ply unidirectional S-glass/1034 skins and a 3501-6 core. The skins displayed a linear stress-strain relationship in direct axial compression and failed catastrophically at composite strains approaching 4%. The stresses at failure, in excess of 2200 MPa, are believed to be the highest measured for a unidirectional glass/epoxy composite. Failure occurred via a combination of fiber fracture, longitudinal splitting and delamination, with subsequent core cracking. In contrast, unidirectional all-composite coupons tested under similar conditions buckled globally at approximately 2.5% strain, yielding considerably lower failure stresses (see Table 1). Representative composite stress-strain curves for both types of specimens are shown in Figure 14. This comparison illustrates the influence of specimen and test variables on the composite failure stress. It also clearly indicates the error in misrepresenting any failure stress under compressive loading as the intrinsic composite compressive strength without first examining the specimen stress-strain behavior and failure mode. The linear stress-strain behavior of the composite is characteristic of the glass fiber reinforcement. In conjunction with the nonlinear stress-strain behavior observed in carbon-fiber composites, these results suggest that composite stress-strain behavior is indeed a function of fiber stress-strain behavior. In the four-point flex test, the considerable bending strains experienced by these specimens resulted in premature core cracking beneath the loading pins, with attendant skin/core delamination and longitudinal splitting of the composite. As a result compressive stresses at failure were not as high as those obtained in direct axial compression.

5.4 Compression of Unidirectional Boron-Epoxy Composites

Boron is known to be stronger in compression than tension, and this high compression strength makes it difficult to avoid premature failure in compression tests on the corresponding composites. Consequently, this fiber property has never been accurately determined. Data from conventional composite tests give a filament compression strength of 850 Ksi [10]. A miniature sandwich panel was fabricated by employing a single layer of tape on either side of an epoxy core. Specimens from this panel behaved linearly under compressive loading up to failure, and had an average compression strength of 525 Ksi, which translates to a filament compression strength of 1050 Ksi. Failure occurred in the gage section, and was accompanied by longitudinal splitting.

5.5 Testing of Multidirectional AS4/3501-6 Laminates

Initial attempts to fabricate miniature sandwich panels with multidirectional AS4/3501-6 laminate skins and a 3501-6 epoxy core were unsuccessful, as multiple cracks developed in the core due to residual stresses brought on by the elevated temperature cure. To circumvent this problem the skins were first cured independently, and a room-temperature cure epoxy system subsequently cast between them to form the core.

5.5.1 Cross-Ply Laminates

A sandwich panel with [0/90/90/0] cross-ply skins was prepared in the manner described above. Direct axial compression of specimens from this panel gave an average laminate compression strength of 1080 MPa. A number of specimens were subjected to multiple loadings to progressively higher loads and examined after each loading to identify the primary failure site. These examinations revealed initial failure via fracture of the outer 0° ply near or under the tab and delamination between the outer 0° and 90° plies. The two 90° plies as well as the 0° ply in contact with the core appeared undamaged. For comparison, coupons from a $[0/90]_{4S}$ all-laminate panel were also tested in axial compression. Failure in most specimens occurred in the gage section at an average stress of 805 MPa, which is significantly lower than that obtained with the sandwich specimen. Detailed test results are shown in Table 1, and a comparison of typical stress-strain curves is shown in Figure 15. The coincidence of the two laminate stress-strain curves in this figure validates the test results obtained with this sandwich specimen. In these laminates almost all the load is carried by the 0° plies. Since there is an equal number of 0° and 90° plies, the compression strength should therefore be almost half that of a unidirectional composite. A comparison of the test results for sandwich panels with these skin orientations shows this relationship to be true. From the data it appears that, contrary to popular belief, conventional test specimens also underestimate multidirectional laminate compression strengths.

5.5.2 Quasi-Isotropic Laminates

Further laminate compression studies were conducted on two sandwich panels fabricated with quasi-isotropic skins. The first panel had 8-ply [0/45/90/-45/-45/90/45/0] skins, and for comparison, a 32-ply all-laminate panel (with identical ply configuration) was also fabricated and tested. Test results are summarized in Table 1. Surprisingly, laminate compression strengths from the sandwich panel are marginally lower than those of the all-laminate coupons. On examining the same specimen after multiple loadings to successively higher stresses, it was apparent that initial failure occurred in the outer two plies. This failure took the form of surface ply separation, surface ply fracture in the gage section, cracks within the neighboring 45° ply, and delamination of the 45° ply from the 90° ply below it. Figure 16A shows a section of the edge of one such failed specimen where all these fracture features are apparent. Figure 16B shows the flat view of a specimen after final failure. Here, the fracture path in the 0° ply is seen to follow the angle of the adjacent 45° ply, suggesting the following sequence for the failure events: initial shear failure of the 45° ply, subsequent fracture of the outer 0° ply, and finally, delamination between the outer 0°, 45° and 90° plies. In the side view of a specimen after ultimate failure (Figure 16C), delamination between

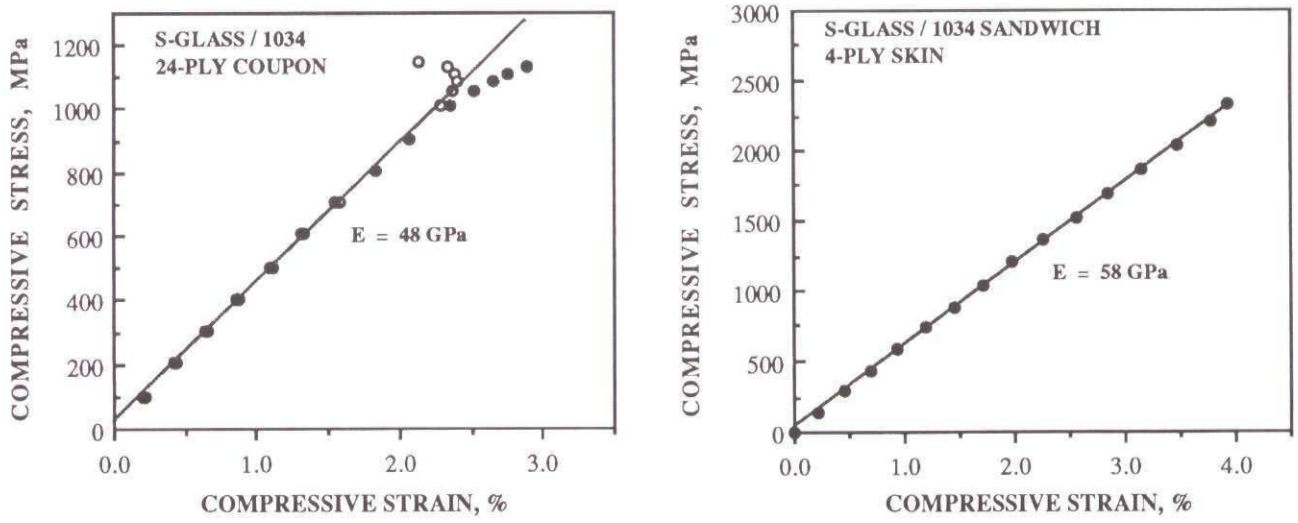

FIGURE 14. Typical stress-strain curves for unidirectional S-Glass/1034 composites tested in axial compression : 24-ply all-composite coupon (LEFT); sandwich specimen with 4-ply skins (RIGHT).

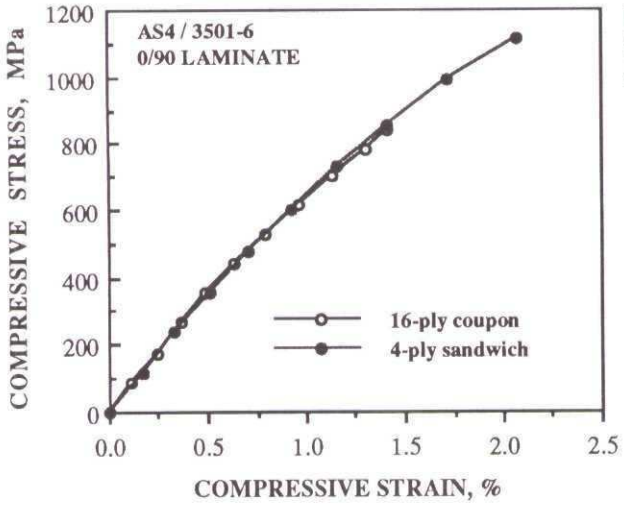

FIGURE 15. Typical compressive stress-strain curves for an AS4/3501-6 cross-ply laminate from a miniature sandwich specimen and an all-laminate coupon.

FIGURE 16. Photographs of three [0/±45/90] AS4/3501-6 sandwich specimens loaded in axial compression. (A) Edge view showing initial damage and fracture of outer 0° and 45° plies; (B) Flat view of gage section showing fracture of outer 0° ply; (C) Edge view after final failure showing separation of skin from core.

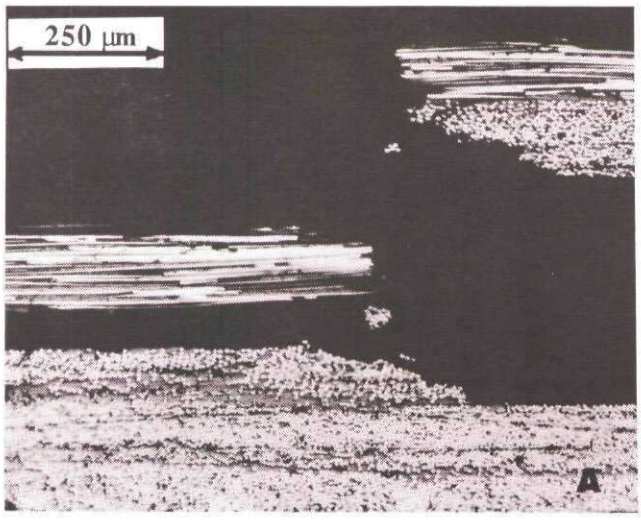

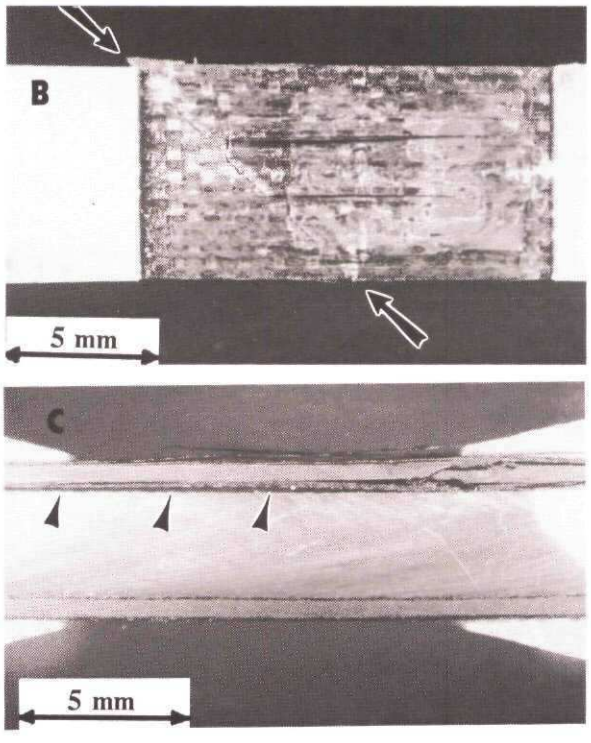

skin and core is clearly apparent in addition to the other fracture events. Initial failure of the all-laminate specimens occurred in a similar fashion, within the outer two plies. Figure 17 shows the side view of an all-laminate specimen where the load was arrested and released after observation of initial failure. An examination of this photograph shows delamination between the 45° and 90° plies under the tab and extending into the gage section, fracture of the 45° ply, and separation of the outer 0° and 45° plies over most of the gage length. After complete failure, multiple fractures and delaminations can be seen, extending into the tabbed region. From the compression strengths generated for this quasi-isotropic laminate by both specimen types, it appears that the miniature sandwich specimen offers no advantage over the conventional laminate coupon.

The results from the second sandwich panel (with quasi-isotropic 6-ply [0/60/-60/-60/60/0] skins) differ dramatically from those of the first quasi-isotropic panel. Again, a 24-ply laminate with similar ply orientations was tested for comparison. Compression strengths for both are summarized in Table 1. For this quasi-isotropic ply orientation, sandwich specimens registered a 35% higher laminate compression strength than corresponding all-laminate coupons. Initial failure was once again discerned in the outermost plies of the sandwich specimen, and surface ply separation was predominant. In this specimen, the first signs of failure were splitting, delamination and fracture of a narrow strip of the outermost ply near a free edge. This occurred at approximately 75% of the ultimate stress. In the laminate coupon, on the other hand, failure was more catastrophic with multiple delaminations and ply fractures, and the failure initiation site could not be identified. In these coupons, failure appeared to be preferentially located near the base of the tab. Comparison of sandwich and coupon test results with this laminate mirror the results from tests on the cross-ply laminates and point to the underestimation of laminate compressive strengths from conventional specimens. The coincidence of sandwich and coupon compression strengths for the first quasi-isotropic panel is likely due to the occurrence of a premature failure event, such as delamination, common to specimens of both types.

5.5.3 Free-Edge Stress Analysis

The delaminations observed in compression tests on multidirectional laminates arise from interlaminar stresses acting in the free-edge region. The magnitude and distribution of these interlaminar normal and shear stresses vary widely according to the stacking sequence and laminate type. The initiation and growth of delamination under load may cause a progressive reduction in strength, or alternatively, catastrophic failure of the laminate. When a laminated composite containing a delamination is subjected to a compressive load, the delaminated section buckles, resulting in a high interlaminar stress concentration at the delamination front (crack tip). As the load is increased the buckled area increases to a critical size which may result in a loss of global stability or total collapse of the plate.

A stress analysis was conducted to calculate the interlaminar stresses at the free edges of sandwich specimens using the global-local model developed by Pagano and Soni [11], and determine if they were sufficient to initiate delamination prior to compressive failure. From an examination of the results, the interlaminar stresses at each layer of the cross-ply and [0/±60] quasi-isotropic laminates were found to be too small to induce interlaminar failure prior to ultimate failure of the specimen. For the [0/±45/90] quasi-isotropic laminate, however, the interlaminar shear stress τ_{xz} of the second layer (between the outermost 45° and 90° plies) exceeds the corresponding interlaminar shear strength (93 MPa) at the applied failure strain. This interlaminar shear stress and the normal stress for this layer are plotted in Figure 18. In this figure, the negative ordinate denotes compressive stress in the laminate skin. In line with this calculation, initial failures observed in tests on this laminate included delamination of the surface (0°) and adjacent (45°) plies (see Figures 16 and 17). Premature failure via delamination in both sandwich and coupon specimens of this laminate would explain the comparable compression strengths and the apparent lack of an advantage in the use of the former.

6. SUMMARY AND CONCLUSIONS

The miniature sandwich beam is a novel adaptation of the conventional honeycomb-core sandwich without the disadvantages of the latter. It is simple and inexpensive to fabricate, requires a smaller volume of composite than an all-composite coupon, and can be tested with the same grips and fixtures used for conventional composite testing. The ultimate composite compressive stresses and strains obtained with this specimen greatly exceed those measured with conventional composite coupons and have much less variation. The ability to achieve these higher strains dramatizes the nonlinearity of the stress-strain curves and the significant drop in composite compressive modulus with increasing strain. For epoxy sandwich specimens with a brittle core sensitive to premature cracking under tensile loading, direct axial compression tests are preferred to four-point flex tests. For specimens with tough, less-sensitive PEEK cores, the reverse is true. With either unidirectional or multidirectional laminate skins, failure modes from carefully prepared specimens are consistent, and premature failure via global buckling or stress concentrations under the grips is eliminated. As a result measured composite compressive strengths are both reliable and reproducible and less influenced by composite and test variables than conventional coupons. These sandwich specimens have also demonstrated that, contrary to wide belief, multidirectional laminate compression strengths are also underestimated by conventional laminate coupons and test methods. Depending on the ply stacking sequence, interlaminar stresses generated in laminate specimens loaded in compression can cause delamination and premature failure, as seen in quasi-isotropic [0/±45/90] laminates. Consequently it is important to report the failure mode along with compression strength data. It must be borne in mind that the data reported here were obtained under precisely-controlled test conditions,

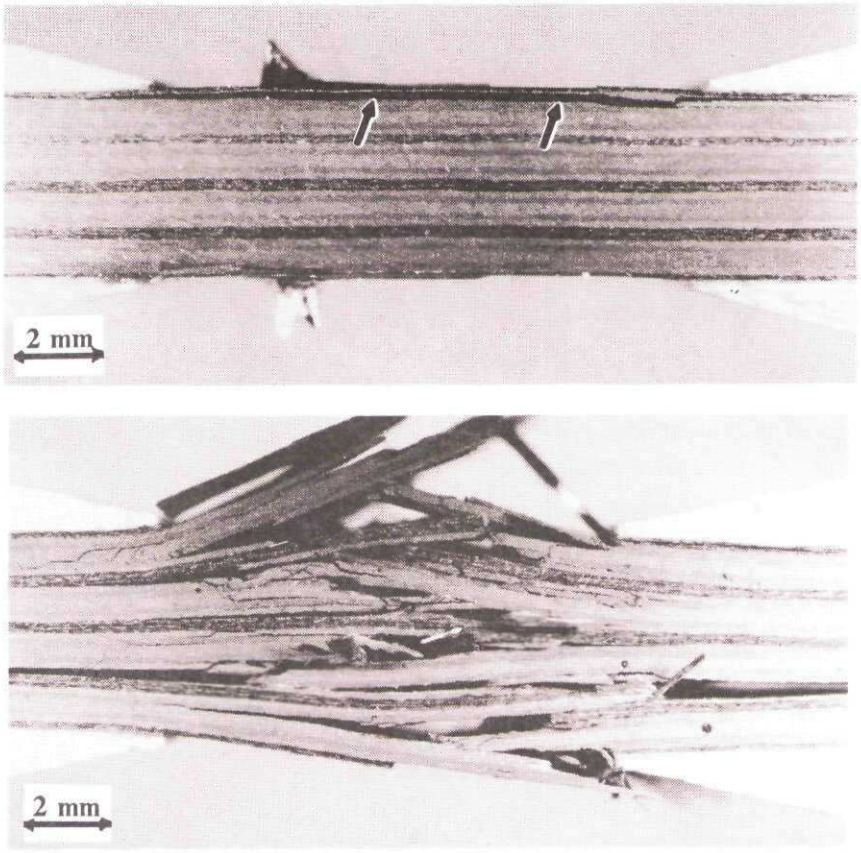

FIGURE 17. Edge views of the gage sections of [0/±45/90] AS4/3501-6 all-laminate coupons tested in axial compression : (A) after initial failure via delamination of outer 0° and 45° plies; (B) after final failure.

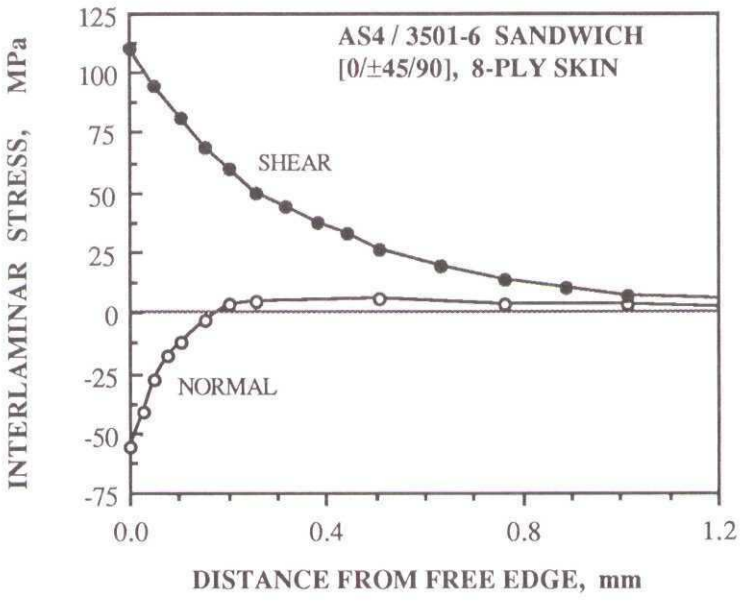

FIGURE 18. Stress distribution at the outermost 45/90 ply interface of the [0/45/90/-45/-45/90/45/0/CORE]$_S$ sandwich specimen under an applied failure strain of 1.3%.

and caution should be exercised in using these strengths to predict compressive failure in engineering composite structures.

7. REFERENCES

1. H. T. Hahn and J. G. Williams, in "Composite Materials: Testing and Design," ASTM STP 893 (American Society for Testing and Materials, Philadelphia, 1986), pp 115-139.
2. ASTM D3410-87, "Standard Test Method for Compressive Properties of Unidirectional and Cross-Ply Fiber-Resin Composites," Annual Book of ASTM Standards (American Society for Testing and Materials, Philadelphia, 1989), p 1996.
3. J. J. Scobbo, Jr. and N. Nakajima, J. Thermoplastic Compos. Mater., 3, 190-201 (1990).
4. L. J. Hart-Smith, Int. SAMPE Symp., 36, 1029 (1991).
5. J. S. Berg and D. F. Adams, J. Compos. Technol. Res., 11(2), 41-46 (1989).
6. K. E. Hofer, Jr. and P. N. Rao, J.Testing and Eval., 5(4), 278 (1977).
7. S. C. Tan (unpublished results).
8. J. M. Whitney, I. M. Daniel and R. B. Pipes, in "Fiber-Reinforced Composite Materials," SESA Monograph No. 4 (Society of Experimental Mechanics, Bethel, CT, 1982), p 184.
9. A. S. Crasto, R. Y. Kim and J. M. Whitney, Int. SAMPE Symp., 36, 1649 (1991).
10. Manufacturer's data (Textron Inc.).
11. N. J. Pagano and S. R. Soni, Int.J. Solid Structures, 19(3), 207 (1983).

TABLE 1. Composite Compression Strengths from Miniature Sandwich Specimens and All-Composite Coupons.

COMPOSITE	MINIATURE SANDWICH SPECIMEN				ALL-COMPOSITE COUPON	
	Skin Layup	Fiber Volume (%)	Compression Strength		Layup	Compression Strength
			Axial Loading* (MPa)	Four-Point Flexure (MPa)		Axial Loading** (MPa)
AS4/3501-6	0 (2 and 4 plies) [0/90/90/0] [0/60/-60] S [0/45/90/-45] S	62	**2070** **1080** **935** **605**	**1780**	0 (20 and 24 plies) [0/90] 4S [(0/60/-60) S]4 [(0/45/90/-45) S]4	**1400** **805** **685** **645**
AS4/APC-2	0° (2 and 4 plies)	57	**1570**	**1630**	0° (24 plies)	**1100**
IM8/3501-6	0° (2 plies)	62	**2300**		0° (24 plies)	**1600**
S-Glass/1034	0° (4 plies)	60	**2280**	**1430**	0° (24 plies)	**1400**
Boron/epoxy	0° (1 ply)	50	**3625**		0°	**2930**

* IITRI Test Fixture; average strengths from 5-10 specimens, coeff. of variation <5%

** IITRI Test Fixture; average strengths from 5-10 specimens

ASPECTS OF COMPRESSION IN AEROSPACE COMPOSITES - FUTURE REQUIREMENTS

Stuart Green
Materials and Development Department
BRITISH AEROSPACE
Warton, Preston, Lancashire, UK

SUMMARY

The significance of structural mass in combat aircraft cannot be overstated, as it affects all aspects of performance, particularly, turn rate, climb rate, acceleration, range and payload.

To keep the overall mass of combat aircraft to a minimum level and optimise performance, designers have over recent years exploited the benefits offered with advanced polymer composite materials. These can offer specific mechanical properties which exceed those of more conventional aircraft materials, for example the alloys of aluminium. In particular, significant benefits can be gained in relation to tensile strength and modulus.

The ability to resist loads in compression is, however, particularly important in some aircraft structures, for example the wing. For minimum mass design, the material chosen for such structures should provide superior specific compression properties. This is particularly true following low energy impact, which in many cases is barely visible, but which can lead to significant strength reductions and limit the design allowable strains.

This paper will highlight the advantages in terms of reduced mass and increased performance to be gained with composite materials, and give a general overview of the materials science aspects of compression and compression after impact. Some of the recent developments aimed at improving the reliability of compression test data will be reviewed, and recent advances in materials technology and the requirements for the future will be discussed, though this paper does not represent a rigorous treatment of the subject.

1. INTRODUCTION

Since the dawn of the aerospace age, developments in materials and production processes have led to the design and manufacture of highly efficient aircraft structures (1). For reasons of improved performance, current and future advanced combat aircraft require to be light-weight. In general, a 1% saving in the overall mass of the aircraft can yield an increase in specific excess power (which can be related to climb rate) of 1%, an increase in subsonic sustained turn rate of 1% and an increase in sustained supersonic turn rate of about 0.5%, though, obviously, the particular gains in aircraft performance depend on the aircraft design. Other benefits gained by minimising the mass of the aircraft include reduced fuel consumption rate, which leads to increased range; reduced drag because the wing and/or the frontal area of the aircraft can be smaller; increased payload and so on. High performance combat aircraft can now be produced lighter than could be achieved previously, using modern materials and by adopting design practices which take advantage of the new materials and processes available. A major class of materials which has emerged, and has been developed considerably over the last thirty or so years, is carbon fibre reinforced polymer composites, or CFC's.

Compared with other common aerospace materials, CFC's offer significant benefits in terms of their high specific mechanical properties, as illustrated in Figure 1. Based on these data, the use of CFC's in design would seem to lead to significant savings in structural mass, especially if intermediate modulus fibres are used such as T800 or IM7. However, it should be noted that the data shown in Figure 1 relate to a unidirectional carbon fibre reinforced composite material. In practice multi-angular fibre configurations are employed, resulting in quasi-isotropic mechanical properties, which are required to resist combined loading conditions. Multi-angular fibre configurations lead to a reduction in the maximum specific properties, as does the introduction of bolt holes (notches), heat and moisture. Figure 2 summarises this. However, even though the mechanical performance is lowered because of these factors, mass savings remain achievable.

Table 1 illustrates the real mass savings achieved for a range of major structural aircraft components when a metallic design is replaced with a carbon fibre composite design. It will be seen that mass savings of the order of 9-30% can be achieved. This, coupled with the fact that the properties can be tailored to suit by predetermining the fibre orientation, has aided the widespread application of CFC's in aerospace structures.

The most significant composite structure on an aircraft is the wing, and it is this structure which forms the basis of the following discussions. Table 1 shows that CFC's can lead to a mass saving of about 13% on the wing torsion box alone, and about 15% on a co-bonded wing assembly overall. Much of the weight saving is achieved through redesign; multi-spar rather than multi-rib configurations being preferred. This design results from the fact that, at the present time, post buckling strength cannot be accounted for. As a result, wing skin buckling must be avoided, which leads to the multi-spar configuration.

One major problem with polymer composites is that they are susceptible to impact damage, in which strength is lowered through the introduction of regions of impact induced delamination. Strength reduction is a particular problem when the material is loaded in compression. The type of impact which is of particular concern is low energy impact, which visibly is difficult to detect (barely visible impact damage, or BVID), but which can significantly lower the compression strength (or strain to failure) of the composite material.

During normal flight the wings of an aircraft are loaded such that the top skin is in compression and the bottom skin is under tension, though during some manoeuvres, such as inverted flight, or during landing, this loading pattern is reversed. This means that for both the top and bottom wing skins, impact induced compression strength reduction factors have to be taken into account at the design stage.

The actual mass saving achieved with a composite design depends upon the design allowable mechanical properties. These are obtained from a statistical treatment of the mechanical test results, taking into account the mean values and the variability of the test data obtained in the material testing laboratory. This means that the data obtained from coupon tests must be accurate, reliable and reproducible, and they must be obtained by methods which are representative of the loading mode being investigated. This is required to be true for all environmental conditions likely to be encountered by the aircraft in service. To achieve this, the coupon test procedures adopted, including the specimen geometry, the method of introducing the load and the rate of loading must be refined to a high level. In the case of simple tension or in-plane-shear testing this is relatively straightforward. It is not so straightforward when testing in compression. It should be noted, though, that coupon testing is only satisfactory for simple loading requirements. For complex loading conditions, structural test elements are needed.

2. TEST METHODS

2.1 Compression Testing

Compression testing is generally considered to be inaccurate and not reproducible. In consequence compression loaded composite structures may often be over designed to gain a secure margin of safety; that is, they may not be optimum mass structures. For minimum mass design, it is important, therefore, that procedures are developed which yield accurate and reliable data.

One of the simplest tests to determine the compression strength of unidirectional composite materials requires parallel sided coupons with adhesively bonded end pads. In such a test the load is introduced into the specimen as a shear load from the grips, through the end-pads and the adhesive. However, such methods yield inconsistent results. Instability and a low out-of-plane shear modulus are significant problems. Variations in the test procedure include changes in specimen geometry, sometimes with the adoption of wasted specimens, and changes the the method of introducing the load. Specimens may be with or without end-pads, which may be flat or may be machined with a radius. Sometimes self stabilising honeycomb cored sandwich specimens are used, but these specimens suffer from high cost.

Many factors can lead to inaccurate or variable data, including the choice of test method (2) and specimen preparation (3). Even the choice of adhesive required to bond the end pads can affect the result. Specimen alignment and fibre alignment within the specimen are crucial in determining the reliability of the results. Fibre misalignments as little as 3 degrees can lead to compression properties somewhere between 13 to 20% below expected values for uniaxially aligned specimens (4). All of these factors contribute towards making it difficult to achieve the necessary levels of reliability with compression data.

With the aim of overcoming some of the problems with testing in compression, BAe have developed test techniques to measure the compression strength of unidirectional, axially aligned specimens and the compression strength and modulus of specimens employing multi-angular fibre arrangements. For unidirectional specimens, this has involved the production of a modified 'Celanese' rig, employing nominally 2 mm thick specimens made from 16 plies of prepreg with bonded end pads. An example of the specimen used with this rig is illustrated inFigure 3. The test rig is illustrated in Figure 4, where it will be seen that it comprises two cylindrical specimen grips with a tubular steel sleeve to aid accurate alignment and provide lateral stability. The problem with this technique, however, is that the specimens are difficult to prepare, as often the adhesive used to bond the end pads spreads into the gauge length. This has to be removed prior to the test. Failure to do so can influence

the result. Work is ongoing in conjunction with other European aerospace companies to develop specimens which do not suffer from this problem.
For specimens with multi-angular fibre arrangements, which yield quasi-isotropic properties, BAe have developed test procedures which employ unique edge stabilisation, as shown in Figure 5. Here the specimen is parallel sided, 280 mm long, 36 mm wide and usually, though not exclusively, 3 mm thick. The stabiliser configuration ensures specimen alignment and allows for the use of specimens which do not have end-pads and which are, therefore, relatively simple to produce. In consequence, these specimens are relatively cheap. An additional feature with this test method is that whilst the specimen is in the compression rig, it may be fitted with a clip-on extensometer to enable the compression modulus to be measured along with compression strength.

More recently, other workers have developed a load transfer device which employs specimens with cylindrical geometry (5). It is claimed that this design provides an accurate, controlled and reliable means of load transfer. However, specimens of cylindrical geometry are not easily made using prepreg materials, with which flat specimens geometry is preferred.

Given the difficulties with compression testing, work in this area, in general, is likely to continue with the development of new specimen geometries and new methods for introducing the load to yield optimum values for both compression strength and modulus.

2.2 Compression-After-Impact Testing

There are a number of compression after impact tests. The three common tests are the NASA/Aircraft Industry Standard Specification (6), the SACMA Recommended Method SRM 2 (7) and a similar method, the Boeing Specification Support Standard (BSS) 7260 (8). All rely on using a small impactor to impart energy to the composite. One of the chief problems with testing in this way is that the tests do not generate design allowables (9), and the results obtained depend upon the test method and equipment (10,11).

3. MODES OF FAILURE IN COMPRESSION

Unidirectional carbon fibre reinforced composite materials, with the fibres aligned parallel to the load axis, can demonstrate several modes of failure when tested in compression. The two principally demonstrated are the micro-buckling and shear modes of failure, although often variations including transverse, branched transverse, split transverse and brooming modes are featured (12). It is worth noting that on a microscopic level, thermoset and thermoplastic composites show similar features (13).

The particular failure mode exhibited by a composite and the resulting stress at failure depend strongly upon the properties of the fibre and matrix, the fibre volume fraction, the properties of the fibre/matrix interface, the specimen geometry and the method of loading (2,12). Improvements in the compression performance of composite materials can only be brought about sensibly if the influence and interaction of the constituents is understood. Here only the role of the fibre and matrix will be considered.

3.1 Role of the Fibre

The role of the fibre in compression has been examined in previous work (14,15). Experiments involving single embedded fibres (14) suggest that compression failure initiates at a micro crack, which then propagates as a shear failure within the fibre. The results from such experiments indicate that improvements in fibre compressive properties will require changes in the micro-crystalline conformation; changes which may be brought about by heat treatment (16). However, single fibre experiments are in direct contrast with tests conducted using composite laminate specimens, which demonstrate different modes of failure, as indicated above. It has been suggested (15) that the compressive properties of the fibres limit the performance of composites only when fibres with low compressive strength are employed. For composites which contain fibres with a moderate/high compressive strength, for example T300 and AS4 fibres, compression properties are strongly influenced by the matrix and fibre/matrix interface properties, and depend upon fibre geometry and modulus.

It is worth noting that for a given fibre modulus, PAN-based fibres show a higher compressive strength than pitch-based fibres (Figure 6). In terms of composite stress/strain behaviour in compression, it can be shown (17) that highly non-linear deformation occurs in tests employing mesophase pitch based fibres, whilst PAN-based fibres exhibit linear deformation. However, whereas the results in reference 17 indicate that non-linear deformation is reversible, other works (18) have demonstrated that this form of deformation may be irreversible for composites with similar pitch-based fibres, suggesting that it is as a result of damage accumulation in the form of fibre failure. Clearly, the true mechanisms leading to failure have yet to be understood.

3.2 Role of the Matrix

The mode of failure in compression exhibited by a composite is strongly influenced by the shear modulus of the matrix (19). Principally, the matrix provides stability against fibre buckling; the onset of which is delayed with increasing matrix stiffness. For a particular fibre/resin combination, it can be demonstrated that a transition from a buckling to a shear mode of failure occurs at a particular test temperature, as the matrix stiffness changes. Clearly, if future aerospace composites are to benefit from improved fibre compression properties, then improvements in matrix shear capabilities must be achieved. Such improvements are not a feature with currently available epoxy matrices, which show now the same shear modulus as they did in the past.

4. COMPRESSION-AFTER-IMPACT (CAI)

Critical structures, for example aircraft wing skins, must be designed to account for any reduction in strength which may occur following low level impact, such as that that may occur from runway debris or from a dropped servicing tool. Any reduction in composite strength necessarily results in increased aircraft mass. Clearly it is desirable that the composite material chosen has a high resistance to impact damage. It is perhaps the post impact compression performance which presents the greatest scope for improvement with composite materials.

The kinetics of damage mechanisms in laminated composites have been considered (20) and several forms of damage accumulation have been identified including: matrix microcracking, delamination and fibre breakage. Of these, delamination is considered to be the most important.

It is difficult to identify which material properties truly dictate the impact performance of a laminated composite. Attempts to correlate matrix fracture toughness with impact performance have proved to be only partially successful, though the toughness of the matrix is an important factor (21).

4.1 Material Developments to Improve the Impact Performance

For reasons of improved toughness, leading to improved compression after impact performance, recent years have seen the development of multi-phase toughened thermoset polymer matrices, usually involving the addition of thermoplastic or rubber modifiers. However, this approach often leads to problems with their solvent sensitivity, handling characteristics and morphology. The morphological nature of the toughening agent affects the toughness performance of the matrix and, generally, this is sensitive to the processing conditions. More recently, some effort has gone into developing two phase (22) and single phase (23) tough epoxy resins, which, it is claimed, overcome the problem of morphology control. Other works have sought to improve the elevated temperature performance of thermoset resins, whilst still maintaining toughness (24). In this respect, new resins based on cyanate chemistry have been developed (25), including toughened cyanates (26) principally yielding a higher temperature performance than epoxies, but which also retain respectable levels of toughness. The requirement for a composite with a higher service temperature than that achieved with epoxies has also led to the development of bismaleimide (BMI) resins, and improved toughness BMI's (27).

It is generally accepted that the best post impact compression results are achieved with thermoplastic composites, particularly those with amorphous matrices such as polyetherimide (PEI). However, amorphous thermoplastics suffer from low solvent resistance. In consequence, much of the research and development effort on thermoplastics for aerospace has focused on semicrystalline thermoplastics such as polyether ether ketone (PEEK), which resist deterioration by all aerospace fuels, hydraulic fluids and solvents.

Though the impact performance of PEEK based composites is considered to be excellent compared with toughened epoxies in general, it can be shown (21) that some of the newest toughened epoxies have similar post impact properties to PEEK composites. This point is emphasised in Figure 7 which illustrates the compression strength after impact performance for a range of thermoset composites, compared with IM6 fibre reinforced PEEK. These data were obtained mainly at an impact energy of 9 Joules using 4 mm thick quasi-isotropic laminates. The test was based on the Boeing 7260 CAI test, employing specimens 101 mm x 152 mm. It will be seen from Figure 7 that compared with T800/5245, PEEK offers a significant advantage in terms of enhanced post impact compression strength, though it will also be seen that IM7/977-2 and T40/1983-2 show similar levels of post impact compression strength to PEEK. Damage diameter, determined by c-scan ultrasonic non-destructive testing, as a function of impact energy for PEEK/IM6 and 5245/T800 is illustrated in Figure 8. Here it will be seen that at low levels of impact energy, the diameter of the delaminated region is significantly less for IM6/PEEK. It appears that for this material there is a threshold level, below which no delamination is detecting using the c-scan method adopted. In this case the threshold level is about 17 Joules.

In an attempt to improve the impact performance of composites, some workers (28) have introduced thermoplastic layers into the composite, the so called interleaving concept. Although improvements can be gained using this method, there is an unacceptable decrease in general mechanical properties.

At the present time, thermoplastics are not widely used throughout the aerospace industry even though they are, in general, more resistant to impact damage than thermosets. This can be explained partly by the fact that high processing temperatures and pressures are usually required (Figure 9), and partly by the fact that thermoplastic prepregs have no or little tack and have limited drape (except for the various forms based on blended fibres). Thermoplastics do, however, present certain advantages in that they require no refrigeration, they can be reworked, and can be welded. Though impact damage can significantly limit the compression performance of a polymer composite material, it should be remembered that the strength, in both tension and compression, is lowered by the introduction of notches, and as a result of fibre misalignment and waviness (29-34). In practice, notches take the form of bolt holes, and fibre misalignment, however small, is a feature of composite components manufactured in the production environment. Fibre waviness is governed by the form and quality of the prepreg. The effect of these factors on the performance of composites is documented in the literature and will not be discussed here.

5. CONCLUDING REMARKS

Future combat aircraft may fly faster and, in consequence, be hotter than current aircraft (Figure 10), or they may have local 'hot-spots' caused by local jet efflux. Future aerospace materials may be required to perform at temperatures in excess of 200 degrees centigrade, and may be required to demonstrate similar levels of post impact compression strength as the best currently available epoxies. The aim may also be for lighter aircraft for an efficient vertical take-off or landing capability or for high agility, placing greater mechanical performance demands on the materials used.

It is probably safe to say that whatever other criteria are placed against a particular material, improved compression performance, particularly post impact will be a priority requirement.

It is evident from the above discussion that improvements in these properties will require matrices with improved shear capabilities, to gain benefit from the compression strength of the reinforcing fibres, and with a high fracture toughness for improved damage tolerance.

From an engineering viewpoint, a greater understanding of the mechanisms of damage formation is needed, as is a method of predicting the level of damage and the resulting strength reduction following an impact of multiple impacts.

In addition, from a production point of view, the matrix should be 'user friendly' (non-toxic) and be cheap enough to yield low cost prepreg. Ideally, it should be capable of being processed at a relatively low temperature (somewhat below 177°C) in order to reduce processing costs. The prepreg should possess good tack, good drape, have a long (preferably indefinite) shelf life and be easily repairable as a cured laminate.

ACKNOWLEDGEMENT

Many thanks to my colleagues at BAe for supplying certain data and figures which have been used in this paper.

REFERENCES

1. T.Sharples, "Advances in Materials Technology and their Applications to Military Aircraft," Proc. Instn. Mech. Engrs. Vol. 204, (1990).

2. D.H.Woolstencroft, A.R.Curtis and R.I.Haresceugh, "A Comparison of Test Techniques Used for the Evaluation of the Unidirectional Compressive Strength of Carbon Fibre-Reinforced Plastic," Composites, October (1981).

3. A.K.Munjal, "Material Characterisation Problems Leading to Inaccurate Composite Design Allowables," 35th International SAMPE Symposium, p 697, (1990).

4. A.E.Pearon, "Capabilities of Compression Test Methods for Evaluating Unidirectional Carbon Fibre Reinforced Composites," 36th International SAMPE Symposium, p 1079, (1991).

5. B.R.Spence, "Compressive Load Transferring Device (End Fitting) For FRP Composite Materials," 35th International SAMPE Symposium, p 1494, (1990).

6. "NASA/Aircraft Industry Standard Specification for Graphite Fibre/Toughened Thermoset Resin Composite Material," NASA Reference Publication 1142, NASA Scientific and Technical Information Branch, 1985.

7. "Suppliers of Advanced Composite Materials Association (SACMA) Recommended Test Method SRM 2-88," SACMA, Arlington, VA, 1988.

8. "Advanced Composite Compression Tests", Boeing Specification Support Standard BSS 7260, rev C, 1988.

9. P.Sjoblom and B.Hwang, 34th International SAMPE Symposium (1989).

10. R.Falabella, K.A.Olesen and M.A.Boyle, "Variations in Impact Test Methods for Tough Composites," 35th International SAMPE Symposium, p 1454 (1990).

11. J.Prandy, J.Boyd, H.Recker and V.Altstadt, "The Effect of Absorbed Energy on the CAI Performance for Composite Materials," 36th International SAMPE Symposium, p 901 (1991).

12. E.M.Odom and D.F.Adams, "Failure Modes of unidirectional Carbon/Epoxy Composite Compression Specimens", Composites, Vol. 21, No. 4, July (1990).

13. D.Purslow, "Fractography of Fibre-Reinforced Thermoplastics, Part 3 Tensile, Compressive and Flexural Failures," Composites, Vol. 19, No. 5, September (1988).

14. D.J.Boll, R.M.Jensen and L.Cordner, "Compression Behaviour of Single Carbon Filaments Embedded in an Epoxy Polymer," Journal of Composite Materials, Vol. 24, Feb (1990).

15. S.Kumar and T.E.Helminiak, "Compressive Strength of High Performance Fibres," SAMPE Journal, Vol. 26, No. 2, March/April (1990).

16. D.K.Brown and W.M.Phillips, "Effects of Heat Treatment on Carbon Fibres," 35th International SAMPE Symposium, p 2052, (1990).

17. K.Kubomura and N.Tsuji, "Compression Nonlinearity of Pitch-Based High Modulus Carbon Fibre Reinforced Epoxy Composites and Structural Responses," 36th International SAMPE Symposium, p 1664 (1991).

18. J.M.Prandy and H.T.Hahn, "Compressive Strength of Carbon Fibres," 35th International SAMPE Symposium, p 1657, (1990).

19. P.D.Ewins and R.T.Potter (1980) "Some Observations on the Nature of Fibre Reinforced Plastics and the Implications for Structural Design," Phil.Trans. R.Soc. London A294, 507-17.

20. A.J.Lesser and A.G.Filippov, "Kinetics of Damage Mechanisms in Laminated Composites," 36th International SAMPE Symposium, p 886 (1991).

21. K.Srinivasan, W.C.Jackson and J.A.Hinkley, "Response of Composite Materials to Low Velocity Impact," 36th International SAMPE Symposium, p 850, (1991).

22. L.A.Pottick, "Recent Advances in Toughened Epoxy Resins with Kraton Thermoplastic Elastomers," 35th International SAMPE Symposium, p 1609, (1990).

23. M.Sugimori, et al, "Highly Damage Tolerant Prepreg System Based on Single Phase Matrix Resin," 36th International SAMPE Symposium, p 863, (1991).

24. J.Riviere, A.Leroy and G.Walton, "Toughened Epoxy Products for Advanced Composites," 36th International SAMPE Symposium, p 1406, (1991).

25. F.W.Lee, M.A.Boyle, P.Lefebvre and J.Botman, "High Service Temperature, Damage Tolerant Prepreg Systems Based on Cyanate Chemistry," 35th International SAMPE Symposium, p 162, (1990).

26. P.C.Yang, D.M.Pickleman and E.P.Woo, "A New Cyanate Matrix Resin with Improved Toughness - Toughening Mechanism and Composite Properties," 35th International SAMPE Symposium, p 1131, (1990).

27. I.Gawin, "A New Tough Bismaleimide Resin System for High Performance Composites," 35th International SAMPE Symposium, p 443, (1990).

28. J.L.Frazier and A.Clemons, "Evaluation of the Thermoplastic Film Interleaf Concept for Improved Damage Tolerance," 35th International SAMPE Symposium p 1620, (1990).

29. M.R.Wisnom, "The Effect of Fibre Misalignment on the Compressive Strength of Unidirectional Carbon Fibre/Epoxy," Composites, Vol. 21, No. 5, September (1990).

30. D.O.Adams and M.W.Hyer, "Fabrication and Compression Testing of Layer Waviness in Thermoplastic Composite Laminates," 36th International SAMPE Symposium, p 1094, (1991).

31. I.M.Kowalski, et al. "The Effect of Small Angular Fibre Misalignments and Tabbing Techniques on the Compressive Performance of Carbon Fibre Composites," 35th International SAMPE Symposium, p 1479, (1990).

32. A.Mrse and M.R.Piggott, "Relation Between Fibre Divagation and Compressive Properties of Fibre Composites," 35th International SAMPE Symposium, p 2236, (1990).

33. C.Soutis and N.A.Fleck, "Static Compression Failure of Carbon Fibre T800/924C Composite Plate with a Single Hole," Journal of Composite Materials, Vol 24, May (1990).

34. C.Soutis, N.A.Fleck and P.T.Curtis, "Hole-Hole Interaction in Carbon Fibre/Epoxy Laminates Under Uniaxial Compression," Composites, Vol. 22, No 1, January (1991).

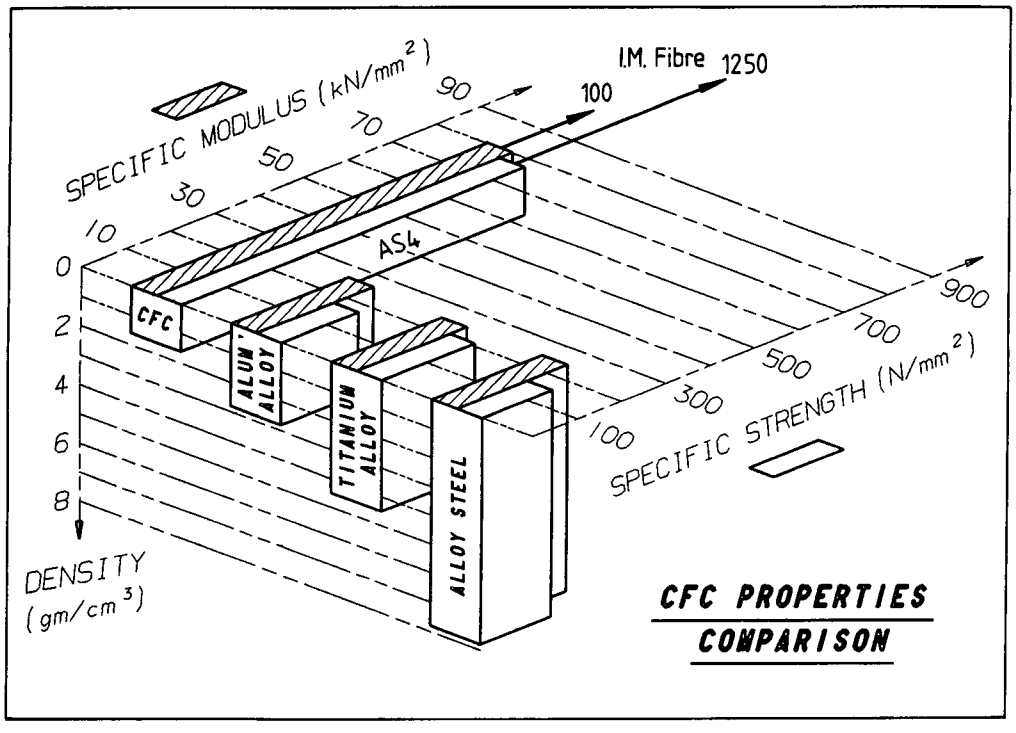

Fig 1. Properties comparison for a number of common aerospace materials. The CFC data relate to a unidirectional laminate.

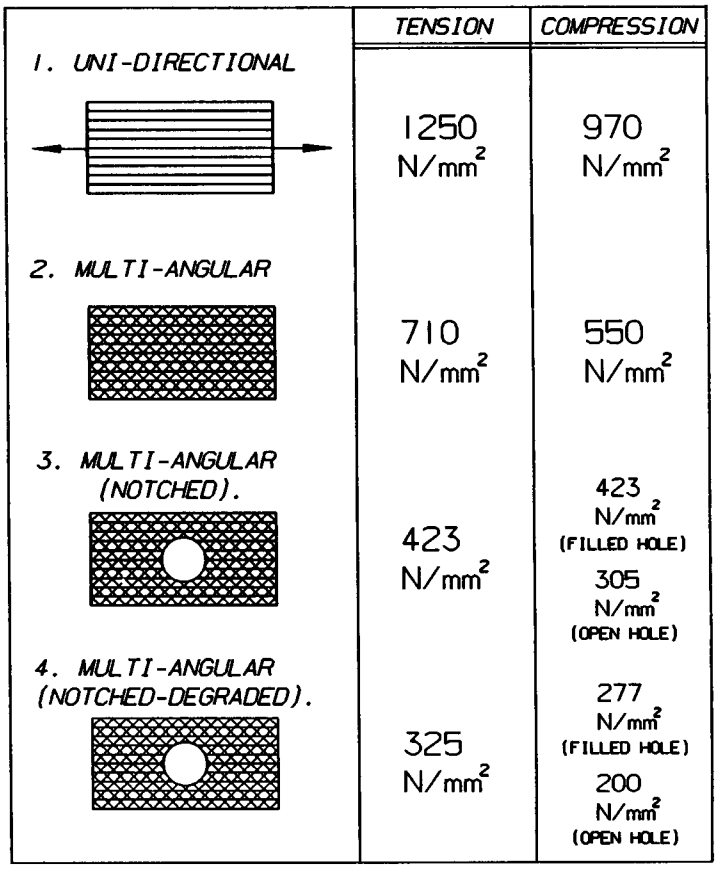

Fig 2. Tension and compression strength reduction through the introduction of a notch and as a result of heat and moisture (case 4).

C.F.C. -V- METALLIC.

COMPONENT	METAL (kg.)	C.F.C. (kg.)	SAVINGS	
			kg.	%
TAILERON TORSION BOX.	146	122	24	16,4
ACCESS DOORS (HINGED).	107	86	21	19,6
ACCESS PANELS (BOLTED).	26,3	18,5	7,8	29,6
WING TORSION BOX (FABRICATED).	642,2	560	82,2	12,8
FABRICATED WING ASSEMBLY.	892	811	81	9,1
FIN TORSION BOX.	276	227	49	17,5
FOREPLANE.	120	106	14	12
WING TORSION BOX (CO-BONDED).	1802	1563	239	13
CO-BONDED WING ASSEMBLY.	1147	997	170	15

Table 1. Mass comparison for a number of aerospace components: Metallic versus non-metallic.

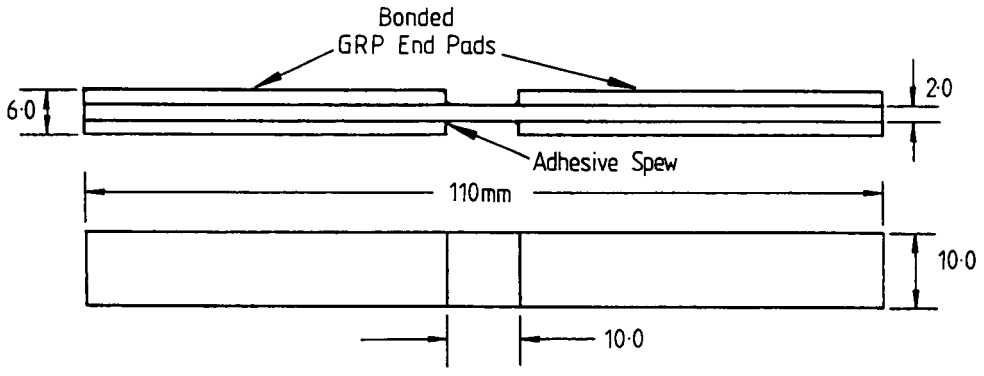

Fig 3. Compression strength test specimen.

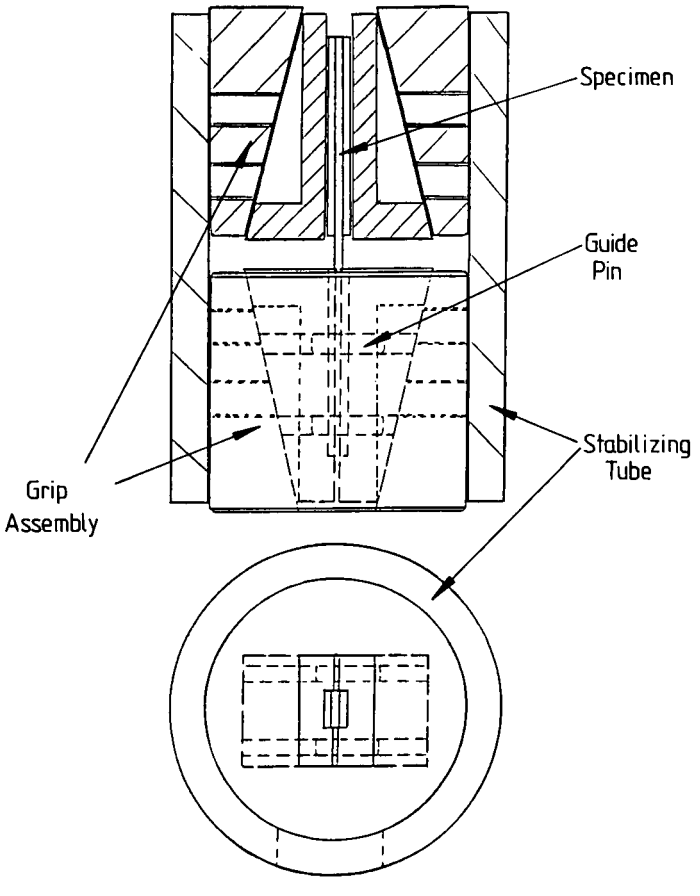

Fig 4. Modified Celanese compression rig.

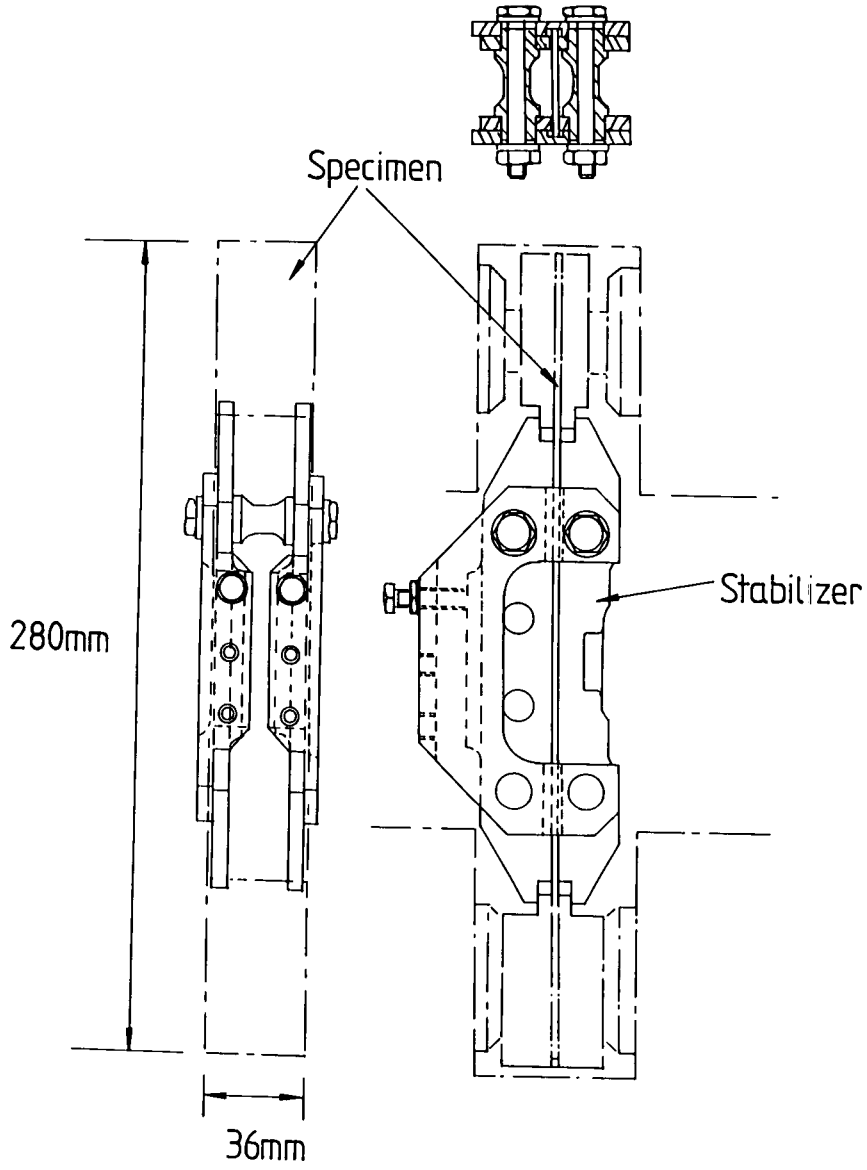

Fig 5. Stabilised compression specimen with a multi-angular (0/±45/90) fibre orientation.

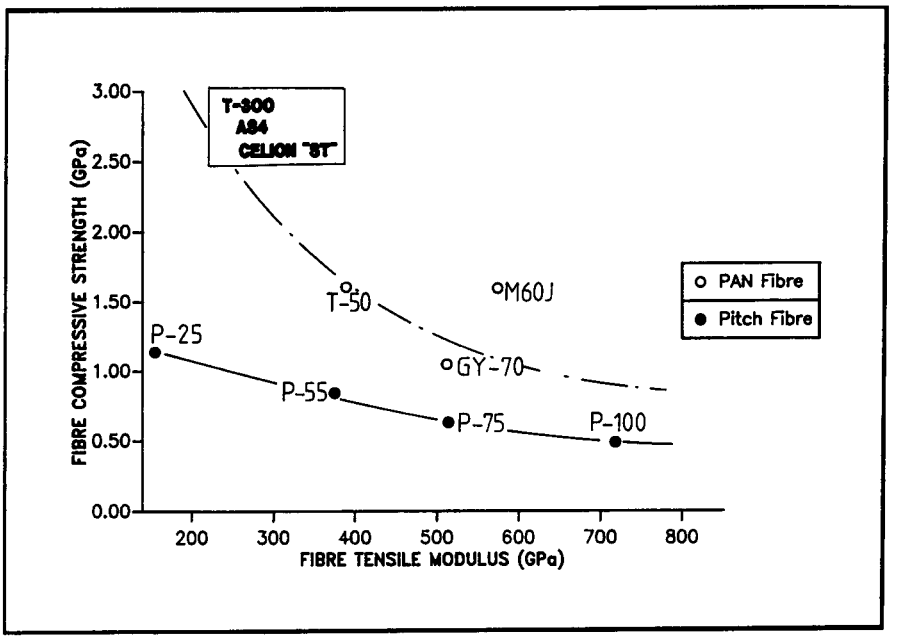

Fig 6. Comparison of fibre properties. (Reproduced from ref. 15).

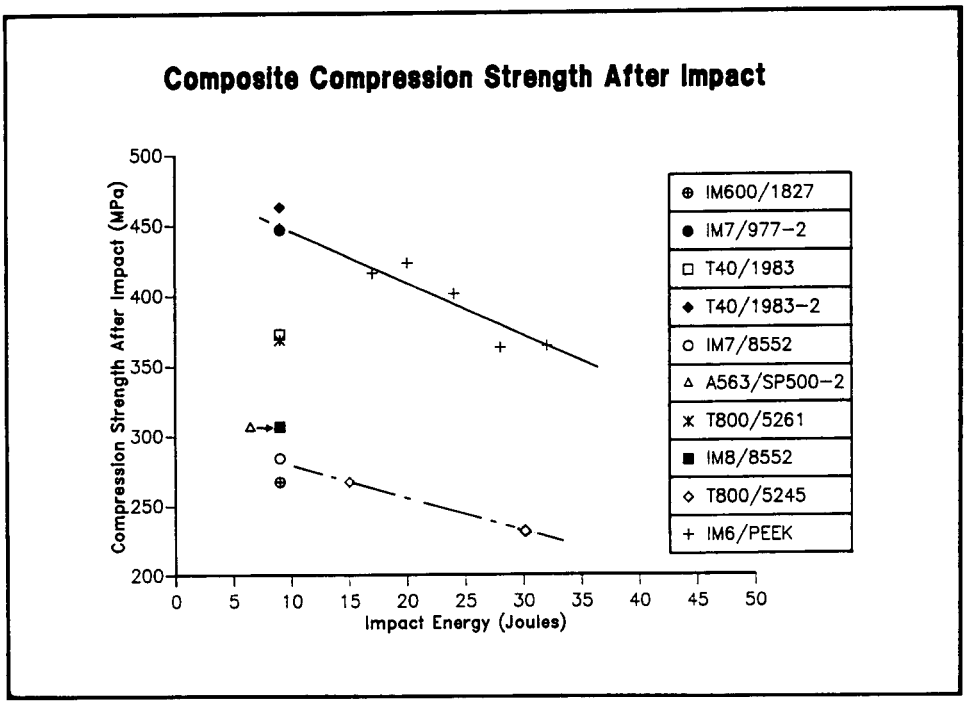

Fig 7. Compression strength after impact results for a range of composite materials. Tests based on the Boeing 7260 CAI test.

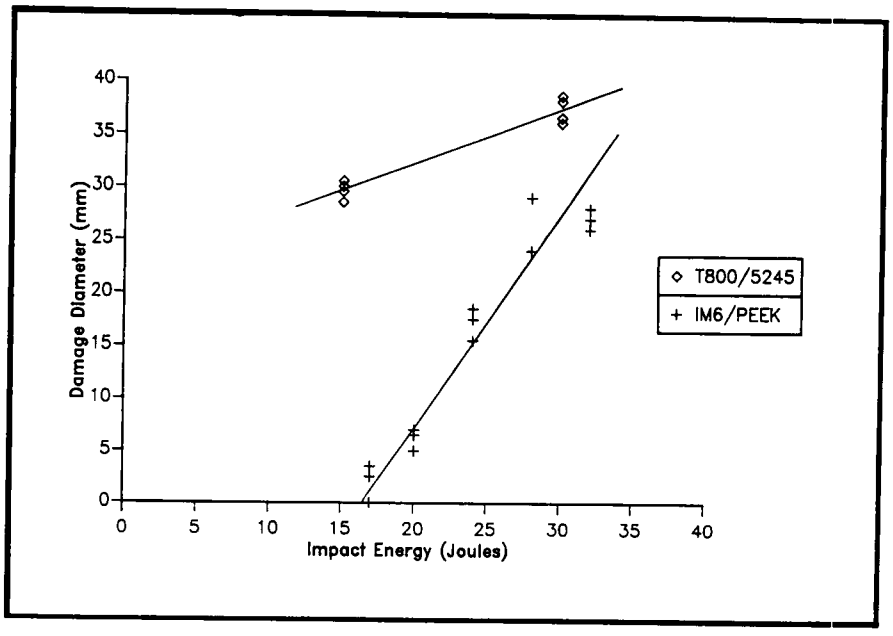

Fig 8. Damage diameter as a function of impact energy for IM6/PEEK and T800/5245.

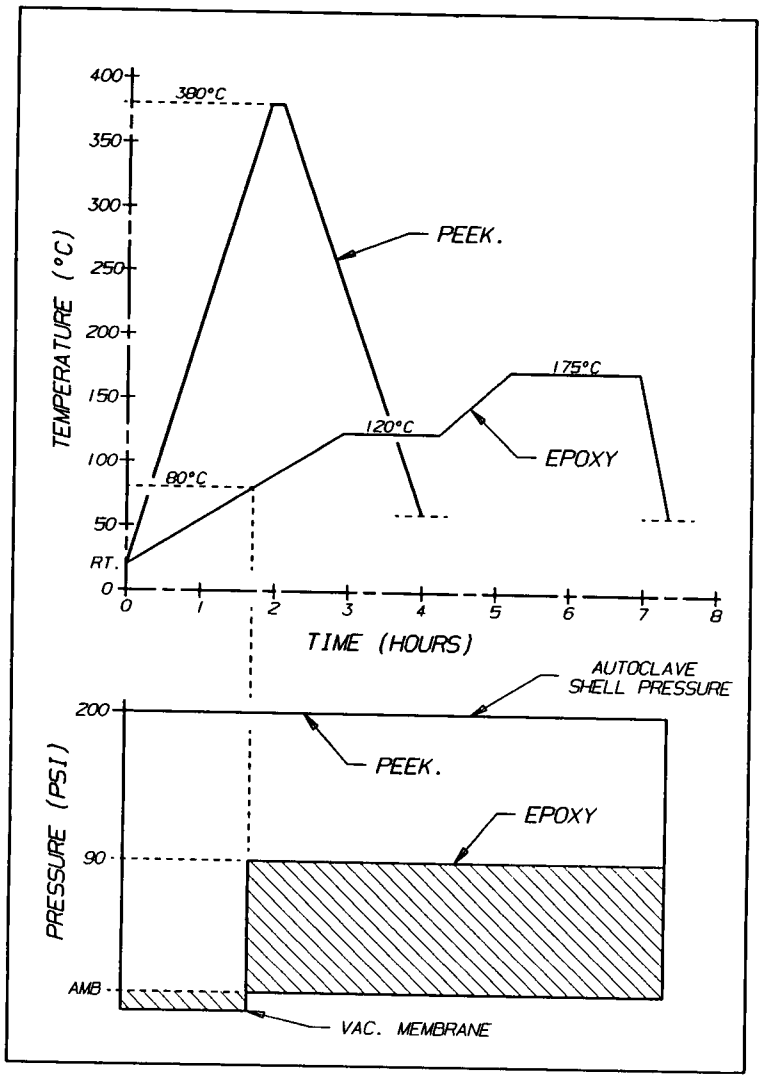

Fig 9. Pressure/temperature/time processing cycle for PEEK and epoxy composites.

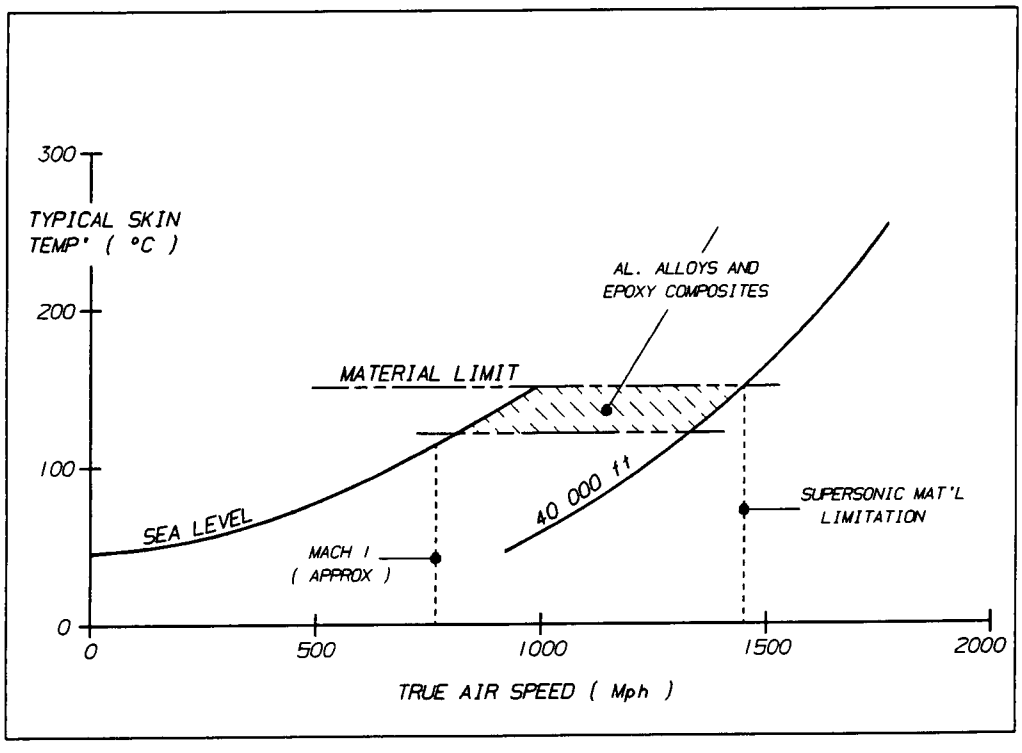

Fig 10. Skin temperature versus true air speed.

THREE-DIMENSIONAL ELASTICITY ANALYSIS OF BUCKLING OF LAMINATED PLATES

A. J. M. SPENCER

Department of Theoretical Mechanics,
University of Nottingham,
Nottingham, NG7 2RD, U.K.

ABSTRACT

The analysis of failure mechanisms for laminated composite materials depends, in the first place, on obtaining a three-dimensional analysis of the elastic stress and deformation in the material, with particular regard to interlaminar stresses. The author and colleagues have developed a procedure for the solution of the equations of three-dimensional linear elasticity for the determination of stress and deformation in laminated plates. The plate is assumed to be composed of anisotropic elastic material containing any number of orthotropic plies with any specified orientations.

A transfer matrix method is used which determines, to any desired degree of accuracy, the stress and displacement at any point in the plate in terms of the stress and displacement at a reference surface, for example the mid-plane. The two-dimensional differential equations governing these reference surface values are found to be the same as those for an equivalent homogeneous plate whose constant elastic moduli are appropriately weighted through thickness averages of the ply elastic moduli. These standard two-dimensional equations may be solved by any available technique, including numerical methods. The appropriate two-dimensional solution then generates the three-dimensional solution in a straight-forward manner.

In this paper we apply this approach to the investigation of elastic buckling of plates subject to pre-stress which may be due to applied initial stress residual stress, thermal load or moisture absorption. Buckling is treated in the usual way as a bifurcation from the initially stressed state, giving rise to an eigenvalue problem. Specific examples for particular plate geometries are described.

1 INTRODUCTION

Most studies of buckling of laminated plates have been based on classical laminate theory, which is described by, among others, Jones [1], Christensen [2] and Whitney [3]. In effect, classical laminate theory approximates the behaviour of a laminated plate by that of a homogeneous plate whose mechanical properties are suitably weighted averages of the properties of the laminate. As such, classical laminate theory is an excellent theory which has been successfully applied to numerous problems in the stress analysis of laminates.

However, like all theories, classical laminate theory has limitations. Since it deals with through-thickness averaged quantities, it cannot directly determine through-thickness variations of stress and displacement, which include important quantities such as interlaminar shear stresses. It is also based on the Euler-Bernouilli bending hypothesis, which exact solutions have shown [4] to be a very coarse approximation for strongly anisotropic laminates, and which neglects transverse shear deformation.

Various refinements of classical laminate theory have been proposed, such as the so-called higher order theories [2]. The point of view adopted here is that rather than develop such theories it is preferable to revert to three-dimensional elasticity theory, the validity of which is not in question. Significant advances have been made recently [5,6] in three-dimensional stress analysis of laminated plates and shells, using propagator or transfer matrix methods. In this paper we apply such methods to the buckling of laminated plates, treating buckling as a bifurcation from a state of initial stress (an alternative approach is to use energy methods [3] but these are not considered here). The initial stress may be due to mechanical loading, but may also arise from thermal or hygroscopic expansion stress [3,5].

2. EQUILIBRIUM OF A PLATE WITH INITIAL STRESS

The theory of equilibrium of elastic bodies with initial stress was developed by Biot [7]. A concise account of the theory is given in Whitney [3].

The system is described in terms of a set of rectangular cartesian coordinates $Ox_1x_2x_3$, and vector and tensor components are referred to this system. We employ suffix notation and the usual summation convention.

We consider a body which in its reference configuration is in a state of initial stress $\underset{\sim}{S}$ with components S_{ij}. The body undergoes a small incremental displacement $\underset{\sim}{u}$ (components u_i) from this reference configuration, which gives rise to an incremental stress. The equilibrium equations in this deformed configuration are expressed in terms of the Kirchhoff stress tensor $S_{ij} + \sigma_{ij}$ as

$$\frac{\partial}{\partial x_i}\left\{(S_{ik}+\sigma_{ik})(\delta_{jk}+u_{j,k})\right\} = 0 , \qquad (2.1)$$

where δ_{jk} is the Kronecker delta and $(\ )_{,k}$ denotes differentiation with respect to x_k. We assume the initial stress $\underset{\sim}{S}$ to be in equilbrium, so that

$$S_{ij,i} = 0 . \qquad (2.2)$$

Then, for small incremental stress and displacement

$$\sigma_{ij,i} + (S_{ik}u_{j,k})_{,i} = 0 . \qquad (2.3)$$

We now consider a flat plate of thickness 2h, bounded by the planes $x_3 = \pm h$. The plate is assumed to be in a state of initial stress $\underset{\sim}{S}$ of the form

$$\underset{\sim}{S} = \begin{bmatrix} S_{11} & S_{12} & 0 \\ S_{12} & S_{22} & 0 \\ 0 & 0 & 0 \end{bmatrix} . \qquad (2.4)$$

For simplicity we assume that $\underset{\sim}{S}$ is uniform in the x and y directions, but allow it to vary through the thickness. Thus

$$\underset{\sim}{S} = \underset{\sim}{S}(x_3) . \qquad (2.5)$$

Clearly $\underset{\sim}{S}$ is an equilibrium stress field and the faces $x_3 = \pm L$ are traction-free.

Upon this initial state of stress, we superpose an additional incremental stress field $\underset{\sim}{\sigma}$, with corresponding small displacement $\underset{\sim}{u}$. Then, with $\underset{\sim}{S}$ given by (2.4) and (2.5), (2.3) becomes

$$\sigma_{11,1}+\sigma_{21,2}+\sigma_{31,3}+S_{11}u_{1,11}+2S_{12}u_{1,12}+S_{22}u_{1,22}=0 ,$$
$$\sigma_{12,1}+\sigma_{22,2}+\sigma_{23,3}+S_{11}u_{2,11}+2S_{12}u_{2,12}+S_{22}u_{2,22}=0 , \qquad (2.6)$$

$$\sigma_{13,1}+\sigma_{23,2}+\sigma_{33,3}+S_{11}u_{3,11}+2S_{12}u_{3,12}+S_{22}u_{3,22}=0 . \qquad (2.7)$$

The condition that the faces $x_3 = \pm h$ of the plate are traction free is

$$\sigma_{13} = 0 , \quad \sigma_{23} = 0 , \quad \sigma_{33} = 0 . \tag{2.8}$$

To recover the equilibrium equations of classical plate theory we introduce the stress resultants and moments

$$(N_1, N_2) = \int_{-h}^{h} (\sigma_{13}, \sigma_{23}) \, dx_3 , \tag{2.9}$$

$$(M_{11}, M_{12}, M_{22}) = \int_{-h}^{h} x_3 (\sigma_{11}, \sigma_{12}, \sigma_{22}) \, dx_3 , \tag{2.10}$$

$$(T_{11}, T_{12}, T_{22}) = \int_{-h}^{h} (S_{11}, S_{12}, S_{22}) \, dx_3 . \tag{2.11}$$

We have to assume that

(a) S_{11}, S_{22} and S_{12} are even functions of x_3;
(b) u_1 and u_2 are even functions of x_3;
(c) u_3 can be approximated by its value $w(x_1, x_2)$ at the mid-plane $x_3 = 0$.

Assumption (a) is plausible if the plate is symmetric about the mid-plane with respect to its elastic properties and the initial stress arises from in-plane loading. It would not be expected to apply if the plate were non-symmetric or, for example, if the initial stress arose from non-uniform heating. Assumption (b) is appropriate for incremental bending of symmetric plates under edge moments, but not for non-symmetric plates. Assumption (c) is conventionally made in plate theory and is usually considered adequate for thin plates.

With these assumption, multiplying (2.6) by x_3 and integrating from $x_3 = -h$ to $x_3 = h$, and integrating (2.7) from $x_3 = -h$ to $x_3 = h$ gives, with (2.8)

$$\begin{aligned} &\frac{\partial M_{11}}{\partial x_1} + \frac{\partial M_{12}}{\partial x_2} = N_1 , \\ &\frac{\partial M_{12}}{\partial x_1} + \frac{\partial M_{22}}{\partial x_2} = N_2 , \\ &\frac{\partial N_1}{\partial x_1} + \frac{\partial N_2}{\partial x_2} + T_{11} \frac{\partial^2 w}{\partial x_1^2} + 2T_{12} \frac{\partial^2 w}{\partial x_1 \partial x_2} + T_{22} \frac{\partial^2 w}{\partial x_2^2} = 0 . \end{aligned} \tag{2.12}$$

These are the classical plate equilibrium equations in the presence of initial stress, as given in, for example, Biot [7], Jones [1] and Whitney [3]. However, it is important to realise that (2.12) depend on the assumptions detailed above and that if these assumptions do not apply then (2.12) can at best be regarded as approximations.

3 CONSTITUTIVE EQUATIONS

We assume the incremental stress-strain behaviour of the material to be linear elastic, with a linear relation between the incremental stress σ_{ij} and the incremental strain e_{ij}, where

$$e_{ij} = \tfrac{1}{2}(u_{i,j} + u_{j,i}) . \tag{3.1}$$

The only material symmetry assumed is that of reflectional symmetry with respect to the surfaces $x_3 = $ constant. Then the stress-strain relation takes the form

$$\begin{bmatrix} \sigma_{11} \\ \sigma_{22} \\ \sigma_{33} \\ \sigma_{23} \\ \sigma_{31} \\ \sigma_{12} \end{bmatrix} = \begin{bmatrix} c_{11} & c_{12} & c_{13} & 0 & 0 & c_{16} \\ c_{12} & c_{22} & c_{23} & 0 & 0 & c_{26} \\ c_{13} & c_{23} & c_{33} & 0 & 0 & c_{36} \\ 0 & 0 & 0 & c_{44} & c_{45} & 0 \\ 0 & 0 & 0 & c_{45} & c_{55} & 0 \\ c_{16} & c_{26} & c_{36} & 0 & 0 & c_{66} \end{bmatrix} \begin{bmatrix} e_{11} \\ e_{22} \\ e_{33} \\ 2e_{23} \\ 2e_{31} \\ 2e_{12} \end{bmatrix} \tag{3.2}$$

where the c_{ij} are moduli for incremental deformations from the initially stressed state, and form the incremental stiffness matrix. Various special cases of (3.2) are of interest. If the material is orthotropic the thirteen c_{ij} can be expressed in terms of nine moduli required for description of orthotropic symmetry and the angle defining the orientation of the orthotropic axes with respect to the coordinate axes. If the material is transversely isotropic five independent moduli and an angle suffice, and if it is isotropic only two moduli are required. All of these cases can be dealt with by appropriate specialisation in (3.2); details are given in the standard texts, such as [1], [2], [3].

In a laminate, each of whose plies has at least elastic reflectional symmetry with respect to planes $x_3 = $ constant, the stress-strain relation is of the form (3.2) in each ply, but the c_{ij} differ from ply to ply. To avoid having to discuss individual plies at this stage, we adopt the useful device of regarding the c_{ij} as specified functions of x_3. In a laminate the c_{ij} are piecewise constant functions of x_3, and later we shall specialise to this case. However at present we may proceed generally and assume arbitrary inhomogeneity in the x_3 direction.

To complete the formulation of plate theory we now integrate (3.2), and (3.2) weighted with the first and second powers of x_3, through the plate thickness, adopt the Euler-Bernouilli hypothesis, and thus express the stress resultants and moments in terms of the mean strains and mid-plane curvatures. However, this procedure inevitably, through the integrations, loses details of the solution, and also involves further approximation. To avoid these restrictions, we continue the analysis in terms of three-dimensional elasticity theory.

4 THREE-DIMENSIONAL ELASTICITY ANALYSIS

The full three-dimensional system of equations comprises (2.6), (2.7) and (3.2); these represent nine equations for the three displacement components u_i and six incremental stress components σ_{ij}. The coefficients S_{ij} and c_{ij} in these equations are specified functions of x_3, but are independent of x_1 and x_2. No approximation is involved in formulating these equations, other than the usual ones of linearised elasticity theory.

After some manipulation, these nine equations can be written in the matrix form

$$\frac{d\underset{\sim}{y}}{dx_3} = \underset{\sim}{R} \, \underset{\sim}{y} , \quad \begin{bmatrix} \sigma_{11} \\ \sigma_{22} \\ \sigma_{12} \end{bmatrix} = \underset{\sim}{C} \begin{bmatrix} u_1 \\ u_2 \\ \sigma_{33} \end{bmatrix} , \tag{4.1}$$

where

$$\underset{\sim}{y}^T = (u_1 \;\; u_2 \;\; \sigma_{33} \;\; \sigma_{13} \;\; \sigma_{23} \;\; u_3)^T , \tag{4.2}$$

$$\underset{\sim}{R} = \begin{bmatrix} \underset{\sim}{0} & \underset{\sim}{A}(x_3) \\ \underset{\sim}{B}(x_3) & 0 \end{bmatrix} , \tag{4.3}$$

$$\underset{\sim}{A} = \begin{bmatrix} s_{55} & s_{45} & -\dfrac{\partial}{\partial x_1} \\ s_{45} & s_{44} & -\dfrac{\partial}{\partial x_2} \\ -\dfrac{\partial}{\partial x_1} & -\dfrac{\partial}{\partial x_2} & -L \end{bmatrix} , \tag{4.4}$$

$$\underset{\sim}{B} = \begin{bmatrix} & -K_{11} & & -K_{12} & & -\dfrac{c_{13}}{c_{33}}\dfrac{\partial}{\partial x_1} - \dfrac{c_{36}}{c_{33}}\dfrac{\partial}{\partial x_2} \\ & -K_{12} & & -K_{22} & & -\dfrac{c_{36}}{c_{33}}\dfrac{\partial}{\partial x_1} - \dfrac{c_{23}}{c_{33}}\dfrac{\partial}{\partial x_2} \\ -\dfrac{c_{13}}{c_{33}}\dfrac{\partial}{\partial x_1} & -\dfrac{c_{36}}{c_{33}}\dfrac{\partial}{\partial x_2} & -\dfrac{c_{36}}{c_{33}}\dfrac{\partial}{\partial x_1} & -\dfrac{c_{23}}{c_{33}}\dfrac{\partial}{\partial x_2} & & \dfrac{1}{c_{33}} \end{bmatrix} , \tag{4.5}$$

$$\underset{\sim}{C} = \begin{bmatrix} Q_{11}\frac{\partial}{\partial x_1} + Q_{16}\frac{\partial}{\partial x_2} & Q_{16}\frac{\partial}{\partial x_1} + Q_{12}\frac{\partial}{\partial x_2} & \frac{c_{13}}{c_{33}} \\ Q_{12}\frac{\partial}{\partial x_1} + Q_{26}\frac{\partial}{\partial x_2} & Q_{26}\frac{\partial}{\partial x_1} + Q_{22}\frac{\partial}{\partial x_2} & \frac{c_{23}}{c_{33}} \\ Q_{16}\frac{\partial}{\partial x_1} + Q_{66}\frac{\partial}{\partial x_2} & Q_{66}\frac{\partial}{\partial x_1} + Q_{26}\frac{\partial}{\partial x_2} & \frac{c_{36}}{c_{33}} \end{bmatrix}, \tag{4.6}$$

$$\begin{bmatrix} s_{55} & s_{45} \\ s_{45} & s_{44} \end{bmatrix} = \begin{bmatrix} c_{55} & c_{45} \\ c_{45} & c_{55} \end{bmatrix}^{-1}, \tag{4.7}$$

$$Q_{ij} = c_{ij} - \frac{c_{i3}c_{j3}}{c_{33}}, \quad i,j = 1,2,6 \tag{4.8}$$

and L, K_{11}, K_{22}, K_{12} are the differential operators

$$L = S_{11}\frac{\partial^2}{\partial x_1^2} + 2S_{12}\frac{\partial^2}{\partial x_1 \partial x_2} + S_{22}\frac{\partial^2}{\partial x_2^2}, \tag{4.9}$$

$$K_{11} = (Q_{11}+S_{11})\frac{\partial^2}{\partial x_1^2} + 2(Q_{16}+S_{12})\frac{\partial^2}{\partial x_1 \partial x_2} + (Q_{66}+S_{22})\frac{\partial^2}{\partial x_2^2},$$

$$K_{12} = Q_{16}\frac{\partial^2}{\partial x_1^2} + (Q_{12}+Q_{66})\frac{\partial^2}{\partial x_1 \partial x_2} + Q_{26}\frac{\partial^2}{\partial x_2^2},$$

$$K_{22} = (Q_{66}+S_{11})\frac{\partial^2}{\partial x_1^2} + 2(Q_{26}+S_{12})\frac{\partial^2}{\partial x_1 \partial x_2} + (Q_{22}+S_{22})\frac{\partial^2}{\partial x_2^2}. \tag{4.10}$$

In this formulation, $(4.1)_1$ may be regarded as a system of six first order linear homogeneous ordinary differential equations, albeit with coefficients that are differential operators in x_1 and x_2, for the six variables which form the vector y. We note that these are the variables that are required to be continuous through the plate thickness. If a solution for these variables is obtained, it is a matter of simple substitution in $(4.1)_2$ to determine the remaining stress components. The dependence on x_1 and x_2 can be removed by taking Fourier transforms in these variables, but this gives rise to the problem of eventually inverting the transforms, and we do not proceed in that way. Formulations of the type (4.1) seem to have first been used by Bufler [8] in the context of isotropic elasticity without initial stress. Related formulations have been employed in problems of elastic wave propagation in layered media, as for example in Kennett [9].

The advantage of the formulation (4.1) is that we can write down an exact formal solution, namely

$$\underset{\sim}{y}(x_3) = \underset{\sim}{P}(x_3, x_3^*)\ \underset{\sim}{y}(x_3^*), \tag{4.11}$$

where $x_3 = x_3^*$ is some chosen reference plane (normally the upper or lower plate surface, or the midplane) and $\underset{\sim}{P}(x_3, x_3^*)$ is the transfer matrix or propagator matrix, given by

$$\frac{d\underset{\sim}{P}}{dx_3} = \underset{\sim}{R}\ \underset{\sim}{P}, \qquad \underset{\sim}{P}(x_3^*) = \underset{\sim}{I}. \tag{4.12}$$

Formally, $\underset{\sim}{P}$ can be expressed in the series form.

$$\underset{\sim}{P}(x_3, x_3^*) = \underset{\sim}{I} + \underset{\sim}{P}_1(x_3, x_3^*) + \underset{\sim}{P}_2(x_3, x_3^*) + \underset{\sim}{P}_3(x_3, x_3^*) + \ldots, \tag{4.13}$$

where

$$\underset{\sim}{P}_1 = \int_{x_3^*}^{x_3} \underset{\sim}{R}(\xi)\, d\xi, \tag{4.14}$$

$$\underset{\sim}{P}_2 = \int_{x_3^*}^{x_3} \int_{x_3}^{\xi} \underset{\sim}{R}(\xi)\, \underset{\sim}{R}(\eta)\, d\eta\, d\xi, \tag{4.15}$$

$$\underset{\sim}{P}_3 = \int_{x_3^*}^{x_3} \int_{x_3^*}^{\xi} \int_{x_3^*}^{\eta} \underset{\sim}{R}(\xi)\underset{\sim}{R}(\eta)\underset{\sim}{R}(\zeta)\, d\zeta\, d\eta\, d\xi, \tag{4.16}$$

and so on. For a homogeneous material with uniform initial stress, so that c_{ij}, Q_{ij} and S_{ij} are constants, $\underset{\sim}{P}$ takes the exponential form

$$\underset{\sim}{P}(x_3, x_3^*) = \exp\{(x_3 - x_3^*)\underset{\sim}{R}\}. \tag{4.17}$$

We note that successive terms in the series (4.13) are of successively increasing orders in the plate thickness 2h.

In principle, (4.11) determines the full elasticity solution if the variables which form the elements of y are known on the reference plane $x_3 = x_3^*$. In general, of course, these quantities are not known a priori; for example, if the lateral surfaces are traction-free, we would have

$$\sigma_{13} = 0, \quad \sigma_{23} = 0, \quad \sigma_{33} = 0 \quad \text{on } x_3 = \pm h$$

but no initial information about u_1, u_2 and u_3, other than information that might be inferred from any physical and geometrical symmetry properties.

5 LAMINATE TREATMENT

For simplicity, we consider a symmetric laminate; the procedure readily extends to the non-symmetric case. We consider each lamina to be of homogeneous linear elastic material with the material symmetry described by (3.2). The laminae in the half-thickness $0 < x_3 < h$ are numbered 0 to N, so that the whole laminate comprises 2N+1 laminae. The interface between lamina r-1 and lamina r is at $x_3 = z_r$, so that lamina 0 lies between $x_3 = \pm z_0$, and for $r \geq 1$ lamina r is in the region $z_{r-1} < x_3 < z_r$. We also denote $h = z_N$.

The elastic moduli, reduced elastic moduli and initial stress in lamina r are denoted by $c_{ij}^{(r)}$, $Q_{ij}^{(r)}$ and $S_{ij}^{(r)}$ respectively, and the matrices $\underset{\sim}{R}$, $\underset{\sim}{A}$, $\underset{\sim}{B}$ and $\underset{\sim}{C}$ correspondingly by $\underset{\sim}{R}_r$, $\underset{\sim}{A}_r$, $\underset{\sim}{B}_r$ and $\underset{\sim}{C}_r$. The transfer matrix $\underset{\sim}{P}$ in lamina r is denoted by $\underset{\sim}{P}_r(x_3, z_{r-1})$ and is obtained by substituting the lamina values of c_{ij}, Q_{ij} and S_{ij} in the expression for $\underset{\sim}{P}$. Clearly we have (in the general case)

$$\underset{\sim}{P}(x_3, x_3^{**}) = \underset{\sim}{P}(x_3, x_3^*)\underset{\sim}{P}(x_3^*, x_3^{**}) \tag{5.1}$$

and so, in lamina r, taking the mid-plane $x_3 = 0$ as reference plane

$$\underset{\sim}{P}(x_3, 0) = \underset{\sim}{P}_r(x_3, z_{r-1})\underset{\sim}{P}_{r-1}(z_{r-1}, z_{r-2}), \ldots \underset{\sim}{P}_1(z_1, z_0)\underset{\sim}{P}_0(z_0, 0), \tag{5.2}$$

which determines $\underset{\sim}{P}(x_3, 0)$ for the entire laminate. With (4.17), we may express this as

$$\underset{\sim}{P}(x_3, 0) = \exp\{(x_3 - z_{r-1})\underset{\sim}{R}_r\}\exp(h_{r-1}\underset{\sim}{R}_{r-1}) \exp(h_{r-2}\underset{\sim}{R}_{r-2}) \ldots \exp(h_1\underset{\sim}{R}_1)\exp(h_0\underset{\sim}{R}_0) \tag{5.3}$$

where $h_r = z_r - z_{r-1}$ is the thickness of lamina r (r=1,2,...N) and $h_0 = z_0$.

6. DETERMINATION OF MID-PLANE VARIABLES

Again for brevity, we consider symmetric laminates and symmetric initial stress, although the general case is of interest and is tractable. We also restrict consideration to bending mode deformations, in which u_1, u_2 and σ_{33} are odd functions of x_3, and σ_{13}, σ_{23} and u_3 are even functions of x_3. We take the mid-plane $x_3 = 0$ as reference plane. Then $u_1 = 0$, $u_2 = 0$, $\sigma_{33} = 0$ at $x_3 = 0$, and (4.11) becomes

$$\begin{bmatrix} u_1(x_3) \\ u_2(x_3) \\ \sigma_{33}(x_3) \end{bmatrix} = \begin{bmatrix} P_{14} & P_{15} & P_{16} \\ P_{24} & P_{25} & P_{26} \\ P_{34} & P_{35} & P_{36} \end{bmatrix} \begin{bmatrix} \tau_1 \\ \tau_2 \\ w \end{bmatrix}, \qquad \begin{bmatrix} \sigma_{13}(x_3) \\ \sigma_{23}(x_3) \\ u_3(x_3) \end{bmatrix} = \begin{bmatrix} P_{44} & P_{45} & P_{46} \\ P_{54} & P_{55} & P_{56} \\ P_{64} & P_{65} & P_{66} \end{bmatrix} \begin{bmatrix} \tau_1 \\ \tau_2 \\ w \end{bmatrix}, \tag{6.1}$$

where P_{ij} are the elements of $\underset{\sim}{P}(x_3, 0)$, and τ_1, τ_2 and w are values of σ_{13}, σ_{23} and u_3 respectively at the midplane, and are functions of x_1 and x_2.

The boundary conditions (2.8) then give

$$\begin{bmatrix} \bar{P}_{44} & \bar{P}_{45} & \bar{P}_{46} \\ \bar{P}_{54} & \bar{P}_{55} & \bar{P}_{56} \\ \bar{P}_{34} & \bar{P}_{35} & \bar{P}_{36} \end{bmatrix} \begin{bmatrix} \tau_1 \\ \tau_2 \\ w \end{bmatrix} = 0 , \qquad (6.2)$$

where $\bar{P}_{ij}$ are elements of the transfer matrix from the mid-plane to the surface, so that

$$\underset{\sim}{\bar{P}} = \underset{\sim}{P}(h,0) = \underset{\sim}{P}(x_N,0) . \qquad (6.3)$$

Eliminating τ_1 and τ_2 from (6.2) then gives

$$\Delta w = 0 , \qquad (6.4)$$

where

$$\Delta = \begin{vmatrix} \bar{P}_{44} & \bar{P}_{45} & \bar{P}_{46} \\ \bar{P}_{54} & \bar{P}_{55} & \bar{P}_{56} \\ \bar{P}_{34} & \bar{P}_{35} & \bar{P}_{36} \end{vmatrix} , \qquad (6.5)$$

and (6.4) is the equation that determines $w(x_1,x_2)$ and from which the rest of the solution follows. The difficulty is that Δ is an infinite-order differential operator, so the solution of (6.4) poses some problems. Nevertheless, progress can be made.

The solution requires the calculation of $\underset{\sim}{\bar{P}}$, or at least those elements of $\underset{\sim}{\bar{P}}$ that appear in (6.5). This is most easily carried out using (5.3), from which

$$\underset{\sim}{\bar{P}} = \exp(h_N \underset{\sim}{R}_N)\exp(h_{N-1}\underset{\sim}{R}_{N-1}) \ldots . \exp(h_1 \underset{\sim}{R}_1)\exp(h_0 \underset{\sim}{R}_0) . \qquad (6.6)$$

To obtain approximate solutions we expand the exponentials as, for example

$$\exp(h\underset{\sim}{R}) = \underset{\sim}{I} + h\underset{\sim}{R} + \tfrac{1}{2}h^2\underset{\sim}{R}^2 + \tfrac{1}{6}h^3\underset{\sim}{R}^3 + \tfrac{1}{24}h^4\underset{\sim}{R}^4 + \ldots \qquad (6.7)$$

(noting that successive terms are of successive orders in h) and truncate the series at an appropriate point. The expansions are simplified by the form of each $\underset{\sim}{R}$

$$\underset{\sim}{R} = \begin{bmatrix} 0 & \underset{\sim}{A} \\ \underset{\sim}{B} & 0 \end{bmatrix} , \qquad (6.8)$$

which gives

$$\underset{\sim}{R}^2 = \begin{bmatrix} \underset{\sim}{A}\underset{\sim}{B} & 0 \\ 0 & \underset{\sim}{B}\underset{\sim}{A} \end{bmatrix} , \quad \underset{\sim}{R}^3 = \begin{bmatrix} 0 & \underset{\sim}{A}\underset{\sim}{B}\underset{\sim}{A} \\ \underset{\sim}{B}\underset{\sim}{A}\underset{\sim}{B} & 0 \end{bmatrix} ,$$

$$\underset{\sim}{R}^4 = \begin{bmatrix} \underset{\sim}{A}\underset{\sim}{B}\underset{\sim}{A}\underset{\sim}{B} & 0 \\ 0 & \underset{\sim}{B}\underset{\sim}{A}\underset{\sim}{B}\underset{\sim}{A} \end{bmatrix} . \qquad (6.9)$$

If the series (6.7) are truncated at the h^3 terms, and S_{ij} are neglected compared to Q_{ij}, it can be shown that (6.4) recovers the classical laminate theory equation

$$\tilde{Q}_{11}w_{,1111} + 4\tilde{Q}_{16}w_{,1112} + 2(\tilde{Q}_{12}+2\tilde{Q}_{66})w_{,1122} + 4\tilde{Q}_{26}w_{,1222} + \tilde{Q}_{22}w_{,2222} = T_{11}w_{,11} + 2T_{12}w_{,12} + T_{22}w_{,22} , \qquad (6.10)$$

where

$$\tilde{Q}_{ij} = 2\int_0^h x_3^2 Q_{ij}\, dx_3 . \qquad (6.11)$$

This result in itself is significant, as it shows that the laminate theory equation can be derived systematically from three-dimensional elasticity theory, without the use of any arbitrary assumptions such as the Euler-Bernouilli hypothesis.

To develop the next order approximation it is necessary to retain terms up to h^5 in (6.7). This leads to an equation for w of the form

$$h^2 A_{ijk\ell mn} w_{,ijk\ell mn} + B_{ijk\ell} w_{,ijk\ell} - T_{ij} w_{,ij} = 0 , \qquad (6.12)$$

where summation convention is used with the indices taking values 1,2, and $B_{ijk\ell}$ are the coefficients on the left of (6.10). The coefficients $A_{ijk\ell mn}$ are too complicated to be written here; their calculation is greatly facilitated by use of symbolic algebraic manipulation software, and with this aid does not present a real obstacle.

7 CYLINDRICAL BENDING OF A THREE-PLY LAMINATE

To illustrate the effect of the higher-order terms in (6.12) we consider cylindrical bending of a three-ply cross-ply laminate with the orthotropic axes parallel to the x_1 and x_2 directions. Thus we seek solutions with N=1 and

$$u_2 = 0 , \quad \sigma_{23} = 0 . \qquad (7.1)$$

$$c_{16} = c_{26} = c_{36} = c_{45} = 0, \quad S_{12} = S_{22} = 0 \qquad (7.2)$$

We also suppose that c_{33} takes the same value in each lamina, and normalise the stress and stiffness components with respect to c_{33}; that is, we choose units of stress such that $c_{33} = 1$. We also take $h_0 = h_1 = \frac{1}{2}h$.

It is emphasised that these simplifications are made purely for illustration, and that it is perfectly possible to proceed generally.

Adopting these simplifications, and neglecting S_{ij} in comparison to c_{ij} and Q_{ij}, we find that (6.12) reduces to

$$A\frac{d^6w}{dx_1^6} + \tilde{Q}_{11}\frac{d^4w}{dx_1^4} - T_{11}\frac{d^2w}{dx_1^2} = 0 , \qquad (7.3)$$

where

$$A = \frac{h^5}{960}\left\{ \frac{1}{c_{55}^{(0)}}\left[13Q_{11}^{(0)2} + 30Q_{11}^{(0)}Q_{11}^{(1)} + 40Q_{11}^{(1)2}\right] - \frac{1}{c_{55}^{(1)}}\left[15Q_{11}^{(0)2} + 70Q_{11}^{(0)}Q_{11}^{(1)} + 62Q_{11}^{(1)2}\right] + c_{13}^{(0)}\left[4Q_{11}^{(0)} + 80Q_{11}^{(1)}\right] + 44c_{13}^{(1)}Q_{11}^{(1)}\right\} . \qquad (7.4)$$

8 BUCKLING IN UNIAXIAL COMPRESSION - SIMPLE SUPPORT

As a simple application we consider buckling in the cylindrical bending mode of the plate described in Section 7, with simple support at $x_1 = 0$, $x_1 = a$. Thus we seek non-trivial solutions of (7.3) such that

$$w = 0 , \quad d^2w/dx_1^2 = 0 , \quad x_1 = 0, \; x_1 = a . \qquad (8.1)$$

The appropriate solutions are of the form

$$w = c \sin\frac{n\pi x_1}{a} \qquad (n=1,2,\ldots) . \qquad (8.2)$$

Then from (7.3) the critical loads T_{11} are given by

$$-T_{11} = \frac{n^2\pi^2\tilde{Q}_{11}}{a^2}\left[1 - \frac{h^2An^2\pi^2}{a^2\tilde{Q}_{11}}\right] . \qquad (8.3)$$

The effective mode is clearly n = 1. We note the following

(a) the leading term (given by setting h = 0 in (8.3)) gives the result according to classical laminate theory,

(b) the result (8.3) involves the shear modulus c_{55}, and so includes effects of transverse shear,

(c) the expression (8.3) is not dissimilar (but not identical) to the result quoted by Whitney [3] using a shear deformation theory.

ACKNOWLEDGEMENT

In preparing this paper I have made substantial use of results presented by Mr. P. Watson in a forthcoming Ph.D. thesis to the University of Nottingham. I am grateful to Mr. Watson and Professor T. G. Rogers for many discussions on this and related subjects.

REFERENCES

1. Jones, R.M. 'Mechanics of composite materials'. Hemisphere Publishing Corp, 1975.

2. Christensen, R.M. 'Mechanics of composite materials'. Wiley, 1979.

3. Whitney, J.M. 'Structural Analysis of Laminated Anisotropic Plates'. Technomic Publishing Co. 1987.

4. Pagano, N.J. 'Exact solutions for composites in cylindrical bending'. J. Comp., Mater. **3** (1969), 398.

5. Basi, S., Rogers, T.G. and Spencer, A.J.M. 'Hygrothermoelastic analysis of anisotropic inhomogeneous and laminated plates'. J. Mech. Phys. Solids **39** (1991), 1.

6. Spencer, A.J.M., Watson, P. and Rogers, T.G. 'Stress analysis of anisotropic laminated circular cylindrical shells'. In 'Recent Developoments in Composite Materials Structures', (eds. D. Hui and C.T. Sun) ASME, New York 1990.

7. Biot, M.A. 'Mechanics of incremental deformations'. Wiley, 1965.

8. Bufler, H. 'Theory of elasticity of a multilayered medium'. J. Elasticity **1**, 1971, 125.

9. Kennett, B.L.N. 'Seismic wave propagation in stratified media'. Cambridge U.P. 1983.

A REVIEW OF RAE SPONSORED WORK ON THE COMPRESSIVE BEHAVIOUR OF COMPOSITE MATERIALS

P.T. Curtis
Materials and Structures Department
DRA Aerospace Division
RAE Farnborough
Hants GU14 6TD, UK

SUMMARY

The Non-metallic Materials Division at RAE Farnborough has mounted a major programme of work to study the compressive behaviour of composite materials and seek improvements in compressive strength. This is being done by developing improved compressive test techniques, studying failure processes fractographically, investigating the effect of notches and impact damage and modelling behaviour mathematically to develop predictive capability. In this paper an overview of this work is presented, with critical results and conclusions, and references to fuller treatments are cited.

INTRODUCTION

In recent years the tensile properties of composite materials have increased dramatically, mainly due to significant increases in fibre strength and stiffness, but also to improvements in polymer matrix toughness and ductility. Unfortunately there has been no parallel improvement in compressive properties with the consequence that the vast majority of strength critical designs are now compression limited.

The Non-metallic Materials Division at RAE Farnborough has mounted a major programme of work, both intramural and extramural, to address this problem. This is being done by developing improved compressive test techniques, studying failure processes fractographically, investigating the effect of notches and impact damage, modelling behaviour mathematically to develop predictive capability and seeking material improvements. In this paper an overview of this work is presented, with critical results and conclusions, and references to fuller treatments are cited.

COMPRESSION FAILURE PROCESSES

In attempting to improve the compressive properties of composite materials there is an urgent need for a greater understanding of the way the materials behave under compressive loading and how they fail. In an attempt to improve our understanding of the way these materials behave, RAE Farnborough has supported work at Cambridge University aimed at modelling, experimentally, the behaviour of unidirectional composite materials (Ref 1).

The early models of compressive failure derived from Rosen and his fellow workers in the USA (Ref 2). They argued that compressive strength was determined by fibre microbuckling involving elastic matrix deformation. By applying a strain energy balance to this mode of failure an expression for UD compressive strength was obtained:-

$$S_c = \frac{G_m}{1 - V_f} + \frac{(pi)^2 E_f d^2}{3 L^2} V_f$$

where V_f and E_f are fibre volume fraction and modulus. G_m is the matrix shear modulus, d the fibre diameter and L the buckling wavelength. Given a composite that truly fails by the elastic microbuckling, good agreement can be obtained with experiment. Fig 1 shows data generated by Cambridge University on a model spaghetti/elastomer system, which undergoes true elastic microbuckling, which agrees well with the Rosen equation.

In general, the Rosen expression has been found to greatly overestimate the compressive strength of the more usual polymer based composites. This is perhaps partly because it makes no allowance for plastic yield of the matrix. Argon and Budiansky (Refs 3,4) identified the shear yield stress k of the matrix and the initial fibre misalignment ϕ of the fibres as the main factors controlling the compressive stress when plastic microbuckling occurs. For a perfectly rigid plastic body Budiansky showed that the compressive strength can be approximated by:-

$$S_c = \frac{k}{\phi}$$

Most of the high performance composites in use exhibit some degree of plasticity and thus this model generally gives quite reasonable agreement with experiment (Fig 2). It does, of course, rely on a knowledge of the fibre misalignment, which is not an easy parameter to measure or indeed control.

The last major mechanism of compressive failure is by failure of the fibres either by crushing or by shearing. The latter is frequently observed in high modulus carbon fibres. If failure is by shear, then a reasonable estimate of compressive strength can be made by assuming tensile and compressive strength are equal. No models currently exist to predict the columnar crushing failure of the fibres.

Clearly in all this there are four key materials variables which we could expect to influence the rate of degradation and failure of polymer matrix composites. These are:-

1 Fibre geometry (diameter, misalignment, cross-section etc).

2 The fibre/matrix interface.

3 Fibre mechanical properties.

4 Matrix mechanical properties.

The work being supported by RAE Farnborough is seeking to optimise these key variables without detriment to other properties.

TEST METHODS

One of the major obstacles to furthering our knowledge of compressive failure processes and improving compressive strength has been the difficulty of testing composite materials in compressive loading and obtaining true compressive failures. Recognising this problem, RAE Farnborough has participated in a Garteur round robin exercise to compare standard test methods, the results of which are to be presented later in this meeting by 't Hart (Ref 5). In addition, RAE has also supported work at Imperial College, London University studying the effect of test variables on compressive strength (Ref 6). As a result of this work, RAE has developed an improved test method by modifying slightly the test configurations that gave the highest failure stresses and yielded failures that appeared to be mostly compressive in nature in the Imperial College and Garteur work.

RAE has modified the standard Celanese test method based on a 16 ply unidirectional test coupon (Refs 7,8). A test piece based on a 35 ply coupon, having 8 plies of ±45° material on each side has been developed. A waist is machined through this and through 1½ plies of the unidirectional material (Fig 3). On loading this coupon, splits form under the moulded tabs and these reduce the stress concentrations at the tab ends. Failures then no longer occur at the tabs and much greater compressive strengths are recorded. A mean value of 1816 MPa was measured by RAE for a standard CFRP using the new technique, compared with 1156 MPa for the standard Celanese type coupon, which clearly better reflects the true compressive strength of the material.

NOVEL FIBRES

Hollow and non-circular fibres offer the possibility of improved compressive strength due to greater fibre stability and thus resistance to the microbuckling failure mode characteristic of these materials. Owens-Corning have produced hollow glass fibres that do indeed lead to improved specific compressive strength (Table 1) (Ref 9). Although the tensile strength (UTS) is understandably reduced, compressive strength (UCS) remains unchanged, emphasising that this is clearly a stability problem. Allowing for the lower density of the hollow fibres, the specific properties of the hollow S-glass material looks very attractive, with only a slight reduction in UTS but a desirable improvement in UCS. Since these fibres are not currently available in the UK, RAE is supporting work to manufacture both hollow glass and carbon fibres and to assess their performance in composites.

Other fibre manufacturers have been experimenting with large diameter fibres and with non-circular fibre cross-sections aimed at improving fibre stability and increasing compressive strength. With carbon fibres there is a realistic upper limit on fibre diameter of about 10 microns, dictated by gaseous diffusion requirements during fibre production. Non-circular fibres, such as trilobal cross-sections, offer potentially increased fibre stability. Unfortunately, the principal UK fibre supplier, Courtaulds Grafil, with whom RAE had been collaborating in this area, has recently announced that it is withdrawing from carbon fibre manufacture in the UK. Sadly our work in this area has thus ceased, although RAE continues work on composites with hollow fibres.

FIBRE/MATRIX INTERFACE

It would be a reasonable assumption that the level of adhesion between the fibres and the resin matrix should have a significant effect on the compressive strength of these materials. Premature disbonding due to poor adhesion would be expected to result in fibre instability and thus reduced compressive strength. In the case of carbon fibres, the level of fibre/matrix adhesion is determined by the degree of oxidative surface treatment applied to the fibres. In general the adhesion increases with treatment, but a plateau is usually reached at moderate levels of treatment, above which the shear strength of the interface is not improved (Ref 10).

RAE funded work at Imperial College, London University (Ref 6), however, has shown that carbon fibre surface treatment has relatively little effect on the unidirectional compressive strength of CFRP. Intramural work at RAE has also shown that fibre surface treatment has a relatively small effect on compressive strength (Ref 11). Fig 4 shows RAE data for compressive strength as a function of fibre surface treatment for a standard laminated CFRP material, in two different layups. At low levels of surface treatment the compressive strength rises rapidly at first, reaching a maximum at 10-30% of the standard level of treatment. Further increases in the level of fibre surface treatment lead to a small reduction in compressive strength, but it is unclear why this should be. The lack of sensitivity of compressive strength to fibre surface treatment is an important finding and has permitted the exclusion of this variable from further work.

TABLE 1 Owens-Corning Data for Unidirectional GRP comparing hollow and solid glass fibres

	S2 Hollow	S2 Solid	E Hollow	E Solid
Density	1.63	2.02	1.44	2.10
UTS - MPa	1450	2000	450	1100
Modulus GPa	47.7	58.6	29.0	44.8
UCS - MPa	1260	1240	990	1001
Specific UTS	888	990	313	524
Spec. Modulus	29.2	29	20.2	21.3
Specific UCS	770	614	688	481

RESIN DEVELOPMENT AND MODIFICATION

Since the predominant mode of degradation and failure in these materials has been shown to be based on fibre microbuckling, the properties of the matrix resin would be expected to have a major effect on compressive strength. To improve stability the resin matrix should be stiffened to better resist fibre buckling. This might be achieved either by modification of the resin chemistry or by the use of resin additives. Some resin suppliers are researching resins with improved stiffness, but generally improved stiffness equates with increased brittleness, not a desirable trait in modern composite materials.

Fig 5 shows a collection of RAE and RAE sponsored data on how composite unidirectional compressive strength varies with composite shear strength, the latter being a very resin dependent property. Clearly compressive strength increases with increasing composite and thus resin shear strength. The only exception is the thermoplastic based system, which has a poorer compressive strength than expected. This is believed to be because in all the thermoset systems the general degree of fibre misalignment is very similar, typically around ±2°, but in the thermoplastic based composite the fibre misalignment is greater, typically ±4°. This results in a reduced compressive strength and indeed emphasises the importance of fibre alignment on compressive strength.

RAE is currently engaged in a programme of work of modifying standard resin matrices aiming to gain improvements in compressive strength, but currently few results are available. However, work by Narkis and Chen (Ref 12) has shown that the simple addition of glass microspheres to the matrix resin can lead to a noticeable increase in compressive strength (Fig 6).

PREDICTIVE MODELLING

The lack of predictive capability in general is limiting the application of composite materials in aerospace structures, partly because of the prohibitive costs of having to generate all data experimentally and partly because of the inefficient exploitation of the materials capabilities. The problem is particularly acute for the case of compressive loading, especially for the design critical cases of notched compression and compression after impact.

To tackle this problem, RAE has supported work aimed at developing a predictive model for the notched compressive strength of CFRP (Refs 13,14). The model developed assumes that compressive failure is dominated by fibre microbuckling from the notch and this has been verified experimentally for a range of polymer based laminates. Unlike the tensile case, in compression microbuckles usually grow without initiating a significant damage zone, thus the problem is actually simpler than tension and does indeed lend itself to the application of fracture mechanics. The model treats the microbuckle as a crack, making allowance for the material crushed in the microbuckle zone, and applies fracture mechanics. The inputs to the model at present are the unnotched strength plus a fracture toughness parameter measured on the actual laminate. However, current work is aimed at reducing these requirements to the unidirectional compressive strength and toughnesses measured on unidirectional material. The comparison with experiment is shown in Fig 7 for 6 different laminates and as can be seen is remarkably good. The model holds the prospect of becoming a true design tool, capable of predicting notched compressive strength for any composite system.

Work is also in progress to model all aspects of impact behaviour (Ref 15). This includes trying to predict the type and amount of damage produced in an impacting event, the effect this has on residual mechanical properties and whether the damage will subsequently grow. An example is shown in Fig 8, for the growth of delaminations in compression. In this an FE model has been used, with toughness inputs for G_{1c} and G_{2c}, to predict the extent of subsequent delamination growth as a result of an applied compressive load. The model predicts the experimental

delamination growth well. This model is being further developed to cope with fibre fracture and splits as well as delamination, and their interaction, and thus cope with complex interacting areas of damage similar to those produced during impact.

CONCLUSIONS

A brief survey of work sponsored by the Royal Aerospace Establishment, Farnborough, UK, on the compressive behaviour of composite materials, has been described.

Compressive strength has improved little in recent years despite dramatic increases in composite tensile strength. This has been partly because of a lack of understanding of the failure processes in these materials and perhaps also because of difficulties in testing in compression. An improved test method has been described in this work that yields significantly increased coupon compressive strengths with failure modes that appear to be material based rather than associated with macro-instability.

Recent detailed micromechanical studies have been described that reveal that plastic microbuckling is the predominant failure process in advanced polymer matrix composites. Matrix properties and fibre misalignment appear to be key factors in determining composite compressive strength. The fibre/matrix interface has little effect on compressive strength; relatively small degrees of fibre surface treatment being sufficient to realise standard levels of compressive strength.

Modified fibres with non-circular and hollow cross-sections and stiffer or modified matrix resins appear to offer the prospect of improved composite compressive strength.

Predictive techniques capable of estimating notched compressive strength and determining the onset of delamination growth have been described. With further development these offer the prospect of becoming composite design tools.

REFERENCES

1. Jelf, P.M., Fleck, N.A., "Compression Failure mechanisms in Unidirectional fibre composites", Submitted to J.Comp.Mats. 1991

2. Rosen, V.W., "Mechanics of Composite strengthening in fibre composite materials", American Society for Metals, 1965, pp 37-75.

3. Argon, A.S., "Fracture of Composites", Treatise on Materials Science and Technology, vol. 1, Academic Press, New York 1972.

4. Budiansky, B., "Micromechanics", Computers and Structures, 16(1), 1983, pp 3-12.

5. 't Hart, W.G.J., Aoki, R., Bookholt, H., Curtis, P.T., Kröber, I., Marks, N., Sigety, P., "Garteur Compression Behaviour of Advanced CFRP", in "Utilisation of Advanced Composites in Military Aircraft", AGARD CP, to be published October 1991, Paper 10.

6. Haeberle, J. and Matthews, F.L., "The compressive mechanical properties of fibre-reinforced plastics", Imperial College, London University, Reports under RAE agreement 2037/235 XR/MAT, 1989-1991.

7. Curtis, P.T., Gates, J., Molyneux, C., "An improved engineering test method for the measurement of the Compressive Strength of Unidirectional Carbon Fibre Composites", RAE Technical Report TR91031, May 1991.

8. Curtis, P.T., Gates, J., Molyneux, C., "An improved engineering test method for the measurement of the Compressive Strength of Unidirectional Carbon Fibre Composites", Accepted for publication in "Composites", 1991.

9. Owens-Corning preliminary data sheet, April 1990.

10. Curtis, P.T., "The effect of the interface on carbon fibre composite properties", RAE Technical Memo TM Mat/Str 1166, February 1991.

11. Curtis, P.T., Morton, J., "The effect of fibre surface treatment on the compressive strength of CFRP laminates", in Proc.ICCM4, Tokyo, 1982.

12. Narkis, M. and Chen, E.J.H., "Unidirectional hybrid thermoplastic composites reinforced with continuous fiber and glass spheres", SAMPE J., vol 26(3), May/June 1990. pp 11-18.

13. Soutis, C. and Fleck, N.A., "Static Compression Failure of Carbon fibre T800/924C Composite Plates with a single hole", J.Comp.Mats., May 1990.

14. Soutis, C., Fleck, N.A., Smith, P.A., "Failure Prediction Technique for Compression loaded Carbon fibre-epoxy Laminate with Open Holes", J.Comp. Mats., 1990.

15. Pavier, M.J., "Finite Element Modelling of artificial damage in carbon fibre epoxy laminates", Cambridge Consultants Ltd, Final Report under RAE contract SLS41b/1266, December 1990.

Figure 1 ELASTIC MICROBUCKLING

Rosen predictions v. Experiment
Spaghetti/Elastomer

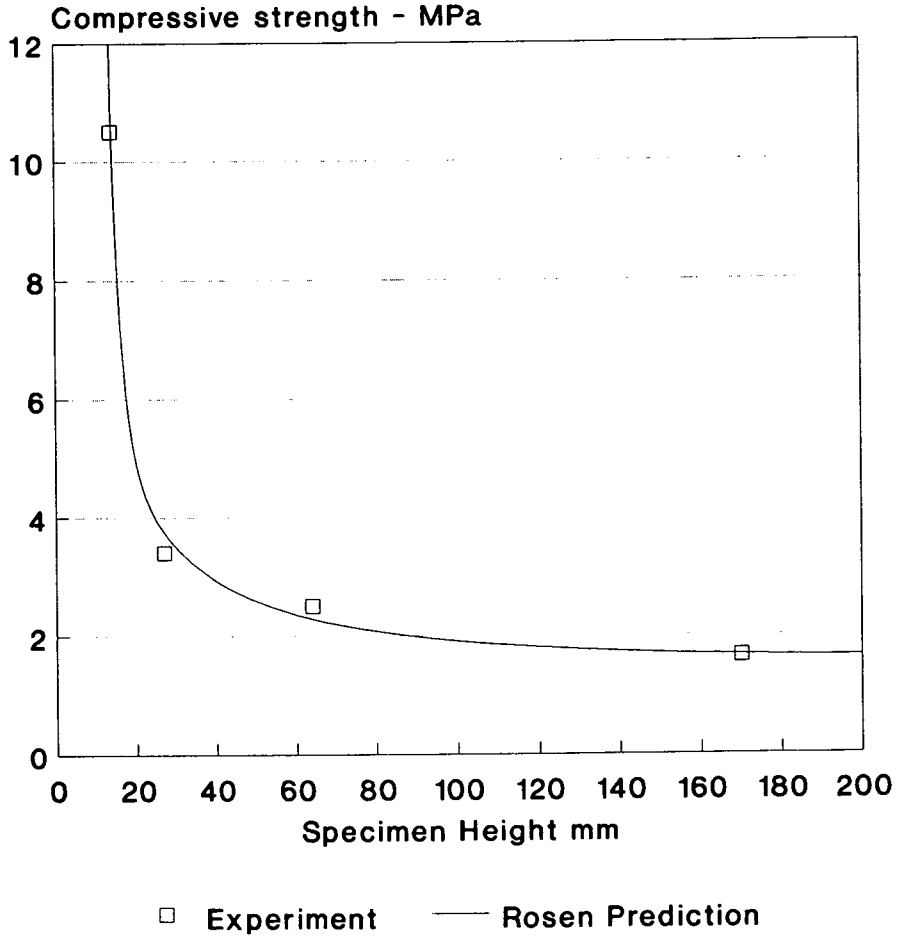

Figure 2 - PLASTIC MICROBUCKLING

Budiansky v. Experiment

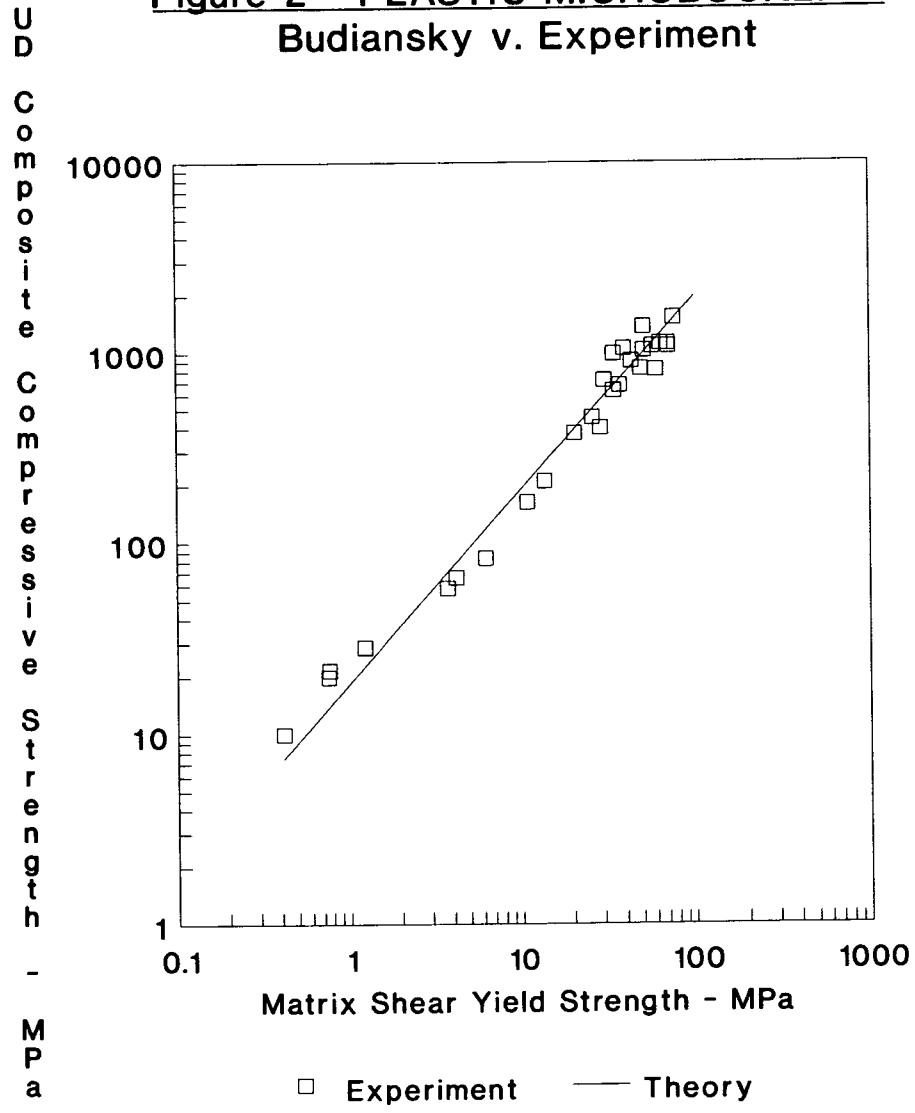

Figure 3

RAE MODIFIED CELANESE COUPON WITH INTEGRAL TABS

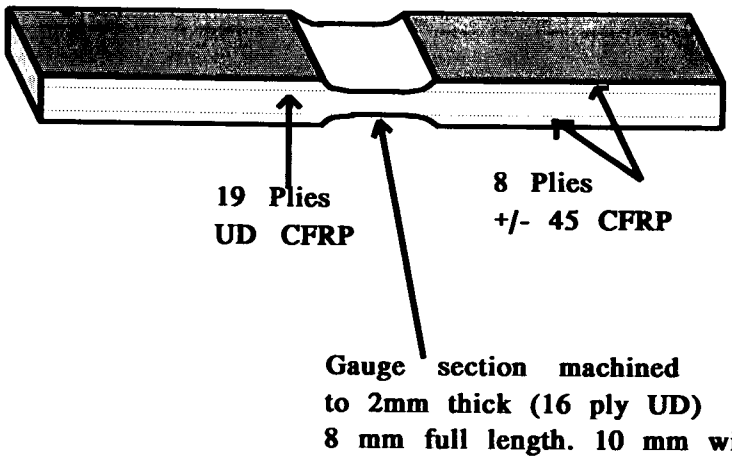

TYPICAL TEST DATA - COMPRESSIVE STRENGTH

T800/924 - CFRP

PLAIN COUPON WITH AL.ALLOY TABS - 1156 MPa

RAE MODIFIED COUPON (ABOVE) - 1816 MPa

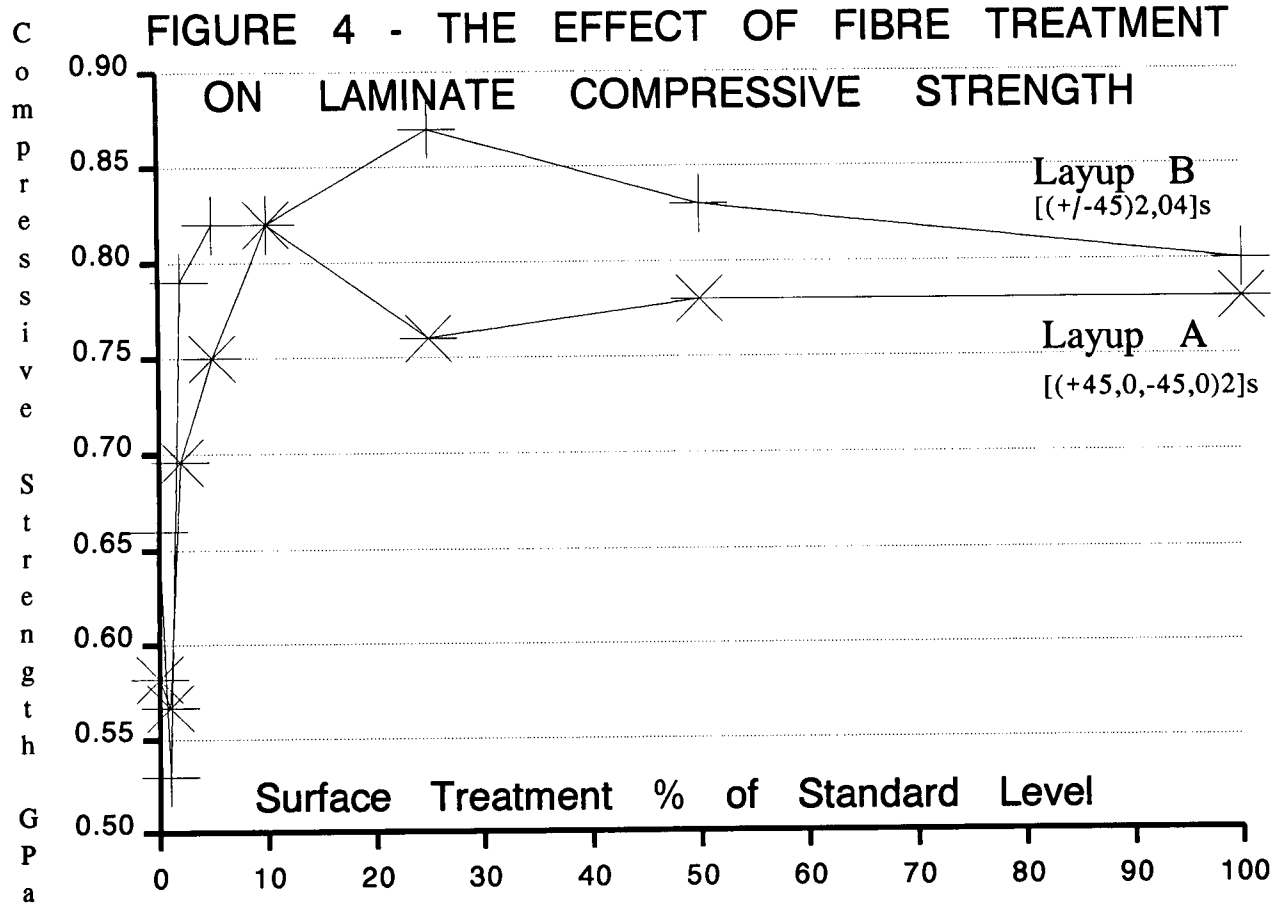

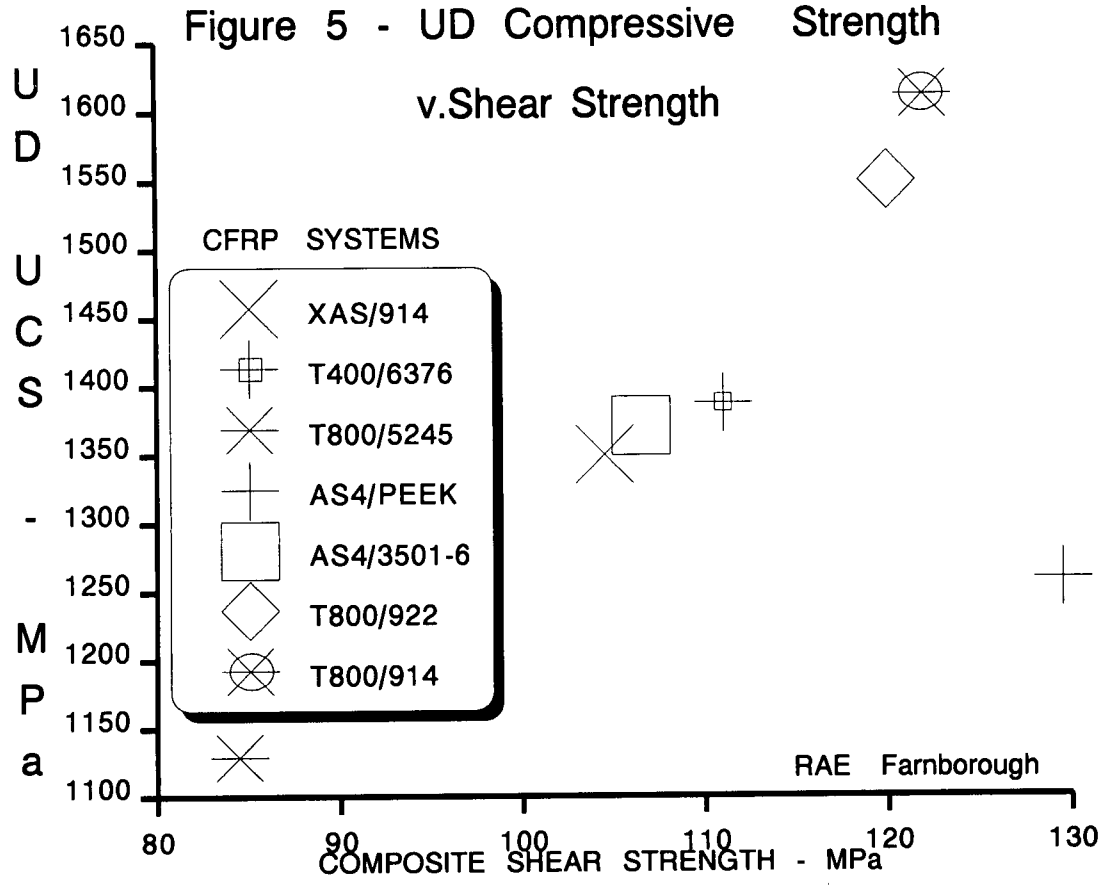

Figure 6 - COMPRESSIVE STRENGTH OF UD COMPOSITES

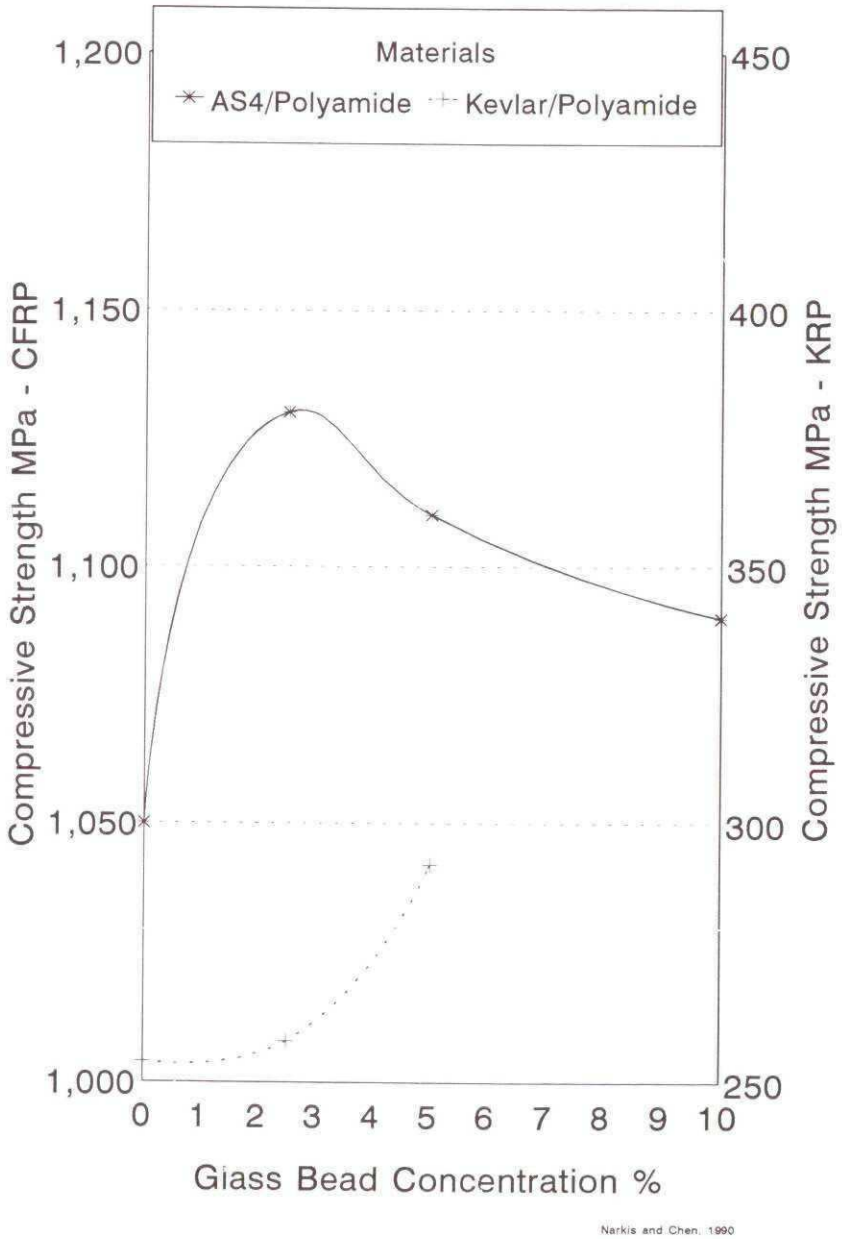

Narkis and Chen, 1990

Figure 7 NOTCHED STRENGTH DATA

Comparison between theory and experiment

CFRP (0n,45n,90n) w=25mm r=2.5mm

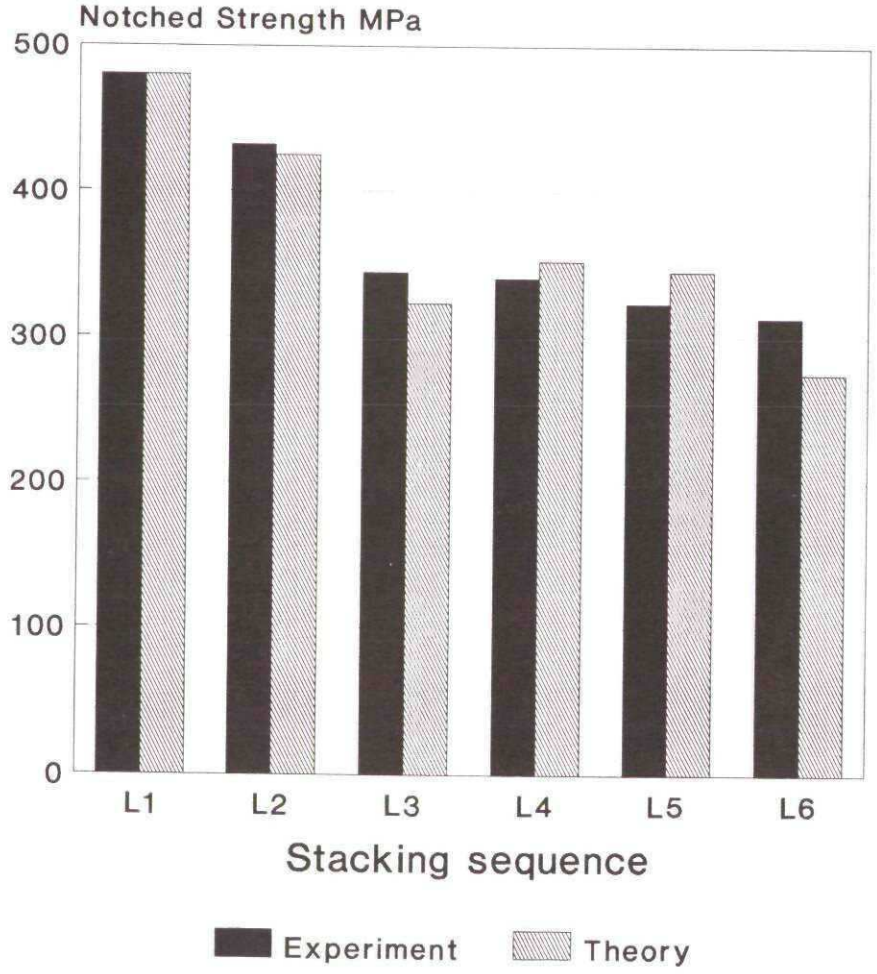

Figure 8 DELAMINATION GROWTH - PREDICTION v. EXPERIMENT

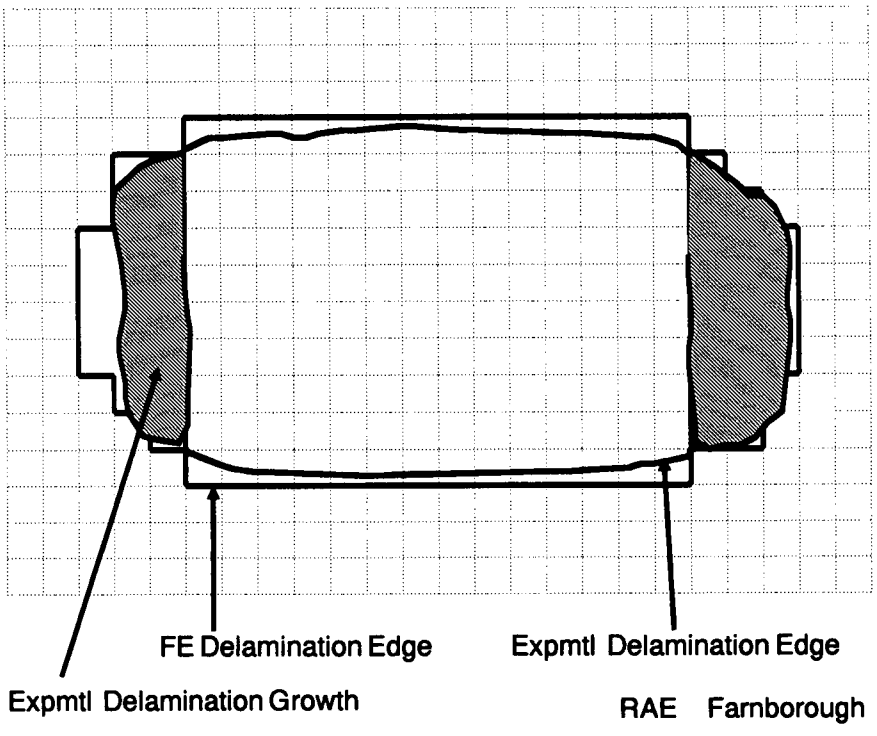

INFLUENCE OF EDGE EFFECT ON COMPRESSION-TENSION FATIGUE OF TOUGHENED GRAPHITE/EPOXY LAMINATES

J.P.KOMOROWSKI[1], J.B.R.HEATH[1], D.LEFEBVRE[2], C.ROY[2] and R.MASMOUDI[2]

1 - Institute for Aerospace Research, National Research Council, Canada, Ottawa, Ontario, K1A 0R6

2 - Faculty of Applied Sciences, University of Sherbrooke, Sherbrooke, Quebec, J1K 2R1

ABSTRACT

Results are reported of fatigue tests on a toughened graphite/epoxy (IM6/5245C) using a specimen and grip design that allows a relatively large volume of material to be tested. The loading was compression dominated (R=-3.75). Two different stacking sequences of an 18 ply laminate were tested. The lamination was typical of an aircraft wing skin (0/45/90) - (44.4%,44.4%,11.1%). The specimens were 25.4mm wide, 290mm long with a gauge length of 150 mm. During the test program specimen stiffness and residual strength were measured. In parallel, local damage development was monitored using ultrasonic C-scans, photoelastic coatings and optical microscopy. The use of thin (.25 mm) photoelastic coatings to observe in-situ damage initiation and growth is new. It is based on the sensitivity of coatings to the change in mechanical properties of specimens due to damage. The C-Scan inspection results correlate closely with photoelastic observations.

Results indicate that fatigue in composite specimens is dominated by the edge effect. Differences in the fatigue lives of the two stacking sequences used were close to two orders of magnitude. The proper selection of stacking sequence is crucial to achieving long fatigue lives. Under compression dominated loading fatigue damage is a local process. Damage always initiated at the edge and could be related to edge interlaminar shear stresses. The fatigue process consists of a relatively long period before initiation, usually in several locations, followed by a period of growth from one initiation site that finally leads to rapid compressive failure.

Introduction

Advanced composite materials for aircraft structures have not been used to their full potential due to their sensitivity to low energy impact damage. The low design allowables preclude impact damage growth under cyclic loading. This has lead some researchers to suggest that fatigue is not an issue in composite structures. While this may be true at present, future requirements and progress in NDI technology will certainly allow the design allowables to be increased[1]. Both the edge effect and fatigue have received considerable attention in the literature and analytical and experimental papers on the subject are numerous as reviewed in references [2-3].

Despite the high fatigue resistance of fiber dominated graphite/epoxy laminates under cyclic loading, physical evidence of damage such as matrix cracking, fiber matrix interface failure and delamination is well documented [2]. A good understanding of various aspects of the fatigue behavior of laminates (influence of the stacking sequence and testing variables such as stress levels, mean stress, cycling mode, etc) will certainly assist the engineer in designing fatigue resistant and damage tolerant structures.

It is recognized that the interlaminar stresses can be significantly influenced by the laminate stacking sequence[4-6] and that their magnitude can increase very rapidly near the free edge[7,8]. The narrow region close to an edge (the sides of a laminate, holes or cutouts) are thus very susceptible to damage initiation and can accelerate the failure process. The details of the microscopic events and the way in which the matrix-related damage modes influence the growth of delaminations are not well understood.

The work reported here is part of a research program investigating the mechanical behavior of graphite/epoxy (IM6/5245C) laminates subjected to static and cyclic loading. The lay-up for all specimens was [0°/45°/90°] (44.4%/44.4%/11.1%) 18 ply symmetric . The purpose of the investigation is to determine how edge effects influence the static strength, fatigue resistance and damage growth in laminates. This was done by altering the stacking sequence which directly controls the edge effects[9-12].

A finite element model was employed to obtain numerical results for the stress-field distribution for seventeen different stacking sequences. In this paper, the results of compression-tension cyclic loading tests are reported for two laminates with the following stacking sequences:

Laminate 2 : $[+45/-45/0/0/90/0/0/-45/+45]_s$

Laminate 12 : $[90/0/+45/0/+45/0/-45/0/-45]_s$

These were selected because under loading, normal stresses at the free edge of opposite signs were calculated. The dependence of the static strength on these laminate stacking sequences was examined in reference 13.

Analysis of the Free-Edge Phenomenon

The free-edge interlaminar stress problem is 3-D in nature. Following the initial work of Pipes and Pagano[7] and numerous other investigators, Wang et al.[20] studied the tensile behavior of a $[0_2/90_n]$ graphite/epoxy laminate. They demonstrated that matrix cracking in the narrow region close to the edges at the 0°/90° interfaces and at the 90° plies resulted from the combined actions of the normal and shear stresses σ_z, τ_{xz} and τ_{yz} respectively (Figure 1).

A variety of failure criteria have been proposed to predict the static failure strength of multidirectional laminates from a knowledge of the strength of unidirectional laminates and the nominal stresses in the laminae at a given load. They range from the very simple to the rather complex. None, as yet, has been found to be entirely satisfactory because the classical laminated plate theory only provides accurate stress values in laminae far from the free edges. Sun and Zhou[14] have computed, for a laminate incorporating 0°, 90° and ±45°

laminae, the stress states at 0.5t, t, 1.5t, 2t, 2.5t and 3t from the free edge (t=ply thickness). They showed that with the Tsai-Hill and Hashin-Rotem strength criteria, the stress-state calculated at 2t from the free edge gave the best correlation with experimental observations.

Computed Laminate Strengths

A finite element program developed by Lahoud[15] was used to account for the different lamina orientations and to define the stress distributions within the laminates 2 and 12 under a uniaxial tensile or compressive strain of $\pm$ 1%. The stress values computed at 2t from the free edges were chosen as representative of the stress-state at the free edges as suggested by Sun and Zhou[14]. The distance 2t was equal to 0.28 mm for these laminates. As an example, the stress distributions, σ_z and τ_{xz}, at the free edges and at a distance 2t are shown for the laminate 2 under tensile loading (Figure 2). Detailed stress analysis for both laminates can be found in Ref. 18. The failure strengths of laminates 2 and 12 were predicted using the modified Tsai-Wu, Tsai-Hill and Hashin-Rotem failure criteria[14,16,17]. The values of the mechanical properties of an IM6/5245C lamina are reported in Table 1 and these were used with each criterion expression. The failure strengths of the 0° and 90° plies are presented in Table 2. The calculated strengths can be compared to the values determined experimentally[13].

Under a compressive strain ε=-1%, the interlaminar stresses computed in each laminate at the free edge and at 2t from the edge are given in Table 3. It can be observed that, at the free edge, maximum positive normal stresses σ_z and shear stresses τ_{xz} are at the 45°/-45° interfaces (8th/9th ply) in laminate 2. At 2t (0.28mm) from free the edge the stresses are of a significant magnitude at the 0°/45° and 0°/-45° interfaces (3rd to 9th ply) and the maximum is between the 6th and 7th ply.

On the basis of these calculations, the delamination of laminate 12, in a mixed mode, would occur due to the presence of a tensile value of σ_z, and a positive shear stresses (as calculated at a distance 2t from the free edge in the 0°/-45° interface). Delamination in Mode II in laminate 2 could also occur but because the shear stress level (τ_{xz}) is smaller than in laminate 12 it is unlikely that the delamination would grow to the same extent. Initiation and propagation of delaminations during fatigue loading is complex process which in simple cases can be modeled using strain energy release rate calculations[20].

Experimental

The specimens used in this investigation were prepared and tested in the Structures and Materials Laboratory of the Institute for Aerospace Research (IAR). Large panels (61 cm x 30.5 cm) of the IM6/5245C graphite/epoxy were fabricated with stacking sequences 2 and 12. The 2.5 mm thick panels were cut into specimens 290 mm long by 25.4 mm wide. Prior to testing the specimens were inspected using an ultrasonic C-scan and were found to be free of detectable flaws.

The specimens were tested using an MTS 100 kN servo-hydraulic testing machine under stroke control. The load was transferred to the specimens through a hydraulic gripping system[19] which maintained a constant pressure of about 35 MPa over a 60 mm length at each extremity. The gripping areas of both the specimen and the jaws were lightly sand-blasted to prevent slippage during loading. Aluminium anti-buckling guides (12.6 mm wide x 152.4 mm long) supported the central portion of the specimens tested in compression. A thin Teflon sheet was inserted between the specimen and the anti-buckling guide to minimize the friction.

Tension-compression fatigue tests were conducted using load control with a sinusoidal wave form, under a load ratio $R = P_{max}/P_{min} = -3.75$. The P_{min} load varied from a low of $0.6P_{uc}$ (P_{uc} being the static strength in compression) to a high of $0.9P_{uc}$. The P_{uc} load for each laminate was determined from a number of static tests. The values were -43.5 kN and -35.9kN for laminate 2 and 12 respectively. The number of cycles to failure recorded in the test data corresponded to the final fracture of the specimen.

Specimen deformation was measured using an MTS clip gauge extensometer. A 12.7 mm distance separated the pointers of the clip gauge mounted on one side of the specimen. The maximum range of the gauge was 15% strain.

Following failure, sections of laminate 2 specimens outside the fracture zone were converted into a short gauge length specimens. These were tested to determine their residual compressive strength. Given the gauge length of 5mm the specimen could be tested in compression without any need to use anti-buckling guides. Side loading wedge type MTS hydraulic grips were used in these tests. Sand-blasted aluminum alloy tabs were placed between the specimen and the wedges, to protect the specimens from damage by the serrations on the wedges. A total of twelve specimens were tested, four from each selected fatigue load level. Another 13 virgin specimens were also tested to verify that the short gauge length static test corresponds to the long gauge (with anti-buckling guides) used predominantly in this project. The coefficient of variation of recorded strength in these 13 specimens was 15.2% versus 7.2% in long gauge specimens. However, the average strengths measured using the two methods were less than 0.5% different.

A travelling microscope was used to observe the development of edge interlaminar damage during the cyclic tests. In addition, two inspection techniques, Shadow Moiré interferometry and photoelastic coatings were employed. Shadow Moiré was used to observe out of plane deformations due to delamination or specimen buckling in compression (to test the design of the antibuckling guides). Photoelastic coatings were used to observe the progression of damage, in real time, during testing. The method is especially effective in laminates with residual curing stresses. The coatings (typically 0.25 mm thick) are applied before testing. Since the specimens used are coupons subjected to uniform strain loading any nonuniformities in the observed isochromatic patterns are related to damage accumulation and the associated redistribution of residual stresses in the specimen. The coatings are sensitive to the difference in the principal normal strains. Due to the accumulating damage, stiffness and Poisson's ratio will change and affect the response of the coating during loading. The damage development during the fatigue testing was observed with a reflection polariscope model 031 manufactured by Measurements Group. Still photography at selected intervals gave a permanent record of damage growth. Periodically these observations were verified by removing the test specimens from the load frame and carrying out an ultrasonic C-scan inspection.

Results and Discussion

The long gauge length static test results are summarized in Table 2. The tensile strength P_{ut} and the compressive strength P_{uc} are defined as the load recorded at ply failure. The Young's modulus was computed at half the maximum load using the secant drawn on the stress-strain curve.

Results of fatigue tests are presented in Fig. 3 as a plot of the applied load (S) against number of cycles to failure (N). The data scatter is characteristic of the fatigue behavior of composites. However, the results clearly show that for any cyclic loading corresponding to a precise percentage of static strength in compression of each laminate the logarithmic lifetime of laminate 2 is much greater than that of laminate 12. For example, at a cyclic stress level $S= 0.7\ P_{uc}$ the nominal average fatigue life of laminate 2 was approximately 800,000 cycles and only 8,000 cycles for the laminate 12. Another way of comparing the fatigue strength of both laminates is to estimate their respective cyclic stress level (relative to the static compression strength) yielding a common logarithmic lifetime. For example at Log N = 3.9 (N = 8,000 cycles), the cyclic loading level for laminate 2 was $S= 0.9\ P_{uc}$ but corresponding only to $S= 0.7\ P_{uc}$ for laminate 12. The difference in the stress level is rather striking since the corresponding P_{min} values are -39.15 kN and -25.13 kN for laminate 2 and 12 respectively.

Local delaminations observed at the free edge of laminate 12 grew towards the interior of the test specimen rather than longitudinally along the free edge. The delaminations were located at the $0^o/45^o$ interfaces (6th/7th ply). In laminate 2 damage initiated in the 45^o plies at the free edge. The damage had the appearance of erosion sites in the laminae (not cracks) and were partly filled with small dust like particles. This form of damage appeared at specimen midlife close to the $45^o/-45^o$ interfaces where the shear strains are the highest (see Table 3). In laminate 12 both the σ_z and τ_{xz} seem to drive the damage growth while in laminate 2 only τ_{xz} is significant at 2t from the edge. Since the shear stresses responsible for damage in laminate 2 are nearly half the stresses in laminate 12, the significant difference in the fatigue lives seems to correlate well with the calculated stress magnitudes.

Post-failure short gauge length test results for laminate 2 are shown in Figure 4. While the trend for lower residual compressive strength is consistent, only the specimens tested at 70% show a statistically significant static strength reduction from that of the virgin material. At the 70% load level, specimens were on average subjected to 800,000 cycles and it should be noted that their 'global' strength was reduced only by 10%.

Figure 5 shows damage development as recorded with photoelastic coatings in a laminate 2 specimen. Four images taken at 0, 350,000, 744,000 and 797,000 cycles represent respectively 0, 0.44, 0.94 and 1 life time (LT) (specimen failed at 797,794 cycles). The particular images were selected for their significance in the damage evolution. The 0.44LT image shows the first signs of damage and nominally ends the period of damage initiation. The 0.94LT image shows slow damage growth. It is interesting that most of the damage is generated in the last stage of specimen life (6%), which is contrary to the characteristic required for damage tolerant design. The photoelastic coatings and C-scan results show that there are usually several damage initiation sites at the edges. One of these shows a pronounced growth in the second stage of the specimen life and is the cause of final failure. The post-failure residual strength tests demonstrating high strength retention outside the final failure affected zone correlate well with the damage growth observations. It can be concluded that under the compression dominated fatigue loading used in these tests, the fatigue damage is a local process.

Conclusions

Experimental observations during fatigue confirmed that the stresses computed at 2t from the free edge may be regarded as critical for the determination of fatigue damage initiation.

Stacking sequence selection can affect the fatigue life of composite specimens by a factor of 100.

Under compression dominated compression-tension cycling fatigue damage growth seems to be a local process. Most of the damage is generated during the last 6% of the specimen life.

The photoelastic coating technique is effective in the real-time monitoring of damage growth in composites.

Acknowledgments

The financial support of the Department of National Defence under FE220788NRC21 is gratefully acknowledged. The work reported was performed under IAR/NRCC Program 3G3: "Aerospace Structures, Structural Dynamics and Acoustics", Subprogram 304: "Fatigue and Damage Tolerance of Structures", Project JGK00: "Fatigue and Environmental Test Techniques for Composites".

The authors appreciate the helpful comments and suggestions of Dr. J.J.Kacprzynski of the IAR regarding the free-edge analysis. The contribution of Mr. Z.Fawaz of University of Sherbrooke in suggesting post failure residual strength tests and in carrying some of the testing is gratefully acknowledged.

References

1. J.P.Komorowski, D.L.Simpson, R.W.Gould, "A technique for rapid impact damage detection with Composites, Vol.21, No.2,March 1990.
2. L.Dupont, C.Roy, J.P.Komorowski, "Revue de litterature portant sur l'endommagement, la perte de rigidité et la résistance résiduelle d'un stratifié graphite/epoxy soumis á un chargement cyclique.", NAE, NRC, LTR-ST(CR)-1711, July 1989.
3. D.Lefebvre, R.Masmoudi, C.Roy, "Délaminage en mode I et II en mode mixte des composites graphite-epoxy soumis á des charges statiques et cycliques en tension et compression.", NRC, IAR-CR-8, Jan.1991.
4. J.M. Whitney, "The Effects of Transverse Shear Deformation on the Bending of Laminate Plates" J. Compos. Mater., 3, p. 534 (1969).
5. N.J. Pagano, "Exact Solutions for Composite Laminates in Cylindrical Bending" J. Comp. Mater., 3, p. 398 (1969).
6. N.J. Pagano and J.C. Halpin, "Influence of End Constraints in the Testing of Anisotropic Bodies" J. Comp. Mater., 2, p. 18 (1968).

7. R.B. Pipes and N.J. Pagano, "Interlaminar Stresses in Composite Laminates under Uniform Axial Extension", J. Compos. Mater., 4, p. 538 (1970).
8. R.B. Pipes and I.M. Daniel, "Moiré Analysis of the Interlaminar Shear Edge Effect in Laminated Composites" J. Compos. Mater., 5, p. 255 (1971).
9. J.M. Whitney, "Free-Edge Effects in the Characterization of Composite Materials" ASTM STP 521, p. 167 (1973).
10. N.J. Pagano, "On the Calculation of Interlaminar Normal Stress in Composite Laminates" J. Compos. Mater., 8, p. 65 (1974).
11. J.D. Whitcomb and I.S. Raju, "Analysis of Interlaminar Stresses in Thick Composite Laminates with and without Edge Delamination" ASTM STP 876, p. 69 (1985).
12. L. Dupont, "Etude du comportement mécanique d'un composite stratifié graphite/epoxy soumis à des sollicitations monotones et cycliques" NAE Report - NAE CR-2 NRC #30833 (1989).
13. D.Lefebvre, J.P.Komorowski, C.Roy, R.Masmoudi, "Free-Edge Influence on the Static Strength of Graphite/Epoxy Laminate.", Proc. of First Canadian International Composites Conference, Montreal, 4-6 September 1991.
14. C.T. Sun and S.G. Zhou, "Failure of Quasi-Isotropic Composite Laminates with Free Edges" J. of Reinf. Plast. and Compos.7, p. 515 (1988).
15. A.E. Lahoud, "AEE: A Finite Element Program for the Analysis of Edge Effects in Composites, Research Dept. # AEL-11-86, U. Sherbrooke Civil Eng. Dept (1986).
16. S.W. Tsai, Composite Design, 4th Edition, Think Composites (1988).
17. M.N. Nahas, "Survey of Failure and Post Failures Theories of Laminated Fiber-Reinforced Composites" J. of Comp. Techn. and Res. 8 p. 138 (1986).
18. D. Lefebvre, R. Masmoudi and C. Roy, "Comportement des stratifiés carbone-epoxy IM6/5245C sous charges de tension-compression statique et cyclique", IRA - Contract Report, NRCC Ottawa (to be published), (1991).
19. J.B.R. Heath, J.P. Komorowski and B.E. Shaver, "Design and Development of Hydraulically-Clamped Grips for Composite Material Testing" NAE Technical Report LTR-ST-1729 (1989).
20. A.S.D. Wang, M. Slomiana and R.B. Bucinell, "Delamination Crack Growth in Composite Laminates" ASTM STP 876, p. 135 (1985).

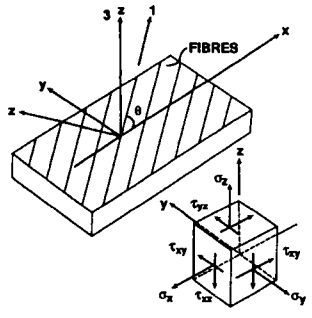

Figure 1. Reference axes and stress representation in a laminate.

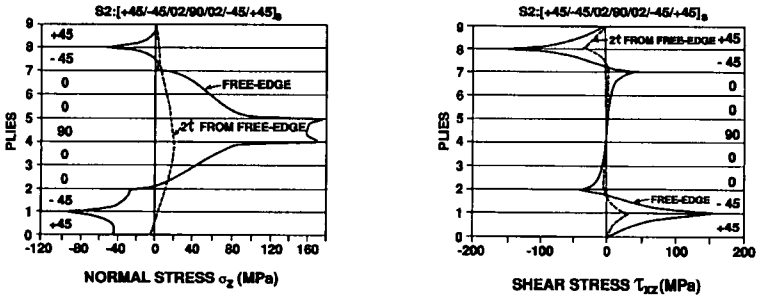

Figure 2. FEM calculated normal and shear stresses at the free edge and 2t away from the edge. Laminate stacking sequence 2.

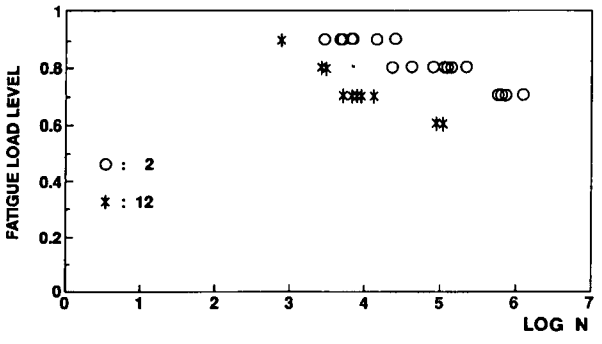

Figure 3. Laminates 2 and 12. Load level versus number of cycles to failure (R=-3.75, f=5Hz).

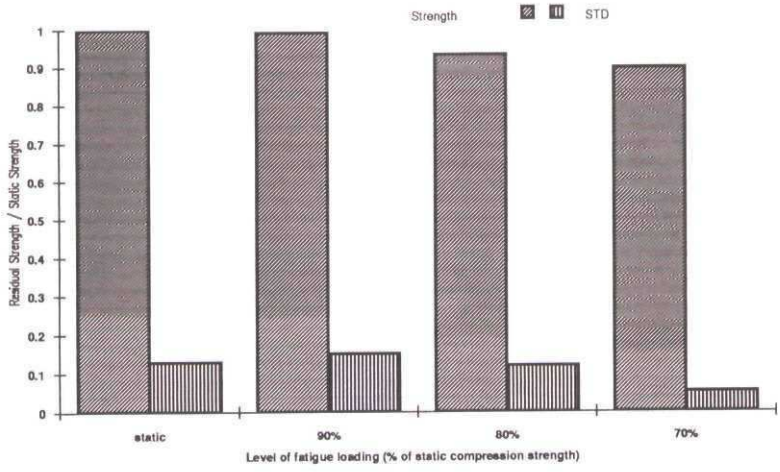

Figure 4. Post failure residual compression strength in laminate 2. Smaller bars show standard deviation (STD) observed in tests.

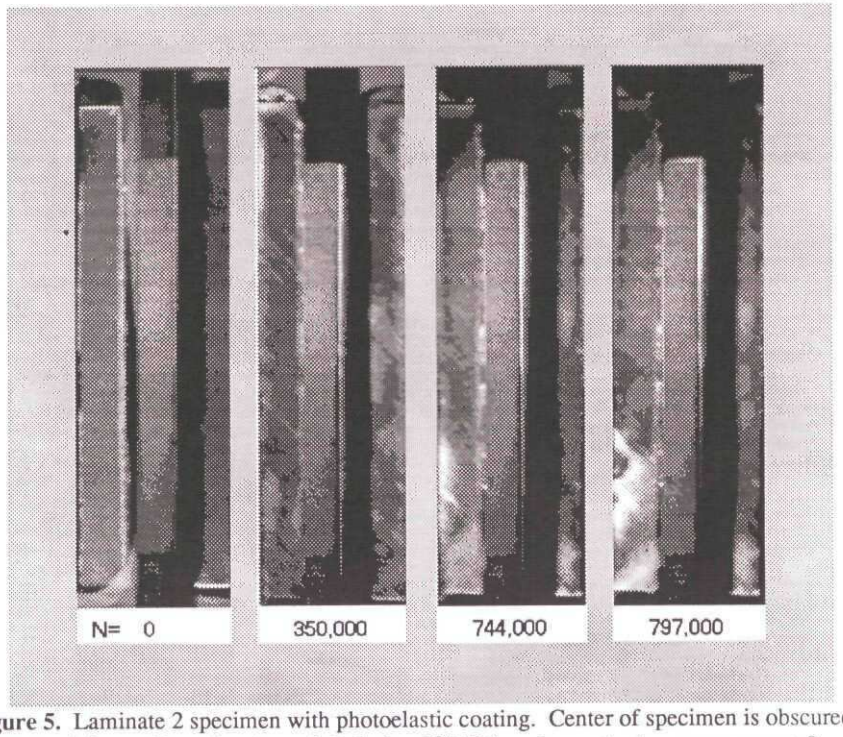

Figure 5. Laminate 2 specimen with photoelastic coating. Center of specimen is obscured by antibuckling guides. Specimen failed after 797,794 cycles so the images represent 0, 0.44. 0.94 and 0.999 life time (LT). The white area in the lower left corner of specimen seen at 0.94 and 0.999 LT indicates damaged zone.

Properties		Manufacturers Data	IAR Data Used in this study
σ_u tension (0^o) = X^T	(MPa)	2516	2610
σ_u compression (0^o) = X^C	(MPa)	-1462	-1280
$E_{tension}$ (0^o) = $E_1{}^T$	(MPa)	156 000	173 000
$E_{compression}$ (0^o) = $E_1{}^C$	(MPa)	152 000	141 000
ε_u tension (0^o)	(%)	1.6	1.5
ε_u compression (0^o)	(%)	1.01	0.96
σ_u tension (90^o) = Y^T	(MPa)	83	60
σ_u compression (90^o) = Y^C	(MPa)	-145	-220
$E_{tension}$ (90^o) = $E_2{}^T$	(MPa)	3300	8500
$E_{compression}$ (90^o) = $E_2{}^C$	(MPa)	-	7040
$E_{bending}$ (90^o)	(MPa)	3400	-
ε_u tension (90^o)	(%)	-	0.72
ε_u compression (90^o)	(%)	2.9	3.10
τ_u = S	(MPa)	105	118
G_{12}	(MPa)	-	5550
ν_{12}		-	0.29
G_{1C} (matrix)	(kJ/m^2)	0.158	-

Table 1. Mechanical properties of unidirectional IM6/5245C laminates.

Laminate	Ply	Criteria	Tension		Compression	
			P_{ut} (kN)	ε_{max} (%)	P_{uc} (kN)	ε_{max} (%)
12	0^o	Hashin-Rotem (plane x-y)	88.7	1.490	45.3	0.920
	0^o	Hashin-Rotem (plane x-z)	83.4	1.400	42.9	0.870
	0^o	Tsai-Wu (F^*_{12}=0)	-	-	37.7	0.765
	0^o	Tsai-Hill (plane x-y)	87.0	1.460	42.9	0.870
	0^o	Tsai-Hill (plane x-z)	76.8	1.290	38.9	0.790
12	90^o	Hashin-Rotem (plane x-y)	44.5	0.746		
	90^o	Hashin-Rotem (plane x-z)	44.6	0.750		
	90^o	Tsai-Wu (F^*_{12}=0)	42.3	0.710		
	90^o	Tsai-Hill (plane x-z)	47.0	0.790		
2	0^o	Hashin-Rotem (plane x-y)	89.6	1.505	44.3	0.899
	0^o	Hashin-Rotem (plane x-z)	89.6	1.505	44.4	0.900
	0^o	Tsai-Wu (F^*_{12}=0)	-	-	41.0	0.831
	0^o	Tsai-Hill (plane x-y)	81.0	1.360	43.9	0.890
	0^o	Tsai-Hill (plane x-z)	81.6	1.370	44.4	0.900
2	90^o	Hashin-Rotem (plane x-y)	40.5	0.680		
	90^o	Hashin-Rotem (plane x-z)	40.5	0.680		
	90^o	Tsai-Wu (F^*_{12}=0)	39.3	0.660		
	90^o	Tsai-Hill (plane x-z)	45.0	0.755		
12	0^o	Experimental value	80.9	1.470	37.2	0.920
	90^o	Experimental value	45.0	0.900		
2	0^o	Experimental value	84.9	1.580	45.9	1.080
	90^o	Experimental value	45.0	0.900		

Table 2. Calculated and measured strengths and fracture strains of laminates 2 and 12.

Interfaces		Free edge		2t from the free edge	
		σ_z (MPa)	τ_{xz}(MPa)	σ_z (MPa)	τ_{xz}(MPa)
S2	45/-45	48	174	-5	20
	-45/0	-6	-56	-11	0
	0/0	-43	-6	-15	-1
	0/90	-124	-2	-15	0
	90/0	-119	-1	-15	0
	0/0	-32	-6	-11	0
	0/-45	16	58	-7	-2
	-45/45	83	-186	0	-22
S12	90/0	-20	-10	7	-2
	0/45	51	-74	11	-1
	45/0	55	86	20	21
	0/45	56	34	26	26
	45/0	66	137	30	43
	0/-45	68	138	33	43
	-45/0	60	35	36	24
	0/-45	57	90	38	17

Table 3. Interlaminar stresses at free edge and at 2t (0.28mm) from free edge in laminates 2 and 12 under compressive loading (ε_x=-1%).

DAMAGE PROGRESSION UNDER COMPRESSIVE LOADING IN COMPOSITE LAMINATES CONTAINING AN OPEN HOLE

C. Poon
N.C. Bellinger
R.W. Gould
M.D. Raizenne
Institute for Aerospace Research
National Research Council Canada
Ottawa, Canada K1A-0R6

SUMMARY

This paper describes an experimental investigation into damage progression in compressively loaded quasi-isotropic laminates with a circular hole and the prediction of damage initiation using 3D finite element failure analysis. Notched laminated plates were fabricated from Narmco IM6/5245C with three stacking sequences; $[+45/0/-45/90]_{6s}$, $[(+45)_3/(0)_3/(-45)_3/(90)_3]_{2s}$ and $[(+45)_6/(0)_6/(-45)_6/(90)_6]_s$. Most specimens were tested to ultimate failure but some were stopped prior to failure. The criterion for stopping the test was the detection of audible acoustic emission. The tests revealed that the notched strength decreased as the ply group thickness increased. An examination of the hole surface of those specimens not taken to ultimate failure revealed delaminations at the $+45°/0°$ and $-45°/0°$ interfaces and failure of the $+45°$ and $0°$ ply groups. For the specimen where six plies with the same fibre orientation were grouped, the midplane of the $0°$ ply group also contained a delamination. A tensor polynomial failure criterion which used all the six stress states determined from the 3D finite element analysis at the laminate characteristic dimension was used to predict initial laminate failure. Although this failure criterion was able to predict the strain at initiation for the laminate $[(+45)_6/(0)_6/(-45)_6/(90)_6]_s$, it could not distinguish between the different ply group thicknesses. Therefore another failure criterion based on the interlaminar stresses was proposed to predict strain at initiation. This criterion, when used in conjunction with the nodal stresses at the hole edge, predicted the strain at initiation reasonably well.

Based on the numerical and experimental results, a mechanism for damage initiation and progression was proposed. However, considering that damage initiation occurred at over 90% of the ultimate load, a damage progression model would not be practical for the material systems presently used in aircraft. As the material systems are improved, it may be possible to apply such a model in the near future.

LIST OF SYMBOLS

d_o	characteristic dimension
ϵ_x	applied axial strain
F_i, F_{ij}	strength tensors
R	load factor
σ_N	compressive notched strength
σ_o	far field applied stress
σ_1, σ_2, σ_{12}	in-plane stresses
σ_3	interlaminar normal stress
σ_{23}, σ_{13}	interlaminar shear stresses

1. INTRODUCTION

Structures manufactured from carbon fibre reinforced polymer composites have significantly lower compressive strengths when holes are present. It appears that the toughness of the polymer matrix, the properties of the fibre/matrix interface and the stability of the fibres are the major factors influencing the compressive notched strength. The importance of these factors is manifested by the complex failure modes which involve matrix cracking, delamination, localized buckling and shear failure.

In the early stage of model development, semi-empirical approaches based on the point stress or average stress failure criteria were adopted to predict the compressive notched strength.[1-4] These macroscopic models require two empirical parameters, the characteristic dimension and the ultimate unnotched strength of the laminate, for notched strength prediction. Although these models are simple and practical to apply in designing composite structures with notches, they are limited to uniaxial loading cases and cannot address failure modes. Further development[5,6] had extended the earlier models to handle general in-plane loading cases and to predict the location of failure on the hole boundary and the critical ply within the laminated plate based on a first ply failure hypothesis. The major deficiency in the first ply failure models is that the ultimate failure of a notched laminate does not usually occur immediately following the failure of the first ply.

The progressive nature of failure in compressively loaded laminates containing a circular cutout was investigated experimentally by Waas, et al.[7] Using real time holographic interferometry and in-situ photomicrography, they observed that failure was initiated as a localized instability in the $0°$ plies at the hole surface at approximately right angles to the loading direction. Subsequent to the $0°$ ply failure, extensive delamination cracking was observed with increasing load. The delaminated regions propagated to the undamaged areas of the laminate by a combination of delamination, buckling and growth of damage, the buckling further enhancing the growth of damage. Analytical models for the prediction of damage progression were not developed.

A two dimensional model was developed by Chang and Lessard[8] to predict damage progression and failure modes of notched laminated plates under compressive loading. Using a nonlinear finite element method, stresses and strains were calculated based on finite deformation theory with consideration of material and geometric nonlinearities. The types and extent of damage in the material were predicted by a set of proposed failure criteria and material degradation models. Numerical results from the model were compared with data obtained from an experimental investigation[9] and good agreements were found between

predictions and test results. Because of the two dimensional analysis used in the model, interlaminar normal and shear stresses were not determined.

Failure models must be able to predict delamination since it is a major progressive failure mode in compressively loaded laminated plates with holes. In order to predict delamination, interlaminar normal and shear stresses must be determined and incorporated into appropriate failure criteria. However, the calculation of these interlaminar stresses requires three dimensional analysis which is complicated and costly. Consequently, very few papers concerning three dimensional analysis are reported in the literature.

Barboni et al[10] recently reported an investigation into edge effects in composite laminates with circular holes. A quasi-3D analysis was performed to study the importance of stacking sequence and geometric parameters on the stress field around the hole. In the numerical tests a power series expansion for displacement in the z-direction was adopted to satisfy the equilibrium conditions of the stresses at ply interfaces. No attempts were made to develop criteria for failure predictions.

Burns et al[11] developed an efficient 3D finite element failure analysis of compressively loaded angle-ply laminates with holes. The tensor polynomial failure criterion was used to predict the location and mode of failure. They found that failure initiated at the interface between layers on the hole edge and the angular location of the initial failure was a function of the fibre orientation.

The compressive response of notched and unnotched laminated plates has been investigated at the Institute for Aerospace Research.[12,13] The long term objective is to improve the understanding of the failure mechanisms of compressively loaded laminates with holes or impact damage. The present paper describes an experimental investigation into damage progression in compressively loaded quasi-isotropic laminates with a circular hole and the prediction of damage initiation using a 3D finite element failure analysis.

2. EXPERIMENT

2.1 Specimen Preparation

The laminated plates used in the tests were fabricated from a composite material consisting of Hercules IM6 graphite fibres preimpregnated with Narmco 5245C resin. The IM6 fibre is a continuous graphite fibre with a tensile modulus of 280 GPa and a tensile ultimate strain of 1.5%. The 5245C is a 177°C cure modified bismaleimide resin with an intended wet service capability up to 121°C. The layup of the laminated plates was quasi-isotropic and consisted of 48 plies. Three types of specimens, designated A, B and C, with ply stacking sequences, $[+45/0/-45/90]_{6s}$, $[(+45)_3/(0)_3/(-45)_3/(90)_3]_{2s}$ and $[(+45)_6/(0)_6/(-45)_6/(90)_6]_s$, respectively, were adopted to study ply grouping effects. The angles of the fibre orientation are presented in Figure 1. The plates were consolidated using the vacuum bagging and autoclave curing procedure recommended by the prepreg manufacturer. After curing, the plates were inspected nondestructively using an ultrasonic C-scanning method. The fibre volume fraction, determined using a burn-off test[14], was between 0.6 and 0.65. Mechanical and strength properties of IM6/5245C are shown in Table 1.

The geometry of the open hole compression test specimen is shown in Figure 2. The short edges of the specimen were ground flat and parallel to within 0.013 mm. The hole in the centre of the specimen was drilled and reamed using high speed carbide tools to a nominal diameter of 25.4 mm. Drilling was performed without lubricant and the specimens were clamped between two plexiglass plates to reduce the chance of drill-induced delamination. After machining, the specimens were again C-scanned. A pair of back-to-back strain gauges was mounted on each specimen. For a selected group of specimens, back-to-back strain gauges were also mounted at the edge of the hole.

2.2 Testing Procedures

A typical test setup is shown in Figure 3. Specimens were end loaded in compression under stroke control on an MTS testing machine connected to a computerized control and data acquisition system. An hydraulic actuator displacement rate of 1.27 mm/min was used. The short edges of the specimen were clamped in a pair of steel blocks to prevent end brooming under the compressive load. Anti-buckling guides were mounted on the longitudinal edges to suppress global buckling. Extreme care in alignment was exercised to ensure that the specimen was loaded in the centre of the testing machine with the longitudinal axis of the specimen maintained parallel to the loading axis of the machine. All tests were done at room temperature without environmental conditioning.

For each stacking sequence, most specimens were tested to ultimate failure but one or two tests were stopped prior to ultimate failure. The criterion for stopping the test was the detection of audible acoustic emission which indicated damage had initiated. For these tests, one specimen of each stacking sequence was treated with a photoelastic coating. The changes in surface strain distribution were continuously monitored using an image analyzing system.

2.3 Experimental Results

A summary of the experimental results is presented in Table 2. The open hole compressive strength, σ_N, was computed by dividing the ultimate load by the gross cross sectional area of the specimen. Typical stress vs strain curves for the specimens with stacking sequence A, B and C are shown in Figure 4. The far field stress-strain relationships for all specimens show linear and nearly identical behaviour under the compressive loading. Slight bending of the specimens is indicated by the divergence of curves which becomes more obvious when the stress level is close to the ultimate failure load. The disturbance in the linear behaviour for the type C specimen indicates delamination of the outer plies which extends to almost the full length of the specimen, see Figure 5. However, this was not the situation for the type A and B specimens which contained localized delaminations in the vicinity of the hole, see Figures 6. The average compressive notched strengths for type A, B and C specimens are 238.3 MPa, 196.9 MPa and 176.2 MPa respectively. This trend clearly indicates the reduction in compressive notched strength due to ply grouping.

During the compression tests, audible acoustic emissions were detected when the applied load was over 90% of the

ultimate collapse load. In most cases, localized bulging of the surface at the hole edge was observed when the acoustic emissions were heard. The bulging of the surface indicates localized buckling of the outer plies. After the first appearance of localized buckling, the specimen continued to sustain load for approximately 10 seconds before the buckled regions extended rapidly to the side edges of the specimen. As a result of this observation, it was decided that for each stacking sequence, one or two tests were halted at the detection of audible acoustic emissions. These specimens were removed from the test machine and the damage zones were studied using photomicroscopy and ultrasonic time-of-flight C-scan method. The failure modes observed are discussed in the following subsection.

2.4 Failure Modes

A typical localized bulging of the plate surface at the hole edge of a type B specimen is shown in Figure 7. For this stacking sequence, each ply group has three plies of fibres with the same orientation stacked together. The test for this specimen was halted at the first detection of audible acoustic emission. A photoelastic image of the specimen, shown in Figure 8, shows the size and shape of the damage. A photomicrograph of the hole surface shown in Figure 9 reveals delamination between the ply group interfaces of +45°/0° and -45°/0°. Also, the failures of the outermost groups of +45° and 0° fibres and the second group of 0° fibres are shown. For type A specimens where plies with the same fibre orientation are dispersed, initial damage at the hole edge similar to that described for the type B specimen was observed. For type C specimen where six plies with the same fibre orientation are grouped, initial damage at the hole surface as shown in Figure 10 consists of delamination between the ply group interfaces of +45°/0° and -45°/0°, delamination within the 0° ply group, and failure of the 0° fibres.

3. FINITE ELEMENT STRESS ANALYSIS

Since delamination at the ply interface is one of the major failure modes observed in the experimental results, a three dimensional finite element analysis was carried out to determine the interlaminar stresses. These stresses are well known to influence failure at the ply interfaces. The objective of this study was to determine the effect of ply group thickness on the interlaminar stresses, the location and mode of the initial damage, as well as the strain at initial failure.

3.1 Finite Element Model

The finite element model is based on the assumption of linear elastic material behaviour and linear strain displacement relationships. Three models were generated using 20 node solid brick elements available in the NISA code to simulate the stacking sequences (type A, B, C) used in the test specimens. Two of the models were identical except for the ply group thickness. One of the models, type B, contained ply groups that were one-half the thickness of the type C model. Both models had elements that were concentrated in the vicinity of the ply interfaces, see Figure 11(a). The other model, type A, contained plies that were one-third the thickness of the type B model, see Figure 11(b). This model had elements that were concentrated only in the 0° and -45° plies. Each of the models contained four concentric arcs, with the first one being 1 mm from the edge of the hole. The first arc allowed the ply stresses to be determined along the laminate characteristic dimension, d_o, from the edge of the hole at the element Gauss points. The laminate characteristic dimension was experimentally determined in a previous study to be 0.94 mm[13]. An axial strain of ϵ_x=-0.1%, was applied to all the models. The mechanical and strength properties used in the analysis are given in Table 1.

Since the axes of orthotropy of the laminae are not aligned with the global X or Y axes, see Figure 1, the laminates do not exhibit reflection symmetry about either of these global axes. An exact model of the problem would require a finite element mesh comprising the entire half of the laminate about the midplane. Such a mesh could not be used because of the large computer storage and long running times required for such a model. Instead, the X axis was taken to be an axis of approximate reflection symmetry, see Figure 11. The adverse effects of this symmetry approximation have been shown to be limited to the elements adjacent to the line of assumed symmetry which is far from the experimentally observed failure point[11].

A convergence study was carried out on the type A model to refine the size of the elements through the ply thickness. This was accomplished by comparing the element Gauss stress in the vicinity of the hole edge from one run to another run with a finer mesh. When the interlaminar normal stress did not vary by a significant amount between the two runs and the amount of computer time required to complete a run was still within reason, the results were assumed to have converged.

3.2 Ply Stress Distributions at Hole

One of the goals of this study was the prediction of failure, therefore, stress is presented primarily in the material (1-2-3) coordinate system which facilities the evaluation of different failure criteria more directly. All stresses are normalized with respect to the laminate far field applied stress, σ_o. Since the experimental results showed that failure initiates at the hole boundary, stresses are presented around the hole edge.

Stress plots for the type C model are shown in Figures 12 (a), (b) and (c) for the stress components σ_x, σ_z and σ_{xz}, respectively. As can be seen from this figure, the maximum stress occurs in the 0° ply for the axial and interlaminar normal stresses while the maximum interlaminar shear stress occurs at the +45°/0° and -45°/0° interfaces which is also the case for the type A and B models. Based on these stress results, for the remainder of the paper, only the stresses in the 0° ply and the +45°/0° and -45°/0° interfaces will be presented since they are the critical areas. However it should be pointed out that all the interfaces were examined to ensure that the +45°/0° and -45°/0° interfaces were the most critical.

The stress distributions of σ_1, σ_2 and σ_{12} at the Gauss point around the hole edge in the centre of the 0° ply for each model are given in Figures 13(a), (b), (c), respectively. As can be seen from this figure, the in-plane stress components are not significantly affected by the ply group thickness. Also, the axial stress, σ_1, is the dominant stress for all the models.

The distributions of the interlaminar normal stress, σ_3, at the Gauss point around the hole edge in the centre of the 0° ply as well as at the +45°/0° and -45°/0° interfaces are given in Figure 14(a), (b) and (c), respectively. From these figures, it can be seen that the maximum interlaminar normal stress occurs at the midplane of the 0° laminae for each model with the type C model possessing the highest stress. Also, the +45°/0° interface exhibits a slightly higher interlaminar stress than the -45°/0° interface. The difference between the midplane σ_3 and the interfacial normal stress is quite significant in the type C model, where six plies of the same orientation are grouped, as compared to the other models. Figure 14(a) clearly shows that as the ply group thickness increases the normal stress also increases. The location of the maximum stress occurs approximately at the same angle for all the models, ±27°, which was measured with respect to the hole boundary perpendicular to the applied load counterclockwise.

The distributions of the interlaminar shear stresses, σ_{13} and σ_{23}, at the Gauss point for the -45°/0° and +45°/0° interfaces are shown in Figures 15 and 16, respectively. The effect of ply group thickness is not as evident for the interlaminar shear stresses as for σ_3. The stress magnitudes once again increase as the ply group thickness increases but not as dramatically as for σ_3. The absolute maximum stress occurs at the -45°/0° interface at an angle of approximately -27° for σ_{13} and +27° for σ_{23}.

4. FAILURE PREDICTION

4.1 Laminate Failure Prediction

Laminate failure was predicted on the basis of the tensor polynomial failure criterion[15]. A load factor R was defined as one of the two roots of the quadratic equation describing the failure criterion[11]:

$$F_i\sigma_i R + F_{ij}\sigma_i\sigma_j R^2 = 1$$

where i = 1-6
j = 1-6

The load factor was calculated along a circular path concentric to the hole at a distance d_o from the hole edge. The stresses at the Gauss point around this path at each ply interface and at the midplane of the 0° ply were separately used in the failure criterion to determine the critical area. The point with the absolute minimum load factor, $|R_{min}|$, is the point at which damage initiation is first predicted to occur. This absolute minimum load factor is then multiplied by the far field strain, -0.1%, to predict the lowest strain necessary to initiate damage. It should be pointed out that the interactive terms in the failure criterion were ignored since the appropriate allowables were not known.

The absolute minimum load factor was found to occur at the -45°/0° interface for the type B and C models while the -45°/90° interface was the most critical for the type A model. The strain at initiation was equal for all the models at 3200 μmm/mm. As can be seen from Table 2, the type C specimen had an average failure strain of 3163 μmm/mm and a strain at initiation of 3017 μmm/mm which is close to that predicted by the model. However Table 2 also shows a clear difference in the strain at initiation for the different ply group thicknesses. Therefore it can be concluded that the tensor polynomial criterion, in its present form, cannot distinguish between the different ply group thicknesses. Also, the failure location for the type A model does not correlate to the experimental results since the -45°/90° interface was not damaged during testing.

These results are not unexpected since it is known that interlaminar stresses are a localized effect at the edge and decrease rapidly at very small distance from the hole. Thus, at the characteristic dimension, the dominant stresses are the in-plane stresses which were shown earlier to be equal for all the models (Figure 13). If this failure criterion were to be applied closer to the hole edge, the strain at initiation would be even smaller than that predicted at the characteristic dimension since all the stresses including the interlaminar stresses would be significantly higher. Therefore to avoid the dominating effect that the in-plane stresses had on the prediction of the strain at initiation, another failure criterion had to be applied which would only take into account the interlaminar stresses at the hole edge.

4.2 Interlaminar Failure Prediction

Since the experimental results revealed that delamination is a dominant failure mode, it was decided to implement a failure criterion which uses only the interlaminar stresses. As in the case of the laminate failure prediction, $|R_{min}|$, was used to determine the strain at initiation. The quadratic equation describing the failure criterion is:

$$\sigma_3 F_3 R + R^2(\sigma_3^2 F_{33} + \sigma_{13}^2 F_{44} + \sigma_{23}^2 F_{55}) = 1$$

where F_3, F_{33}, F_{44}, F_{55} are identical to the terms used in the tensor polynomial failure criterion. The load factor was calculated using both the nodal stresses at the hole edge and the stresses at the Gauss points closest to the edge. The stresses at each ply interface and at the midplane of the 0° ply were used in this analysis.

A bar chart comparing the predicted strain at initial failure, which was determined using both Gauss and nodal point stresses, to the experimental results are presented in Figure 17. As can be seen for this figure, both numerical results predict the observed trend that as the ply group thickness increases, the strain to initial failure decreases. The nodal stress results compare reasonably well with the experimental results but are consistently lower for all the laminates studied while the Gauss point results are higher for all types of specimens. The lower predicted values can be explained by the fact that the failure model predicts the first interface failure which could not be accurately determined during testing and thus the experimental results would be expected to be higher. To experimentally determine the load at first interface failure, nondestructive in-situ inspection techniques such as acoustic emission, penetrant enhanced X-ray or ultrasonic techniques would have to be used.

Table 3 compares the experimentally determined strain at initiation to the predict strain for the -45°/0°, +45°/0° interfaces and the midplane of the 0° ply. The critical location and angle is the same for all the models, that is the -45°/0° interface at ±15°, with the +45°/0° interface being the second most critical location. It should be pointed out that the strain required to cause a delamination to form at the midplane of the 0° ply is quite low for the type C specimen as compared to the other specimens. This

would explain the midplane delamination that was observed in the type C specimens during testing, see Figure 10.

4.3 Mechanism of Damage Progression

The numerical results and the failure characteristics at the hole surface support a proposed mechanism for damage initiation and progression. The mechanism for initiation based on the finite element results is that damage begins as a localized delamination in the -45°/0° interface at the hole edge at an angle that is slightly off axis, ± 15°. Very shortly after this initiation, localized delamination occurs at the +45°/0° interface also at an angle slightly off axis. This is verified by the fact that the finite element results showed that the +45°/0° interface was the second most critical area and the experimental results showed both interfaces contained delaminations. A photoelastic image of a specimen which was not taken to ultimate failure revealed that the resulting delamination after the first acoustic emission which signified initiation, was slightly off axis, see Figure 8. Depending on the thickness of the ply group, the growth of these delaminations would lead to the formation of sub-laminates which promote localized buckling of the 0° plies at the hole surface approximately at right angles to the loading direction. If the ply is too thick, localized buckling could not occur. However due to the large interlaminar normal stress that would be present in the 0° ply, delaminations could form within the 0° ply group creating thinner sub-laminates thus facilitating local buckling. This view on damage initiation is slightly different from the view of Waas et al.[7] that the failure is initiated as a localized instability in the 0° plies at the hole surface.

The initial delamination growth is arrested quickly due to the constraint of the adjacent plies and no further growth is detected. Under increasing load, further buckling of the 0° plies increases the strain at the edge of the interface delamination which leads to the resumption of the delamination growth when a critical strain level is exceeded. This resumption in growth and the subsequent immediate arrest is usually accompanied by distinct audible acoustic emissions. This delamination and fibre buckling process is responsible for damage growth. Once the delaminated regions reach a critical size, damage spreads to both side edges of the specimen causing the final collapse. In the case of laminates with thick ply groupings, the delaminations may spread to a much larger area if midplane delaminations occur within the 0° plies, as was the case for the type C specimens.

Based on the experimental results, very little damage progression took place in the specimens tested. Typically, damage initiated between 90% to 95% of the ultimate load. Therefore to apply a damage progression model to this material system would not be practical since the time required to grow the damage from initiation to failure is very short. This is also true for other material systems that have been investigated[4,7,9].

Detailed scanning electron microscopy is planned in the near future to determine the failure mode for each specimen examined including those tests that were not taken to ultimate failure.

5. CONCLUSIONS AND RECOMMENDATIONS

The damage initiation of compressively loaded quasi-isotropic laminates was predicted using a failure criterion based on the interlaminar normal and shear stresses. This criterion determined the strain at damage initiation which agreed reasonably well with the experimental results. The observed trend that as the ply group thickness increased, the strain to initial failure decreased, was also predicted. This was not the case for the tensor polynomial criterion which could not distinguish between the different ply group thicknesses.

The failure criterion showed that the -45°/0° ply interface was the most critical. This aspect was not verified by the experimental results because the first interface failure could not be accurately determined during testing. To more accurately determine the strain at initiation, it is proposed to carry out further tests using nondestructive in-situ inspection techniques such as acoustic emissions combined with ultrasonic methods or enhanced X-ray techniques.

Based on the numerical results and the failure characteristics, a mechanism for damage initiation and progression was proposed. This mechanism involved the delamination of the -45°/0° and +45°/0° ply interfaces and the subsequent localized buckling of the 0° plies at the hole surface which occurs at approximately 90% of the ultimate load. The growth process entails a delamination and fibre buckling process which develops in stages and is accompanied by a distinct audible acoustic emission. Eventually the delaminated regions reach a critical size after which ultimate failure occurs.

Considering that damage initiation occurs at over 90% of the ultimate load, a damage progression model is not practical for the material systems presently being used in aircraft. However, as the material systems are improved, it may be possible to apply such a model.

6. ACKNOWLEDGEMENTS

This work was carried out under IAR Structures and Materials Laboratory Project JGM-00: Development of Composite Test and NDI Procedures. The financial support of DND through FE C0220788NRC21 is gratefully acknowledged. Also, the contributions of Mr. T.J. Benak, Dr. G.F. Marsters, Dr. W. Wallace, Mr. D. Simpson, Mr. R.F. Scott and Mr. W.H. Ubbink are gratefully acknowledged.

7. REFERENCES

1. Whitney, J. M. and Nuismer, R. J., "Stress Fracture Criteria for Laminated Composites Containing Stress Concentrations," Journal of Composite Materials, Vol. 8, July 1974, pp. 253-265.

2. Nuismer, R. J. and Labor, J. D., "Applications of the Average Stress Failure Criterion: Part II - Compression," Journal of Composite Materials, Vol. 13, January 1979, pp. 49-60.

3. Rhodes, M. D., Martin M. M., Jr. and McGowan, P. E., "Effect of Orthotropic Properties and Panel

Width on the Compression Strength of Graphite-Epoxy Laminates with Holes," AIAA Paper No. 82-0749, 1982.

4. Starnes, J. H., Jr., Rhodes, M. D. and Williams, J. G., "Effect of Impact Damage and Holes on the Compressive Strength of a Graphite/Epoxy Laminate," Nondestructive Evaluation and Flaw Criticality for Composite Materials, ASTM STP 696, American Society for Testing and Materials, 1979, pp. 145-171.

5. Garbo, S. P., "Compression Strength of Laminates with Unloaded Fastener Holes," AIAA Paper No. 80-0709, 1980.

6. Tan, S. C., "Tensile and Compressive Notched Strength of PEEK Matrix Composite Laminates," Journal of Reinforced Plastics and Composites, Vol. 6, July 1987, PP. 253-267.

7. Waas, A. M., Babcock, C. D., Jr. and Knauss, W. G., "Damage Progression in Compressively Loaded Laminates Containing a Circular Cutout," AIAA Journal, Vol. 29, No. 3, March 1991, pp. 436-443.

8. Chang, F. K. and Lessard, L. B., "Damage Tolerance of Laminated Composites Containing an Open Hole and Subjected to Compressive Loadings: Part I - Analysis," Journal of Composite Materials, Vol. 25, January 1991, pp. 2-43.

9. Lessard, L. B. and Chang, F. K., "Damage Tolerance of Laminated Composites Containing an Open Hole and Subjected to Compressive Loadings: Part II - Experiment," Journal of Composite Materials, Vol. 25, January 1991, pp. 44-64.

10. Barboni, R., Gaudenzi, P. and Carlini, S., "A Three-Dimensional Analysis of Edge Effects in Composite Laminates with Circular Holes," Composite Structures, Vol. 15, 1990, pp. 115-136.

11. Burns, S. W., Herakovich, C. T. and Williams, J. G., "Compressive Failure of Notched Angle-Ply Composite Laminates: Three-Dimensional Finite Element Analysis and Experiment," CCMS-85-11, VPI-E-85-22, Virginia Polytechnic Institute and State University, Blacksburg, Virginia, November 1985.

12. Poon, C., Lee, S., Gould, R. W. and Scott, R. F., "Compression Testing of Advanced Composite Laminates," Proceedings of the 34th International SAMPE Symposium, Reno, Nevada, May 8-11, 1989.

13. Poon, C., Bellinger, N. and Gould, R. W., "Compressive Response of Notched Composite Laminates," Proceedings of the First Canadian International Composites Conference CANCOM'91, Montreal, Quebec, September 4-6, 1991.

14. Gaudert, P. C., Scott, R. F. and Lee, S., "Development of a Burn-Off Test for the Fibre Content of Carbon Fibre Reinforced Epoxy Composites," LTR-ST-1631, Institute for Aerospace Research, National Research Council Canada, Ottawa, June 1987.

15. Tsai, S.W. and Wu, E.M., "A General Theory of Strength for Anisotropic Materials," Journal of Composite Materials, 1971, 5, p. 58

Table 1: Properties of IM6/5245C Graphite-Epoxy

Elastic Properties		
$E_1 = 166$ GPa	$E_2 = E_3 = 8.3$ GPa	$G_{12} = G_{13} = G_{23} = 5.4$ GPa
	$\nu_{12} = \nu_{13} = \nu_{23} = 0.31$	
Strength Properties		
$X_T = 2620$ MPa	$Y_T = Z_T = 60$ MPa	$S_{12} = S_{13} = S_{23} = 117.9$ MPa
$X_C = 1278$ MPa	$Y_C = Z_C = 220$ MPa	

Table 2: Summary of Experimental Results

Stacking Sequence	Specimen Number	Failure Load, kN	σ_N, MPa	Average Strain at Failure	Initial Failure Strain
Type A	579-1	-209	-241	-4355	-3964
	579-2	-204	-235	-4267	-3989
	579-3	-208	-238	-4381	-----
	579-4*	-187	-215	-----	-4022
	Average	-207	-238	-4334	3985 (92%)*
Type B	577-2	-175	-202	-3492	-3373
	577-3*	-159	-183	-----	-3187
	577-4*	-174	-202	-3675	-3647
	578-1	-165	-193	-3467	-----
	578-2	-172	-198	-3508	-----
	578-3	-167	-193	-3463	-2950
	578-4	-167	-193	-3440	-----
	Average	-170	-197	-3508	3289 (94%)
Type C	575-2	-152	-174	-3091	-2919
	575-3	-151	-173	-3116	-3087
	575-4	-155	-179	-3294	-3291
	576-2	-166	-188	-3302	-2907
	576-3	-150	-169	-3012	-2883
	576-4*	-145	-164	-----	-3012
	Average	-155	-177	-3163	3017 (95%)

*Test was stopped prior to ultimate failure

Table 3: Summary of analytical Results

Stacking Sequence	Experimental	Analytical		
		-45°/0°	+45°/0°	Midplane of 0° ply
Type A	-3985	-3650	-4700	-9800
Type B	-3289	-2640	-2833	-5041
Type C	-3017	-2340	-2467	-3950

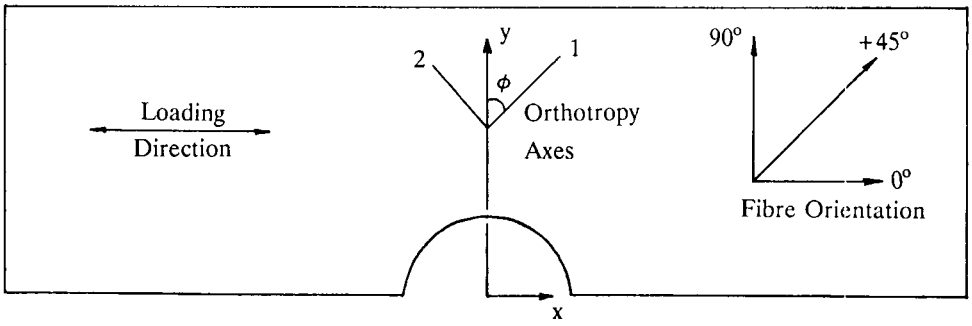

Figure 1: Fibre orientation and laminae orthotropy axes

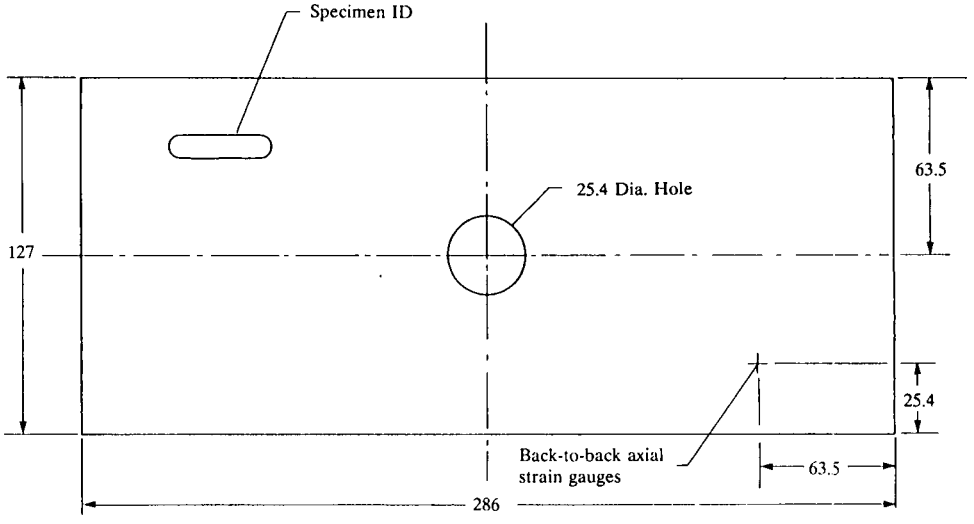

Figure 2: Configuration of open hole compression specimen (dimensions are in mm.).

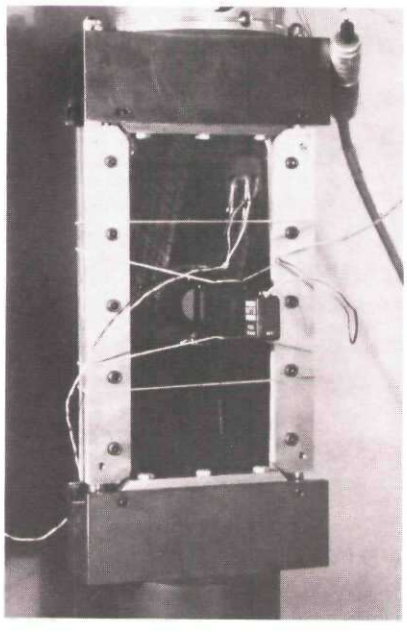

Figure 3: Open hole compression test setup.

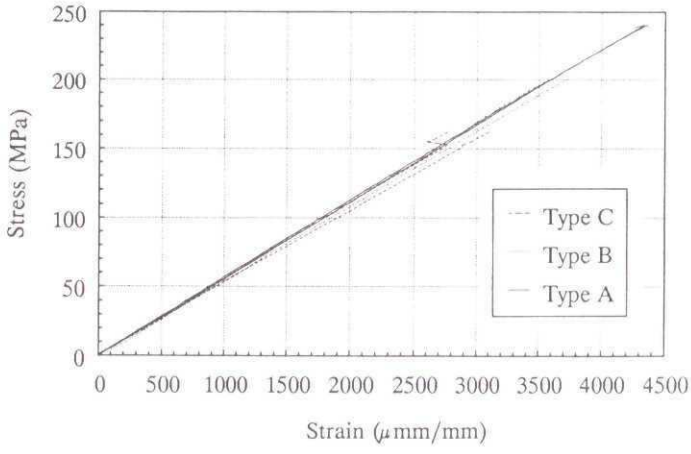

Figure 4: Typical stress vs. strain curves for type A, B and C specimens.

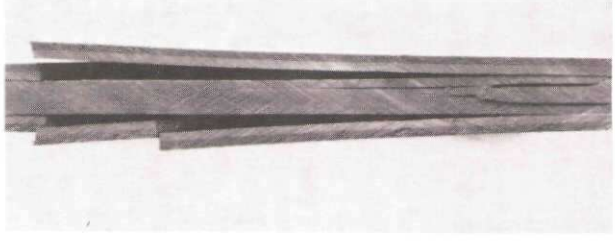

Figure 5: Photomicrograph of type C specimen showing edge delamination.

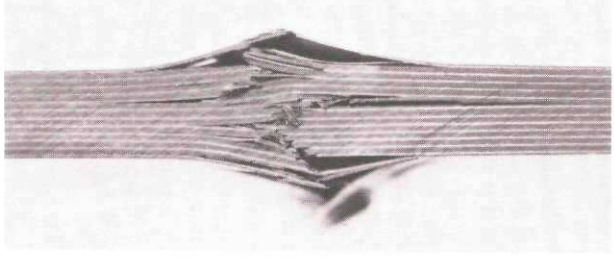

a) Type A

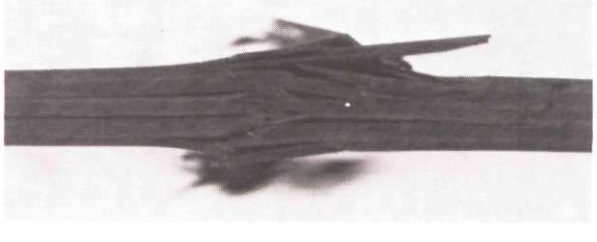

b) Type B

Figure 6: Photomicrograph of type A and B specimens showing localized edge delaminations.

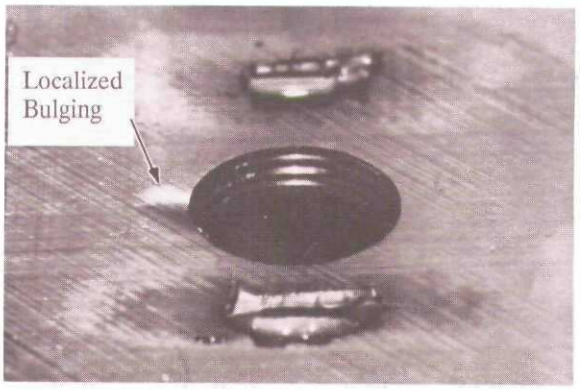

Figure 7: D-sight image of localized bulging of plate surface at hole edge of type B specimen.

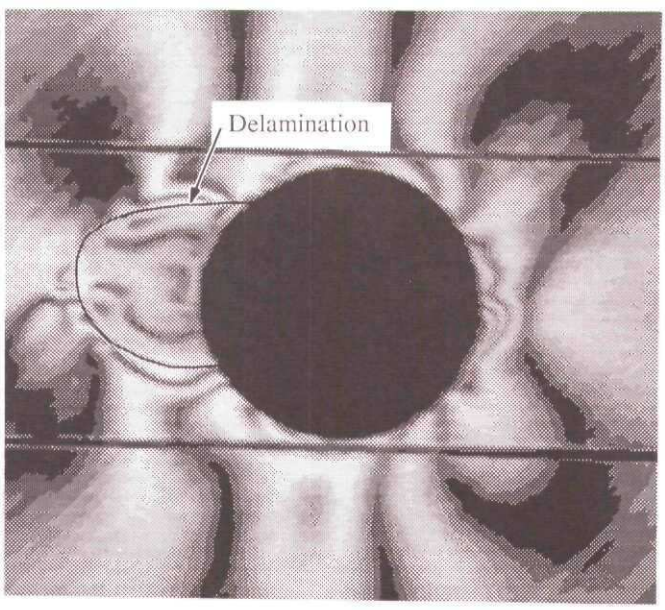

Figure 8: Photoelastic image of initial damage.

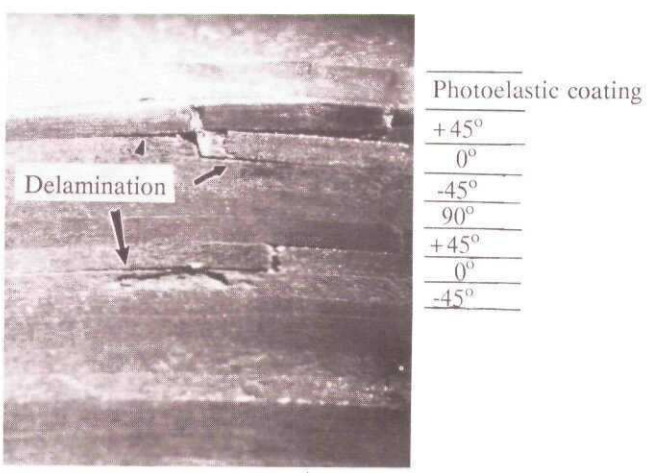

Figure 9: Photomicrograph of hole surface of type B specimen showing initial damage.

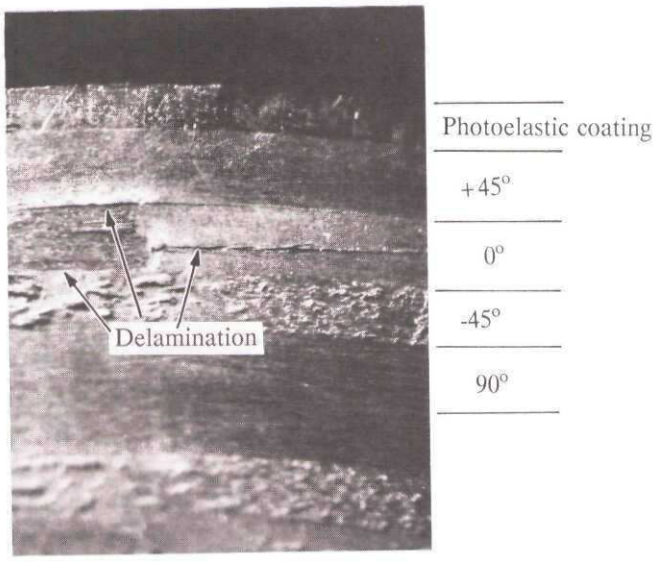

Figure 10: Photomicrograph of hole surface of type C specimen showing initial damage. Note the occurrence of the delamination within the 0° ply group.

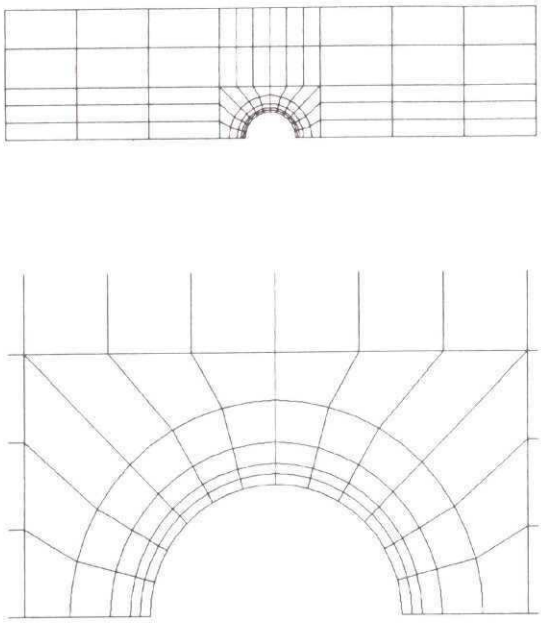

a) Element distribution through-the-thickness for type B and C models

b) Element distribution through-the-thickness for type A model

Figure 11: Finite element models

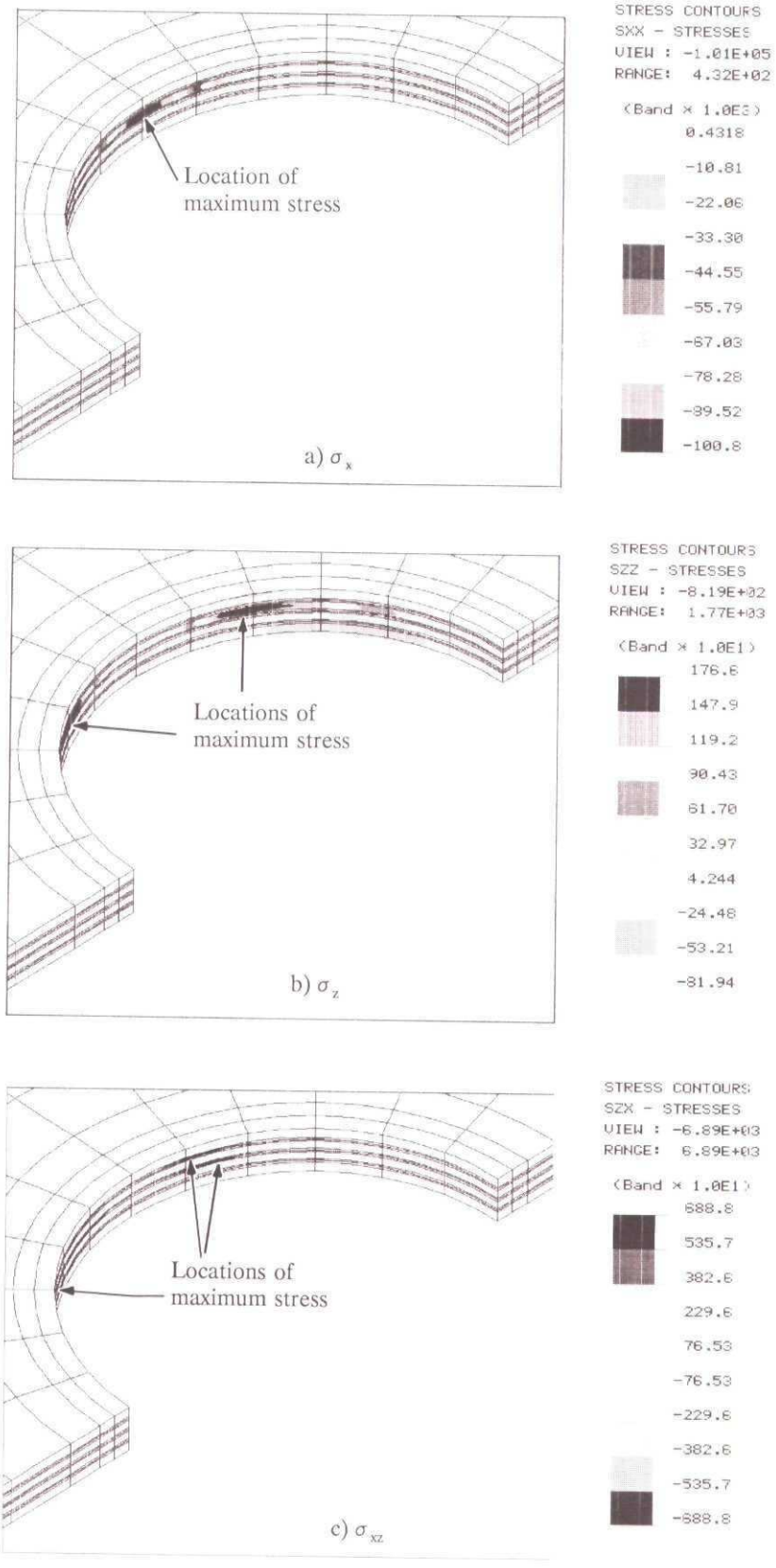

Figure 12: Finite element stress plots of the type C model.

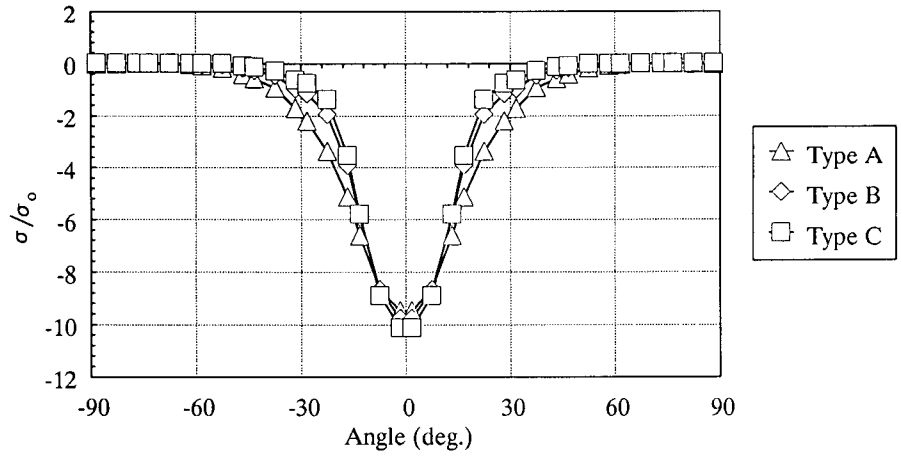

a) σ_1

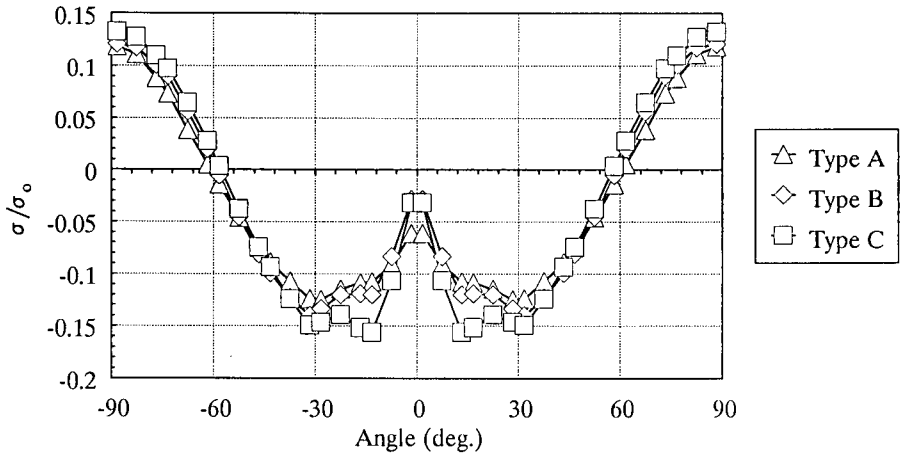

b) σ_2

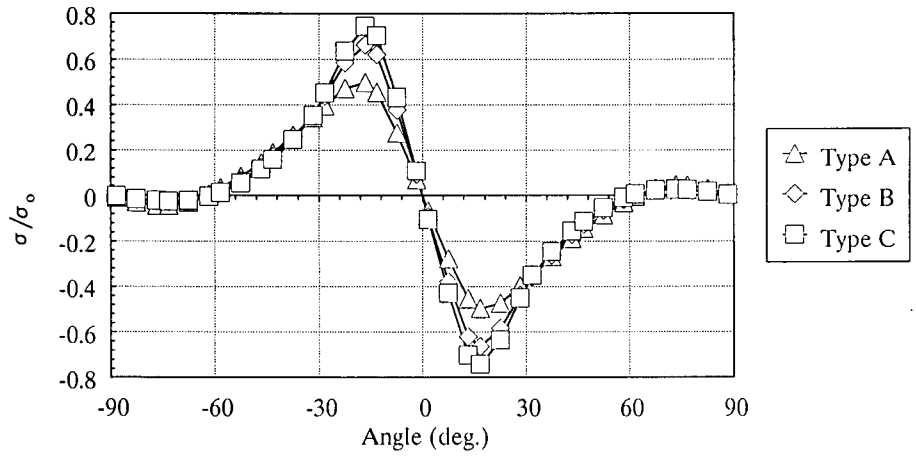

c) σ_{12}

Figure 13: In-plane stress distributions taken at the midplane of the 0° ply.

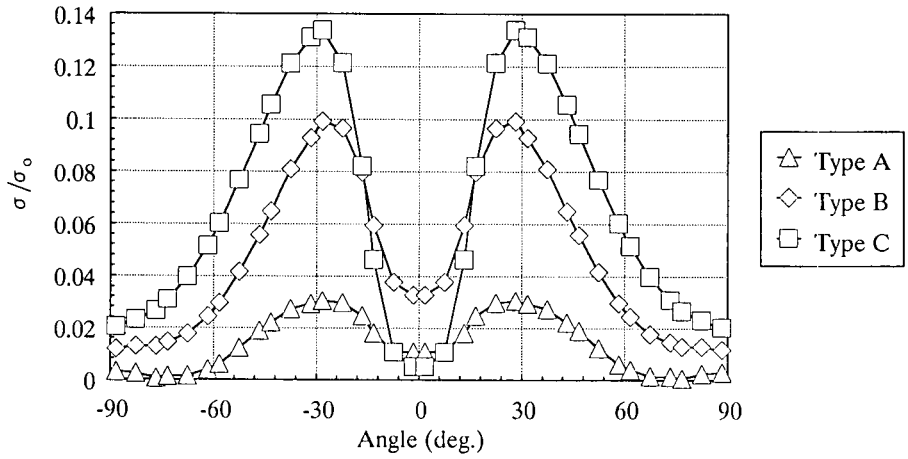

a) Midplane of 0° ply

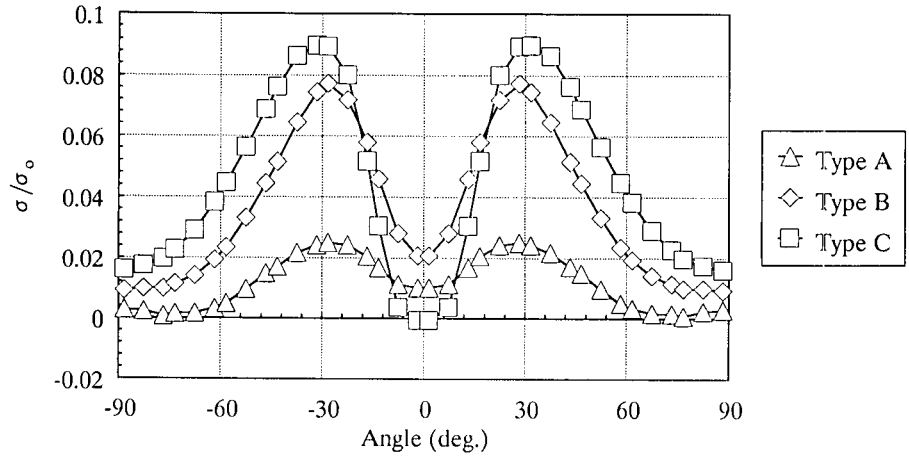

b) +45°/0° interface

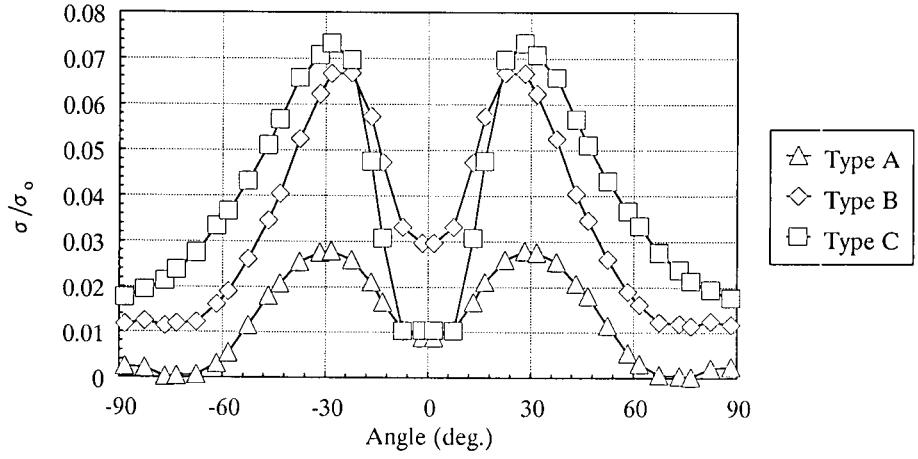

c) -45°/0° interface

Figure 14: Interlaminar normal stress, σ_3, distributions.

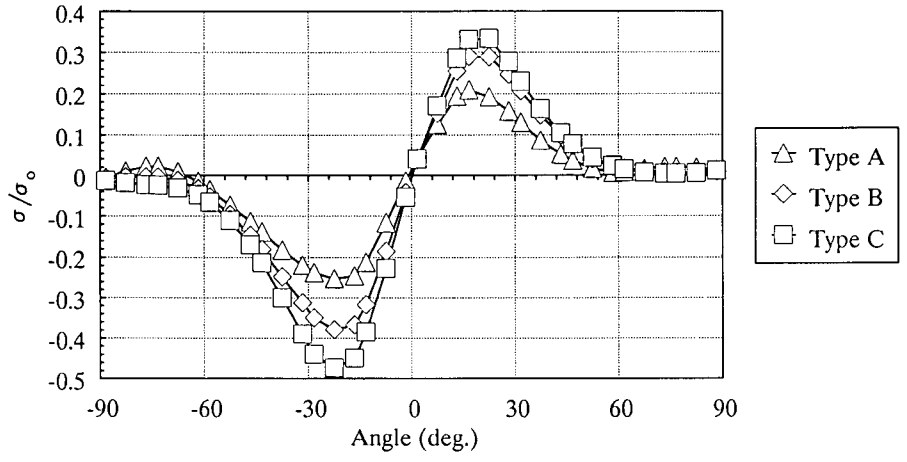

a) -45°/0° interface

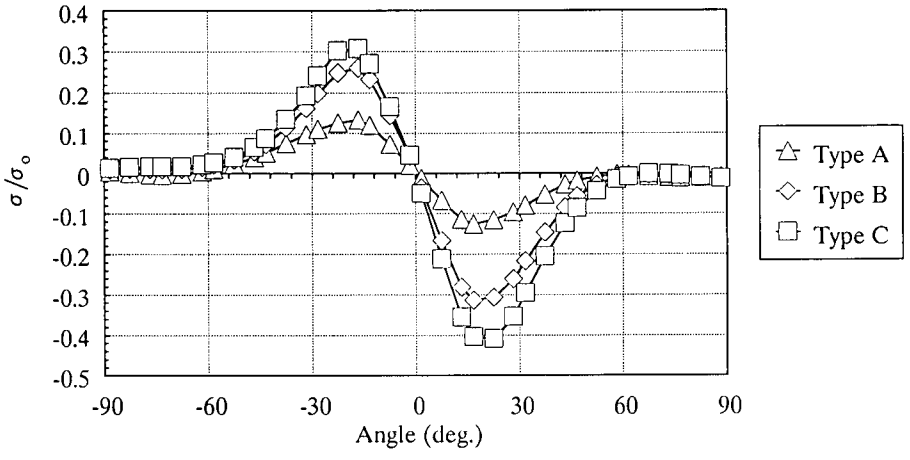

b) +45°/0° interface

Figure 15: Interlaminar shear stress, σ_{13}, distributions.

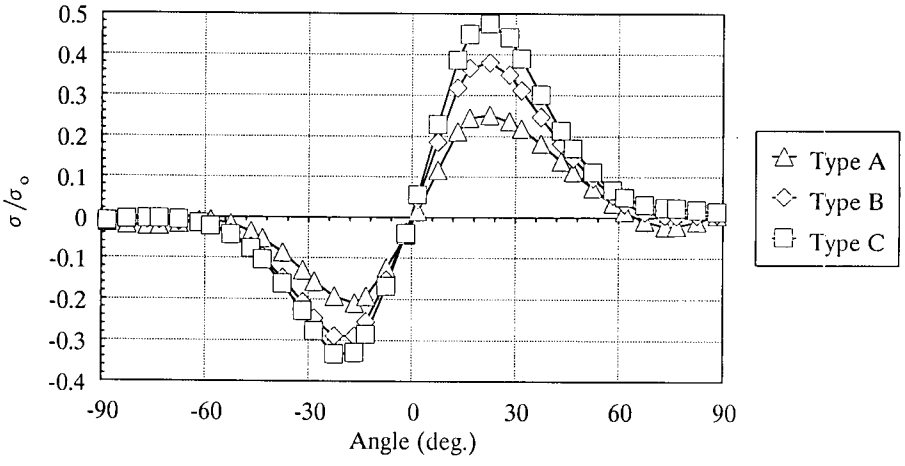

a) -45°/0° interface

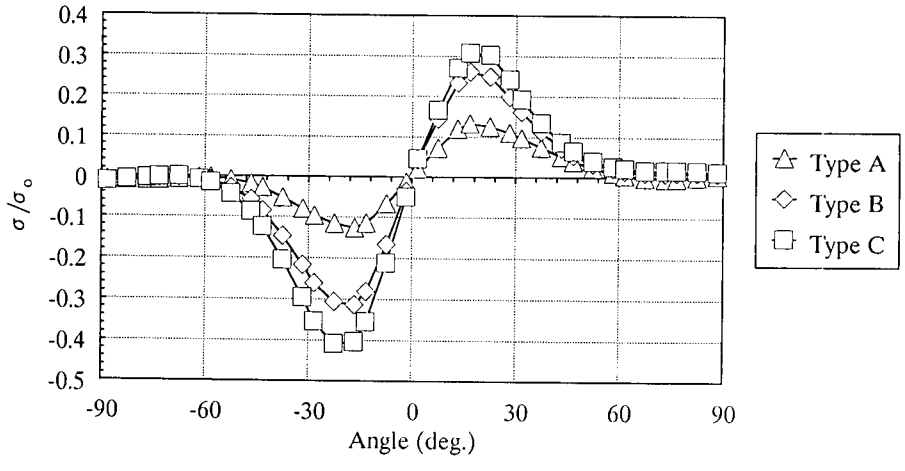

b) +45°/0° interface

Figure 16: Interlaminar shear stress, σ_{23}, distributions.

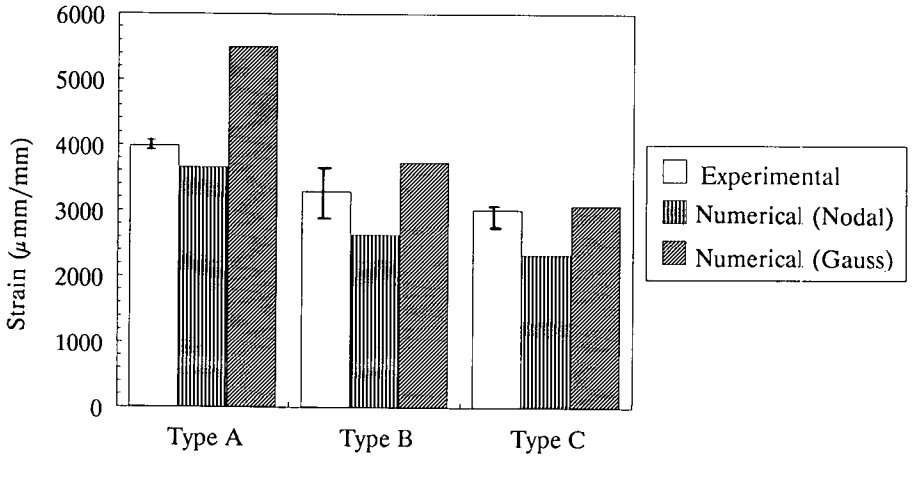

Figure 17: Bar chart comparing the predicted strain at initiation to experimental results.

PROPAGATION D'UN DELAMINAGE DANS UN PANNEAU COMPOSITE SOUMIS A UN CHARGEMENT DE COMPRESSION

par R. GIRARD

Office National d'Etudes et de Recherches
Aérospatiales (ONERA)
92322 CHATILLON CEDEX - France

RESUME

Ce travail concerne la propagation d'un délaminage artificiel entre deux couches d'une plaque composite stratifiée soumise à des forces de compression. La propagation proprement dite est précédée d'un flambage local et d'une rupture des couches le long des deux côtés de la zone rectangulaire du délaminage.

Par suite, l'analyse du problème doit être effectuée dans le cadre des grands déplacements dans les domaines du flambage et post-flambage. De plus, au voisinage du front de délaminage, une loi de comportement non linéaire est introduite de façon à tenir compte de l'endommagement des plis du stratifié. Ce modèle d'endommagement est basé sur des variables internes d'endommagement décrivant la perte de rigidité du matériau due à la micro-fissuration transverse.

Par ailleurs, la prédiction du délaminage nécessite le calcul du taux de restitution d'énergie le long du front de délaminage (calcul explicite des dérivées de l'énergie potentielle par rapport aux coordonnées) et la connaissance expérimentale des taux critiques pour les matériaux composites.

Les outils numériques correspondants ont été implantés dans un code spécifique d'éléments finis non linéaires utilisant des éléments isoparamétriques dégénérés et une formulation lagrangienne totale. Ce code a été appliqué à la simulation numérique de résultats expérimentaux existant (groupe GARTEUR sur l'endommagement des matériaux composites). La prédiction numérique de la propagation du délaminage est relativement satisfaisante.

INTRODUCTION

Les structures stratifiées composites sont susceptibles de présenter des défauts localisés qui peuvent exister dès le stade de la fabrication ou apparaître en service à la suite de chocs divers. Lorsque la structure est soumise à certaines sollicitations, ces défauts provoquent des délaminages internes qui ont tendance à se propager.

Cette propagation s'observe notamment dans le cas de structures travaillant en compression pour des défauts situés au voisinage des faces externes de la structure. La partie du stratifié située au-dessus du défaut est alors sensible au flambage et se déforme par cloquage entraînant la progression de la zone délaminée.

Dans le travail qui est présenté ici, la progression est étudiée sur un panneau composite présentant un délaminage interne introduit artificiellement. On ne cherche pas à caractériser l'apparition des défauts, mais seulement à en prévoir et étudier la progression.

La simulation numérique de cette progression est basée sur un certain nombre d'outils numériques permettant de décrire les phénomènes mis en jeu :

. Analyse non linéaire en post-flambage
Une telle analyse est nécessitée par une progression du délaminage qui est observée après flambage de la zone délaminée.

. Endommagement des matériaux
Les contraintes au raccord de la zone de cloquage avec le reste de la structure sont suffisamment importantes pour provoquer l'apparition de micro-fissures modifiant le comportement des plis du stratifié.

. Taux de restitution d'énergie
Ces quantités, calculées le long du front de délaminage, permettent de prévoir la propagation lorsqu'elles atteignent des valeurs critiques caractéristiques des matériaux utilisés

Ces outils sont à la base du code de calcul DAM-STRAT développé à l'ONERA [1] et appliqué à un problème de propagation de délaminage analysé expérimentalement au D.L.R-Draunschweig [2] et à l'ONERA-IMFL [3]. Les travaux expérimentaux du D.L.R et les méthodes numériques de l'ONERA ont été réalisés dans le cadre d'une concertation européenne GARTEUR, ayant pour thème la mécanique de l'endommagement des matériaux composites [2].

1 - LE PROBLEME ETUDIE

1.1 Panneau et montage expérimental

Le panneau testé est un stratifié constitué de 16 plis d'un matériau composite classique à fibres de carbone et résine époxy (T.300-914). L'épaisseur de chaque pli est de 0.125mm et la séquence d'empilement mesurée par rapport à la direction des efforts longitudinaux de compression, est la suivante :

$[+2°, -2°, +45°, 0°, 0°, -45°, 0°, 90°]_S$

où l'indice s indique que la séquence doit être complétée par symétrie.

Afin de simuler un délaminage initial, cette séquence est modifiée par insertion, au centre du panneau, de 2 pastilles de teflon superposées et situées entre les 2ème et 3ème plis à partir de la face supérieure. Ces pastilles ont un diamètre de 10mm et une épaisseur de 25 μm. Pour les calculs numériques, la surface de délaminage est assimilée à l'interface entre les 2 pastilles et les pastilles ne sont pas modélisées (leur épaisseur est négligeable devant celle des plis).

L'introduction de ce défaut artificiel rompt la symétrie dans l'épaisseur du panneau. Soumis à des efforts de compression, celui-ci se déforme donc par flambage latéral. De façon à éviter ce flambage global, il a été conçu un dispositif expérimental constitué de 2 plaques rigides entre lesquelles le panneau peut coulisser librement (voir figure 1).

De plus, au centre de la plaque supérieure est aménagée une fenêtre rectangulaire autorisant les déplacements transversaux du panneau. Les dimensions de cette fenêtre sont choisies suffisamment grandes pour permettre le flambage local de la partie de panneau située au-dessus de la zone de délaminage.

1.2 Résultats expérimentaux
Les mesures effectuées reposent, d'une part sur des techniques de Moiré permettant la visualisation de la taille du délaminage (voir figure 2) et, d'autre part, sur des mesures de flèches à l'aide de capteurs à mutuelle inductance [3]. Ces mesures sont effectuées pour différents niveaux de charge imposés graduellement (essais quasi-statiques).

Dans une première phase, disons jusqu'à 400N/mm^2, le défaut reste circulaire et la partie de panneau située au-dessus du défaut se déforme par cloquage Aux environs de 400N/mm^2, ce cloquage donne naissance à deux macros-fissures longitudinales situées de part et d'autre de la zone délaminée et nettement visibles à 450N/mm^2 (voir figure 2). La zone de délaminage devient alors quasiment rectangulaire puis progresse régulièrement en étant guidée par les 2 macros-fissures.

Les niveaux de charge, donnés ci-dessus, correspondent aux résultats du D.L.R, ceux de l'IMFL étant généralement inférieurs (la différence pouvant atteindre 20% environ). Les résultats expérimentaux ne sont donc connus qu'avec une certaine précision due au fait que l'initialisation des phénomènes observés s'effectue à l'échelle microscopique et n'est pas directement observable. Néanmoins, les résultats sont suffisamment concordants pour envisager un calcul prévisionnel de la progression du délaminage.

2 - SIMULATION NUMERIQUE

2.1 Les outils de calcul
2.1.1 Analyse en post-flambement
Le code de calcul DAM-STRAT [1], lui-même issu du module de calcul ISONL réalisé à l'ONERA [4], est basé sur une formulation lagrangienne totale du problème des grands déplacements et une discrétisation de type éléments finis. Les équations d'équilibre sont résolues par un processus incrémental portant , soit sur un facteur multiplicatif du chargement, soit sur un paramètre de type abscisse curviligne relativement à la courbe charge-déplacements.

A l'intérieur de chaque incrément les équations non linéaires sont résolues par une méthode itérative de type Newton avec possibilité de garder constante la matrice de rigidité au cours des itérations. Les singularités inhérentes aux phénomènes de flambement sont traitées, soit en utilisant la paramétrisation en abscisse curviligne (franchissement des points de limites), soit en introduisant des imperfections de chargement adéquates (franchissement des points de bifurcation).

Les éléments finis utilisés sont du type tridimensionnel dégénéré avec interpolation linéaire dans l'épaisseur. Leur formulation est de type isoparamétrique avec interpolations surfaciques linéaires, quadratiques ou cubiques. Mécaniquement les éléments sont multicouches, chaque couche pouvant être constituée de matériaux isotropes, isotropes transverses ou orthotropes. Les lois de comportement sont formulées de façon tridimensionnelle, bidimensionnelle (plaques et coques) ou unidimensionnelles (poutres droites ou curvilignes). Dans ces deux derniers cas le recours aux techniques d'intégration réduite et de pénalisation des déformations normales transverses est nécessaire pour éviter les phénomènes de blocage en cisaillement transversal des structures minces.

2.1.2 Prise en compte de l'endommagement
L'endommagement introduit dans le calcul DAM-STRAT [5], a pour but de rendre compte de la microfissuration transverse d'un matériau composite à fibres unidirectionnelles, c'est-à-dire l'apparition au sein de la résine de micros-fissures dirigées selon la direction des fibres.

Pour un matériau en état de contraintes planes, cet endommagement affecte essentiellement le module de cisaillement G_{12} et le module de Young transerval E_2 (les fibres sont orientées selon la direction 1) et peut être décrit par 2 variables internes d et d' telles que :

$$G_{12} = G^0_{12}\,(1-d)$$

$$E_2 = \begin{cases} E^0_2\,(1-d') & \text{si} \quad \varepsilon_{22} > 0 \\ E^0_2 & \text{si} \quad \varepsilon_{22} \leq 0 \end{cases}$$

où G^0_{12} et E^0_2 sont les valeurs correspondant au matériau non endommagé. En cas de compression transversale, le module E_2 n'est pas affecté car une telle sollicitation a pour effet de refermer les micros-fissures.

Aux 2 variables d et d' sont associées, via l'expression de l'énergie de déformation $2E = \mathrm{Tr}[\sigma.\varepsilon]$ deux variables Y_d et $Y_{d'}$ définies par

$$Y_d = -\frac{1}{2}\left.\frac{\partial E}{\partial d}\right|_{\varepsilon} = 4\,G^0_{12}\,\varepsilon^2_{12}$$

$$Y_{d'} = -\frac{1}{2}\left.\frac{\partial E}{\partial d'}\right|_{\varepsilon} = E^0_2\,\langle \varepsilon_{22}\rangle_+^2$$

où $\langle \varepsilon_{22}\rangle_+$ désigne la partie positive de ε_{22} (ε_{22} si $\varepsilon_{22}>0$ et 0 sinon)

Sur la base de résultats expérimentaux, les lois physiques d'endommagement reliant d et d' à Y_d et $Y_{d'}$ sont choisies comme fonctions linéaires d'une seule et même variable Y telle que :

$$d = \frac{\langle Y - Y_0\rangle_+}{Y_c} \qquad d' = \begin{cases} \dfrac{\langle Y - Y_0\rangle_+}{Y'_c} & \text{si} \quad \varepsilon_{22} > 0 \\ 0 & \text{si} \quad \varepsilon_{22} \leq 0 \end{cases}$$

$$Y = \sup_{\tau \leq t} Y|_\tau \qquad \text{avec} \qquad Y = (2Y_d + 2\beta\, Y_{d'})^{1/2}$$

Les quantités Y_0, Y_c, Y'_c et β sont des coefficients caractéristiques du matériau dont les valeurs sont à déterminer expérimentalement.

Le paramètre τ décrit l'histoire du matériau jusqu'à l'état actuel $\tau = t$. La définition de Y traduit l'irréversibilité de l'endommagement, alors que la valeur $Y = Y_0$ correspond à un seuil en-dessous duquel il n'y a pas d'endommagement.

La mise en oeuvre pratique d'un tel modèle d'endommagement ne pose pas de difficultés majeures, si ce n'est la valeur de χ qui nécessite en toute rigueur une sauvegarde aux fins de comparaison à l'incrément suivant.

Toutefois, lorsque Y est une fonction non décroissante au cours de l'histoire du matériau et c'est le cas dans le problème qui nous préoccupe, la valeur de χ n'est autre que la valeur instantannée de Y .

Le modèle d'endommagement ainsi défini présente la particularité de pouvoir conduire à une instabilité lorsque $\varepsilon_{22} > 0$. Plus précisemment, la loi de comportement endommageable écrite sous forme incrémentale devient singulière lorsque le déterminant de la matrice associée devient nul, soit :

$$\frac{4\,G_{12}^{0}\,\varepsilon_{12}^{2}}{\chi\,(Y_0+Y_c-\chi)} + \frac{\beta\,E_2^{0}\,\varepsilon_{22}^{2}}{\chi\,(Y_0+Y_c'-\chi)} = 1 \quad , \quad \varepsilon_{22} > 0$$

Physiquement cette instabilité est interprétée comme une rupture en traction de la résine du composite, les autres modes principaux de rupture (rupture en compression de la résine et rupture des fibres) étant simplement pris en compte dans DAM-STRAT à l'aide de limites à ruptures ($-\bar{\varepsilon}_{22}$ et $\bar{\varepsilon}_{11}$)

2.1.3 Taux de restitution d'énergie

Soit Π l'énergie potentielle de la structure discrétisée, considérée en tant que fonction des déplacements nodaux u_i^m et des coordonnées nodales a_i^m de chacun des m points du maillage (i = 1, 2, 3). A une perturbation infinitésimale ∂a_i^m de la $i^{ème}$ coordonnée du noeud m est associée une variation d'énergie $\partial\Pi$ telle que :

$$\partial\Pi = \frac{\partial\Pi}{\partial u_i^m}\,\partial u_i^m + \frac{\partial\Pi}{\partial a_i^m}\,\partial a_i^m \quad , \quad \frac{\partial\Pi}{\partial u_i^m} = 0$$

la seconde égalité étant vérifiée, en l'abscence d'efforts exercés au noeud m, car les déplacements réels minimisent l'énergie potentielle.

Cet accroissement d'énergie $\partial\Pi$ représente l'énergie qu'il faut fournir à la structure pour perturber la $i^{ème}$ coordonnée du noeud m de la quantité ∂a_i^m . Or le taux de restitution G est défini, pour la progression d'un délaminage, comme l'énergie dissipée lorsque le délaminage progresse d'une longueur unité. Pour une longueur $\partial\ell_0$ de progression d'un délaminage résultant de la seule perturbation de la $i^{ème}$ coordonnée du noeud, le taux d'énergie sera donc :

$$G = -\frac{\partial\Pi}{\partial\ell_0} = -\frac{\partial\Pi}{\partial a_i^m}\,\frac{\partial a_i^m}{\partial\ell_0}$$

De par la formulation isoparamétrique des éléments finis utilisés dans DAM-STRAT, il est possible d'expliciter les dérivées $\partial\Pi/\partial a_i^m$ en fonction des coordonnées a_j^m et des gradients des déplacements u_j^m . Et par suite il en est de même de G (voir [1] pour les détails de ce calcul).

Dans le calcul de G il n'est tenu compte que de la seule perturbation de la coordonnée a_i^m . Pour calculer le taux de restitution $\tilde{G}$ relatif à la propagation de l'ensemble du front, on utilise une formule d'interpolation

$$\tilde{G}(A) = \sum_{m=1}^{N} L_m(A)\,\tilde{G}_m$$

où A est l'abscisse courviligne le long du front, L_m la fonction d'interpolation linéaire par morceaux égale à 1 au noeud m du front et nulle aux autres noeuds, $\tilde{G}_m$ la valeur de $\tilde{G}$ au noeud m ($m = 1, N$; N nombre de noeuds du front).

La progression du front de délaminage résultant de la seule perturbation du noeud m est donnée en première approximation par

$$\delta\ell(A) = L_m(A)\,\delta\ell_0^m$$

Cette progression fait intervenir tous les points matériels du front situés entre les noeuds $m-1$ et $m+1$ et par suite un taux de restitution d'énergie tel que :

$$\int_{m-1}^{m+1} \tilde{G}(A)\,\delta\ell(A)\,dA = G_m\,\delta\ell_0^m$$

où G_m est la valeur pour la perturbation du noeud m , du taux G défini précédemment.

Cette relation étant vérifiée pour chacun des N noeuds du front, on obtient ainsi un système linéaire de N équations pour déterminer les N valeurs $\tilde{G}_m$ en fonction des G_m . Dans le cas où les noeuds du front sont équi-distants, le système obtenu est tridiagonal de sorte que son inversion est quasi explicite.

2.2 Comparaison avec les essais

2.2.1 Calculs effectués

L'application du code de calcul DAM-STRAT à l'étude d'un problème concret repose sur un processus incrémental des sollicitations appliquées, chaque incrément faisant l'objet d'une analyse non linéaire. Ce processus est interrompu dès que des critères appropriés signalent l'apparition de l'un des phénomènes suivants :

- instabilité de flambement
- rupture d'un pli
- progression du délaminage

Selon le phénomène rencontré, une nouvelle stratégie de calcul ou une nouvelle modélisation est alors adoptée et un nouveau calcul non linéaire est entrepris.

Dans le problème qui nous intéresse ces différentes étapes sont les suivantes :

- montée en charge jusqu'à l'instabilité associée au flambage local de la partie de panneau située au-dessus du défaut initial
- passage au chemin bifurqué correspondant aux équilibres post-flambage et montée en charge jusqu'à la rupture associée à l'initialisation des macros-fissures (voir 1ère partie)
- simulation de la progression du délaminage par analyse du panneau pour différentes tailles de la zone délaminée ; chacune de ces analyses est poursuivie tant que le critère de propagation du délaminage n'est pas vérifié.

Le calcul du panneau pour différentes tailles du délaminage nécessite autant de modélisations distinctes. Pour simplifier ces dernières, le défaut circulaire inital a été remplacé par une zone de délaminage rectangulaire de largeur constante égale au diamètre du défaut initial. Selon les résultats expérimentaux, cette approximation est parfaitement justifiée après apparition des 2

macro-fissures longitudinales tangentes au défaut initial. Par contre, dans les phases de flambement et de formation des macro-fissures cette approximation est plus discutable. Néanmoins, le défaut étant très localisé et de taille relativement restreinte, cette modification ne devrait pas remettre en cause, au moins qualitativement, le calcul prévisionnel.

Compte tenu des symétries du problème, la modélisation ne porte que sur le quart du panneau. Un maillage éléments finis typique est donné à la figure 3. La zone de délaminage est schématisée par 2 couches d'éléments superposés non raccordés le long de leur interface, mais raccordés au reste de la structure le long des côtés AB et AC. Ce maillage comporte environ 1500 degrés de liberté, les éléments utilisés étant du type quadratique à 2x8 noeuds.

Les modules d'élasticité introduits sont ceux du matériau T.300-914 classiquement utilisé dans l'industrie aéronautique. Par contre, les caractéristiques du modèle d'endommagement proviennent du LMT-Cachan, laboratoire au sein duquel a été conçu le modèle utilisé [5]. Les orientations des plis sont celles qui ont été mentionnées dans la 1ère partie, excepté pour les 2 plis externes à $\pm$ 2° qui ont été remplacés par des plis à 0°.

En ce qui concerne les conditions aux limites, outre celles résultant des conditions de symétrie, il faut tenir compte de la présente du guide anti-flambage, ce qui conduit à imposer la nullité des flèches et rotations aux noeuds situés entre les 2 faces de ce guide. Dans le programme DAM-STRAT, la nullité des rotations est réalisée par une technique de pénalisation forçant l'égalité des déplacements inférieur et supérieur des éléments (introduction d'une rigidité fictive suffisamment importante entre degrés de liberté concernés).

2.2.2 Flambage et fissuration

Une première série de calculs concerne la mise en compression du panneau jusqu'à l'apparition d'une instabilité de flambement (voir figure 4, point F) Dans le code DAM-STRAT, cette instabilité est caractérisée par l'apparition d'un pivot négatif sur la diagonale de la factorisation de la matrice de rigidité tangente (de définie positive l'énergie potentielle devient négative).

Une procédure de dichotomie des incréments du niveau de charge appliqué permet alors d'encadrer la position critique d'instabilité avec une précision requise. Pour le panneau étudié, la charge de flambement ainsi calculée est voisine de 220N/mm^2. Elle est relativement plus élevée que la valeur expérimentale qui a pu être déduite des essais de l'IMFL et qui se situerait entre 180 et 200N/mm^2.

Outre des difficultés expérimentales d'appréciation du niveau de cloquage (en pratique les courbes charge-déplacements présentent seulement un coude plus ou moins prononcé au voisinage de la charge critique), il faut rappeler que la modélisation numérique est, elle aussi, susceptible d'amélioration tant au point de vue de la finesse du maillage que de l'approximation du défaut circulaire.

A défaut d'études supplémentaires sur la convergence du modèle éléments finis ou sur l'influence de la forme et de la taille du défaut initial, on peut simplement affirmer que le phénomène de flambement est effectivement prévue par le calcul, mais qu'une modélisation vraisemblablement non suffisamment affinée, conduit à une surestimation de la charge critique correspondante.

Quoiqu'il en soit, les calculs ont été poursuivis en post-flambement (branche F-R des courbes de la figure 4). Dans le code DAM-STRAT, le passage au chemin bifurqué est réalisé en appliquant temporairement une légère imperfection de chargement destinée à faire apparaître le cloquage de la zone susceptible de flamber. Dans le cas présent, l'imperfection introduite consiste en des efforts normaux de faible intensité appliqués sur la face externe de la partie du panneau située au-dessus du panneau.

Les positions d'équilibre post-flambement étant ainsi atteintes, la montée en charge est poursuivie. Au fur et à mesure de l'accroissement de la charge, l'endommagement, tel que décrit par les variables d et d' définies en 2.1.2, apparaît et se développe en face inférieure de la partie délaminée le long du côté longitudinal AB de la zone de délaminage. Noter que dans l'état actuel du cloquage, la déformée de la figure 3 se raccorde continûment le long des côtés AB et BC de la zone de délaminage (la figure 3 est relative à une phase ultérieure de progression du délaminage).

Cette extension de l'endommagement est conforme aux observations expérimentales selon lesquelles la macro-fissuration apparaît d'abord au point A puis progresse dans la direction de AB. Numériquement l'endommagement au point A devient suffisamment important pour provoquer, selon le critère défini en 2.1.2, une rupture par instabilité du matériau composite. Cette rupture est atteinte pour une valeur calculée de la contrainte appliquée égale à 260N/mm^2 environ (point R de la figure 4)

Physiquement cette rupture doit être interprétée comme l'initialisation de la macro-fissuration observée expérimentalement entre 330 et 360N/mm^2 pour l'IMFL et aux environs de 400N/mm^2 pour le D.L.R. La différence avec la valeur prévue par le calcul est donc relativement importante. Signalons cependant que les observations expérimentales sont purement macroscopiques et ne peuvent déceler que les premières fissures débouchant sur la face du panneau, alors que la rupture calculée correspond à un phénomène de fissuration interne des plis de la zone délaminée. De plus, l'introduction du défaut rectangulaire dans les calculs conduit à une surestimation des courbures au bord de la zone délaminée et par suite à une surestimation des contraintes et des endommagements provoquant une rupture anticipée.

Ainsi, de même que pour le flambement, le phénomène de macro-fissuration est quantitativement prévu par le calcul, mais les difficultés expérimentales et les approximations de la modélisation numérique font que la comparaison quantitative n'est pas satisfaisante.

2.2.3 Propagation du délaminage

Après apparition de la macro-fissuration, la phase suivante de l'étude est l'analyse de la progression du délaminage. Celle-ci est simulée numériquement en calculant le panneau pour différentes longueurs a de la zone de délaminage, la largeur de cette dernière étant maintenue à sa valeur initiale de 10mm. Le côté longitudinal de cette zone est maintenant désolidarisé du reste du panneau et les déformées obtenues sont du type de celles de la figure 3 (a = 12.5mm).

Sur la figure 4 est reportée l'évolution de la flèche au centre de la zone délaminée en fonction de la contrainte appliquée. Les différentes longueurs de délaminage considérées sont respectivement :

a = 10, 12.5, 18.6, 25mm

Pour chacun des calculs correspondants, le fait essentiel concernant la distribution de l'endommagement est que ce dernier reste localisé à l'extrémité du front de délaminage (point B) quelque soit la contrainte appliquée. En fait, celui-ci croît régulièrement et quasi linéairement avec la charge appliquée jusqu'à ce que le critère d'instabilité soit atteint (approximativement à 300N/mm^2 pour a = 18.6mm). Cette instabilité correspond à une rupture du pli inférieur de la zone délaminée.

Cette rupture très localisée ne signifie nullement la ruine du panneau et le calcul est poursuivi en maintenant constantes les valeurs d'endommagements atteintes (irréversibilité du dommage). En fait, au delà de la macro-fissuration, l'endommagement a peu d'influence sur le comportement global du panneau comme cela a pu être confirmé en effectuant des calculs purement élastiques sans introduction du modèle d'endommagement.

Au fur et à mesure de la poursuite de la montée en charge, le cloquage de la zone délaminée va en s'accentuant jusqu'à ce que la courbure le long du front de délaminage soit suffisamment importante pour provoquer l'ouverture et la progression de ce front. La prévision de cette progression est basée sur des valeurs critiques des taux de restitution d'énergie le long du front, ces valeurs critiques étant associées à différents modes d'ouverture.

Classiquement ces modes sont classés selon le type de sollicitation : sollicitations normales au plan de délaminage (mode I) ou situées dans ce plan et tangentes (mode II) ou normales (mode III) au front. Mais de par leur anisotropie, les matériaux composites se prêtent mal à un tel classement car même pour une sollicitation en mode I pur, le mode d'ouverture n'est pas un mode du type I.

Pour cette raison il a été proposé dans [1] une approche originale basée sur une évaluation directe du travail de fermeture. Liée à la modélisation éléments finis, cette approche utilise les discontinuités de courbure ΔK, de déformations planes $\Delta\varepsilon_0$ et de cisaillement transverse $\Delta\gamma$, au droit du front, pour estimer ce travail selon la formule :

$$G \sim \frac{1}{2}\left(\Delta M.\Delta K + \Delta N.\Delta\varepsilon_0 + \Delta T.\Delta\gamma\right)$$

où M, N, T sont les efforts généralisés associés respectivement à K, ε_0, γ.

Dans le problème qui nous intéresse, le terme de cisaillement transversal est pratiquement négligeable, alors que les contributions des termes de courbure $\Delta M.\Delta K$ et de déformation plane $\Delta N.\Delta\varepsilon_0$ varient respectivement de 80 à 100% et de 0 à 20% pour toutes les longueurs de délaminage considérées. Les termes de courbure sont donc prépondérants et l'on peut considérer que le mode d'ouverture du front de délaminage est essentiellement de type I. L'avantage de la méthode est de pouvoir chiffrer approximativement les différentes contributions énergétiques participant à l'ouverture du front.

A la suite de ces observations il est donc naturel de supposer que la progression du délaminage ne dépend que de la seule valeur critique G_c^I. Pour les matériaux composites cette valeur critique est fonction de l'angle θ constitué par les directions des fibres situées de part et d'autre de l'interface de délaminage et il est donc nécessaire de disposer de résultats expérimentaux décrivant l'évolution de G_c^I en fonction de θ.

De tels essais ont été réalisés à l'ONERA [6] pour une éprouvette à plis alternés $\pm\,\theta/2$, sollicitée en mode I. Les résultats obtenus montrent une réduction d'environ deux tiers pour G_c^I quand on passe de $\theta = 0$ à $\theta = 45°$:

$$G_c^I = G_c^I(0) \times \pi \quad , \quad \pi = 2/3$$

La valeur $G_c^I(0)$ étant relativement bien connue pour le matériau T.300-914, à savoir 0.185N/mm, c'est la valeur de G_c^I, déduite de la formule précédente, qui sera utilisée pour dicter la progression du délaminage (rappelons que dans le problème étudié, la direction des fibres de part et d'autre du délaminage, est respectivement de 45° et 0°).

Les taux de restitution d'énergie, calculés selon la méthode esquissée en 2.1.3, ont une répartition relativement uniforme le long du front de délaminage, excepté au voisinage des extrémités du front où des singularités de contraintes conduisent à des taux sans signification physique réelle. Par suite, la valeur de ce taux au centre du front semble la mieux adaptée pour la prévision de la progression du délaminage. Les évolutions de ces valeurs en fonction de la contrainte appliquée, sont données à la figure 5. Sur cette même figure a également été reportée la valeur critique définie comme il a été dit plus haut.

Pour chacune des longueurs de délaminage considérées, le taux de restitution d'énergie est une fonction croissante de la contrainte appliquée. Tant que ce taux reste inférieur à la valeur critique G_c^I, le délaminage ne progresse pas, mais dès que cette valeur est atteinte (points P des courbes de la figure 4) il y a progression et les positions d'équilibre au delà de cette valeur ne sont plus représentatives du comportement réel du panneau.

Ainsi, à chaque longueur de zone délaminée, est associée la valeur de la contrainte appliquée provoquant la progression du délaminage. L'ensemble de ces valeurs, ainsi que leur homologues expérimentales, sont reportées sur la figure 6. On constate, en première approximation, que la progression s'effectue linéairement en fonction de la charge appliquée et que les valeurs calculées se situent grosso modo entre les diverses valeurs expérimentales.

De façon à mesurer l'influence de la valeur adoptée pour le taux critique de progression, il a également été reporté sur la figure 6 les valeurs de propagation associées à une variation de $\pm$ 10% de la valeur de G_c^I (cette variation correspond à $\pi = 0.6$ et $\pi = 0.73$ sur la figure 5). La majorité des résultats expérimentaux est alors encadrée par les valeurs calculées. Compte tenu de l'imprécision expérimentale sur la valeur de G_c^I, la progression du délaminage semble donc relativement bien prévu par le calcul.

Toutefois, selon les résultats les plus récents de l'IMFL (courbe pointillée de la figure 6 associée à une moyenne de tous les essais réalisés jusqu'à présent), il apparaît que l'écart essais-calculs soit nettement plus important. Remarquer cependant que la vitesse moyenne de propagation a peu évoluée par rapport aux premiers essais et est tout à fait conforme à celle obtenue par le calcul. Cette vitesse moyenne est de l'ordre de 10mm de progression pour 100N/mm^2 de contrainte appliquée.

CONCLUSION

Qualitativement, les résultats obtenus montrent que le code DAM-STRAT est un outil de calcul permettant la prévision des différents phénomènes mis en jeu lors de la compression de panneaux composites présentant un délaminage initial : flambement localisé, macro-fissuration longitudinale et propagation du délaminage.

Outre l'introduction des non-linéarités géométriques nécessaires à l'analyse du flambement et post-flambement, la prise en compte de non-linéarités physiques de type endommagement est essentiel à la prévision de l'initialisation de la macro-fissuration, elle-même responsable de l'avancée initiale du délaminage. Par contre, il est apparu que cet endommagement était sans influence notable dans la phase proprement dite de progression.

Sur la base des résultats expérimentaux, le mécanisme de la propagation a pu être schématisé simplement, la zone de délaminage restant rectangulaire et de largeur constante. L'estimation des diverses contributions énergétiques au travail de fermeture du front a montré que la progression s'effectuait principalement en mode I. Le calcul des taux de restitution d'énergie éffectué dans DAM-STRAT permet alors la prévision de la propagation à l'aide du seul taux critique G_c^* .

Quantitativement, la comparaison essais-calculs révèle des écarts importants notamment en ce qui concerne les valeurs des charges critiques de flambement et d'initialisation de la macro-fissuration. Par contre, compte tenu de la dispersion expérimentale relativement élevée, le calcul de la progression du délaminage s'avère plutôt satisfaisant. En particulier, la vitesse moyenne de propagation semble très correctement évaluée.

La détermination expérimentale précise des valeurs théoriques des charges critiques de flambement et d'initialisation de la macro-fissuration est un problème difficile : le phénomène réel de flambement est toujours entaché d'une certaine imprécision résultant des imperfections inhérentes aux structures testées, alors que la macro-fissuration résulte de phénomènes microscopiques qui ne sauraient être décelés sans le recours à des techniques particulières permettant de décrire l'état de la fissuration au sein des plis du composite.

De plus, aux incertitudes expérimentales, s'ajoutent les imperfections de la modélisation numérique. En particulier, des études numériques portant sur la finesse du maillage et l'influence de la forme initiale du défaut devraient permettre de mieux comprendre les écarts constatés lors des phases initiales de flambement et de macro-fissuration.

REFERENCES

[1] D. Gilletta
Théories non linéaires des stratifiés composites en compression avec délaminage.
R.T n° 19/3542 RY 081 R - ONERA - Janvier 89

[2] M. Gädke
Damage Mechanics of Composites
TP GARTEUR, D.L.R - Braunschweig (en cours de publication)

[3] J.L Petitniot - J. Fabis
Analyse expérimentale du flambement local de panneaux composites sollicités en compression.
R.T n° 89/28 - ONERA-IMFL - Octobre 89

[4] R. Girard
Un module de calcul non linéaire pour les structures composites.
R.T n° 15/3542 RY 062 R - ONERA - Mars 87

[5] D. Gilletta
Composite 2D : modélisation mécanique et identification de la couche élémentaire.
Thèse - Université Paris VI - LMT-ENS Cachan - Octobre 87

[6] J.P Favre - C. Marais - J.C Laizet
Comportement mécanique des composites carbone/résine. Délaminage en mode I et multifissuration transverse des couches.
R.T n° 46/7086 M - ONERA - Janvier 88.

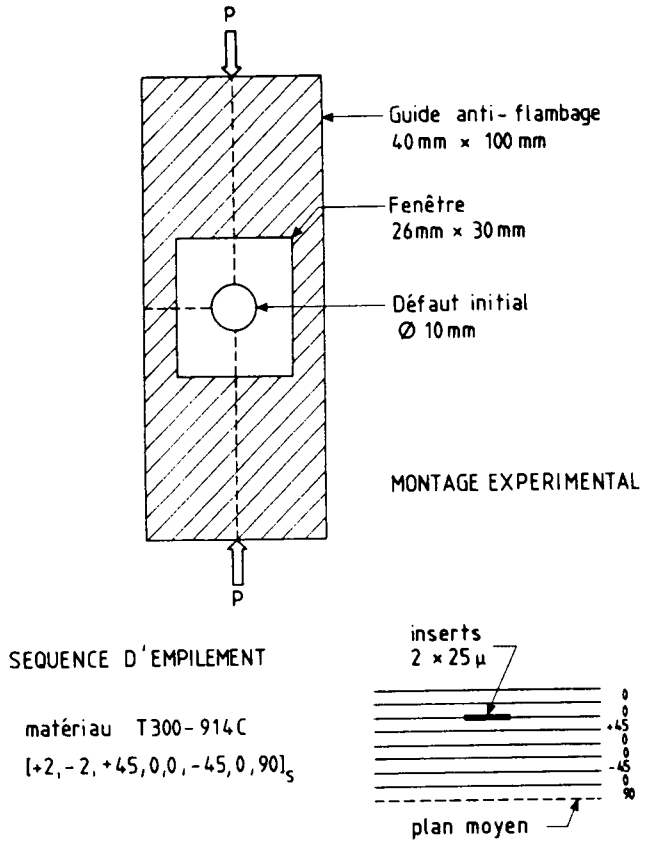

Fig: 1_DEFINITION DU PANNEAU

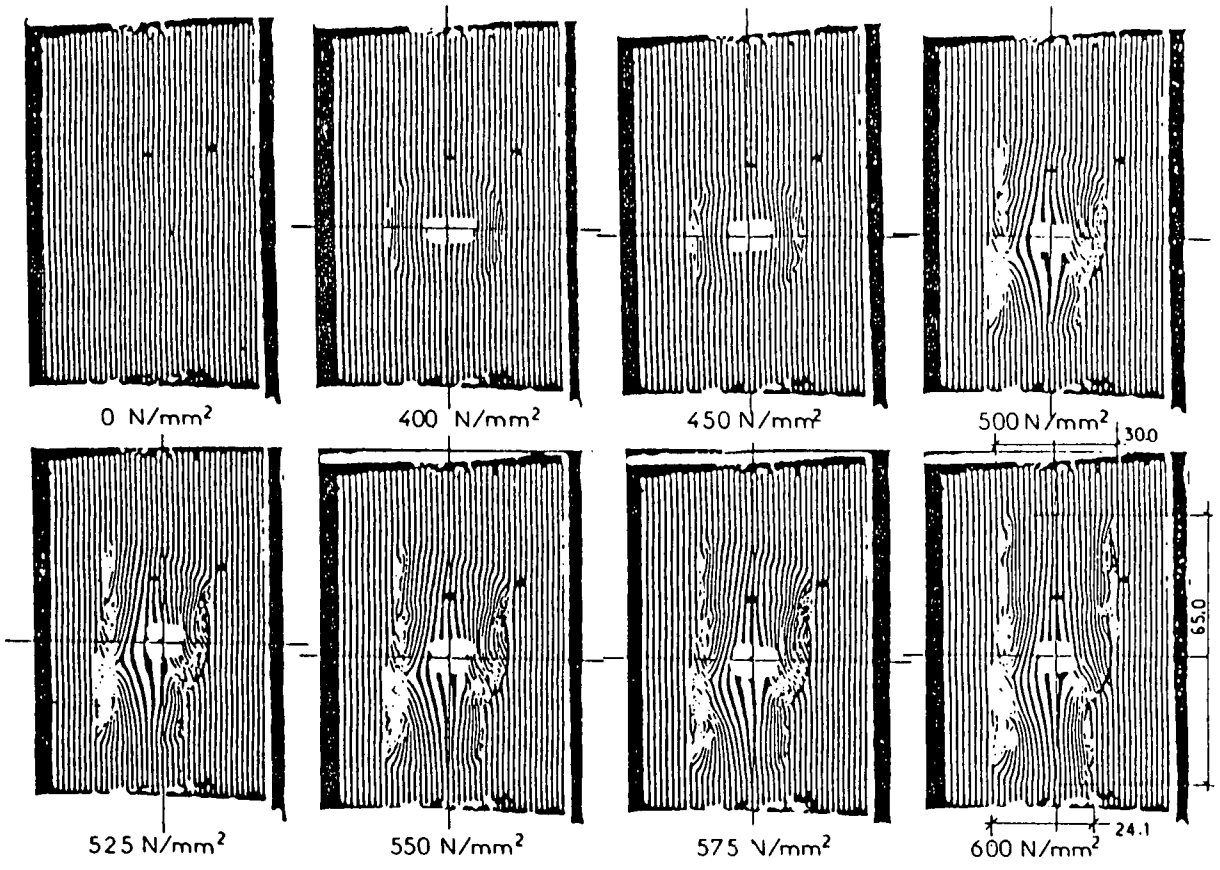

Fig: 2_VISUALISATION DU DELAMINAGE (DLR)

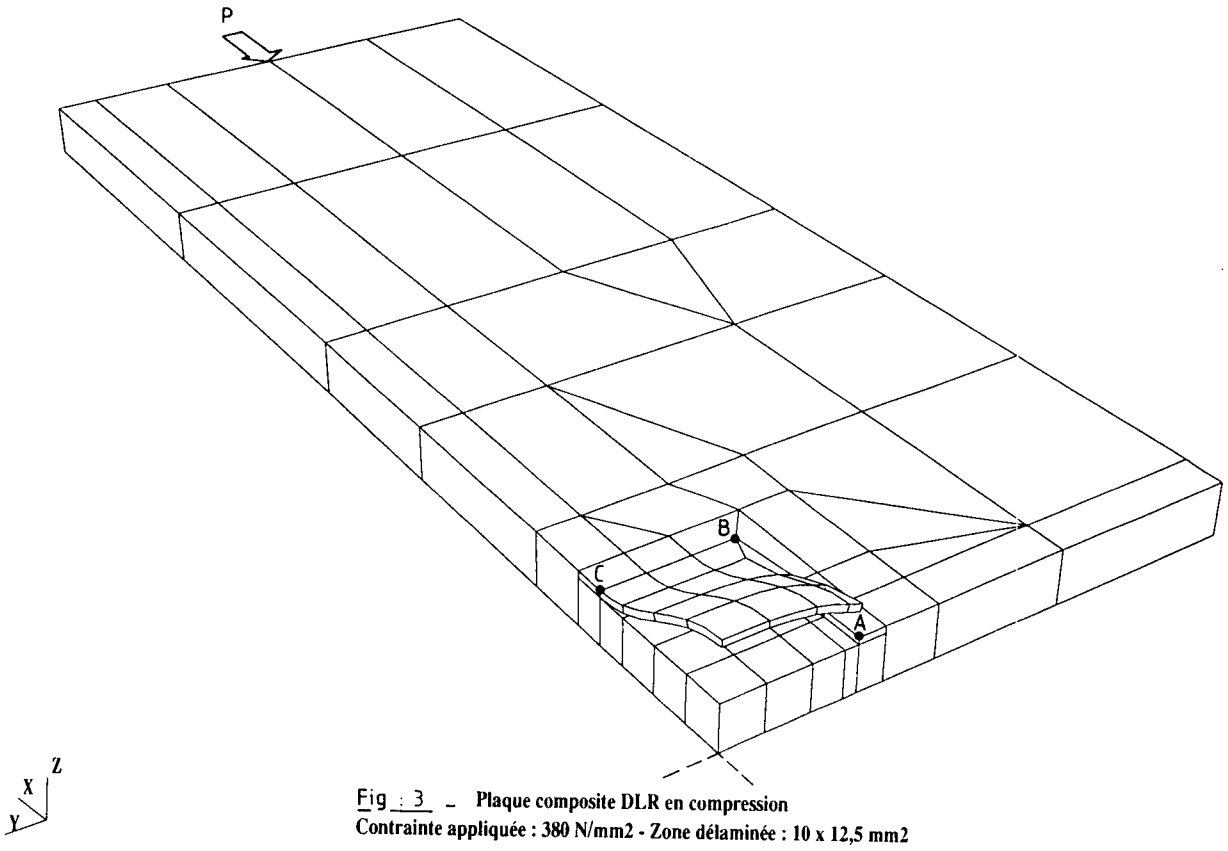

Fig : 3 – **Plaque composite DLR en compression**
Contrainte appliquée : 380 N/mm2 - Zone délaminée : 10 x 12,5 mm2

Coef. multipl. des dép. : 4.00

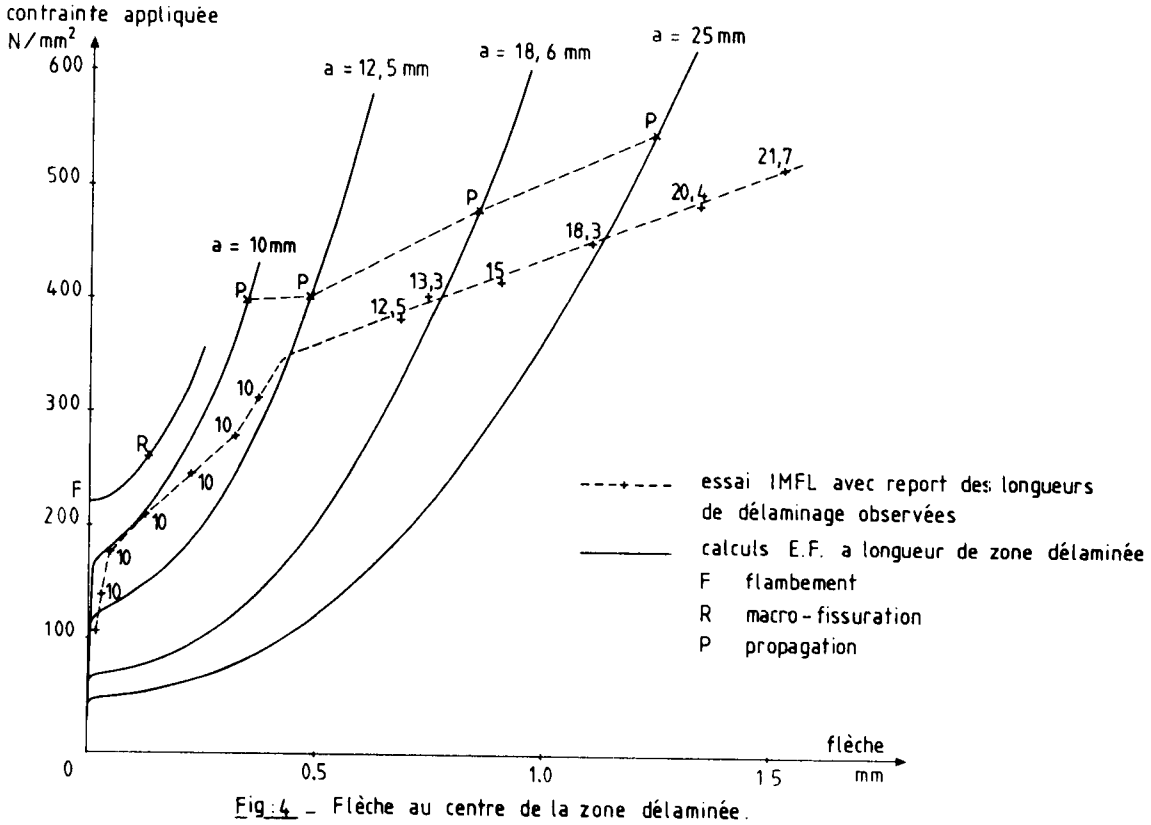

Fig : 4 – Flèche au centre de la zone délaminée.

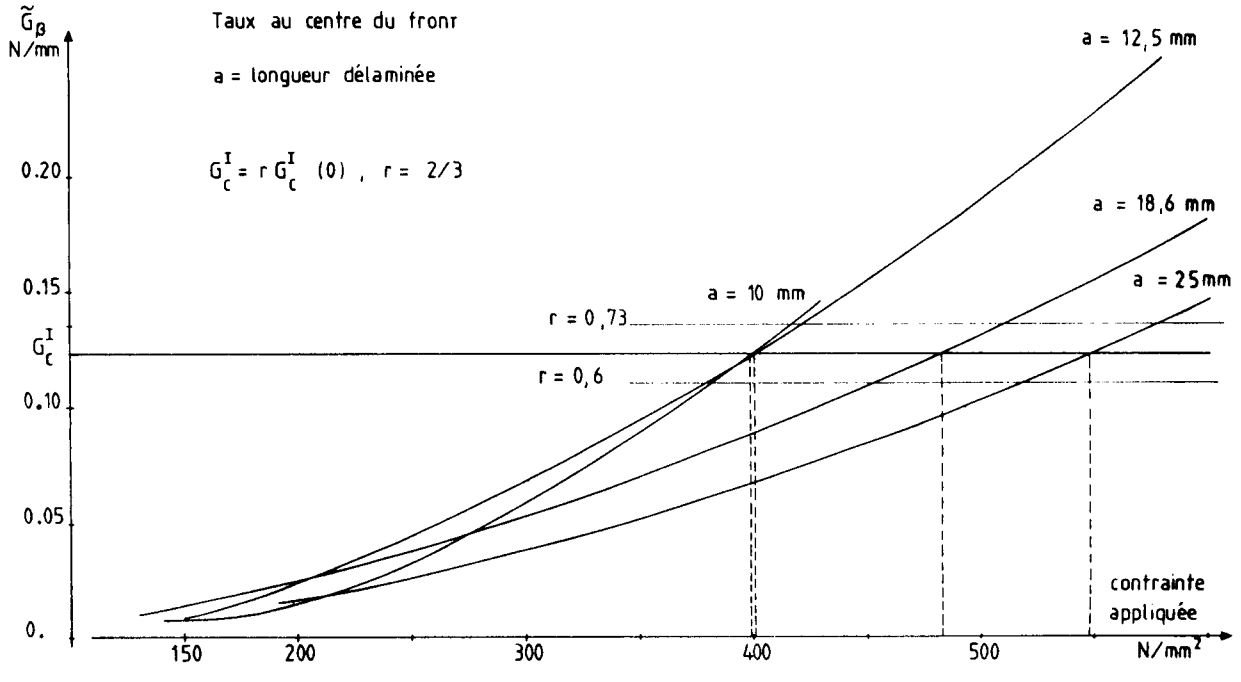

Fig : 5 _ Evolution du taux de restitution d'énergie

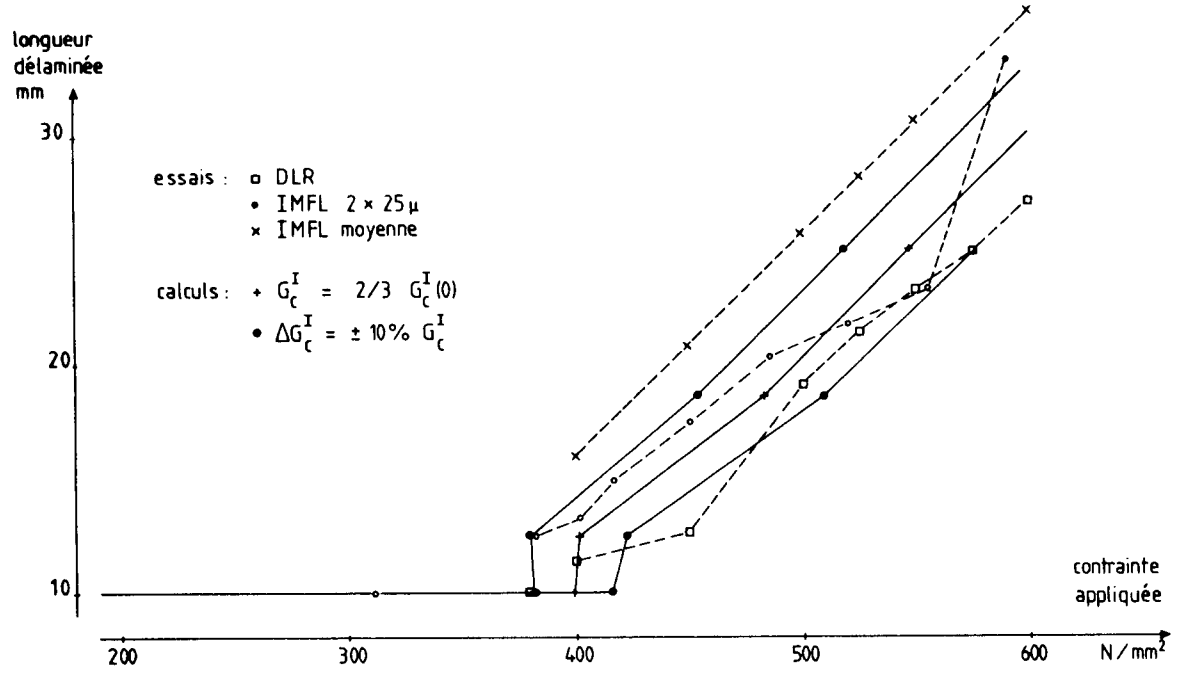

Fig : 6 _ Propagation du délaminage
(comparaison essais-calculs)

GARTEUR COMPRESSION BEHAVIOUR OF ADVANCED CFRP

by

W.G.J. 't Hart (NLR, The Netherlands)
R. Aoki (DLR, Germany)
H. Bookholt (Fokker, The Netherlands)
P.T. Curtis (RAE, United Kingdom)
I. Kröber (DA, Germany)
N. Marks (WHL, United Kingdom)

P. Sigety
ONERA
29, Avenue de la Division Leclerc
92322 Châtillon
France

SUMMARY

The susceptibility of currently used CFRP to impact damage has stimulated the development of improved composites. This new generation of composites usually shows increased toughness and damage tolerance as well as improved tensile performance. This is generally not matched, however, by a similar improvement in compressive properties which then becomes a limiting design factor.
For improvement of the compressive strength a better understanding of the compressive failure behaviour is needed. This aspect is part of a cooperation programme within GARTEUR*. The compressive failure behaviour is being examined at the microscale level (single fibre and bundle tests) and at coupon level.
For experimental verification of failure models special attention has to be paid to compressive test procedures in order to archieve optimal strength values with a minimum of scatter. To evaluate the most appropriate compression test method a Round-Robin test programme was performed on unidirectional laminates of the materials T800/6376; HTA7/982; HTA7/6376; T800/5245; T800/924; IM400/5245 and T400/6376.
In the present paper the results of the Round-Robin test programme are discussed.

Keywords: carbon fibre reinforced plastics, compressive strength, test methods.

1 INTRODUCTION

The low resistance to impact damage of carbon fibre reinforced plastics (CFRP) is one of the major restrictions for applications of CFRP in load-bearing primary aircraft structures. In current composite structures the designer is forced to restrict design loads to levels far below the capabilities of the composites in order to compensate for possible impact damage. Effects of low velocity impacts (e.g. dropping tools) have been widely described in the literature (Ref. 1).

Large static strength reductions can be expected without a visible indication of the damage. The effect is most significant for compression loaded structures where internal delaminations contribute to premature local buckling of the composite. The consequences of this susceptibility to impact damage is that design strain levels of only 3000 μ strain and 4000 μ strain are used for compression and tension loaded components in current composite structures.

This susceptibility of CFRP to impact damage has stimulated the development of improved composites. It was recognized that impact resistance could be improved by applying fibres with a higher tensile failure strain in combination with a tough matrix. Evaluation of a number of these improved composites in the framework of GARTEUR cooperation revealed an increased tensile performance which was not generally matched by a similar improvement in compression properties (Ref. 2). The reason for this is that a higher toughness of a resin is frequently coupled with a lower modulus, and lower modulus may lead to a lower compressive strength for the undamaged composite. Further, some higher fracture strain fibres are smaller in diameter, which can promote microbuckling.

To predict changes in compressive strength as a result of changes in constituent properties more accurately, a better understanding of the compressive failure behaviour is needed. This could be achieved by studying and modelling the failure process and by experimental verification. The most critical parameters and failure modes have to be identified to enable the development of composites with better compressive strengths.

A GARTEUR cooperation programme was initiated to enable better understanding of compressive failure mechanisms. The participating members are the national European aerospace institutes DLR, ONERA, RAE and NLR, and the aerospace industries, Fokker, DA and Westland Hel. The objectives of the cooperation are

- To improve the understanding of the mechanisms by which compressive failure is caused in relation to critical parameters.
- To develop and correlate failure models with experimental data.
- To formulate guidelines for CFRP with a higher compressive strength.

Verification of improved compressive performance should, in fact, be done on a structural level but compressive failure models should be verified on the lowest material level, that is, in the unidirectional ply. For this particular purpose a Round Robin Programme on compression testing was performed first. The main goal of the test programme was to examine whether the current test methods can be used for experimental investigation of the effect of changes in constituent properties on the compressive strength.

In the present paper the results of a Round-Robin compression test programme are discussed. Compression tests were carried out on seven types of unidirectional and three multidirectional CFRP's. In this manner the best performance is evaluated not only in assessing strength values but also in ranking of materials. The latter aspect is of importance when differences in strength between basic and improved material systems have to be established.

2 MATERIALS AND EXPERIMENTAL PROGRAMME

The materials selected for this investigation were 7 advanced CFRP's. Each participant moulded

* Group for Aeronautical Research and Technology in Europe, a cooperation agreement between the Governments of France, Germany, The Netherlands and United Kingdom

unidirectional laminates* of one specific material and distributed pieces of the u.d. laminate among the other participants for compression testing. Three partners also tested multidirectional laminates. Table 1 shows the materials involved and the lay-up for the multidirectional laminates.

* Laminates were processed in accordance with the specifications given by the manufacturer. After moulding the laminates were C-scanned to guarantee that void-free laminates were used in the test programme.

In the Round-Robin test programme about 6 room temperature compression tests were performed on each material. The compressive strength was calculated for nominal and actual specimen thicknesses. Nominal thicknesses of 2 mm and 3 mm were used for unidirectional and multidirectional laminates, respectively. For specimens with strain gauges the secant E-modulus was determined for the strain range ϵ = 0.1 to 0.5 %

$$\left[E = \frac{\sigma(\epsilon=0.005) - \sigma(\epsilon=0.001)}{0.004}\right].$$

TABLE 1
Overview of materials used for Round-Robin compression tests

unidirectional laminates		multi directional laminates	
moulded by	material code/manuf.		
ONERA	T800/5245 BASF	WHL	HTA/982 $(0, 90, \pm 45)_{s2}$
RAE	T800/924 Ciba Geigy Fibredux	RAE	T800/924 $(\pm 45, 0, 90)_{3s}$
Fokker*	T800/6376 " " "	NLR	T400/6376 $(45, 0_2, -45, 0_3, -45, 0_2, 45)$
NLR	T400/6376 " " "		
DA	HTA7/6376 " " "		
WHL	HTA7/982 ICI Fiberite		
DLR	IM400/5245 BASF		

* Aerospatiale moulded the laminates and sent them to Fokker for distribution and testing

PARTNER	SPECIMEN TYPE		TEST METHOD
ONERA *	L x W mm 10 x 10	• NO TABS • END LOAD INTRODUCTION • TEST RATE 1 mm/min	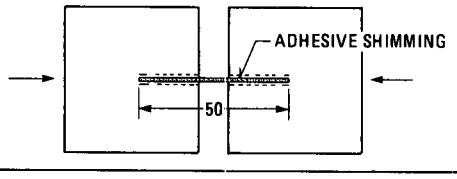
RAE	10 x 10	• Al–TABS, STRAIGHT, t = 0.9 mm • CLAMPING LENGTH 12 mm • SPECIMEN ADJUSTMENT WITH ADHESIVE SHIMMING	**MODIFIED CELANESE** CONICAL WEDGES
FOKKER	12.7 x 6.35	• GLASS TABS TAPERED • CLAMPING LENGTH 16 mm	**CELANESE** CONICAL WEDGES
NLR *	12.7 x 6.35	• GLASS TABS TAPERED • END LOAD INTRODUCTION • CLAMPING LENGTH 16 mm • TEST RATE 1 mm/min	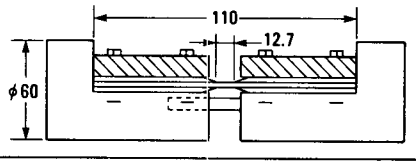
DA	8 x 6.35	• MACHINED SURFACE • CARBON ±45 TABS CO–CURED, 1 mm • CLAMPING LENGTH 12.7 mm • TEST RATE 1 mm/min	**MODIFIED CELANESE** RECTANGULAR WEDGES 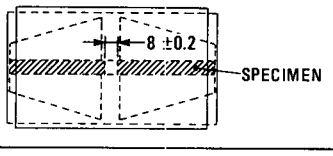
WHL	10 x 10	AS RAE	**STANDARD CELANESE**
DLR *	8 x 6.35	• GLASS FABRIC TABS • NOT TAPERED • CLAMPING LENGTH 12.7 mm	**MODIFIED CELANESE** AS DA

* *SPECIMENS PROVIDED WITH 2 STRAIN GAUGES*

L = FREE LENGTH
W = SPECIMEN WIDTH

Fig. 1 Test methods and used specimen type (u.d. material)

3 COMPRESSION TEST METHODS

3.1 U.D. Laminates

Each partner in the compression test programme used his own compression test method and specimen type. These test methods are frequently the result of an evaluation of many years for obtaining the best test method. This has unfortunately not resulted in an unambiguously accepted test method.

In figure 1 detailed information is given on the used test methods and specimen types. It is seen that the Celanese test fixture (standard or modified) is used most frequently: by RAE, DA, DLR, Fokker and WHL. At ONERA the compression specimens are fixed in steel clamping blocks using adhesive shimming. The NLR used a simplified IITRI based test fixture with load introduction through the specimen ends.

The compression test specimens involved were quite different concerning free gauge length, length between clamping, and specimen width. Furthermore different tab materials, chamfered or not, were applied. The free gauge length of the DA specimens is achieved by machining of the bonded tabs into the base material, see figure 2. This resulted in a specimen thickness that was about 20 % below the moulded laminate thickness, see specimen thickness in table 2.

3.2 Multidirectional Laminates

For multidirectional laminates the RAE and WHL used the CRAG test method (Ref. 3). An anti-buckling guide as shown in figure 3 was used to support the 250 mm long, 20 mm wide strip specimens. The NLR used the same specimen type and testing device as used for the u.d. laminates.

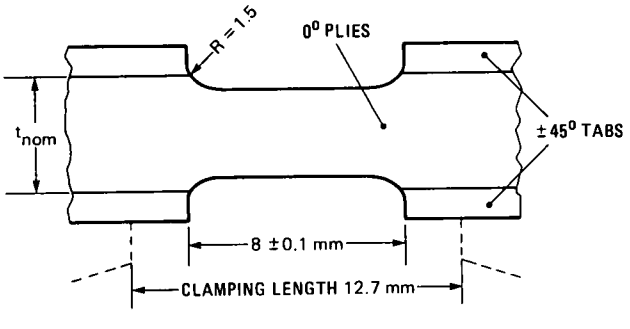

Fig. 2 Detail of DA compression specimen

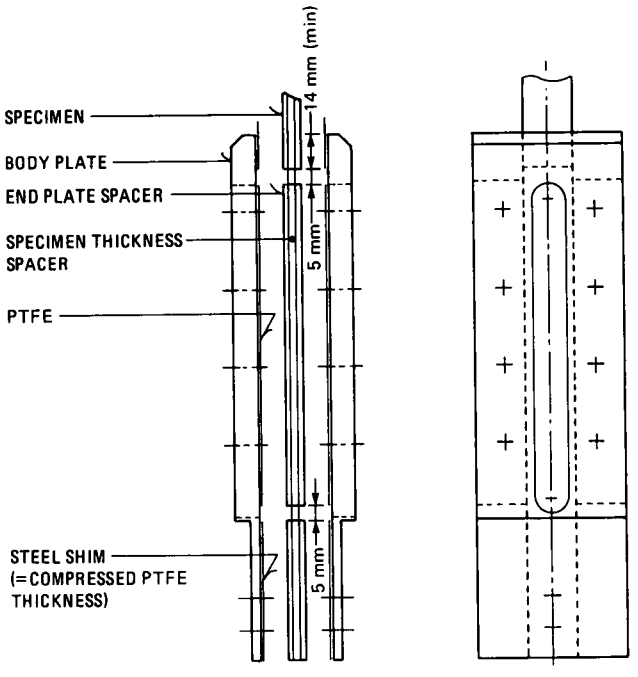

Fig. 3 Anti-buckling guide for multidirectional laminates (CRAG ref. 3)

4 TEST RESULTS

4.1 Unidirectional laminates

An overview of compressive strength and standard deviation is given in table 3. The strength values are based on actual and nominal thickness. The large scatter in mean compressive strength between the participants is striking. To visualize the effect of different test methods and test procedures including human factors on composite strength a comparison was made for the mean strength of the tested materials, see figure 4. Material T800/6376 was excluded since this material was not tested by all participants. Figure 4 shows that the highest strength values are obtained by DA with their test method and specimen type. Relatively low values were obtained by ONERA, RAE and Fokker.

Despite the large differences in strength, depending on test method, the material ranking for the tested materials was generally similar. This is illustrated in figure 5a,b for T800 composites and resin system Narmco 5245 with two fibre types.

TABLE 2
Specimen thickness: mean values and standard deviation

material / member u.d.	T800/5245	T800/924	T800/6376	T400/6376	HTA7/6376	HTA7/982	IM400/5245	number of specimens
ONERA	1.91 (0.04)	2.17 (0.11)		1.89 (0.01)	2.19 (0.03)	1.98 (0.02)	2.24 (0.02)	5
RAE	1.98 (0.03)	2.22 (0.02)	2.16 (0.02)	1.88 (0.04)	2.35 (0.11)	2.02 (0.05)	2.37 (0.05)	10
Fokker(AS)	1.95 (0.01)	2.13 (0.11)	2.02 (0.11)	1.81 (0.01)	2.03 (0.02)	2.04 (0.02)		10
NLR	1.92 (0.02)	2.22 (0.03)	2.09 (0.01)	1.87 (0.04)	2.09 (0.03)	1.97 (0.04)	2.24 (0.05)	6
DA**	1.62 (0.05)	1.50 (0.08)		1.59 (0.04)	1.91 (0.03)	1.81 (0.04)	1.43 (0.07)	6
WHL	1.86 (0.08)	2.12 (0.07)		1.85 (0.04)	2.28 (0.02)	1.91 (0.04)	2.23 (0.03)	6
DLR	1.90 (0.02)	2.14 (0.01)	2.00 (0.01)	1.84 (0.02)	2.06 (0.02)	2.02 (0.02)	2.19 (0.01)	6
mean val.*	1.92 (0.04)	2.17 (0.04)	2.07 (0.07)	1.86 (0.03)	2.17 (0.13)	1.99 (0.05)	2.25 (0.07)	

* without DA
** specimens were machined to a specific thickness

Elastic moduli determined for the strain range ϵ = 0.1 to 0.5 % are given in table 4. For the different testing techniques used by ONERA, NLR and DLR equal moduli were obtained with a low standard deviation. The relatively low strain to failure for materials tested by ONERA can be associated with the low compressive strength values given in table 3.

4.2 Multidirectional laminates

The compressive strength for two quasi-isotropic (QI) and one highly anisotropic laminate is given in table 5. There is a large difference between the RAE and WHL results. This is striking since the same CRAG test method was used. For the anisotropic

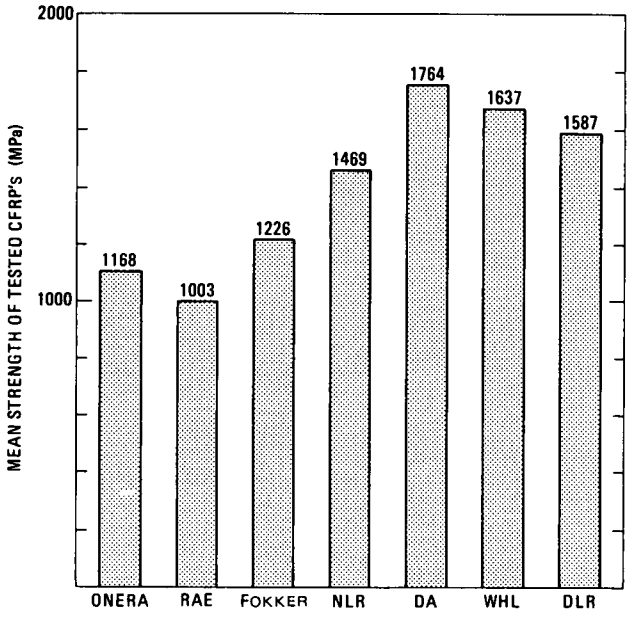

Fig. 4 Compression test performance of participating institutes and industries based on testing the same package of u.d. materials

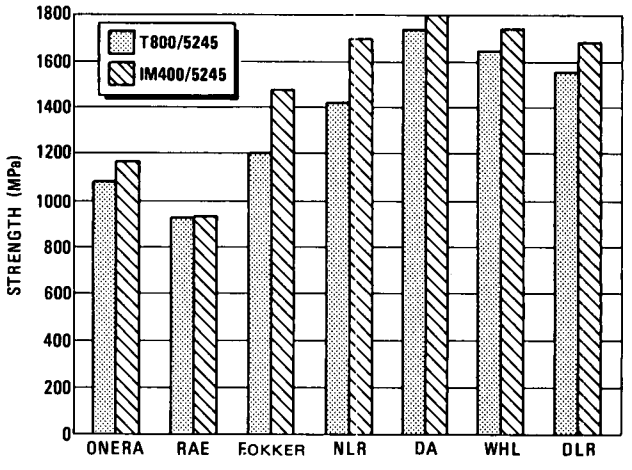

a) *Fibres T800 and IM400 in Narmco 5245*

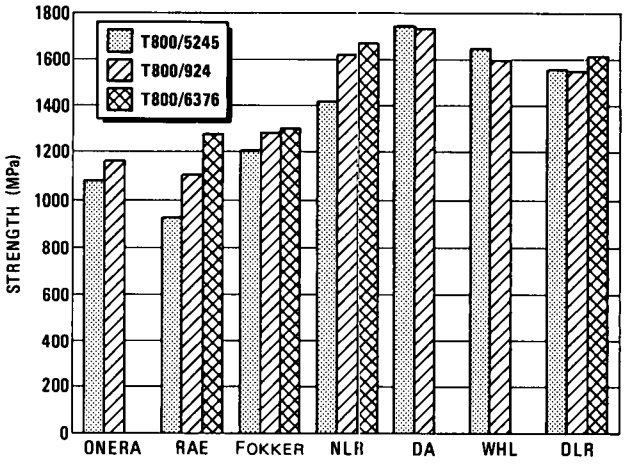

b) *Fibre T800 in various resin systems*

Fig. 5 Compressive strength of various fibre/matrix systems showing the same material ranking

TABLE 3
Overview of compressive strength (MPa) and standard deviation for u.d. laminates

material / member	T800/5245	T800/924	T800/6376	T400/6376	HTA7/6376	HTA7/982	IM400/5245	number of specimens
ONERA	1081 (115)	1166 (122)		1156 (43)	1270 (55)	1172 (89)	1163 (44)	5
	1132 (120)	1074 (113)		1222 (39)	1255 (61)	1181 (81)	1038 (39)	
RAE	927 (118)	1105 (103)	1278 (96)	970 (57)	1206 (118)	882 (106)	931 (100)	10
	937 (130)	994 (91)	1184 (92)	1031 (61)	1026 (85)	873 (98)	785 (77)	
Fokker(AS)	1204 (70)	1288 (129)	1303 (45)	1030 (19)	1169 (82)	1189 (53)	1478 (62)	5
	1228 (71)	1241 (61)	1293 (43)	1135 (17)	1165 (84)	1161 (84)	1298 (56)	
NLR	1422 (60)	1627 (45)	1669 (78)	1248 (64)	1457 (59)	1358 (54)	1703 (73)	6
	1479 (52)	1465 (46)	1594 (73)	1334 (74)	1392 (64)	1381 (53)	1518 (78)	
DA*	1745	1736		1470	2008	1827	1799	6
	1818 (163)	1600 (129)		1581 (107)	1851 (93)	1836 (134)	1599 (111)	
WHL	1651 (84)	1603 (135)		1613 (90)	1941 (42)	1477 (123)	1751 (250)	6
	1780 (107)	1510 (75)		1750 (87)	1700 (42)	1550 (124)	1570 (220)	
DLR	1558 (102)	1554 (116)	1619 (70)	1504 (122)	1674 (82)	1544 (107)	1689 (56)	6
	1640 (107)	1469 (96)	1619 (70)	1634 (77)	1627 (77)	1528 (112)	1555 (39)	
mean val.*	1370	1440	1467	1284	1532	1350	1502	44

strength based on nominal thickness
strength based on actual thickness

* for DA specimens the mean actual strength was transferred to nominal strength using the mean laminate thickness from table 1

TABLE 4
Compressive moduli (GPa, average values and standard deviation) and failure strains (%) for unidirectional laminates

material member	T800/5245	T800/924	T800/6376	T400/6376	HTA7/6376	HTA7/982	IM400/5245
ONERA	139 (2.0)	149 (3.8)		120 (1.1)	119 (6.3)	122 (2.7)	160 (1.8)
	145 (2.0)	138 (3.8)		127 (1.1)	117 (7.3)	123 (2.6)	143 (1.5)
	0.84	0.83		1.06	1.07	1.09	0.91
NLR	142 (1.5)	152 (3.9)	150 (4.3)	121 (1.4)	125 (3.9)	122 (1.6)	160 (2.6)
	148 (2.8)	137 (3.4)	143 (4.3)	129 (2.4)	119 (4.7)	124 (1.8)	142 (3)
	1.12	1.16	1.25	1.2	1.30	1.21	1.22
DLR	145 (4.0)	149 (5.5)	155 (1.0)	121 (1.3)	125 (2.7)	121 (1.6)	161 (1.8)
	152 (4.4)	139 (2.5)	155 (1.2)	132 (1.9)	121 (2.4)	120 (1.3)	147 (1.5)
ϵ	1.15	1.14	1.13	1.40	1.49	1.41	1.15

ϵ: mean of 2 strain gauges extrapollated to maximum load

modulus based on nominal thickness
modulus based on actual thickness

TABLE 5
Compressive strength for multidirectional laminates (standard deviation between brackets)

material lay-up member	HTA7/982 $(0, 90, \pm 45)_{S2}$	T800/924 $(\pm 45, 0, 90)_{3S}$	T400/6376 $(45, 0_2, -45, 0_3, -45, 0_2, 45)$	number of tests
RAE	542 (28)	645 (46)	957 (72)	12
	534 (35)	621 (43)	982 (71)	
WHL	380 (66)	564 (83)	481 (157)	6
	342 (58)	538 (75)	531 (170)	
NLR	631 (17)	786 (27)	963 (36)	6
	578 (18)	755 (37)	1011 (38)	
$\bar{\epsilon}$(%)	1.46	1.77	1.32	
E GPa	43.5	50.5	89.3	
NLR $\bar{\epsilon}_{u.d.}$(%)	1.21	1.16	1.20	

strength based on nominal thickness
strength based on actual thickness

laminate the NLR and RAE results were similar but for the QI laminates the NLR tests showed somewhat higher compressive strengths.

Comparison of strain to failure under compressive loading for multidirectional and u.d. laminates showed higher values for the multidirectional laminates (NLR results). This effect was most pronounced for the T800/924 material.

5 DISCUSSION

The main goal of the present investigation was to examine whether the compression test methods in use are suitable for experimental verifications in modelling compression failure. In this respect the results of comparative testing of different material systems with different compressive performance are valuable by-products.

The differences in strength values obtained for the same material system on specimens made from the same laminate must be attributable to differences in specimen type and size, the clamping and loading technique and to human factors involved in preparing and performing the tests. The latter aspect cannot be traced but the former two effects will be discussed in some detail.

As shown in figure 1, the free gauge length of the DA and DLR specimens was only 8 mm. This resulted in high strength values. The specimen length

TABLE 6
Mean strength values (MPa) for different fibre/matrix combinations

Resin / Fibre	5245	924	6376	982
T800	1370	1440	1467	
T400			1284	
HTA7			1532	1350
IM400	1502			

between the grips was 12.7 mm for both specimen types but since the DA specimens were machined to a thickness about 20 % below the moulded laminate thickness, the tabs were somewhat more effective in supporting the free gauge length than the tabs for the DLR specimen. This could explain the somewhat higher strength values for DA specimens. Fokker and the NLR used chamfered glass tabs and the length between the grips was 16 mm. As compared to the previous specimens, a lower compressive strength is not unexpected. The low values obtained by ONERA and the RAE cannot be explained properly. However, both institutes apply adhesive shimming for specimen adjustment and this might effect the stiffness of the gripping resulting in premature specimen failure. A more thorough evaluation of the effect of test conditions on failure strength is not possible due to lack of information on the failure modes experienced in the tests.

The compression test results for multidirectional laminates were rather confusing. No proper explanation could be given for the low strength values of WHL as compared to the RAE and NLR results. Strain measurements performed by the NLR showed higher failure strains for multidirectional laminates than for the u.d. laminates, table 5. Especially for the T800/924 material the difference was significant. This indicates that a uniform distribution of load bearing 0° layers between layers with a different orientation has a positive effect on the compressive strength (strain to failure). Further, it should be noted that the standard deviation for the tests on multidirectional laminates is significantly smaller than that for the tests on unidirectional specimens.

6 PRACTICAL SIGNIFICANCE OF THE RESULTS FOR FURTHER INVESTIGATION

The results of the Round-Robin test programme have shown the compressive strength to be strongly dependent on the specimen type and test method. However, the ranking in material strength as obtained by each participant was in general similar. This means that the effects of constituent properties on compressive strength essentially could be investigated by each member using his own test method. On the other hand, for investigation of the most significant parameters in modelling compression failure a low scatter in test results is desirable. It was shown that for multidirectional laminates higher compressive failure strains were obtained than for u.d. laminates with a smaller standard deviation for the strength. Therefore, use of multidirectional laminates should be considered for experimental verification in modelling compression failure.

By testing different fibre/matrix combinations in the present programme, information was obtained on the compressive strength performance of the tested materials. In table 6 the mean strength of the tested materials (from Tab. 2) is given in a format that enables direct evaluation of the best fibre/matrix combinations. The effect of matrix on the compressive strength of composites containing the same fibre is shown for T800 and HTA7 composites. Although the differences are not significant, the 6376 system seems to result in maximum strength values for the mentioned fibres. If different fibre types are combined with 6376, the best compression strength performance is obtained for the HTA7/6376 system.

7 CONCLUSIONS

In the framework of GARTEUR cooperation on compression behaviour of CFRP a Round-Robin testsprogramme was performed involving different test methods and seven modern unidirectional laminates. In addition, limited tests on multidirectional laminates were carried out. The main conclusions that can be drawn from this investigation are:

1 The compressive strengths of u.d. laminates varied significantly dependent on specimen types and test methods.
2 The material ranking obtained by the participants was more or less similar.
3 Testing of quasi-isotropic laminates resulted in an higher strain to failure than that obtained for u.d. laminates, with an smaller standard deviation for the compressive
4 The compression strength of HTA7/6376 was the most promising among the tested fibre/resin combinations.
5 It appears that despite conclusion 1, most of the compression test methods described in this paper can be used for experimental verification of compression failure models that incorporate changes in constituent properties. On the other hand, a low scatter of results is desirable for investigation of the most significant parameters in the modelling of compression failure.

8 REFERENCES

1. Horton, R.E. and J.E. McCarty., "Damage tolerance of composites", Composites ASM Vol. 1, 1987.

2. Bookholt, H., Brokopf, C., Curtis, P.T., 't Hart, W.G.J., Kröber and P. Sigerty, "The investigation of understanding of improved composite materials GARTEUR TP-60, 1991.

3. Curtis, P.T., "GRAG test methods for the measurement of the engineering properties of fibre reinforced plastics, RAE TR 85099, 1985.

INNOVATIVE CONSTITUENTS REQUIREMENTS TO IMPROVE COMPOSITES COMPRESSIVE STRENGTH

L. ANQUEZ & P. VAUTEY

DASSAULT - AVIATION
78 Quai Marcel Dassault
92214 SAINT-CLOUD
FRANCE

1 - INTRODUCTION

While the recent developments of Intermediate Modulus carbon fibers led to very high specific tensile strength over the first generation of High Strength fibers, the composites compressive properties did not improve at all.

Because most of the aeronautical structures are subject to alternate tension and compression, it is not possible to take full advantage of carbon fibers composites, as the compressive loading becomes the design limitation.

After a focus on the matrix dominating role in composite compression behavior, this paper will clear out which matrix characteristic, stiffness or strength, pilotes the unidirectional compressive failure.

2 - PROBLEM STATEMENT

This work mainly deals with organic matrix composite reinforced with continuous PAN based graphite fibers, because aircraft structural composite materials are considered. The understanding of the longitudinal compressive failure and the improvement of compressive strength are the aim of this paper.

2.1 - A matrix dominated behavior

Figure 1 presents some compression experimental results on a multi layers laminate with a hole. It illustrates that all the tested materials exhibit similar compressive strength whatever the carbon fibers are (T300, AS4, IM6, T650-42, T800). The tensile strength of the same materials has to be considered, to point out the fiber influence.

On the other hand, the different resin systems used in these commercially available composites are almost equivalent in terms of stiffness and strength (see appendix A). This can be a first suggestion of the dominant role of the matrix for composite compressive strength.

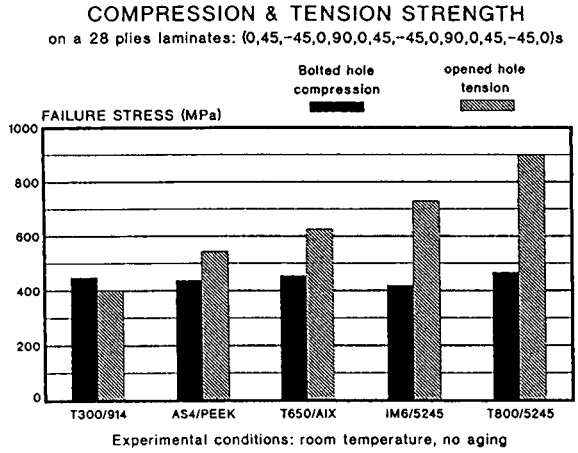

Figure 1 : Compressive and tensile strength of different commercial composites

A second experimental verification has been performed, taking into account the fact that fibers properties are not affected by hot/wet environmental exposures from - 55°C to 120°C, while resin properties are.

Figures 2 and 3 show plots of the composite unidirectionnal compressive strength of some systems versus the respective resin evaluation in the same hot/wet conditions (datas from M. Gädke [1], Rosen [2], Tsai [3], Dassault...).

In both cases, a very strong dependence has been established between either G_{12}, the shear modulus, or τ_{SBSS} the short beam shear strength, which are truly matrix dominated characteristics, and ε_{11}^{c}, the longitudinal compressive strength.

This confirms that composite compressive failure is matrix-governed.

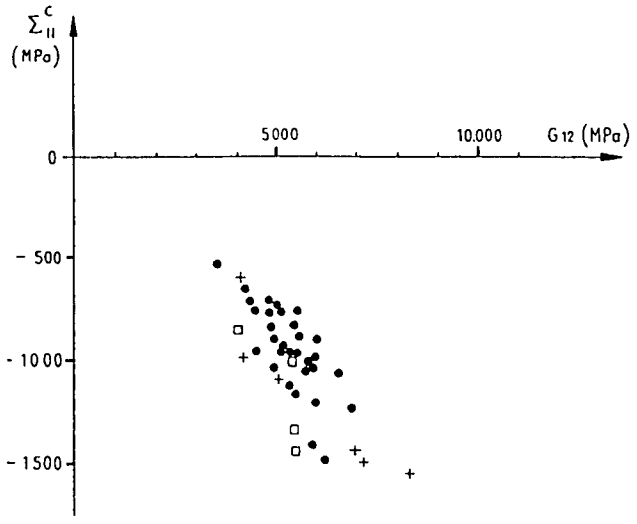

Figure 2 - Correlation between the longitudinal compressive strength and the shear modulus. Several fiber/matrix couples at different hygrothermal ageing have been gathered.

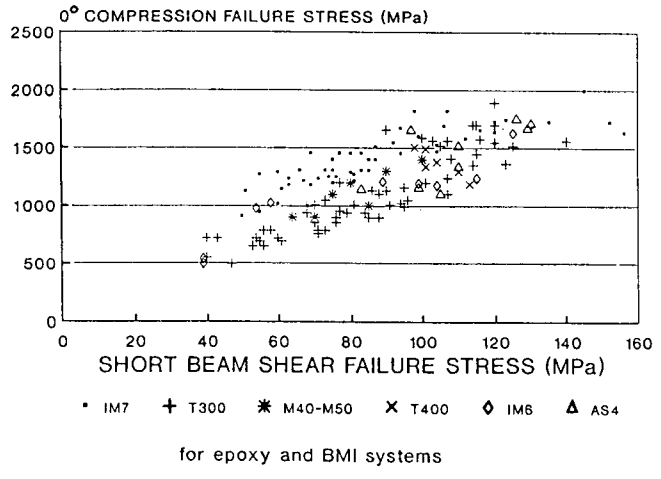

Figure 3 - Correlation between longitudinal compressive failure stress and the short beam shear strength at various hygrothermal test conditions.

2.2 - Low longitudinal compressive strength explanation : initial fibres misalignment

First of all, it is interesting to have in mind an important general result of mechanics :

Appendix B details the mechanics demonstration, which is valid for the following hypothesis :

- **Linear elastic behavior**
- **Homogeneous material**
  - . Isotropic, orthotropic.. (metals, ceramics, composites...).

Σ(compressive stress) $\leq$ G (shear modulus)

In our case, the main result is that the instability occurs when the applied compressive stress on a perfect unidirectionnal laminate (straight fibers, strictly parallel in a regular arrangement) reaches the composite shear modulus.

$$\Sigma^c_{11} = -G_{12}$$

Now, considering the ratio $-G_{12}/\Sigma^c_{11}$ for different fiber/matrix couples, figure 4 emphasizes that the experimental ratio is never equal to 1.

Composite family	Reinforcement type	$-G_{12}/\Sigma^c_{11}$
BFRP	Boron	2.2
CFRP	Carbon	4 - 5.5
GFRP	Glass	6.8

Figure 4 - $-G_{12}/\Sigma^c_{11}$ of different epoxy based composites (TSAI datas).

In the case of carbon/resin, Σ^c_{11} is about 4 times lower than the theoritical G_{12} value. Fibers misalignment is the probable explanation suggested by many authors. Mrse and Piggott [4] reported an experimental confirmation of the fibers initial misalignmenet distribution influence on the longitudinal compressive strength of unidirectionnal laminates.

Up to now, analytical approaches [2] [5] [6] did not give conclusions about the constituents requirements to improve composite compression, because they were dealing with simple and non representative fibers arrangements.

The following numerical simulation will allow us to perform parametric studies by changing constituents (fibers and matrix) properties and to analyze their effect on compressive strength of realistic composite representations.

3 - NUMERICAL SIMULATION

3.1 - Fibers initial misalignment representation

Mesh construction rules :

- 2D model.
- 20 fibers embedded in a matrix.
- Global fiber volumic fraction : 0.58
- Fibers diameter : 5.8 microns.
- No fibers interpenetration.
- A fiber misalignment has to fit in a 10 microns wide band.

- Local fiber misalignment given by a defined distribution of local fiber orientation with respect to the 0° unidirectional basis.

Appendix C presents the 3 cases of distribution and the resulting finite elements meshes.

These distributions have been roughly identified on composites micrographs.

3.2 - Constituents behavior hypothesis

Carbon fibers :

- Homogeneous and isotropic (+ parametric studies of different filaments degrees of orthotropy).

- Linear elastic behavior. (Ef=230000 MPa)

Matrix :

- Homogeneous and isotropic.

- Elasto plastic behavior (see figure 5).

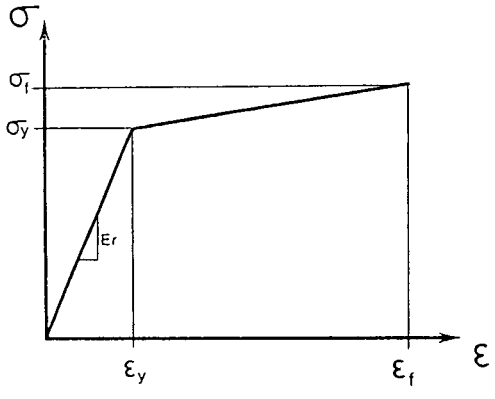

Er = resin modulus
σ_y = yield stress
σ_f = failure stress
ε_y = yield strain
ε_f = failure strain

Figure 5 - Matrix elasto plastic behavior.

After a few parametric studies of resin modulus effect (from 2500 to 5000 MPa), and σ_y, σ_f, ε_y and ε_f combinations, the matrix behavior has been approximated to an elastic quasi plastic behavior for the reference simulations (a slight strength hardening has been introduced to reach a fast calculus convergence). The matrix is therefore fully characterized by its modulus Er and yield stress σ_y.

Appendix D shows that in a shear mode, which is better to characterize the non linear resin behavior up to failure, experimental stress strain curves are close to this theoretical elasto-plastic form.

3.3 - Calculations hypothesis

- Non linear calculations by incremental increases of the applied longitudinal displacement.

- Large displacements.

- Mesh details : 2000 nodes
  3822 triangular finite elements
  4000 degrees of freedom.

- Boundary conditions (see figure 6) :

  . No displacement allowed in the x direction for the left side.

  . No displacement allowed in the y direction for the bottom side.

  . Equal displacement imposed in the y direction for all the nodes of the upper side.

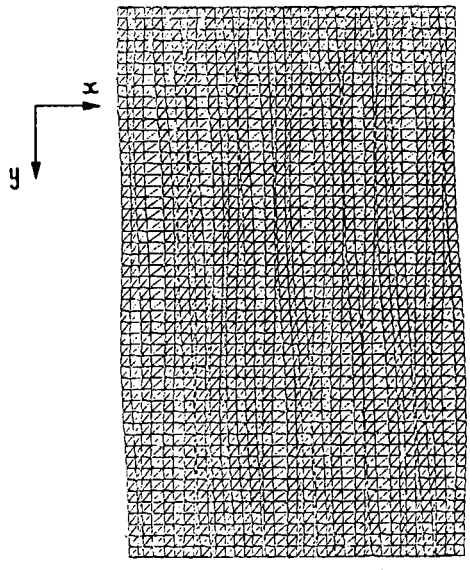

Figure 6 - Mesh representation.

4 - RESULTS AND DISCUSSION

4.1 - Reference simulation

Figure 7 presents the calculations results in the reference case :

- Misalignment case 1.
- Elasto-plastic matrix (Er = 3800 MPa).

Each dot marks the unidirectional laminate global buckling stress for a given resin yield stress. It is interesting to note that it gives near the origin a quasi parabolic form, and for high values of σ_y an asymptote with a value of G_{12}, standing for the theoritical limit $\varepsilon_{11}^c = -G_{12}$ (linear buckling). Notice that the value of G_{12} in 2D simulation is found quasi equal to the value proposed by Rosen ($G_m/(1-V_f) = 3600$ MPa), which is less than what can be computed in 3D : 5000 MPa.

It shows that for very high values of resin yield stress σ_y, no premature fiber microbuckling occurs in spite of the initial misalignment. Like for the perfect 0° laminate, with straight fibers in a regular arrangement, the compressive stress to failure is reached when the global shear instability ($\Sigma = -G$) is spread throughout the composite.

* Unidirectional laminate compressive stress value of the global buckling instability for a given resin yield stress

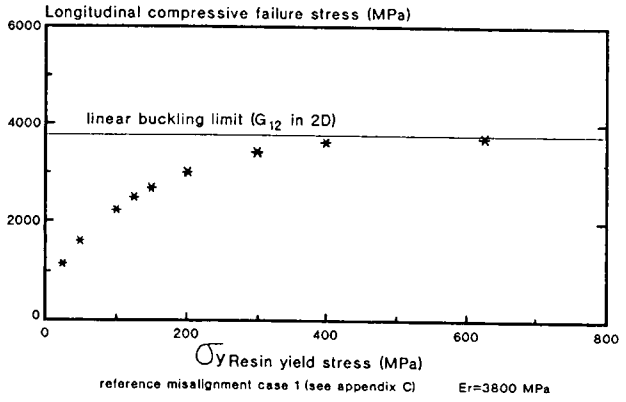

Figure 7 - Compressive failure stress versus resin yield stress (reference simulation).

4.2 - $\varepsilon^c_{11} \sim A\sqrt{\sigma_y}$ relation proposal

In the first part of the $\varepsilon^c_{11} = f(\sigma_y)$ relationship (see figure 8), it seems that a function of $\sqrt{\sigma_y}$ describes the behavior in a first approximation. It will also facilitate the following parametric studies analysis, because we are going to deal with a linear function

* Unidirectional laminate compressive stress value of the global buckling instability for a given resin yield stress square root

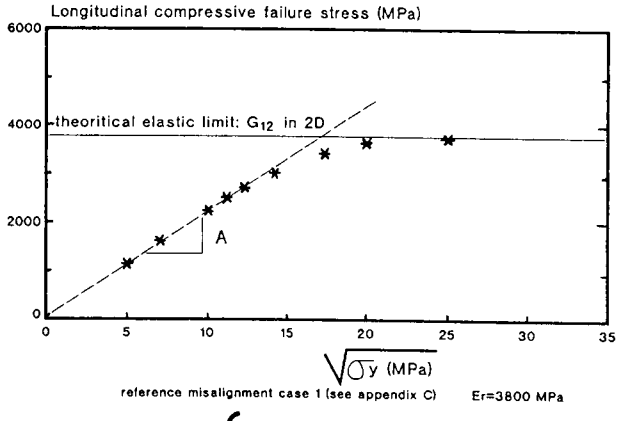

Figure 8 - $\varepsilon^c_{11} \sim A\sqrt{\sigma_y}$

4.3 - Misalignment influence

The simulation results reported in figure 9 confirm the initial fibers misalignment effect on unidirectional compressive failure. In the $\varepsilon^c_{11} \sim A\sqrt{\sigma_y}$ formulation, the slope "A" decreases as the misalignment increases.

On the other hand, when the global shear ruine mode becomes dominant, for high values of σ_y, we only notice a slight difference of the two fibers arrangement cases, which converge to the linear buckling limit G_{12}.

Unidirectional laminate compressive stress value of the global buckling instability for a given resin yield stress square root

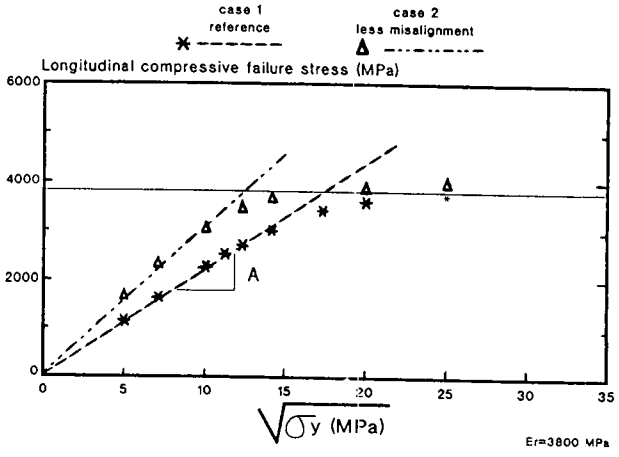

Figure 9 - Slope A dependence of the fibers misalignment distribution.

4.4 - Resin modulus influence

A parametric study has been performed taking the reference case N° 1 of misalignment and 3 elasto-plastic matrices with the following Young modulus :

Er' = 2600 MPa
Er = 3800 MPa (reference case)
Er" = 5000 MPa

As expected, the linear buckling limit is increasing with the resin modulus, as G_{12} is matrix dominated.

But for lower values of matrix yield stress, figure 10 suggests that the resin modulus has a very small effect on the slope "A" of the relationship $\varepsilon^c_{11} \sim A\sqrt{\sigma_y}$

Unidirectional laminate compressive stress value of the global buckling instability for a given resin yield stress square root

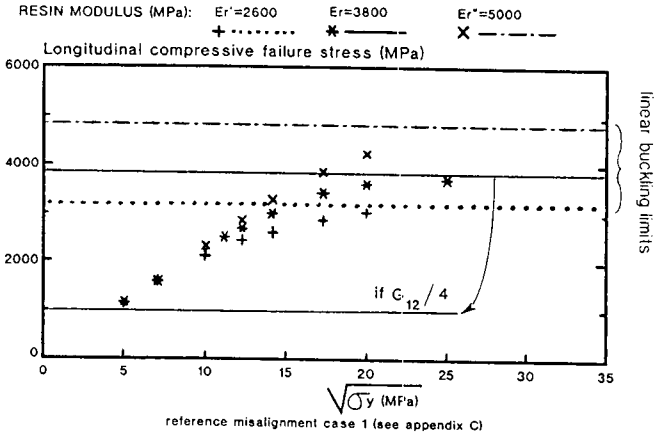

Figure 10 - Resin modulus influence.

4.5 - Matrix properties requirements indications

The analysis of the previous simulations leads to the following comments in the perspective to give matrix mechanical requirements to improve composite compressive strength :

- Preliminary : the fibers misalignment has an important role, but we will consider it as an imposed parameter. It would be very difficult at this point to control the fibers placement through all the manufacturing operations.

- If we consider that current carbon composites exhibit a $-G_{12}/\varepsilon^c_{11}$ ratio in the range of 4, the governing failure mode is definetely described by $\varepsilon^c_0 \sim A\sqrt{\sigma_y}$, being independent of the resin modulus (see figure 10).

- So, an increase of matrix yield stress will increase the unidirectional laminates 0° compressive strength.

5 - COMPARISON WITH COMPOSITE MATERIALS DATAS

In order to gather a great number of combinations of ε^c_{11} and square root of σ_y, we again mixed several materials in different hygrothermal states. According to the same sources as figure 3, and because the litterature is very poor in resin yield stress values at different ageings, we plotted the short beam shear strength "σ_{SBSS}" instead of σ_y (with $\sigma_y = \tau_y/\sqrt{3}$). This interlaminar failure is matrix dominated and appendix E suggests a strong correlation between σ_y and σ_{SBSS} : $\sigma_{SBSS} \sim \sigma_y + 25$ (MPa) . σ_{SBSS} is a good mechanical limit value for our purpose, because within the composite it covers at the same time, resin and fibre/matrix interfacial failures.

In spite of the points dispersion on figure 11, it seems that the experimental data fit a $\varepsilon^c_{11} \sim A\sqrt{\sigma_{SBSS} - 25}$ relationship.

Remarks: The scatter in the composite compressive failure values can be attributed to :

. The low reliability of data, according to the difficult compressive test procedures [7] and the "laboratory effect" [8].

. Not measured and probably different initial fibers misalignments.

for epoxy and BMI systems

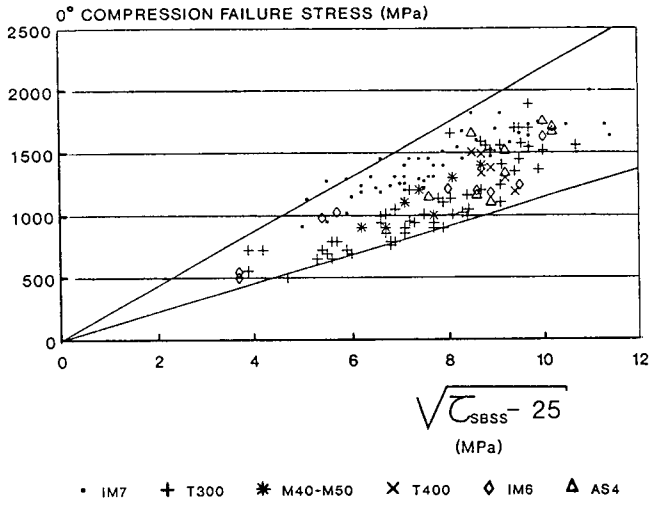

Figure 11 - Litterature experimental data report of ε^c_{11} and $\sqrt{\sigma_{SBSS} - 25}$ value of various carbon/resin systems in different hot/wet conditionnings.

6 - CONCLUSION

Numerical simulations gave a powerfull understanding of composite compressive failure.

As long as the ratio $-G_{12}/\varepsilon^c_{11}$ will be very superior to 1, (factor of 4 to 5 for carbon/resin materials), the resin yield stress will have to be significantly increased to improve composite compressive strength. It is not necessary for carbon reinforced systems to work on the resin modulus.

In order to address resin mechanical requirements to a material supplier, it is better to consider the short beam shear strength information, which includes resin and fibre/matrix interface properties.

The challenge is going to be very important, because considering a square root approximated dependence of the interlaminar yield shear stress, resin elaborators will have to double the short beam shear strength to get significant 0° composite compressive strength improvement.

7 - PERSPECTIVES

Pilot resins, with independent ratios of E_r/σ_y, will be elaborated by SNPE (France), to try to get an experimental verification of the $\varepsilon^c_{11} \sim A\sqrt{\sigma_y}$ relationship for carbon reinforced composites.

8 - REFERENCES

[1] Dr Michael Gädke, thesis : "Hygrothermal behaviour of carbon fibre reinforced epoxies", VDI, Verloq GmbH, Dusseldorf 1988.

[2] Dow, Norris, Rosen : "Evaluations of filament reinforced composites for aerospace structural applications", NASA CR 207, april 1965.

[3] S. W. Tsai Composites design, 4th edition.

[4] A. Mrse & M.R. Piggott, SAMPE april 1990, vol 35, p.2236.

[5] H.T. Hahn & J.G. Williams, Composite materials, ASTM STP 893, 1986, p.115.

[6] P.S. Steif, J. Solids structures, vol 26, 1990, p.549.

[7] G.A. Schoeppner & R.L. Surakowski, "A review of compression test methods for organic matrix composites", 1990, ASTM, J. of Comp. Tech. and Research.

[8] GARTEUR (Group for Aerospace Research and Technology in EURope). Round robin tests about composites compression evaluations, 1990.

APPENDIX A

Mechanical characteristics intervals of typical resins used in commercial composites for structural applications (no aging and room temperature).

Isotropic materials	All
Tensile modulus	3600 to 4000 MPa
Poisson's ratio	0.3 to 0.35
Tensile failure stress	70 to 90 MPa
Compressive failure stresse	-170 to -140 MPa
Shear strength	70 to 90 MPa

APPENDIX B

Shear instability demonstration of a body subjected to uniaxial compressive loading.

The free energy of a linear elastic isotropic material can be written as :

$$\varphi(\varepsilon_{ij}) = \nabla^{\circ}_{ij}\varepsilon_{ij} + \frac{1}{2}\lambda I_1^2 + \mu I_2$$

∇°_{ij} prestress tensor

λ, μ Lame coefficients

$$I_1 = \varepsilon_{xx} + \varepsilon_{yy} + \varepsilon_{zz}$$

$$I_2 = \varepsilon_{xx}^2 + \varepsilon_{yy}^2 + \varepsilon_{zz}^2 + 2\varepsilon_{yz}^2 + 2\varepsilon_{zx}^2 + 2\varepsilon_{xy}^2$$

Where ε_{ij} are the true strains.

$$\varepsilon_{xx} = \frac{\partial u}{\partial x} + \frac{1}{2}\left(\frac{\partial u}{\partial x}\right)^2 + \frac{1}{2}\left(\frac{\partial v}{\partial x}\right)^2 + \frac{1}{2}\left(\frac{\partial w}{\partial x}\right)^2$$

$$\varepsilon_{yy} = \frac{\partial v}{\partial y} + \frac{1}{2}\left(\frac{\partial u}{\partial y}\right)^2 + \frac{1}{2}\left(\frac{\partial v}{\partial y}\right)^2 + \frac{1}{2}\left(\frac{\partial w}{\partial y}\right)^2$$

$$\varepsilon_{zz} = \frac{\partial w}{\partial z} + \frac{1}{2}\left(\frac{\partial u}{\partial z}\right)^2 + \frac{1}{2}\left(\frac{\partial v}{\partial z}\right)^2 + \frac{1}{2}\left(\frac{\partial w}{\partial z}\right)^2$$

$$\varepsilon_{yz} = \frac{1}{2}\left(\frac{\partial w}{\partial y} + \frac{\partial v}{\partial z}\right) + \frac{1}{2}\frac{\partial u}{\partial y}\frac{\partial u}{\partial z} + \frac{1}{2}\frac{\partial v}{\partial y}\frac{\partial v}{\partial z} + \frac{1}{2}\frac{\partial w}{\partial y}\frac{\partial w}{\partial z}$$

$$\varepsilon_{zx} = \frac{1}{2}\left(\frac{\partial u}{\partial z} + \frac{\partial w}{\partial x}\right) + \frac{1}{2}\frac{\partial u}{\partial z}\frac{\partial u}{\partial x} + \frac{1}{2}\frac{\partial v}{\partial z}\frac{\partial v}{\partial x} + \frac{1}{2}\frac{\partial w}{\partial z}\frac{\partial w}{\partial x}$$

$$\varepsilon_{xy} = \frac{1}{2}\left(\frac{\partial v}{\partial x} + \frac{\partial u}{\partial y}\right) + \frac{1}{2}\frac{\partial u}{\partial x}\frac{\partial u}{\partial y} + \frac{1}{2}\frac{\partial v}{\partial x}\frac{\partial v}{\partial y} + \frac{1}{2}\frac{\partial w}{\partial x}\frac{\partial w}{\partial y}$$

Assumptions :

* Plane strain u(x,z) ; v = 0 ; w(x,z)
* Prestress : $\nabla^{\circ}_{zz}(x,z)$ = constant
* w(x,z) negligible compare to u(x,z)

Then :

$$\varphi(\varepsilon_{ij}) = \nabla^{\circ}_{zz}\varepsilon_{zz} + \frac{1}{2}\lambda(\varepsilon_{xx} + \varepsilon_{zz})^2 + \mu(\varepsilon_{xx}^2 + \varepsilon_{zz}^2 + 2\varepsilon_{xz}^2)$$

$$\varepsilon_{xx} = \frac{\partial u}{\partial x} + \frac{1}{2}\left(\frac{\partial u}{\partial x}\right)^2$$

$$\varepsilon_{zz} = \frac{1}{2}\left(\frac{\partial u}{\partial z}\right)^2$$

$$\varepsilon_{xz} = \frac{1}{2}\frac{\partial u}{\partial z} + \frac{1}{2}\frac{\partial u}{\partial x}\frac{\partial u}{\partial z}$$

So, up to the second order :

$$\varphi(\varepsilon_{ij}) = \frac{1}{2}\nabla^{\circ}_{zz}\left(\frac{\partial u}{\partial z}\right)^2 + \frac{1}{2}\lambda\left(\frac{\partial u}{\partial x}\right)^2 + \mu\left[\left(\frac{\partial u}{\partial x}\right)^2 + \frac{1}{2}\left(\frac{\partial u}{\partial z}\right)^2\right]$$

Equilibrium condition :

$$\delta\varphi = 0$$

$$(\nabla^{\circ}_{zz} + \mu)\frac{\partial u}{\partial z}\frac{\partial \delta u}{\partial z} + (\lambda + 2\mu)\frac{\partial u}{\partial x}\frac{\partial \delta u}{\partial x} = 0$$

Integrating by parts :

$$\frac{\partial}{\partial z}\left[(\nabla^{\circ}_{zz} + \mu)\frac{\partial u}{\partial z}\delta u\right] + \frac{\partial}{\partial x}\left[(\lambda + 2\mu)\frac{\partial u}{\partial x}\delta u\right] + \\ - (\nabla^{\circ}_{zz} + \mu)\frac{\partial^2 u}{\partial z^2}\delta u - (\lambda + 2\mu)\frac{\partial^2 u}{\partial x^2}\delta u = 0$$

So, at each point in the volume, we have :

$$(\nabla^{\circ}_{zz} + \mu)\frac{\partial^2 u}{\partial z^2} + (\lambda + 2\mu)\frac{\partial^2 u}{\partial x^2} = 0$$

Loss of ellipticity leads to instability :

$$\nabla^{\circ}_{zz} = -\mu$$

APPENDIX C

Finite elements meshes with 3 different initial fibers misalignment distributions.

Case 1 (reference) :

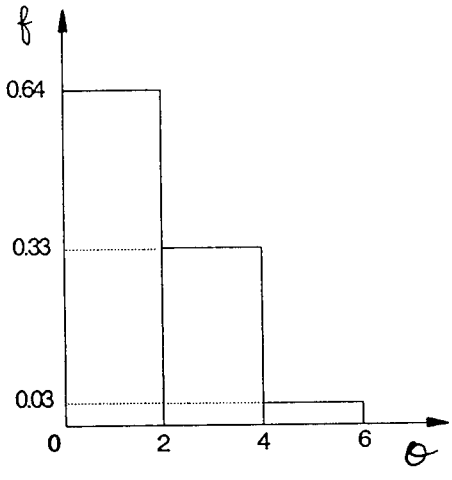

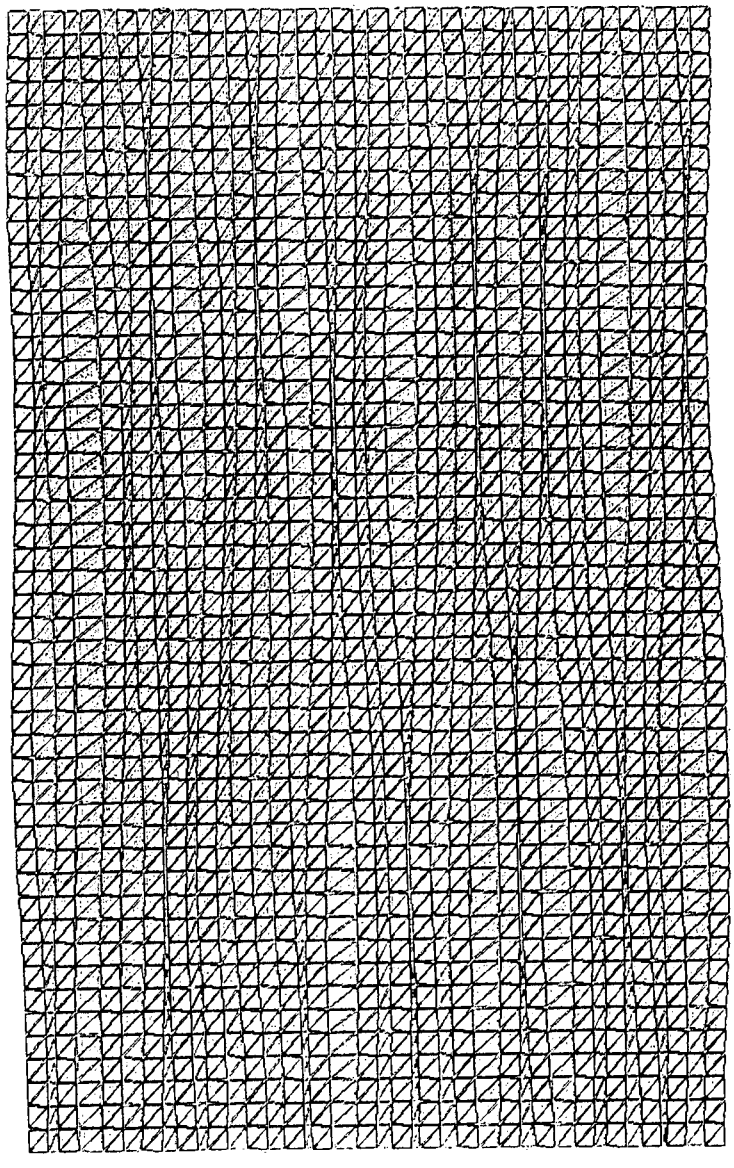

APPENDIX C

Case 2 :

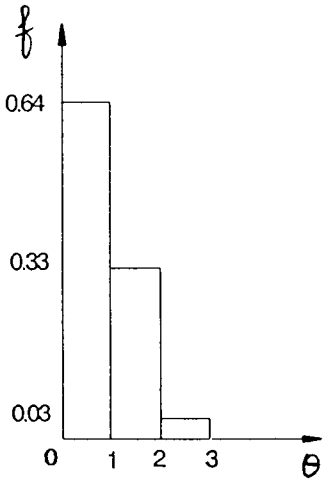

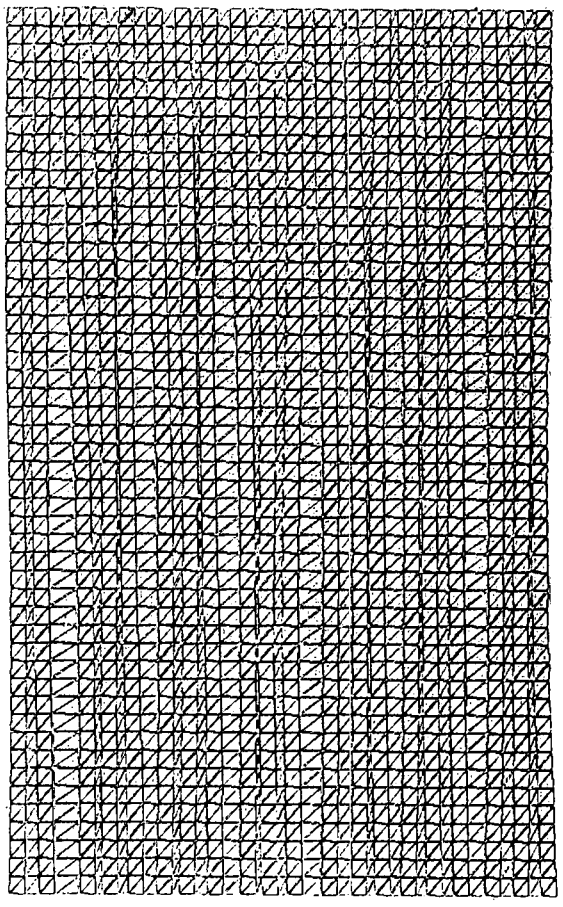

Case 3 :

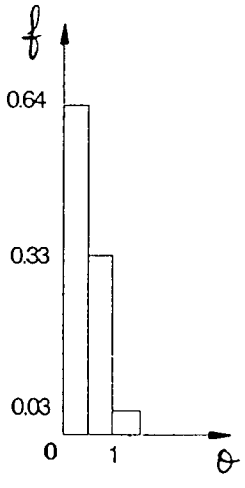

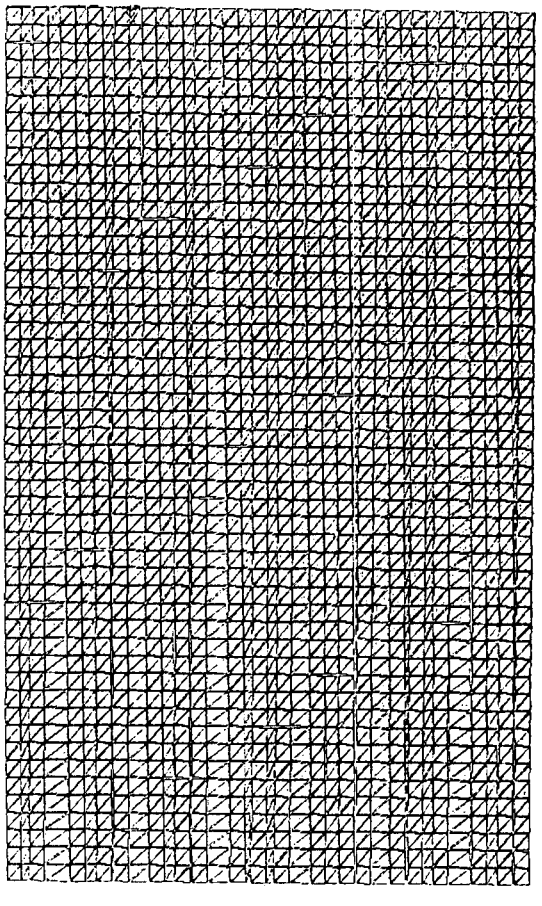

APPENDIX D

Experimental shear stress-strain behavior of industrialized composite resins.

NARMCO 5208 :

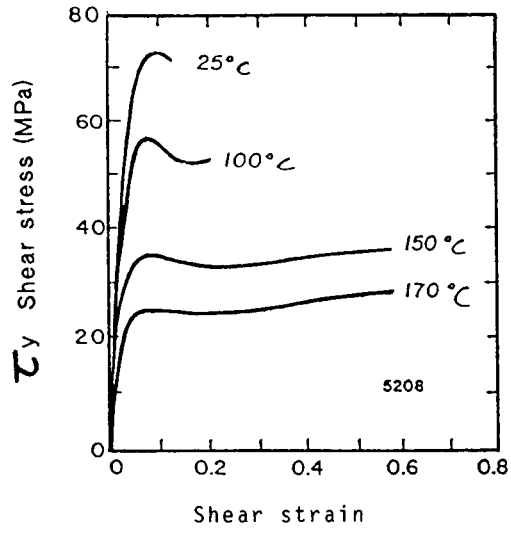

NARMCO 5245 :

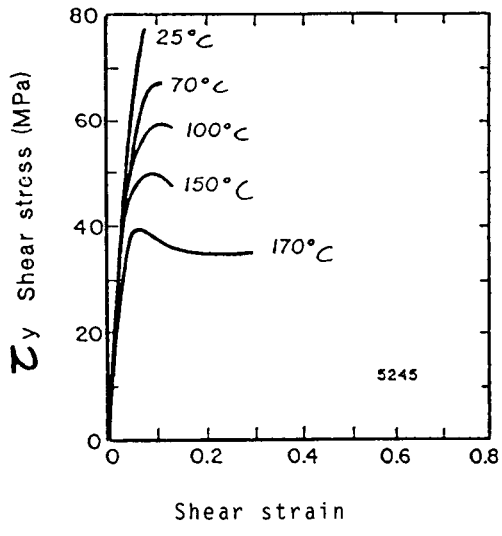

CIBA GEIGY 914 :

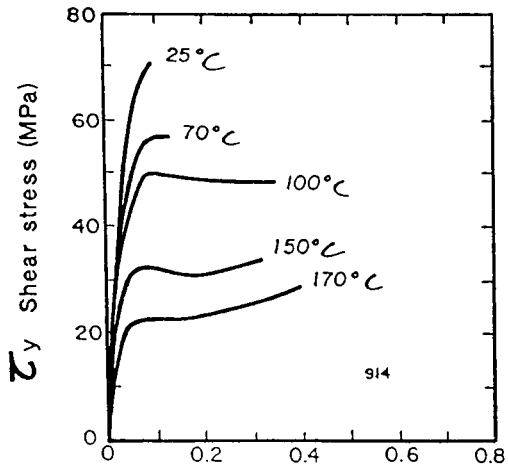

Datas from : Dr Favre, ONERA (F)
Dr G'Sell, Ecole des Mines de Nancy (F).

APPENDIX E

Relationship between the shear yielding of pure resin (τ_y) and the composite interlaminar shear strength (τ_{SBSS}).

$$\tau_{SBSS} = \tau_y + 25 \text{ (in MPa)}$$

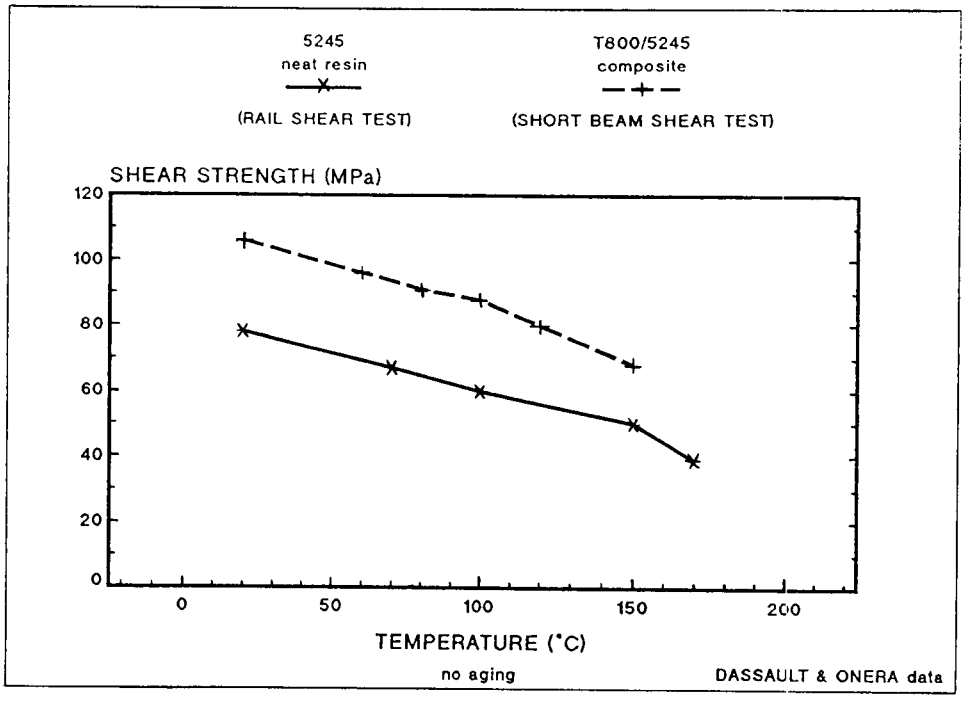

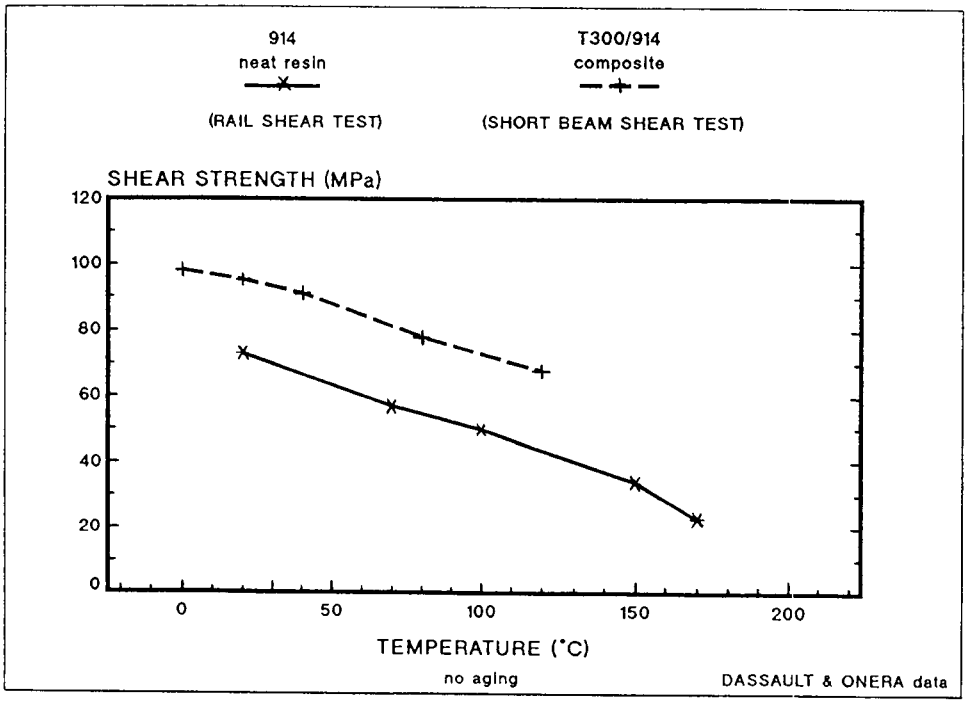

CFRP STIFFENED PANELS UNDER COMPRESSION

A. Bucci
U. Mercurio
Engr. Dept. for Advanced Composite Structures
ALENIA
Zona ASI Incoronata
71100 Foggia - ITALY

SUMMARY

The purpose was to experimentally demonstrate the validity of the conceptual design of a CFRP stiffened panel suitable for application in the unpressurised after fuselage of a middle size aircraft. Both the theoretical and experimental behaviour has been analysed taking into account the effect of:

- Different Materials
- Curvature
- Barely Visible Impact Damage
- Static and Fatigue Loads

Composite materials with stiff fibers of last generation coupled with toughened thermosetting resin system were used.

1. INTRODUCTION

The topics discussed in this paper are part of the work performed at ALENIA Company as part of the Cooperative Technology Development Program on Advanced Composites between Douglas Aircraft Company and ALENIA. One of main objectives of this Cooperation Program was to develop new manufacturing technologies and to study structural solutions adequate for the unpressurized AFT Fuselage of a medium sized transport aircraft.

The paper will deal with the behaviour under compression loads of stiffened panel selected like typical one for AFT Fuselage.
After an investigation between several types of stiffeners to be used for the typical panel, comparing manufacturing costs, weight - savings and structural risks characteristics the bead stiffener was chosen producing the better compromise.

In this case a design no buckled at ultimate load was preferred because the methods to predict delaminations after panel buckling are up to now little reliable.
Finally the configuration shown in Fig. 1 was defined; it consists of a cocured bead stiffened panel designed no buckling up to ultimate load.
At this point the principal target was to investigate its buckling behaviour under compression loads and at the same time to verify the theoretical buckling prediction obtained by a specific code called "BEADBUCK" developed in Douglas. This was realized through a tests program on flat and curved panels subjected to both static and fatigue loading.Some panels were damaged by impacts in such way to have barely visible damages in order to verify their influence on buckling threshold, in accordance with the certification requirements which want a composite structure to withstand ultimate loads in presence of not - visible impact damages.

2. TEST ARTICLE DESCRIPTION

Two panel configurations were tested, they have the same characteristics except that one is flat and the other is curved. In Fig. 2 are shown some sketches of panels.They are constituted by skin, 5 beads cocured with skin in the same cure cycle and two frames sections shaped Z connected to skin by shear ties. The junction frame/shear tie and shear tie/skin is obtained by hy locks.
The two frames sections are provided to generate a stabilizing effect on longerons as much as is realistically possible. In order to allow a realistic comparison between theoretical and experimental results, the test articles height was defined to have instability at the same load calculated in the analysis of fuselage compression panels using an end fixity coefficient equal 2.0. The compression load was applied by potted end surfaces to avoid incoming effects. Alluminum frame (6061 Alloy) surrounded the potting block.

3. MATERIALS

Two CFRP materials, in form both tape and fabric belonging to the last generation of composite materials were used.Both materials were characterized by stiff fibers and toughened thermosetting resin system.
The Tab. 1 shows in detail the types of material.

4. TESTS

The Tab. 2 shows the tests performed taking into account that for each type

of test 1 panel was proved.

STATIC TESTS

The purpose of the static test plan was to demonstrate:

1) The panel is able to withstand the required design ultimade load.
2) The curvature effect respect to flat panels.
3) The reliability of the theoretical analysis.
4) The panel withstands the static ultimate load in presence of barely visible impact damage (BVID).
5) the panel withstands the design limit load in presence of visible impact damage (VID).

At this purpose the principal target was to determine the buckling load of the panels under compression loads.
The load was determined analysing the straingage plots (see fig. 3-4-5-6-7-8) obtained by measures performed in the locations given in Fig. 9.

DAMAGES

The damage tolerance features of the bead stiffened panels were also investigated by compression static and fatigue tests on damaged panels by impact.

Both the barely visible impact damage (BVID) and the visible one (VID) were considered,assuming that the BVID were correspondent to damage with an indentation between 0.3 and 0.5 mm while VID is higher than 0.5 mm.

Stress analysis considerations have singled out like critical location for the damage (in terms of strength after impact) the outer skin area correspondent to bead flange/skin bonding (see Fig. 9).

At this purpose a preliminary investigation, on already failed panels, was performed to define the opportune impact energy.
The impact energies found are shown by Tab. 3. These energies were used to impact the panels to test in presence of damages.
The impactor head had 12.7 mm diameter hemispherical steel tip.

FATIGUE TEST

The purpose of compression fatigue test was to demonstrate the fatigue damage tolerance of this specific design in presence of BVID.

The spectrum applied is given in Fig.10. It represents about 2 lifetimes. Each 10 load blocks the panel was loaded up to static limit load to read the strains in order to control possible variations of panel global stiffnes.
Thus the fatigue test was very heavy because 4 static limit loads were applied in addition to the fatigue cycles during test.
At the end of fatigue test the panel was tested in static way to evaluate the residual static strength.

5. RESULTS

- COMPRESSION STATIC TESTS

The results are given in Tab. 4. They are three different types of results:

Compression Initial Buckling Loads - Theoretical Results:

They have been obtained using the "beadbuck" code. This program calculates the general and local critical buckling loads of a non-anisotropic flat "bead" stiffened panel with four sides simply-supported. The effects of the bead stiffener are included in this analysis.
The geometry of the panel used as input to the program is given in Fig.11.

Compression Initial Buckling Loads - Experimental Results:

They have been evaluated by straingage plots. The buckling load was always recognized at that load where first a straingage loses the linear behaviour (initial buckling load).
This analysis was been also supported by vision of the tests.

Compression Ultimate Failure Load:

They are the loads at which the panels obtained catastrophic failure.

- COMPRESSION FATIGUE TEST

The results given in Tab. 5 are the strain measures performed each 10 load blocks appling the design limit load in static way.
The Fig.12 shows the results of residual static strenght test performed at the end of fatigue test.

6. DISCUSSION

STATIC TESTS

- Buckling load

The definition of the buckling load for all panels was characterized from the same straingages,those located on the portion of outside skin under beads (N.2-5-6 for B-C-D-E-F panels and 7-6-10 for A panel).
In this way it seems that the buckling load of this panel type coincides with the buckling load of the skin strips under the beads. The behaviour was confirmed from evidence of the tests because bumps on the skin under beads were seen during the test.
In any case both CIBA curved panels intact (A) and damaged (D) exceeded the required ultimate load Fig.13. Considering that the HERCULES material is stiffer than CIBA one then we can say that the bead stiffened cocured panel is to be able to withstand compression ultimate loads also in BVID condition.

- Damage effect

During the tests of damaged (BVID) panels no creaking has been heard and the results have demonstrated that BVID doesn't influence the buckling load. On the contrary during the test of the visible damaged (VID) panel have been heard a lot of creaking that witnessed increase of the delamination areas.
The CIBA flat damaged panel (C), as it can be seen by Fig.13, exceeded the required limit load, so we can say,since the panel was flat, that a curved panel in presence of VID damage withstands the compression limit load.

- Theoretical analysis

Another purpose of this test plan was to check the theoretical program used to evaluate the buckling load of composite flat bead stiffened panel (beadbuck).
The results obtained are very close to the experimental values.
The outputs of code given in Tab. 6-7 show that the "skin" (skin between beads) buckling load is close but lower than "base" (skin under beads) buckling load. The experimental evidence has confirmed these results; infact the straingages on the skin under beads and those located back to back skin/bead flange signaled buckling for loads almost coincident. However the code has demonstrated to be reliable to calculate the buckling load for this panel type.

- Curvature effect

Since the tests demonstrated that the BVID damage doesn't influence the buckling load, then comparing the buckling loads of the two CIBA curved panels (A and D) with the CIBA flat intact panel(B), the curvature effect can be estimated equal to
+10%.

- Different materials

The results given in Tab. 4 show clearly the Hercules material is more stiff than CIBA one.The reason is in the different thickness (tows with higher number of filaments) of fabric plies used. Infact for the theoretical analysis the same elastic properties for the two materials have been used but different thickness for fabric plies and the results have been close to the experimental one.

FATIGUE TEST

The global stiffness of the panel did not change after the fatigue test like the straingage readings in Tab. 5 witness.
The panel showed good damage tolerance features compared to BVID.
The delamination widths stopped after an initial growth, thus the panel showed the expected design features after fatigue test: to be no buckling at ultimate load.

7. CONCLUSIONS

Different Composite panels flat and curved have been tested in compression to check a new configuration (bead stiffened cocured panel) for a typical panel to use in an aft fuselage of a medium sized transport aircraft.
The conclusion are summarized in the following:

The curvature effect increases the buckling load of the flat panel approximately +10%.

The results obtained demonstrate the reliability of the theoretical buckling analysis (beadbuck code) for the bead stiffened panels.

The damaged panels tests have shown no effect of the (BVID) barely visible impact damage on the ultimate buckling load and that the (VID) visible impact damage decreases the buckling load of panel but this is still able to withstand the limit load.

There is not fatigue damage also in presence of BVID.After fatigue test (2 lifetimes) the bead stiffened panel keeps the initial global stiffness and the static strength capability.

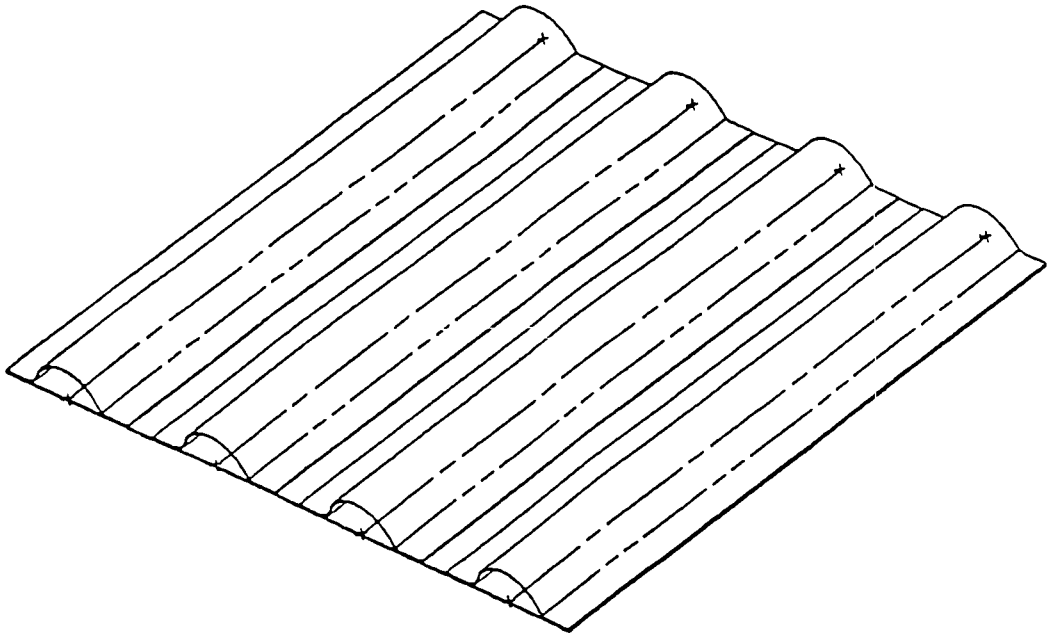

Fig.1 BEAD STIFFENED COCURED PANEL

SUPPLIER	FIBER	MATRIX	NOMINAL CURED PLY THICKNESS (mm)
CIBA	T800H	FIBREDUX 6376 C	0.147
HERCULES	IM7	8551-7	"

TAPE

SUPPLIER	FIBER	MATRIX	NOMINAL CURED PLY THICKNESS (mm)
CIBA	T800H 6K-5H	FIBREDUX 6376C-E2743	0.315
HERCULES	IM7G 12K-5H	MAGNAMITE XSW370-SH/X8551-7	0.356

FABRIC

TAB.1 COMPOSITE MATERIALS

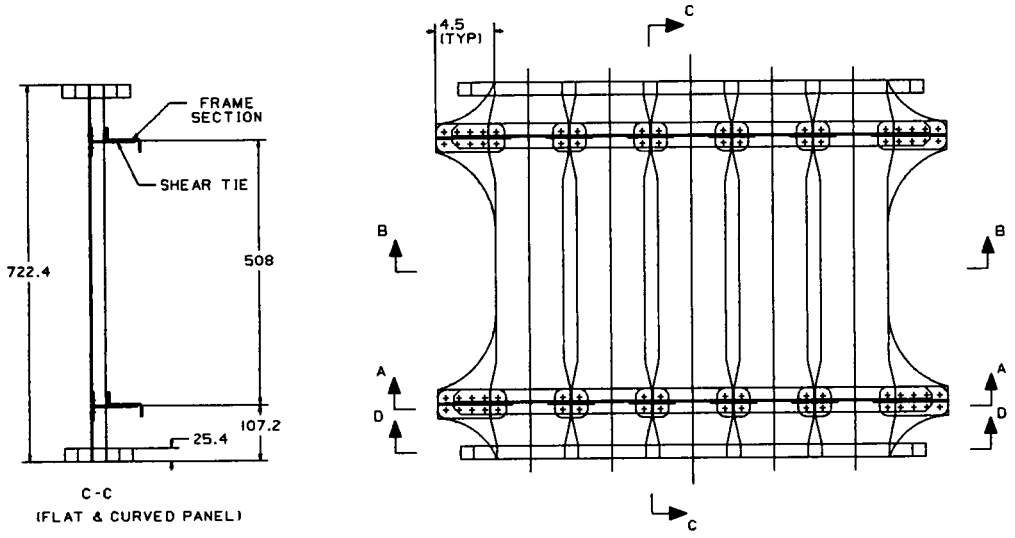

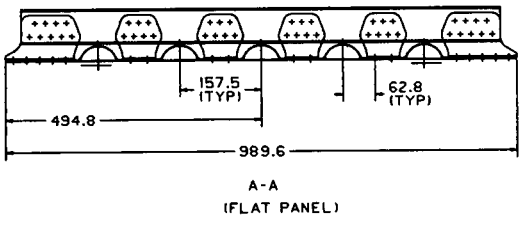

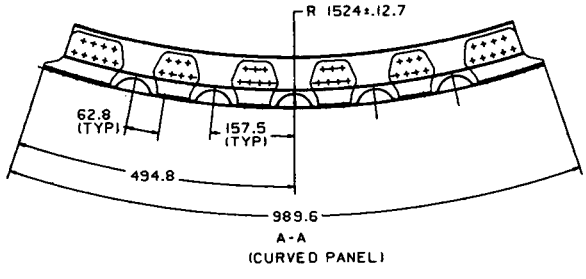

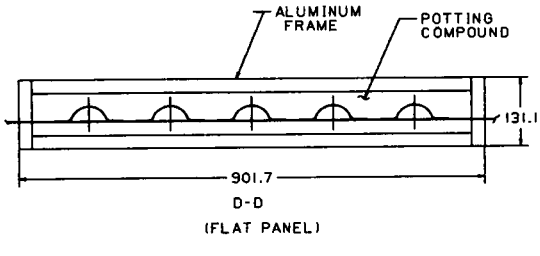

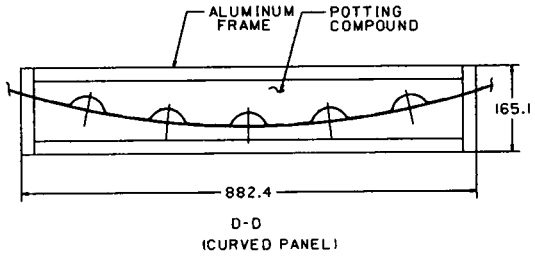

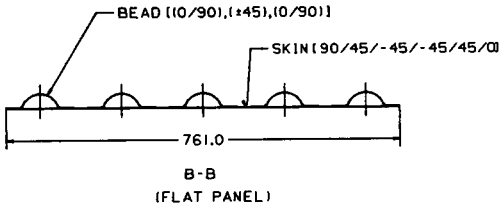

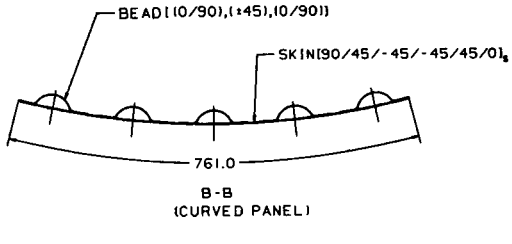

FIG. 2 TEST ARTICLES DESCRIPTION

PANELS CODE	MATERIAL	GEOMETRY		COMPR. LOADS		DAMAGE		INTACT
		FLAT	CURVED	STATIC	FATIGUE	BVID	VID	
A	CIBA		X	X				X
B	CIBA	X		X				X
C	CIBA	X		X			X	
D	CIBA		X	X		X		
E	HERCULES	X		X				X
F	HERCULES	X		X		X		
G	CIBA		X		X	X		

Tab.2 PANELS TESTED UNDER COMPRESSION LOAD

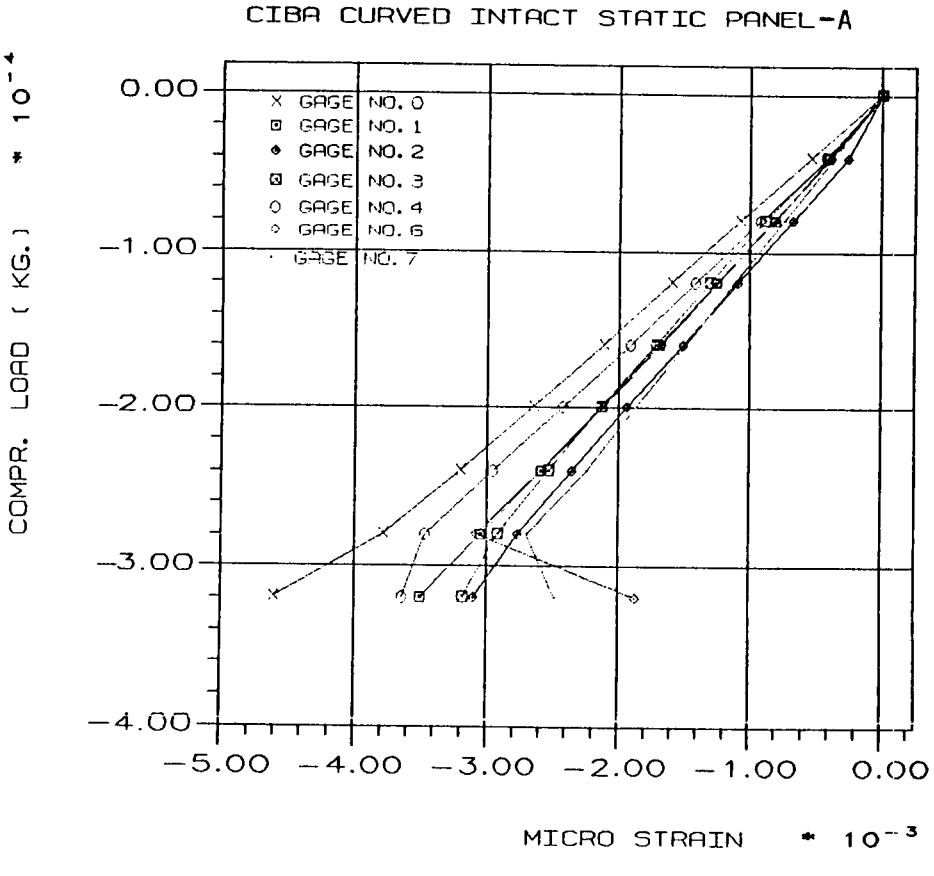

Fig.3

CIBA FLAT INTACT STATIC PANEL-B

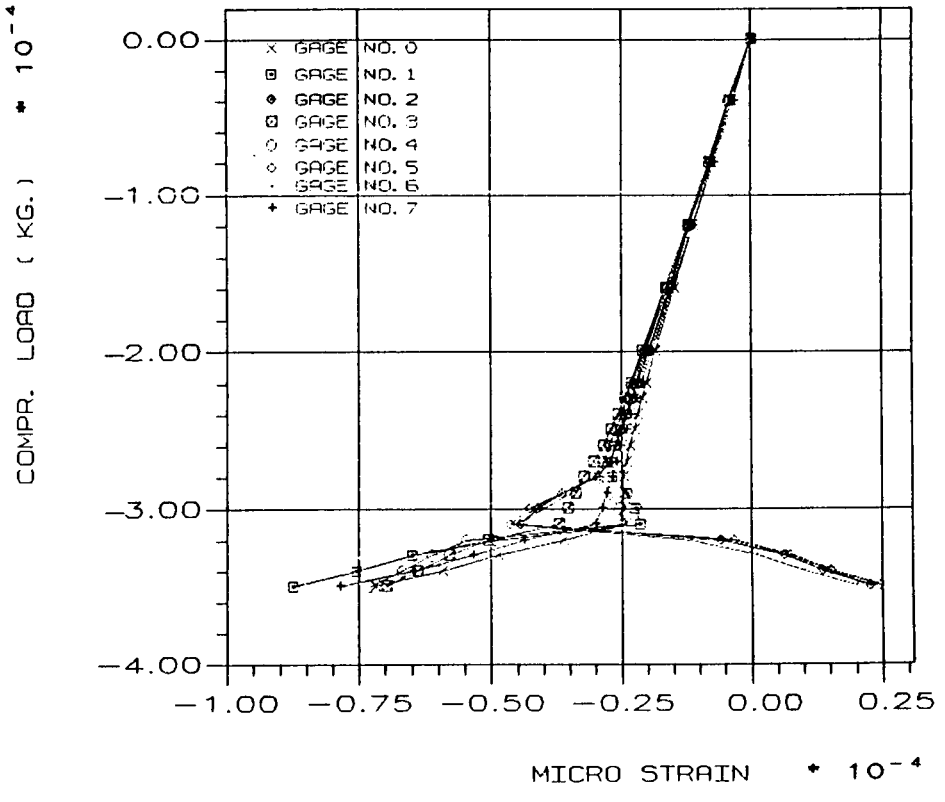

Fig.4

CIBA FLAT DAMAGED STATIC PANEL-C

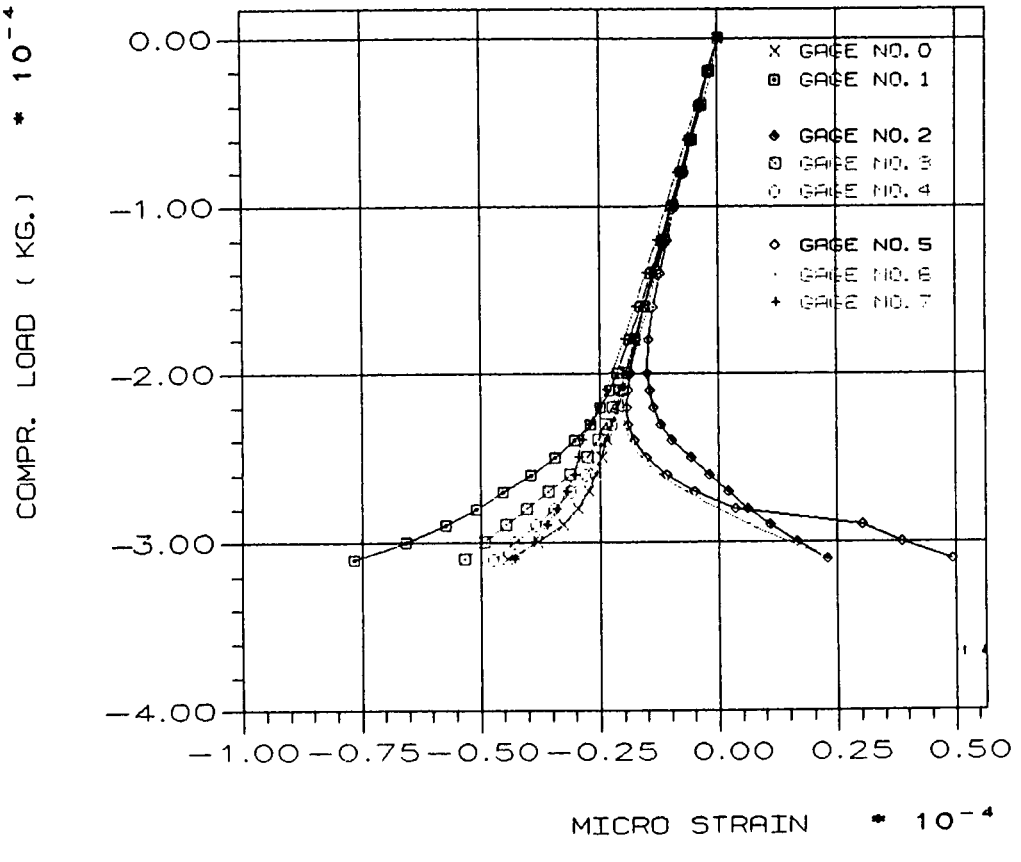

Fig.5

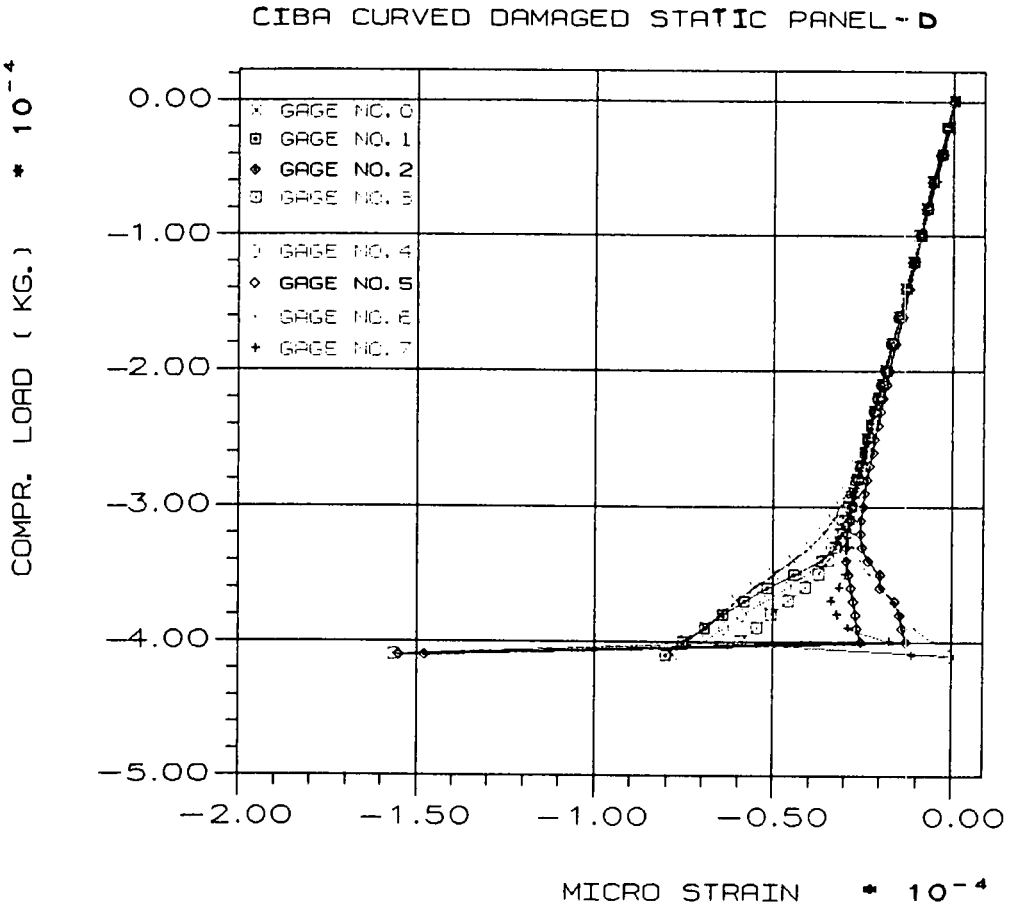

Fig.6

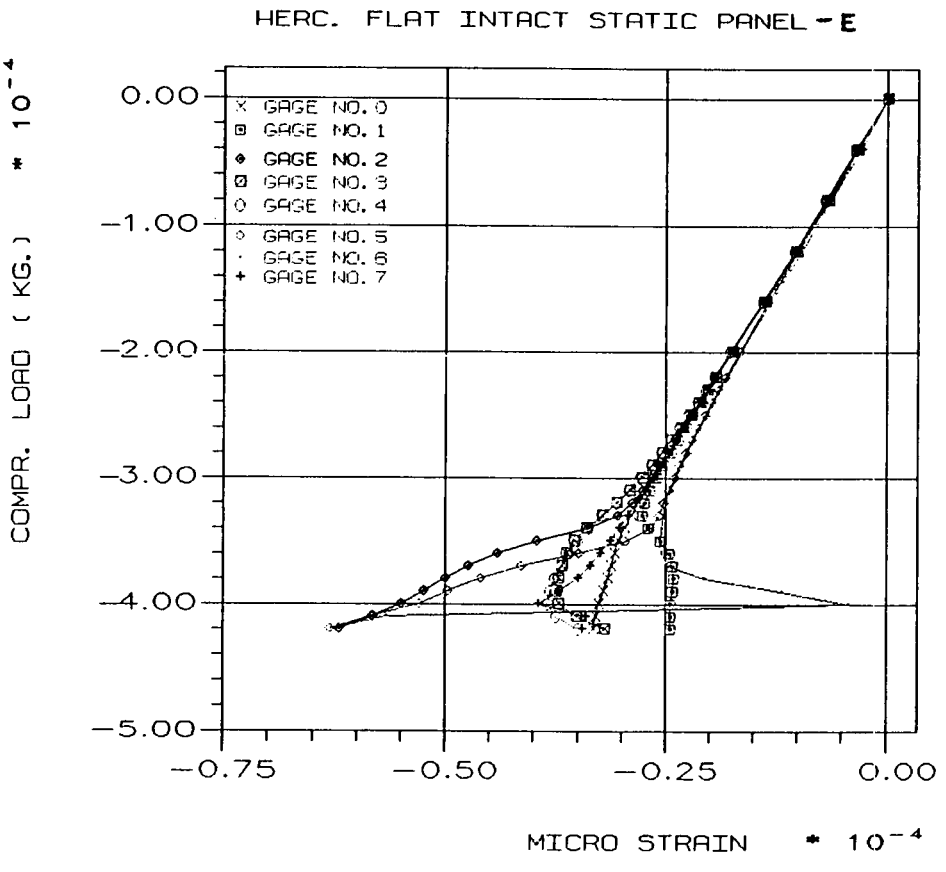

Fig.7

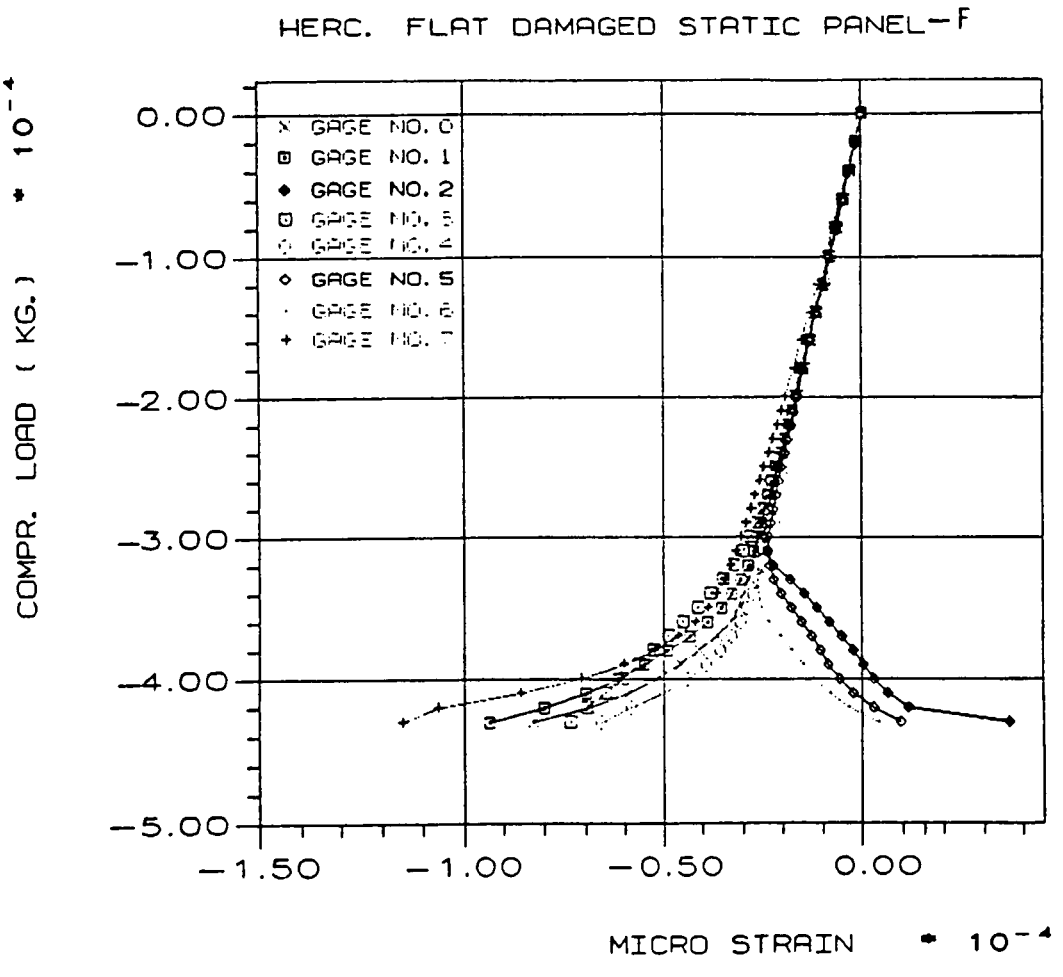

Fig. 8

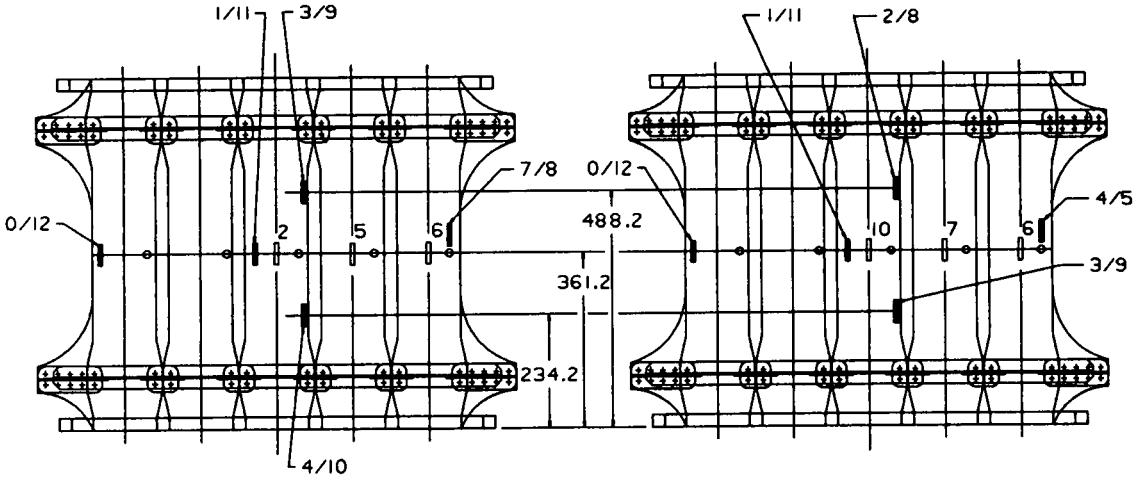

FLAT AND DAMAGED CURVED PANELS

CURVED UNDAMAGED PANEL

▯ SINGLE STRAIN GAUGE (APPLIED ON EXTERNAL SKIN SURFACE ONLY)

▮ TWO STRAIN GAUGES (APPLIED BACK TO BACK ON BOTH THE SKIN SURFACE)

° IMPACT POINT LOCATIONS ON EXTERNAL SKIN SURFACES

FIG.9 STRAINGAUGES AND IMPACTS LOCATION

PANEL TYPE	MATERIAL	DAMAGE TYPE	IMPACT ENERGY (JOULE)
CURVED CIBA	T800/6376C	BVID	19
FLAT CIBA	T800/6376C	VID	24
FLAT HERCULES	IM7/8551-7	BVID	24

Tab.3 IMPACT ENERGY USED ON PANELS

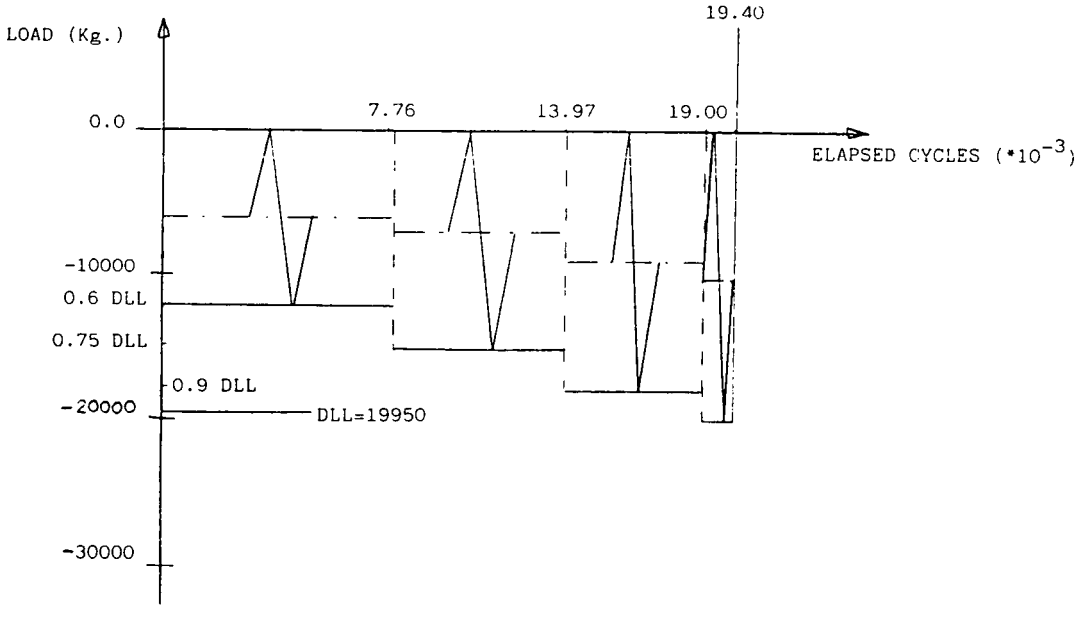

The above sequence was repeated 40 times to cover two lifetimes,approximately.
The test was performed with: R = 0.05

Test Frequency = 2.5 Hz.

DLL = Design Limit Load

Fig.10 LOAD SPECTRUM FOR FATIGUE TEST

TYPE OF PANEL	COMPRESSION INITIAL BUCKLING LOAD				COMPRESSION ULT. FAILURE LOAD		
	INTACT PANEL		DAMAGED PANEL		INTACT PANEL	DAMAGED PANEL	
	THEORE. LOAD	EXPERI. LOAD	BVID EXPERI. LOAD	VID EXPERI. LOAD	EXPERI. LOAD	BVID EXPERI. LOAD	VID EXPERI. LOAD
CURVED CIBA	----	(A) 30000	(D) 31050	----	(A) 36700	(D) 41000	----
FLAT CIBA	(B) 28350	(B) 28000	----	(C) 22000	(B) 35600	----	(C) 31800
FLAT HERCUL.	(E) 30850	(E) 33000	(F) 32000	----	(E) 43000	(F) 43000	----

Note: the ( ) are the panel codes (see Tab.2).

Tab. 4 COMPRESSION STATIC TEST RESULTS

HERCULES

TAPE t_{ply} = 0.147 mm

CLOTH t_{ply} = 0.356 mm

CIBA

TAPE t_{ply} = 0.147 mm

CLOTH t_{ply} = 0.315 mm

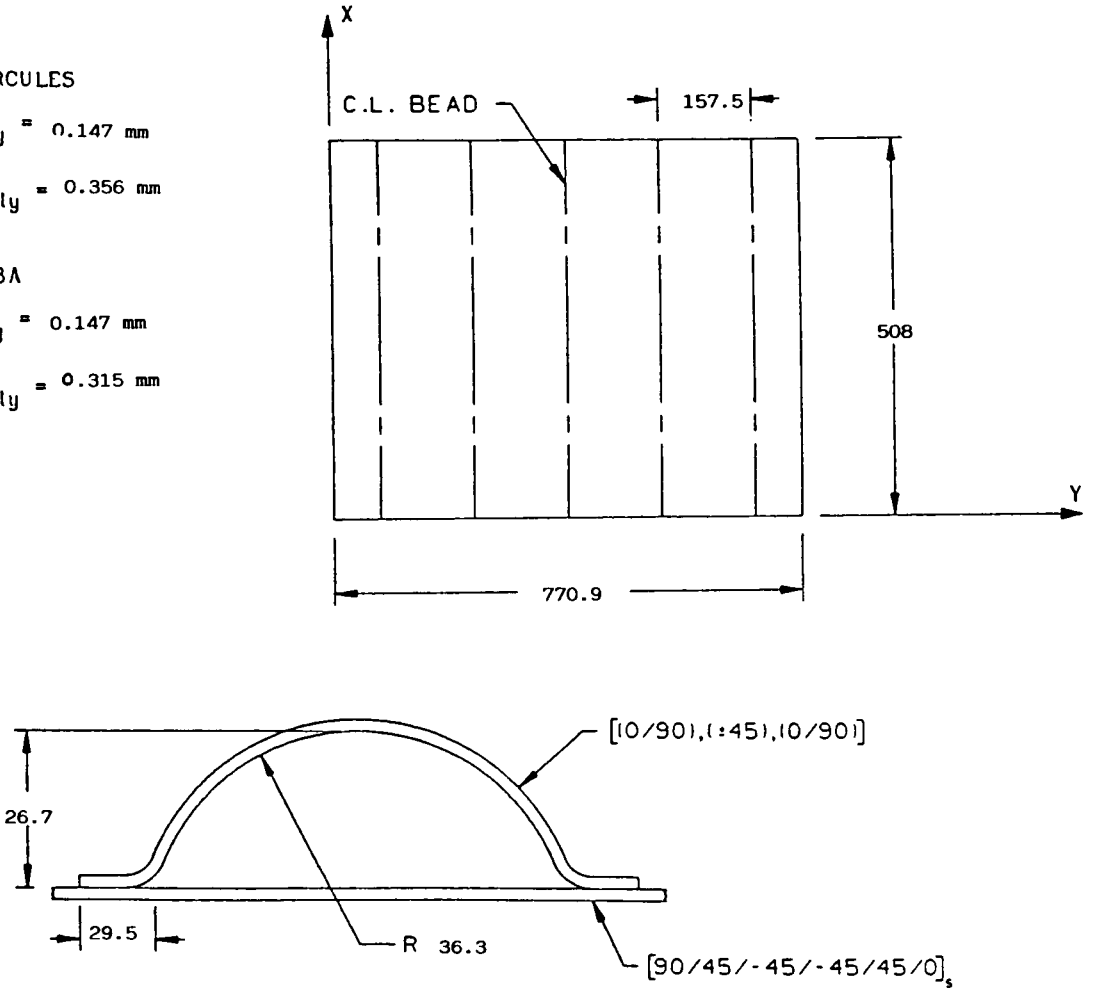

Fig.11 INPUT GEOMETRY TO BEADBUCK CODE

- STRAIN MEASUREMENTS (MICROSTRAIN) -					
STRAINGAGE N°	Before of test (-19960 Kg)	After 10 blocks (- 20000 Kg)	After 20 blocks (- 20000 Kg)	After 30 blocks (- 19950 Kg)	After 40 blocks (- 20000 Kg)
0	- 1970	- 1969	- 1989	- 1967	- 1848
1	- 2007	- 2018	- 2010	- 1986	- 2027
2	- 1957	- 1975	- 1973	- 1941	- 1980
3	- 1993	- 2011	- 2021	- 2006	- 2025
5	- 1968	- 1986	- 1965	- 1942	- 1996
6	- 2086	- 2099	- 2092	- 2106	- 2103
7	- 2017	- 2036	- 2024	- 2043	- 2026
8	- 1963	- 1952	- 1939	- 1964	- 1941
9	- 1939	- 1940	- 1957	- 1947	- 1964
10	- 2053	- 2047	- 2048	- 2032	- 2076
11	- 2074	- 2066	- 2079	- 2140	- 2096
12	- 1927	- 1925	- 1949	- 1930	- 1903

Tab.5 STRAIN MEASUREMENTS DURING FATIGUE TEST

(POISSON'S EXPANSION ALLOWED)

LOCAL AND GENERAL BUCKLING NORMALIZED TO COLUMN LOAD			SHEAR BUCKLING NORMALIZED TO COLUMN LOAD		
BASE	Nx =	39.95 Kg/mm	BASE	Nxy =	49.48 Kg/mm
SKIN	Nx =	37.25 Kg/mm	SKIN	Nxy =	35.09 Kg/mm
BEAD	Nx =	95.34 Kg/mm	GENERAL	Nxy =	149.95 Kg/mm
GENERAL	Nx =	54.80 Kg/mm			

STRAIN = 2880. MICRO mm/mm AT Nx = 37.25 Kg/mm

Tab.6 CIBA PANEL - BEADBUCK CODE OUTPUT

(POISSON'S EXPANSION ALLOWED)

LOCAL AND GENERAL BUCKLING NORMALIZED TO COLUMN LOAD			SHEAR BUCKLING NORMALIZED TO COLUMN LOAD		
BASE	Nx =	41.74 Kg/mm	BASE	Nxy =	50.85 Kg/mm
SKIN	Nx =	40.02 Kg/mm	SKIN	Nxy =	35.98 Kg/mm
BEAD	Nx =	113.34 Kg/mm	GENERAL	Nxy =	168.98 Kg/mm
GENERAL	Nx =	60.45 Kg/mm			

STRAIN = 2952. MICRO mm/mm AT Nx = 40.02 Kg/mm

Tab.7 HERCULES PANEL - BEADBUCK CODE OUTPUT

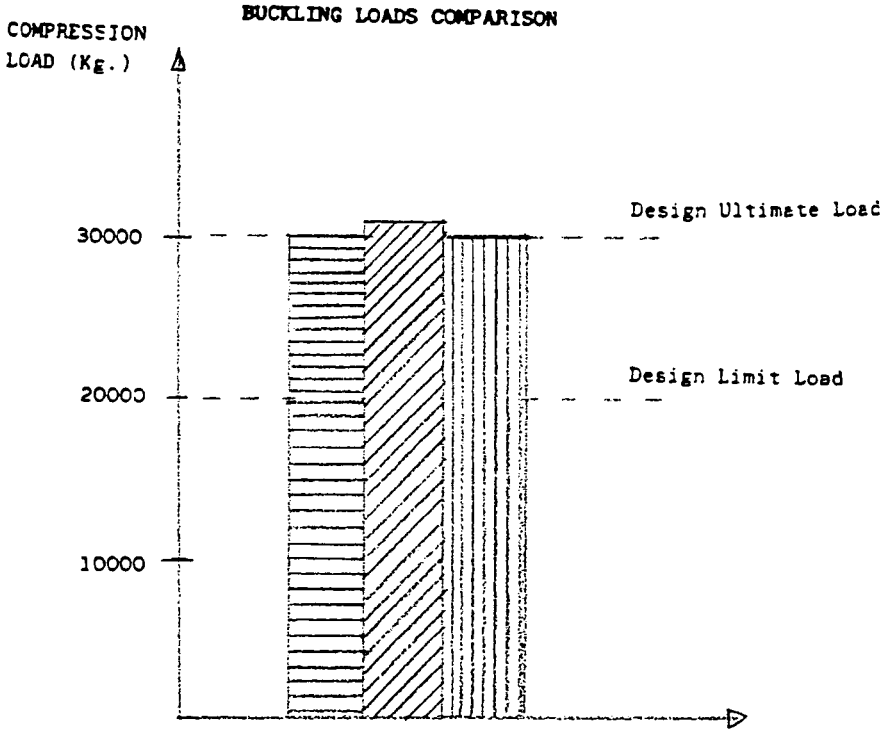

CURVED DAMAGED PANEL - COMPRESSION STATIC TEST AFTER FATIGUE

CURVED INTACT PANEL - COMPRESSION STATIC TEST

CURVED DAMAGED PANEL - COMPRESSION STATIC TEST

Fig.12 RESIDUAL STRENGTH AFTER FATIGUE TEST

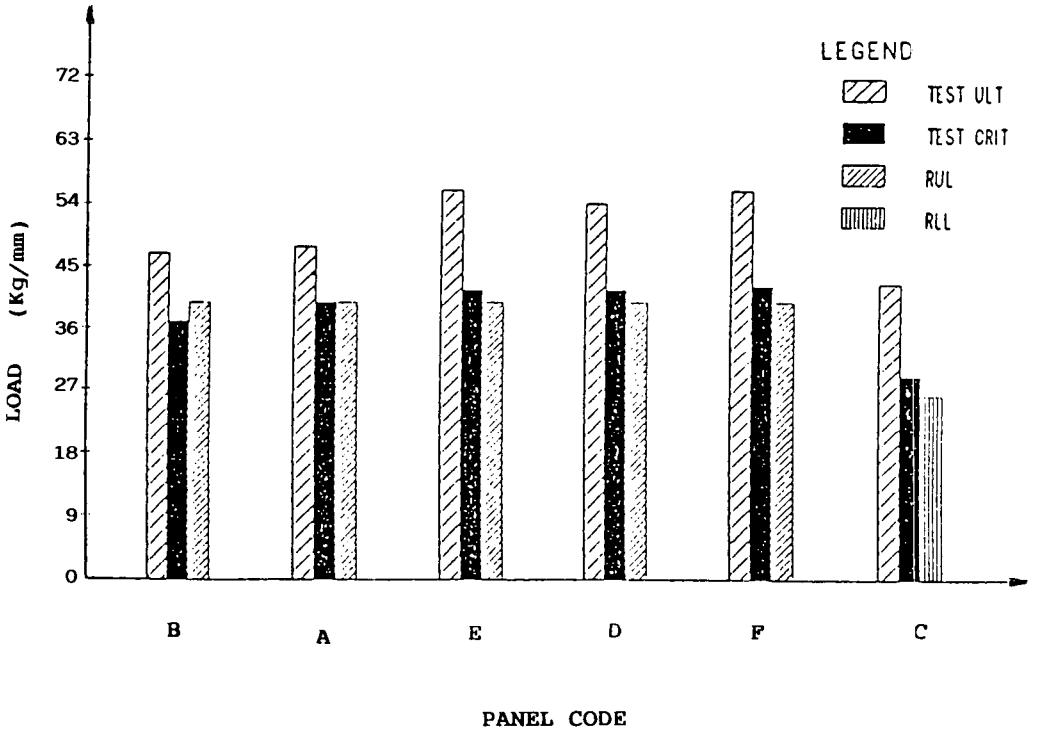

Note: RUL = Required Ultimate load
RLL = Required Limit Load

Fig.13 COMPARISON BETWEEN DESIGN REQUIREMENTS AND TESTS RESULTS

AN OVERVIEW OF CONCERNS RELATING TO FLUID EFFECTS ON COMPOSITES

GEOFFREY A WRIGHT

Materials and Development Department

BRITISH AEROSPACE

Warton, Preston, Lancashire, UK

SUMMARY

The effect of the interaction of fluids and the environment on composite fibre/resin systems plays an important role in determining the suitability and the design values used for these materials. This paper provides a brief overview of the questions posed by the designer and the materials engineer and looks at the test methodologies employed to determine answers to these questions. The advantages for standardisation of these fluid/environment exposure regimes, together with agreement on the range and extent of the follow-up test methods, is examined.

1. INTRODUCTION

Material and Structural Engineers are concerned with the interaction of fluids and the environment with aerospace materials as a necessary part of their optimisation and selection process. The increasing use of organic materials for primary structural applications has accelerated the necessity for evaluation and understanding of these effects.

The interaction between fluids and polymeric materials is extremely complex and has been the subject of many thousands of scientific papers with many theories put forward to explain the mechanisms at work.

From the aerospace material engineering and design view the answers to a number of questions are sought. These relate to:-

o What effects do each of the fluids have on the polymer?

o What effect do they play on the thermal stability of the polymer?

o What are the long term effects of fluid contaminants?

o What effect do thermal spikes and stress have on the fluid/polymer properties?

o Are the fluid effects reversible?

o How, if possible, can we alleviate these effects?

Following on from these, further questions relating to the means of assessing these effects need to be answered and the need for agreement and standardisation of test procedures requires to be achieved. In particular the following points need to be addressed:-

o Specimen configuration.

o Fluid selections.

o Exposure conditions.

o Duration of exposure.

o Test measurement/assessment criteria.

At the end of the day, we must be in a position to translate the above results into Design data and have the ability to predict the implications of supplementary protective treatments.

2. MATERIAL EFFECTS

Aside from dimensional changes which occur when the fluid is absorbed, other effects can also be observed. Typical of these are:-

2.1 Plasticisation

This has been demonstrated to result in a reduction in the Glass Transition value (Tg) of a composite by as much as 50°C compared to the Tg of the dry composite. Other composite properties which can be affected are yield stress and modulus, ductility and dielectric properties.

2.2 Microcracking

Repeated absorption of fluids followed by drying can result in microcracking and other types of mechanical degradation.

2.3 Fibre/Resin Interface Effects

Absorption of fluids can attack the fibre/resin interface which in some cases can be irreversibly weakened. The interface can also offer a primary route for the penetration of fluids into continuous fibre composite materials.

2.4 Polymer Degradation

The interaction of some fluids can cause hydrolysis of, or chemical reaction with, the polymer. This will result in the degradation of the composite properties. An example of this is the effect of alkaline fluids on imide and BMI systems where the resin system is irreversibly degraded.

3. AEROSPACE FLUIDS

Having looked at some of the effects that fluids can impart to composite materials, the designer and the materials specialist must establish the integrity of a selected material with the various fluids with which it will come into contact during its service life. This is not so clear cut a procedure as the problem may seem. Examination of a typical aircraft design, Eurofighter, indicates that the composite material can come into contact with some 40 plus fluid types which include; fuel, oils, greases, heat transfer fluids, hydraulic fluids and cleaning fluids, not including naturally occurring fluids eg rain, salt spray and biological fluids, and, in the case of military aircraft, warfare fluids, eg gun gases, warfare agents etc.

Further analysis of the types of fluid involved indicate that the majority of these are related to specifications based on the performance of the fluid and not on the chemical constituents of the fluid. To demonstrate the problems that this can engender, I quote an extract from British Standard G100 (Ref 1) which is also being considered for an equivalent AECMA specification.

"Standard test fluids

Test results obtained from a number of sources over a considerable period of time have shown clearly that, in many cases, widely varying results can be obtained when using fluids which are used in service. The practice of specifying fluids based on performance criteria rather than their constituents can mean variations in test results between batches of the fluid obtained from different manufacturers, or even from the same manufacturer.

For this reason this British Standard recommends the use, wherever possible, of 'standard test fluids which are specified by their constituents and contain the chemicals which may be found in commonly used fluids. The chemical constituents of the test fluid are considered to be those which are most likely to affect the performance of the test specimen and can be considered as 'worst case' examples for each particular test fluid group category."

A similar statement also appears in ISO 1817 (Ref 3) thus the problem is well recognised. If we can tie in these standard fluids to represent the actual aerospace fluids used then the airworthiness clearance route can be assured. The grouping of fluid types represented by a test fluid simulating the worst case condition will also result in a reduction in the number of fluids required to be tested.

The drive towards the use of standard test fluids is therefore progressing both within ISO and within AECMA, an European standards organisation (Ref 2).

However, this in itself may not be sufficient to cover all aspects of the Material Engineers and the Designer concerns. Questions still need to be resolved relating to temperature of exposure, duration and the effect of realistic service contaminants of normal fluids eg fuel/water mixtures.

Fig 1 shows the effect of temperature on in-plane shear modulus (a matrix dominated property) of a thermoplastic before and after exposure to JP4 fuel. The large reduction in modulus above 80°C of the fuel soaked specimens is indicative of fluid interaction effects that play an important part in determining the suitability or the design value of a composite material.

On top of all this, the effectiveness of supplementary composite protection schemes, eg paint coatings and sealants need, to be assessed.

The disruptive effect of water on fibre/resin system properties is well documented, thus, one of the principal environments used for evaluation is that of moisture conditioning. To achieve moisture uptake within the composite a wide variety of accelerated conditions have been employed by different workers.

Figure 2 indicates the response rate for moisture uptake versus time for two different exposure conditions. Obviously temperature can influence the uptake rate for moisture, Ciba 914 resin is increased by a factor of 5 simply by raising the temperature from 20°C to 60°C, however a limiting factor on this is the need to adopt regimes which maintain the absorption mechanism (Fickian behaviour) to ensure that unrepresentative degradation mechanisms do not occur (Ref 4 and 5). Fig3 indicates the moisture uptake response rate for various composite laminate lay-up configurations and Fig 4 shows the different uptake rates for different composite systems. These two figures go to show that exposure regimes based upon fixed time durations, without pre-knowledge of the moisture uptake behaviour of the system under test, can lead to misleading results if the exposure duration is too conservative. A methodology has therefore been developed whereby environmental testing within practical timescales can be performed (Ref6). Although this is primarily directed towards structural testing the procedure is equally valid for materials testing performance. The subject of thermal spiking, both to elevated and sub-ambient temperatures, is also addressed at Ref 6.

Following the fluid exposure, the selection of the range and types of follow-up tests, to demonstrate the fluid effect, needs consideration. Generally these have centred around interlaminar shear strength,

tensile strength compressive strength and impact tests. With the development of more sensitive thermal analysis instrumentation coupled with computer based data analysis methods an additional range of tools is available to aid the engineer in the evaluation of fluid effects. As an example, a test method based upon Thermo Gravimetric Analysis (TGA) coupled with Evolved Gas Analysis using Mass Spectrometry has been used to study moisture effects on a BMI/Epoxy resin composite (Ref 7).

Examination of the environmental exposure regimes used by a wide range of aerospace and composite manufactures, and the subsequent range and type of tests employed to assess the fluid effects indicate that there is still a need for some standardisation of these regimes if we are to achieve comparability of techniques.

4. CONCLUSION

There are compelling reasons for the materials engineer to evaluate fluid interactions with composite materials. Examination of design reduction factors for a typical intermediate modulus, toughened resin system (Fig 5) indicates the importance of environmental effects, especially on compressive strength aspects.

Agreement on the selection and standardisation of appropriate test methodologies to evaluate the environmental effects by aerospace manufactures will be beneficial both to the aerospace companies and the composite manufacturer. The result of such an agreement would be to:-

(i) Reduce costs of testing with differing regimes.

(ii) Reduce the range of fluids to evaluate.

(iii) Allow better comparability of test results emanating from differing sources, and

(iv) Allow better comparability of data arising from different resin systems.

REFERENCES

1. British Standard G100 Part 2 Section 3.12 1991. General requirements for equipment used on aircraft - Fluid Contamination.

2. PrEN2379 - Aerospace Series, Fluids for Assessment of Non-Metallic Materials.

3. ISO 1817 Rubber, Vulcanized -Effect of Liquids.

4. J.M.Whitney, C.E.Browning, Some Anomalies associated with Moisture Diffusion in Epoxy Matrix Composite Materials ASTM STP 658.

5. T.A.Collings, S.M.Copley, On the accelerated ageing of CFRP. Composites Vol. 14 No. 3 July 1983.

6. Environmental Structural Testing RAE Report 88063 September 1988.

7. S.Lane Unpublished work.

FLUID INTERACTIONS

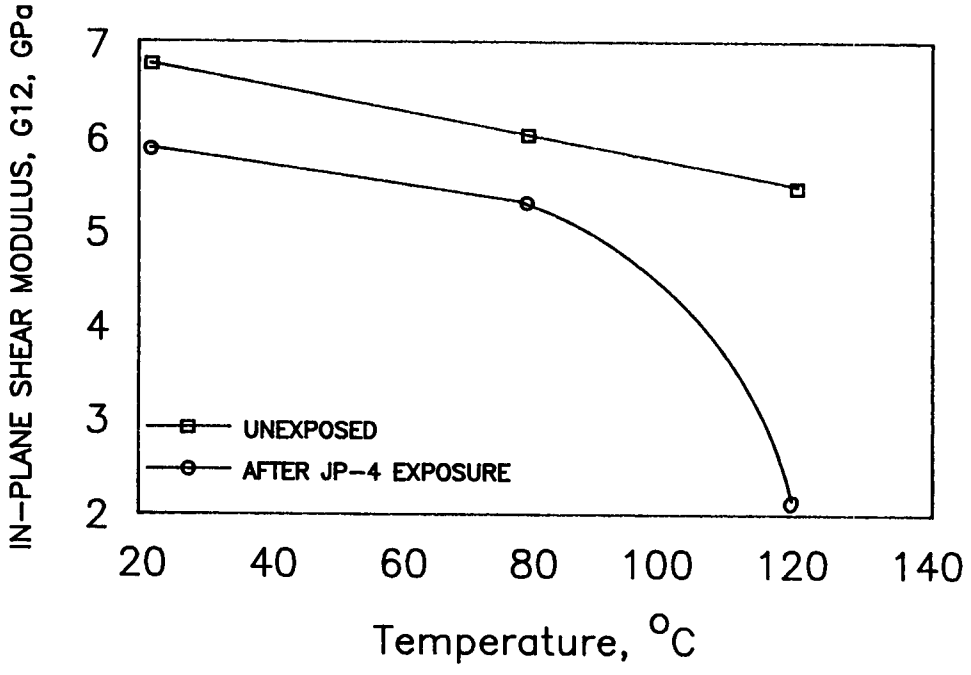

Figure 1

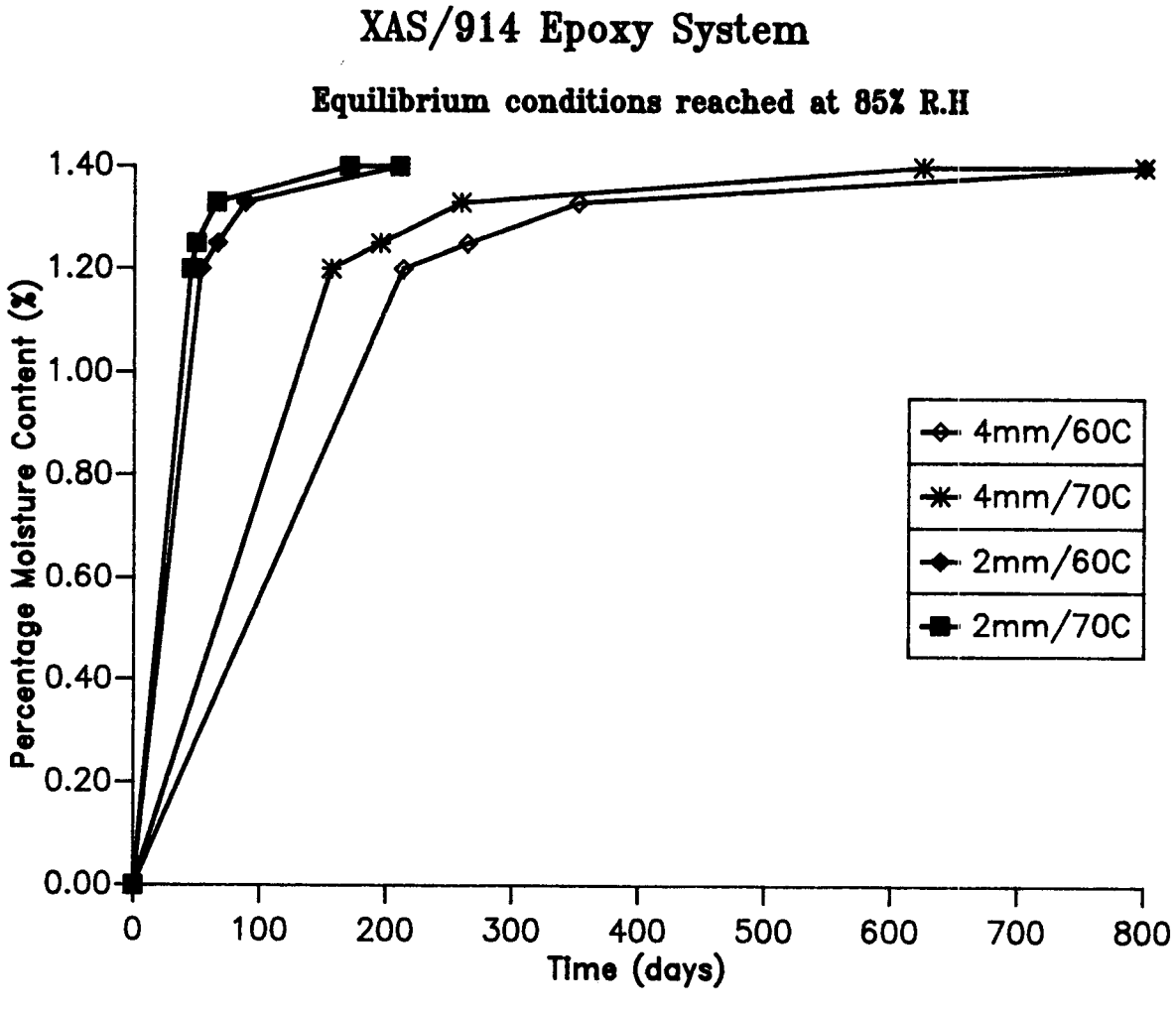

Figure 2

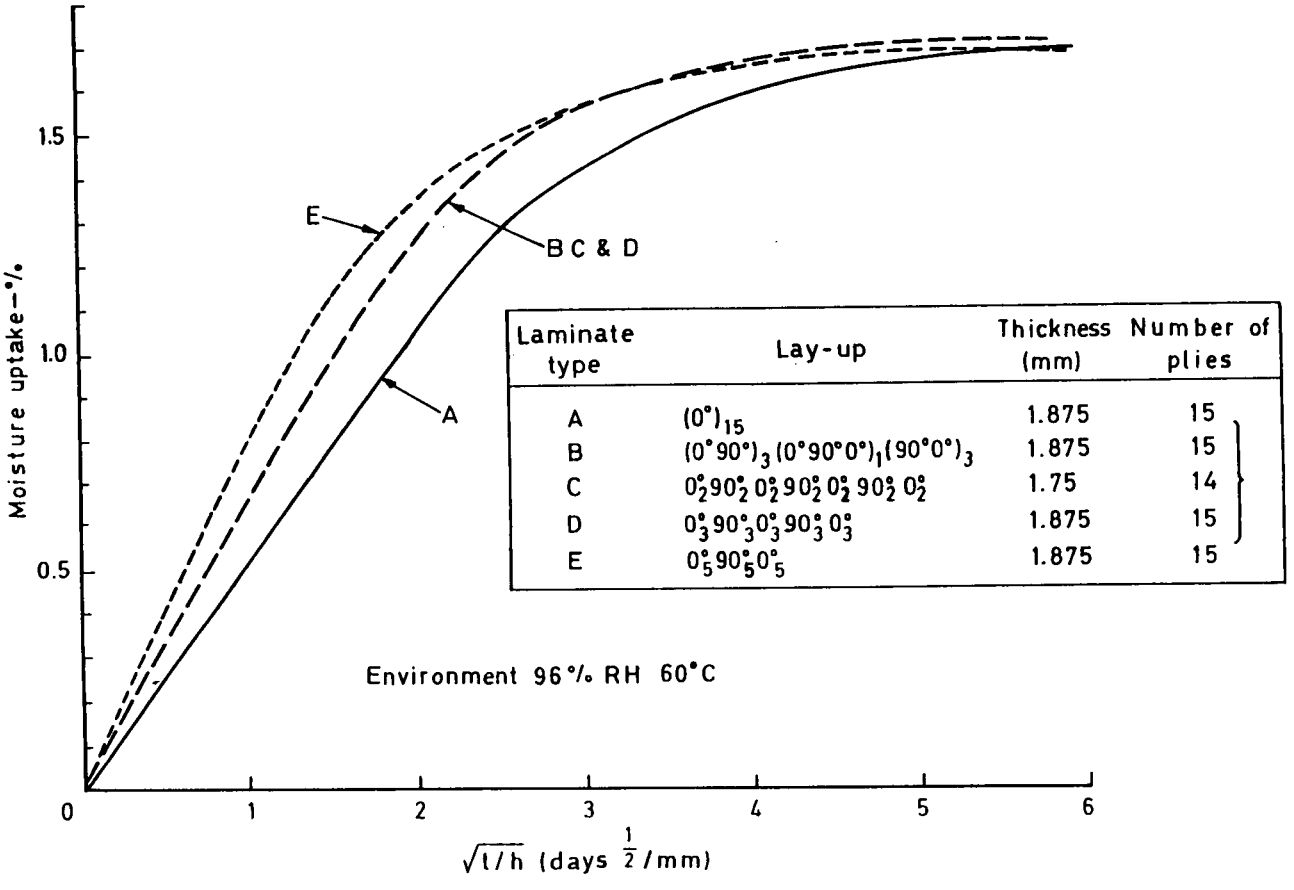

Laminate type	Lay-up	Thickness (mm)	Number of plies
A	$(0°)_{15}$	1.875	15
B	$(0°90°)_3(0°90°0°)_1(90°0°)_3$	1.875	15
C	$0°_2 90°_2 0°_2 90°_2 0°_2 90°_2 0°_2$	1.75	14
D	$0°_3 90°_3 0°_3 90°_3 0°_3$	1.875	15
E	$0°_5 90°_5 0°_5$	1.875	15

Effect of lay-up on diffusion behaviour

Figure 3

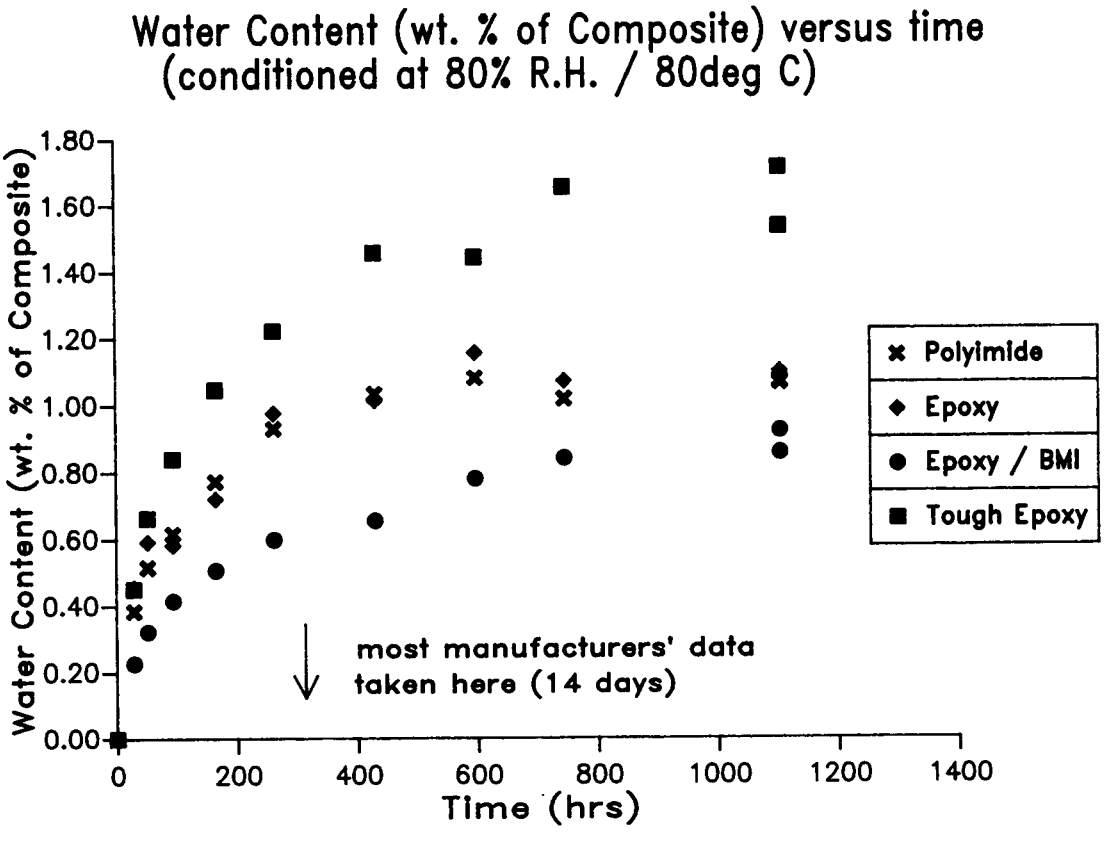

Figure 4a

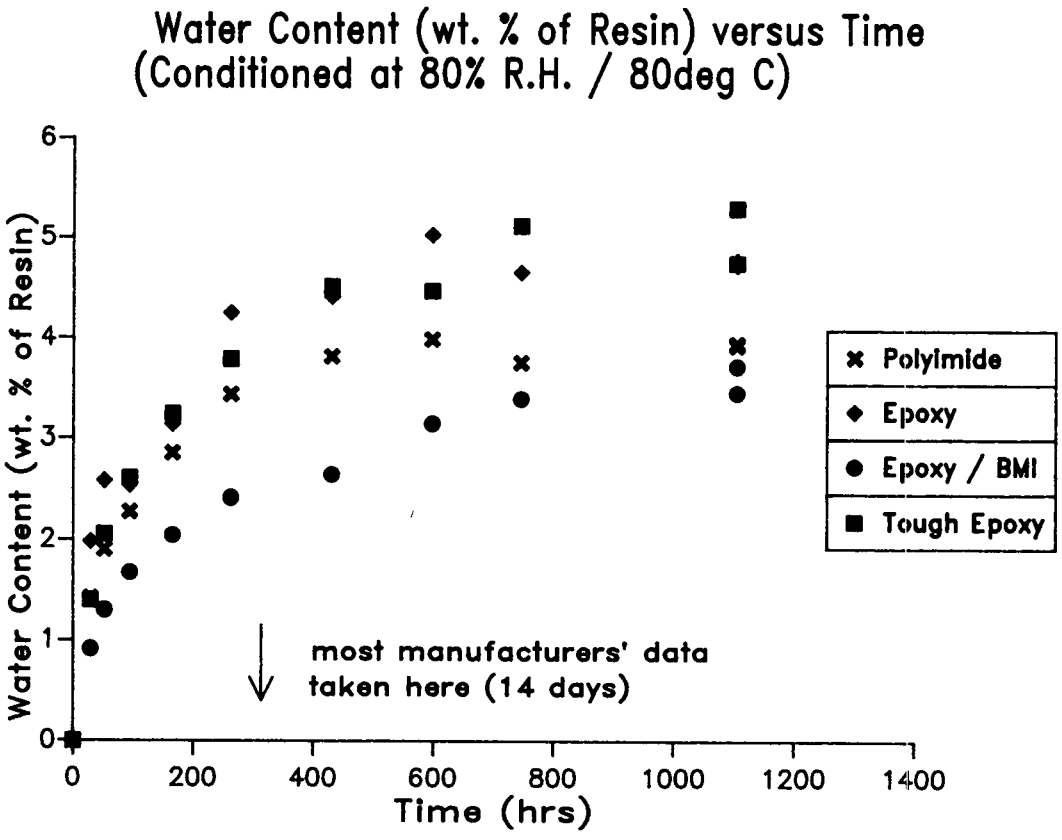

Figure 4b

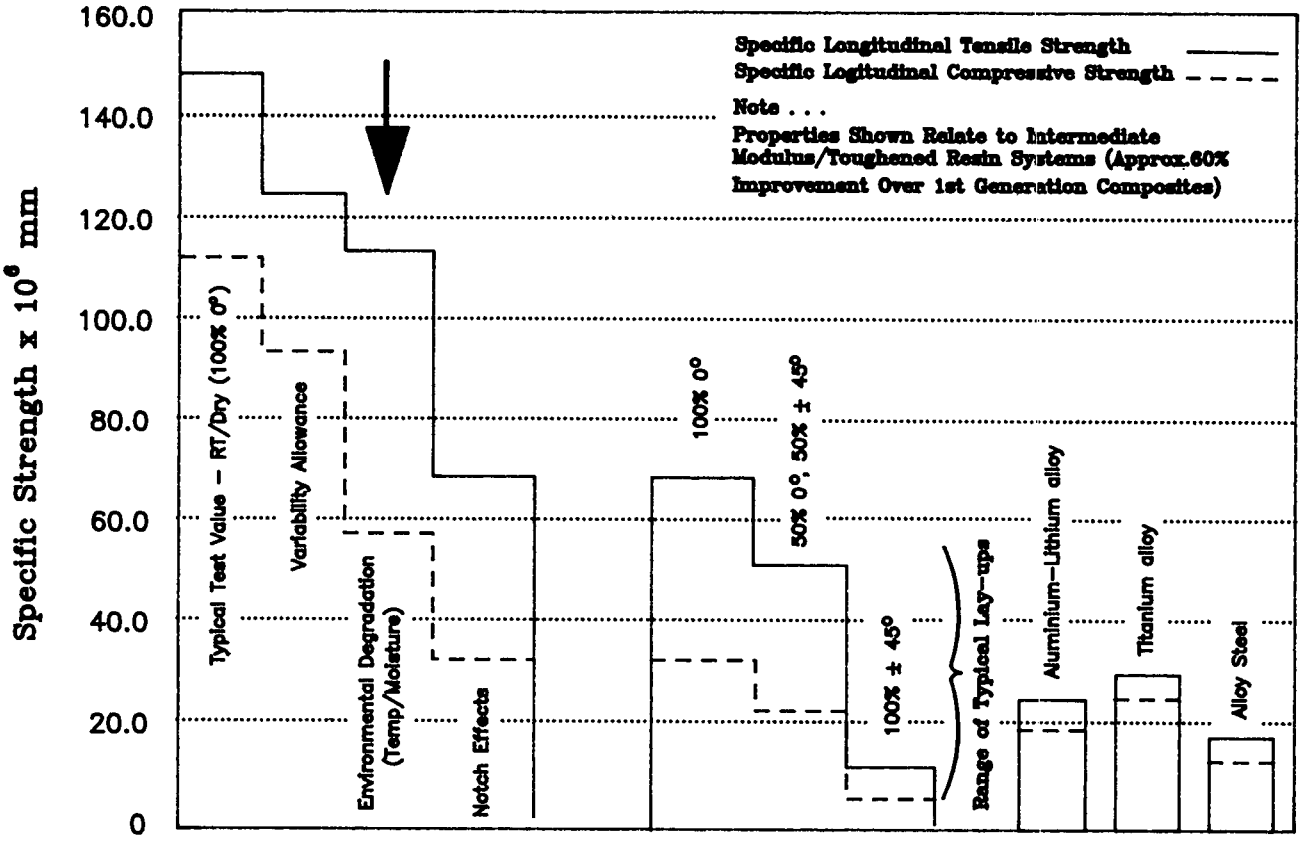

Reduction Factor Effects on Composite Specific Strengths in Structural Applications

Figure 5

EFFECTS OF FUEL ON HERCULES AS-4/8552 COMPOSITE MATERIAL

A.T. Rodríguez
A. Lavía
I. Fernández
E. Redondo
Research and Development, Technology and Materials Dept. (I+D.T.M.)
Project Division

CONSTRUCCIONES AERONAUTICAS, S.A. (CASA)
28906 GETAFE (Madrid)
SPAIN

SUMMARY

The behaviour of an advanced toughened epoxy resin/ carbon fiber composite material, Hercules AS-4/8552, in contact with fuel has been studied.

Interlaminar shear strength and compression strength tests were performed on unidirectional specimens after being exposed at 70°C to several conditions, including a combined exposure to JP8 and water. A correlation between the fluid content (either fuel, water or a mixture of both) and the drop in the mechanical properties was found. However, tests performed on multidirectional specimens immersed in several JP8/additives mixtures and subjected to thermal cycles showed no variation in the interlaminar shear strength values.

The exposure to fuel or to fuel/additives mixtures of impacted samples was found not to produce any effect in the damage size or detectability. Fuel leakage tests were conducted on impacted panels subjected to pressure and results are presented.

Finally, the growth of microorganisms in fuel/water solutions seemed not to affect the material properties, as deduced from some mechanical and microscopy studies carried out on samples exposed to such mixture.

1. INTRODUCTION

The design of some carbon fiber/epoxy composite elements of civil and military aircrafts requires fuel to be in direct contact with structural laminates. There is, therefore, a need to ascertain if this fluid damages the composite. Some investigations conducted on several resin/fiber systems have shown little or no influence in the material properties due to contact with fuel [1-4].However, a recent study [5] has reported that 0°and 90° flexural strength values of three thermoset matrix composites decrease as a consecuence of the expore to fuel. It seems that the effects of fluids on these materials depend largely on the exposure time and conditions, as well as on the chemical resistance of the matrix and the matrix-fiber interface. Further, a realistic approach to fuel effects has to take into account the risk of combined exposure to fuel and water, due to fuel tank sump water, as well as the presence of additives, such as anti-icing or anti-static, in fuel mixtures. The growth of microorganisms in fuel tanks has been also reported [6,7] being necessary to investigate their effects in the composite properties.

In this paper the behaviour of an advanced toughened epoxy/carbon fiber composite material (Hercules AS-4/8552) in contact with fuel is reported.

A first series of evaluations was performed to determine if some mechanical properties such as interlaminar shear strength (ILSS) and compression strength could be affected by static immersion in JP8 and in JP8/water at 70°C. Additional ILSS tests were carried out on specimens immersed in several JP8/ additives mixtures and subjected to thermal cycles and on samples exposed to fuel contaminated by microorganisms. In these samples electron microscopy studies were also performed to analyze if some surface degradation by microorganisms takes place.

The exposure of composite materials to fuel and/or water may cause effect not only on the matrix-dominant mechanical properties, but also in other properties, such as impact related performances. Therefore, tests were conducted on impacted samples of Hercules AS-4/8552 to determine if damage growth or penetration of fluids in the damage area occur as a consecuence of the exposure to fuel and thermal cycles. Further, impact damage may be a potential source of fuel leakage. It has been reported [8] that impacted samples of some epoxy resin/carbon fiber composites showed fuel leakage after a very short time of being subjected to low fuel pressures. Thus,impacted panels of Hercules AS-4/8552 were subjected to pressure and the existence of fuel leakage was investigated.

2. EXPERIMENTAL PROCEDURES

2.1 Specimens preparation

The composite material selected for this study was Hercules AS-4/8552 unidirectional tape. Specimens for the different tests were cut from autoclave cured panels which were fabricated using standard lay-up and vacuum bagging procedures.

2.2 Exposure conditions

Specimens for mechanical tests were immersed in the fluids and fluid mixtures indicated in Table-1.

When required, the temperature of the fluids was kept constant by placing the fluid containers in an oven. The weight of traveller specimens was controlled by weighing them periodically on an analytical balance.

Thermal cycles were performed in an automatically controlled thermal shock chamber. The cycling conditions were those indicated in Figure-1.

A culture of the following microorganisms was made grow in a JP8/water mixture:

Table-1: Exposure conditions

EXPOSURE CONDITION		MIXTURE CONCENTRATION (1)
Fluid	Temperature	
A: JP8	70°C	
B: JP8 + Water	70°C	0.258 ml of water in 1000 ml of disolution
C: Water	70°C	
D: A + C	70°C	
E: B + C	70°C	
F: Water	Thermal cycles	
G: JP8 + Water	Thermal cycles	0.258 ml of water in 1000 ml of disolution
H: JP8 + Anti-icing	Thermal cycles	0.15% (in volume) of anti-icing BP
I: JP8 + Anti-oxidant	Thermal cycles	23.9 mg of anti-oxidant HITEC 4733 in 1000 ml of disolution
J: JP8 + Anti-static	Thermal cycles	1.07 mg of anti-static ASA-3 in 1000 ml of disolution
K: JP8 + Anti-fungi	Thermal cycles	50.3 mg of anti-fungi BIOBOR in 1000 ml of disolution
(1) AS PER ASTM-D-1655 and DERD 2494		

- Claudosporium resinae
- Fusarium s.p.
- Penicillium s.p.
- Micrococcus s.p.
- Pseudomonas s.p.
- Alcaligenes s.p.
- H-4 yeast
- H-5 yeast

The exposure of specimens to this solution was carried out in containers placed in an environmental chamber regulated at 28°C and 35% of relative humidity.

2.3 Mechanical tests

ILSS measurements were performed on two different types of specimens:

- Unidirectional specimens following the standards ASTM D2344 and Pr EN 2563 (AECMA).

- Multidirectional specimens made with 20 plies and a quasi-isotropic lay-up ($[+45/-45/0/-45/+45/0/-45/0/0/]_S$). The nominal dimensions were 32 mm x 25 mm x 3.6 mm.

Compression tests were performed on unidirectional specimens following the ASTM D695 standard.

The test machine used to measure these properties was an Instron 1185.

Tests were performed at 70°C. All the conditioned specimens were tested after being wiped and allowed to stabilize at this temperature for 5±1 minutes.

Impact tests were carried out on 24 plies quasi-isotropic specimens with a lay-up sequence of $[(-45/90/+45/0)_3]_S$. The nominal dimensions were 152 mm x 102 mm x 4 mm. Impact energies ranging from 1 J/mm to 12.5 J/mm were used and the impact device was a vertical dropping weight machine with a semispherical impactor tip of 15.9 ± 1.0 mm diameter and 4.5 kg weight.

Once impacted, the samples were inspected using an automatic scanning equipment Versiscan with C-Scan records.

The fuel leakage tests on impacted samples were performed at 0.34 N/mm^2 (5 p.s.i.) using the pressurizing device described in Figure-2.

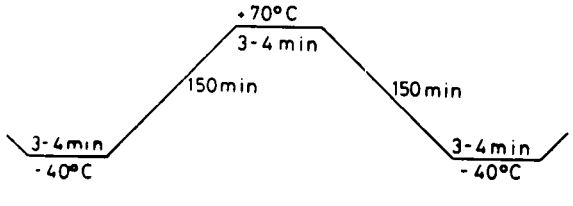

Figure-1: Thermal cycle used for the exposure of multidirectional ILSS specimens.

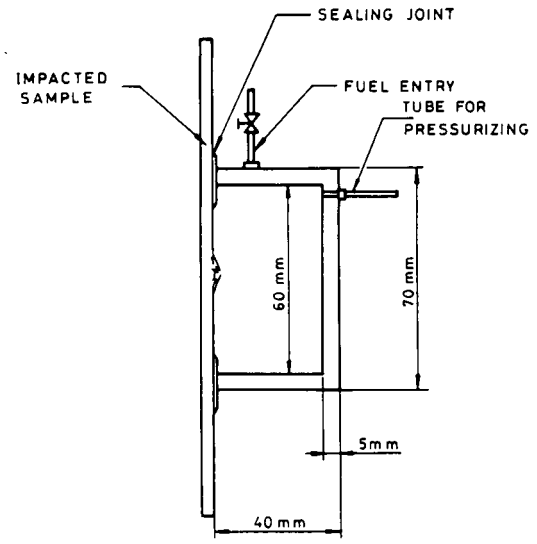

Figure-2: Pressurizing fixture for fuel leakage tests.

2.4 Microscopy studies

Samples were metalized by sputtering with Au-Pd for 30 seconds and subsequently observed in a Hitachi S-570 scanning electron microscope (SEM). When required, the samples surfaces were cleaned by immersion in acetone for 3 minutes in an ultrasonic bath.

3. RESULTS AND DISCUSSION

To determine the effect of the exposure to fuel and to fuel/water on the mechanical properties of the material, unidirectional ILSS and compression strength specimens were immersed in the conditions A to E shown in Table-1. These conditions were chosen in order to take into account the risk of combined exposure to fuel and water and the fact that fuel can carry a small amount of dissolved water.

The weight gain on the travellers was determined as a function of time and tests were performed when the travellers reached the equilibrium fluid contents, which are shown in Table-2. Both ILSS and compression travellers reached similar fluid contents under conditions A and B (JP8 and JP8 + water). These fluid contents were found to be lower than the equilibrium water content absorbed by the travellers when exposed to water at 70°C (condition C).

Similar results have been previously obtained [9] for several epoxy resin/carbon fiber composites where water and aviation fluids uptakes were comparatively studied. These results seem to indicate that the affinity of resins for fuel is lower than the affinity for water. In fact, when specimens previously saturated with fuel at 70°C are placed in water at 70°C (conditions D and E of Table-1) they increase their weight gain up to a new equilibrium level (Table-2). This equilibrium level, which is similar for both ILSS and compression specimens, is lower than the sum of the individual A + C or B + C conditions.

The results of the mechanical tests, carried out at 70°C, on conditioned and reference specimens are summarized in Table-3.

Table-2: Equilibrium fluid contents of Hercules AS-4/8552 travellers under several exposure conditions.

	FLUID CONTENT (%)	
EXPOSURE CONDITIONS	UNIDIRECTIONAL ILSS TRAVELLERS	COMPRESSION TRAVELLERS
A: JP8 (70°C)	0.48	0.61
B: JP8 + water (70°C)	0.55	0.55
C: Water (70°C)	1.36	1.41
D: A + C (70°C)	1.40	1.47
E: B + C (70°C)	1.40	1.47
	MOISTURE CONTENT (%)	
Reference: without conditioning	0.20	0.45

These results show a decrease in the ILSS values obtained for the specimens kept under conditions A to E when compared to reference specimens. This drop is less pronounced for the specimens conditioned in JP8 and in JP8 + water than for the rest of the specimens. The ILSS values obtained for the samples under these conditions are very similar, which indicates that the presence of a small amount of water in the fuel does not seem to have any influence. Identically, the exposure to fuel previous to the immersion in water has not influence as it is shown by the ILSS values obtained for the specimens under conditions C, D and E.

The compression strength values decrease in the samples exposed to water (condition C) or to fuel and water (conditions D and E). When the samples have been exposed only to fuel (conditions A and B) there is only a little effect on the compression strength value, compared to the reference one. It has to be remarked that the fluid contents of the compression specimens after being exposed to conditions A and B are only a bit higher than the moisture content of the reference specimens (Table-2).

Table-3: ILSS and compression strength values obtained at 70°C of Hercules AS-4/8552 after being exposed to conditions A to E. Reference values are included.

EXPOSURE CONDITIONS	UNIDIRECTIONAL ILSS (N/mm^2)	COMPRESSION STRENGTH (N/mm^2)
Reference: without conditioning	96.0	1476.6
A: JP8 (70°C)	89.4	1404.8
B: JP8 + water(70°C)	88.9	1451.9
C: Water (70°C)	68.5	1268.8
D: A + C (70°C)	70.6	1333.3
E: B + C (70°C)	69.3	1314.2

The ILSS and compression strength values, obtained at 70°C, have been represented versus the fluid content of the specimens (either fuel, water or the mixture of both) (Figure-3). It can be observed that both mechanical properties decrease as a function of the fluid content of the material. The interactions fuel-resin and water-resin seem to produce a plasticization of the material which affects the mechanical properties in the same amount, provided that the fluid contents (either fuel or water) of the specimens are the same. A recent study [5] carried out on three types of epoxy resin/carbon fiber composites has shown a decrease in the flexural strength of specimens immersed in fuel at 82°C, but this has been attributed to a degradation of the matrix-fiber interface instead of a matrix plasticization.

A second series of evaluations was performed to ascertain the effect of the exposure to different JP8/additive mixtures (conditions G to K of Table-1) on the ILSS values.

In order to reproduce as close as possible the material in service conditions, ILSS tests were carried out on coupons with a quasi-isotropic configuration (see Experimental Procedures) similar to the one used in the fuel tank skin. Further, the samples were immersed in some JP8/additive mixtures and subjected to thermal cycles, following the scheme shown in Figure-1.

Table-4 shows the ILSS values at 70°C obtained after 200 and 500 cycles. No changes in these values can be observed, when compared to the reference ones.

From these experiments it can be concluded that the ILSS is affected mainly by the static immersion or direct contact with fuel and/or water at 70°C, while the exposure to fuel and thermal cycles does not produce an appreciable variation in the ILSS values. As it is shown in Table-2, the moisture content of reference specimens are only slightly lower than the fuel content of specimens conditioned in fuel or in fuel + water (conditions A and B). Therefore, the fuel content of specimens under thermal cycles, instead of conditioned at 70°C, could be expected to be similar to the moisture content of the reference specimens. This fact could explain the no variation of the obtained ILSS values.

Table-4: ILSS values obtained at 70°C of Hercules AS-4/8552 after being immersed in JP8/additive mixtures and subjected to thermal cycles. Reference values are included.

EXPOSURE CONDITIONS	NUMBER OF THERMAL CYCLES	MULTIDIRECTIONAL ILSS (N/mm^2)
Reference: without conditioning	---	80.0
G: JP8 + Water	200 500	86.0 85.0
H: JP8 + Anti-icing	200 500	82.8 86.4
I: JP8 + Anti-oxidant	200 500	78.5 82.6
J: JP8 + Anti-static	200 500	82.4 83.8
K: JP8 + Anti-fungi	200 500	82.1 82.0

The evolution of the damage area in impacted panels immersed in water and in fuel/additives mixtures and subjected to thermal cycles was subsequently investigated. For that, samples were impacted at an energy of 12.5 J/mm and inspected visually and ultrasonically to evaluate the extent of damage. Then, they were immersed in fluids F to K (Table-1)

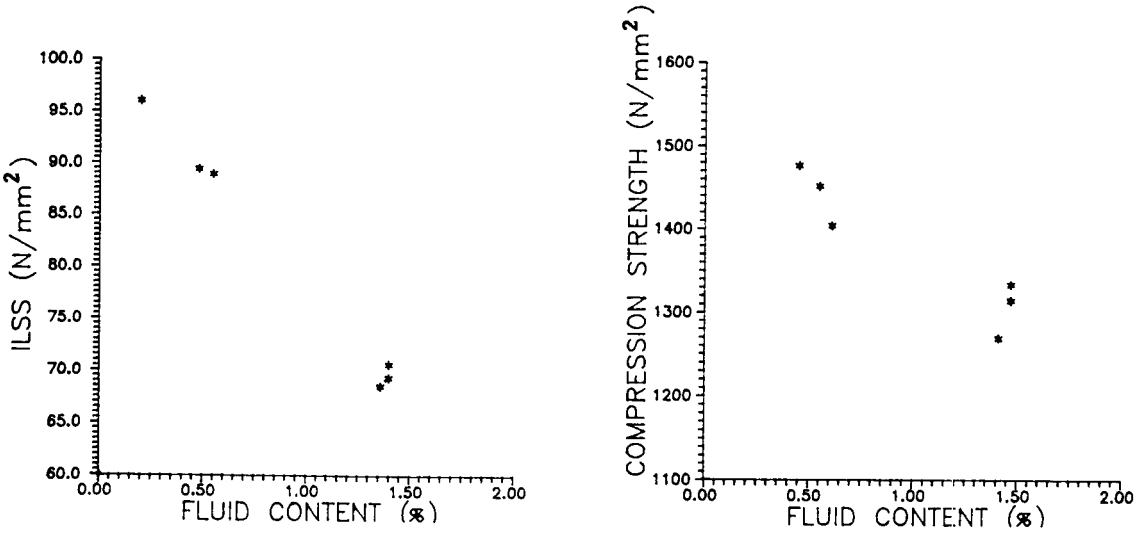

Figure-3: Variation of ILSS and compression strength values of Hercules AS-4/8552 as a function of the fluid content of the specimens.

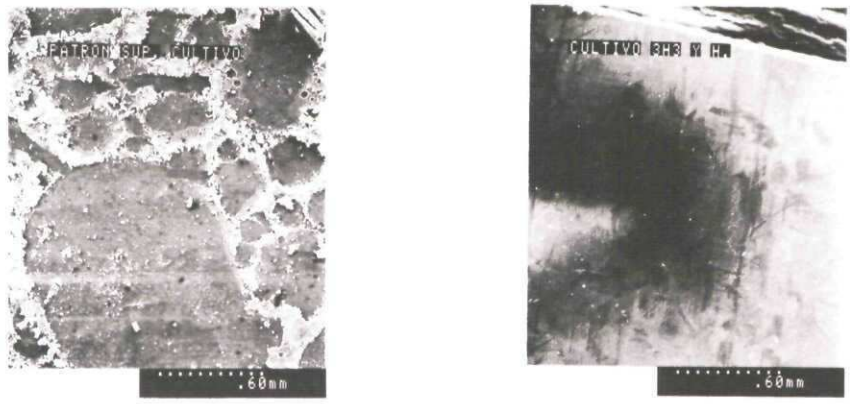

a b

Figure-4 SEM photograph of the surface of an Hercules AS-4/8552 specimen (a) exposed to a culture of microorganisms in JP8/water and (b) after having been wiped with acetone.

and subjected to thermal cycles, as the one represented in Figure-1. Finally, after 500 cycles, the samples were inspected again.

The comparison of the ultrasonic C-Scan records, before and after the exposure, showed no variation in the damage area, except for the samples immersed in water. For these specimens an apparent decrease of the damage area could be observed probably due to trapped water, which acts as a transmitter of the ultrasonic wave. In fact, when these samples were subsequently dried in an oven at 70°C the damage area recovered its original size.

Additional tests to evaluate the presence of fuel leakage through the damage area were conducted using the fixture described in Figure-2, under a nominal pressure of 0.34 N/mm^2 (5 p.s.i.). Samples impacted at several energy levels, ranging from 1 J/mm to 10 J/mm, were analyzed. Fuel leakage through the damage area is not observed in panels impacted at 3.3 J/mm. However, at an energy level of 6.6 J/mm a fuel permeability was detected. To properly evaluate these results, other composite materials with resins of several categories, including not toughened, toughened and bismaleimide resins, were tested. All yielded comparable results, with the appareance of fuel leakage at an impact energy of 6.6 J/mm. It has been reported [10] that aluminium panels show a similar behaviour.

As the final step on the study of the behaviour of Hercules AS-4/8552 in contact with fuel, multidirectional ILSS and impacted specimens, as well as some samples for microscopy studies, were immersed for 250 days in a culture of microorganisms, which composition has been described in Experimental Procedures, and kept at 28°C and 35% RH. ILSS tests at 70°C were performed after this period and an average value of 76.4 N/mm^2 was obtained, which is very close to the value obtained for the reference specimens (see Table-4).

On the other hand, a decrease in the damage area of the impacted specimens was observed after the exposure to the culture, which could be attributed to trapped water in the impacted area. As it has been previously described, after drying the samples in an oven at 70°C for 15 days, the original damage area was recovered.

Finally, some samples immersed in the culture of microorganisms were observed by scanning electron microscopy. The surface of the specimens appeared covered by microorganisms (Figure-4a), but after wiping the surface with acetone, no damage or alteration of the material could be observed (Figure-4b).

4. CONCLUSIONS

The effect of the exposure to fuel on the mechanical properties of Hercules AS-4/8552 has been found to depend on the exposure conditions. Thus, static immersion on JP8 at 70°C produces a decrease on the ILSS and compression strength values of this material, while specimens immersed in JP8/additives mixtures at the indicated concentrations and subjected to thermal cycles, keep practically invariable their ILSS value. The mechanism of properties degradation by the exposure to fuel appears to be a plasticization of the matrix, directly related, therefore, to the fluid content of the specimens.

However, the drop in the mechanical properties due to the contact with fuel has been found to be less pronounced than the one produced by the exposure to water. This can be attributed to the higher affinity of the resin for the water than for the fuel or fuel mixtures.

Other properties, such as the damage growth and detectability in impacted samples, are not affected by the exposure of the material to JP8/additives mixtures and thermal cycles. Fuel leakage was found not to take place in panels impacted at 3.3 J/mm. At an energy level of 6.6 J/mm a fuel permeability was detected. This behaviour is similar to the one observed in other composite materials and aluminium alloys.

The exposure to a JP8/water solution where a culture of microorganisms was made grow neither causes any effect in the material properties.

The investigation reported here, covering several aspects of the material performance under different exposure conditions, has shown the suitability of Hercules AS-4/8552 for the manufacturing of structural elements in direct contact with fuel and fuel/additives mixtures.

5. ACKNOWLEDGEMENTS

The preparation of cultures of microorganisms and the exposure of the material to these cultures were carried out by Mr. Díaz-Plaza and Mr. Heras of CAMPSA, whom we wish to express our gratitude for their helpful collaboration.

REFERENCES

1. Judd, N.C.W., Mathews, B.J., Pritchard, G. and Stokes, F.C. "The effects of Aviation Fluids on Carbon/Epoxy Composite Panels", SAMPE J., 13, May/June 1977, pp 10-15.

2. Hendricks, C.L.,"A Study of the Effects of Long-Term Exposure to Fuels and Fluids on the Behaviour of Advadced Composite Materials", NASA report D-6-41185-6, September 1977.

3. White, B.L., "Effects of JP-4 Fuel on Graphite/Epoxy Composites", AFWAL-TR-83-3086 report, October 1983.

4. Clark, K.G., "Compatibility of Aircraft Operational Fluids with a Graphite/Epoxy Composite - Development of an Exterior Coating System and Remover", NADC-80046-60 report, October 1980.

5. Curliss, D.B., Carlin, D.M. and Arnett, M.S., "The effect of Jet Fuel Absorption on Advanced Aerospace Thermoset and Thermoplastic Composites" in "Advanced Materials: The Challenge for the Next Decade", Proceedings of the 35th International SAMPE Symposium and Exhibition, April 1990, pp 332-345.

6. Spain, J.C., Somerville, C.C., Butler, L.C., Lee, T.J. and Bourquin, A.W., "Degradation of Jet Fuel Hidrocarbons by Aquatic Microbial Communities", AFESC report ESL-TR-83-26, November 1983.

7. Blanchard, G.C. and Goucher, C.R., "Mechanism of Microbiological Contamination of Jet Fuel and Development of Techniques for Detection of Microbial Contamination". Semiannual Progress Report AF Contract No. 33(657)-P186, July 1966.

8. Griffin, C.F.,"Fuel Containment and Damage Tolerance in Large Composite Primary Aircraft Structures", NASA report CR-166-083, March 1983.

9. Loos, A.C. and Springer, G.S.," Moisture Absorption of Graphite-Epoxy Composites Immersed in Liquids and in Humid Air",13, April 1979, pp 131-147.

10. Randazzo, S. "Fuel Resistant Coating for Metal and Composite Fuel Tanks" in " New Generation Materials and Proceses", Proceedings of the 9th International SAMPE Conference, June 1988, pp 155-177.

ENVIRONMENTAL DEGRADATION OF HIGH TEMPERATURE COMPOSITES

R. C. Cochran T. M. Donnellan R. E. Trabocco
Naval Air Development Center
Warminster PA 18974 USA

J. Thompson
Naval Air Systems Command
Washington DC 20361 USA

Summary

A study was performed to assess the effect of galvanic corrosion phenomena on the strength of graphite/bismaleimide(BMI) composites. The results indicate that degradation ocurred in BMI composites galvanically coupled to aluminum alloys. The mechanism responsible for the degradation involves hydroxyl ion generation in the cathodic reaction. Optical and electron microscopy of the surface of coupled specimens showed a great deal of cracking and deterioration of the resin. This phenomenon is thought to be associated with stresses in the resin imposed by thermal or chemical processes. These cracks may be an indication that the mechanism of degradation is not simply the hydroxl attack on the resin but a combination of chemical and mechanical attack. Composite-aluminum material couples were exposed to salt water/fuel solutions and to salt spray environment and then composite properties were determined. Conventional protection schemes were evaluated. The results indicated that the performance retention was test specific and that bearing tests were most sensitive to the galvanically induced degradation. Significant bearing strength loss was found when the protection schemes failed. In addition, a systematic study of the electrochemical conditions which were most important in control of the degradation rates was performed.

Introduction

High temperature composites offer significant weight savings over conventional materials such as steel and titanium. Imide based composites are the only organic matrix materials that have been demonstrated for applications in the 149°C (300°F) to 288°C (550°F) region. The chemical structure of the resin determines the material operating temperature. Polymers based on bismaleimide(BMI) and condensation polyimide chemistries (figure 1) have been developed for engine and airframe components. In many cases the imide based composite is in direct contact with steel or aluminum. In a recent laboratory test program, graphite/bismaleimide composites immersed in salt water while in contact with a metal were observed to degrade. This degradation resulted in removal of resin and delamination of the composite within several days.

Because of the importance of polyimide composites for Navy applications a program was initiated at NADC to examine the degradation phenomena. The Navy's efforts have focussed on evaluation of the severity of the degradation in existing and emerging aircraft, development of a methodology to mitigate the phenomenon and on identification of the degradation mechanisms. The program was performed in three tasks, specifically salt fog exposure, cleaning fluid exposure and electrochemistry. Salt fog and salt water exposures were used to evaluate the severity of the problem and to evaluate currently used protection schemes. These experiments used specimen designs in which composites were electrically coupled to metal. Electrochemistry experiments were used to assess the importance of specific exposure variables in the degradation process.

Background

The effect of water on polymer matrix graphite composites in the fleet is a reduction of the thermal stability of the material. This effect is a well characterized reversible plasticization process. Moisture is also known to cause corrosion in metal aircraft components. The Navy spends considerable time and effort on corrosion maintenance of the metal aircraft in the shipboard environment. One form of corrosion is caused by the electrical coupling of two dissimilar metals. Galvanic corrosion occurs when there is a difference in the electrical potentials of two conducting materials exposed in a corrosive solution. In the couple, the more corrosion resistant material becomes the cathode where reduction reactions occur while the other more active material becomes the anode where oxidation reactions take place. The cathodic reaction that occurs depends on the solution conditions. In neutral or basic solutions, the reaction is the reduction of water and oxygen to produce hydroxyl ions. Graphite is cathodic to aluminum and steel and composites utilizing this type of reinforcement will cause corrosion of these metals when they are

connected electrically. This electrical coupling in structural components is usually accomplished either through the fasteners used to attach composite skins to metal substructure or through adhesive bonds.

Graphite composite driven corrosion of aircraft structural alloys has been studied previously. Fischer and DeLuccia(1) measured a large 1 volt potential difference between graphite/epoxy composites and 7075 aluminum alloys. This potential provided the driving force for extensive corrosion of the alloy. Mechanical testing of the couples indicated that the corrosion was responsible for significant strength loss in the aluminum components. Additional efforts have examined the effectiveness of various protection schemes for the prevention of galvanic corrosion. Thompson, White and Snide(2) reported that protection schemes which consisted of coatings on the composite and the metal, sealant on the faying surface and around the fastener, and a fiberglass barrier ply dramatically reduced the corrosion found in unprotected couples. These authors cautioned that the protection schemes were only effective if all surfaces were coated and if the sealant layers were not porous. Similarly, DeLuccia and Brown(3) found that isolation coatings significantly reduced the galvanic corrosion induced fatigue strength loss in aluminum alloys. In all of the work described in the literature there was no indication of degradation of the epoxy resins used in the composite.

The degradation of imide polymers through hydrolysis by moisture or bases has been studied by a number of workers. Strong bases attack the imide group in the polymer structure and produce amic acid salts and amines figure 2. The most widely studied material has been Kapton wire insulation. Environmental factors such as temperature, stress, moisture concentration and basicity have all been found to affect degradation rates. The actual mechanism responsible for the degradation observed has also been addressed. Askins(4) modelled the degradation phenomena with an arhennius relationship and further found that the strength loss in the material followed an exponential decay, first order reaction type response. Wolf and Soloman(5) showed that under specific exposure conditions, hydrolysis rates could be significantly reduced through annealing of the polymer prior to exposure. These authors speculated that the degradation could be a mechanochemical process.

Discussion of Experimental Results

Evaluation of Galvanic Degradation Processes

Exposure Specimen Study. The initial effort in the program was the verification of the results reported regarding the degradation phenomena. A set of specimens was fabricated with U. S. Polymeric AS-4/V-378A coupons connected to 2024 T-6 aluminum coupons of the same dimensions. The specimen size used was 7.5 cm x 1.25 cm x .2 cm (8 ply quasiisotropic laminate). The composite and Al were tied together with a nylon string. Three samples were placed in glass jars containing various combinations of JP-5 (jet fuel) and 3.5% NaCl solution. The combinations included a 50/50 mix of JP-5 and neutral salt water, a 50/50 mix of JP-5 and pH 2 salt water and a jar half filled with neutral salt water. A forth jar with a 50/50 mix of salt water and JP-5 was made up with only the composite sample in it. These jars were placed in an oven at 82°C (180°F). The jars were removed at 24 hour intervals and the samples were observed. The total exposure period was four days.

The first observation regarding these exposed samples was that there was degradation of the composite in a short period of time. The type of attack varied depending on the nature of the solution. Specimens in water/fuel solutions showed an effect which was concentrated in the interface between the fluids. Over a period of time, the affected zone grew up the edge and in towards the center of the specimen. Specimens half immersed in water showed a more general attack over the portion of the specimen above the water surface. All of the degradation occurred on the surface opposite the mating surface of the specimens. The degradation was evidenced first by a lightening of the surface and then exposure of bare fibers.

The sample exposed to the pH 2 solution showed similar degradation to the pH 7 exposed sample. These pH 2 specimens were not expected to degrade in the same manner as those exposed to neutral water since the nature of the reduction reactions in acid and neutral solutions are different and also because the low pH solution was expected to react with any hydroxl ions. A measurement of the pH of this salt solution showed that it had increased to 4.8 during the exposure time. The pH increased due to the production of aluminum hydroxide. These observations indicate that hydroxyl attack is not the only important feature of the degradation phenomena. It also shows the importance of the local solution chemistry i.e.; the chemistry of the environment where degradation occurs. In the samples exposed to only salt water, the degradation did not appear to be as severe, however it covered a much larger area than the fuel water samples. The degradation was not visible until 48 hours of exposure.

The second observation made was that the aluminum attached to the degraded composite specimens had considerable surface corrosion. The corrosion appeared to be qualitatively similar to that reported by Fischer and De Luccia(1).

After 4 days of exposure the samples were removed from the solutions and inspected with optical and scanning electron microscopy(SEM). Examination of the water/fuel exposed specimens showed that the resin had been completely removed from the fibers on the surface in the area just above the interface. The resin higher up the specimens in the fuel phase but still in the affected zone was cracked and fibers were visible below the surface. SEM micrographs from three areas are shown in figure 3. The specimens exposed to only water had much less exposed fiber, however the cracks and chipped resin were more visible over the surface. The resin had been thinned down a great deal on these specimens. SEMs of the surface of the water fuel samples showed that the resin was heavily cracked above the degraded area, figure 3A. Moving down the specimen a large number of rough chips were observed on the surface of the specimen, figures 3B. Finally in the area of greatest degradation there were fibers with a thin resin coating, bare fibers and chips of resin visible, figure 3C.

The information obtained from these exposure tests does not allow quantitative analysis of the degradation mechanism to be provided. There are some insights into the mechanism that can be stated based on the observations. The degradation of the coupled specimens was affected by the formation of hydroxyl ions at the cathode in the galvanic cell. In the specimens exposed to only salt water the thin layer of water that condensed on the surface of the specimen above the water level was the electrolyte. This thin layer of water provided an area for the reaction to proceed and allowed the hydroxide ions to concentrate on the surface. In the area below the water the hydroxide ions were able to diffuse away from the surface and no degradation was observed. The samples exposed to jet fuel/salt water mixtures showed a concentrated degradation. This effect was due to a concentration of hydroxyl ions and oxygen in the meniscus between the water and fuel. The hydroxyl ions are nearly insoluble in the fuel and when formed diffuse down to the interface. The fact that the acid water solution caused similar degradation to the neutral solution indicates that the degradation process is driven by local chemical environments.

Evaluation of Protection Schemes. The next set of experiments performed were designed to evaluate the effectiveness of currently used protection methods for graphite/epoxy-metal couples for the prevention of BMI composite degradation. The procedure is outlined in MIL-F-7179. The protection schemes proposed for the graphite/BMI composites consist of a layer of fiberglass/BMI cocured on the surface of the composite and epoxy primer on the mating surface of the laminate. A sealant is applied to the mating surface and around any fasteners in the structure. The aluminum in contact with graphite reinforced composites is anodized and primed with epoxy primer. There were three screening studies performed which examined the effect of specific protection schemes on composite strength.

The first set of specimens fabricated were used to screen paints and sealants for their ability to protect the composite under aggressive exposure conditions. Four primers, a topcoat and a one coat primer/topcoat were evaluated. The coatings evaluated included; MIL-P-23377 solvent based epoxy primer, MIL-P-85582 water based epoxy primer, Koroflex flexible epoxy primer, a high temperature urethane primer Desoto 825-009, MIL-C-85285 urethane topcoat and Unicoat, a self priming top coat recently developed at NADC. The composite specimens were 14 ply (+,-,0,0,+,-,90)s IM7/5250-4. The aluminum was chromate conversion coated 2024-T6. Composite and Al specimens coated with these materials were cured for one week at room temperature. The composite and Al were attached using titanium 6,4 fasteners with A286 nuts. Each coating was evaluated with no sealant, an inhibited sealant and an uninhibited sealant. The coupled specimens were immersed to half height in neutral salt water (3.5% NaCl) and exposed at 82°C (180°F). The specimens were removed from the oven and visually inspected once a day for 7 days. After 7 days the specimens were removed for testing. The effects of this exposure on the specimen surface condition are shown in figure 4. The unprotected coupled specimens used as controls completely delaminated after 7 days. The other paint schemes showed various amounts of degradation from none for the urethane primer to severe for the water based primer and koroflex. The use of top coats improved the surface appearance compared to the primer alone. The Unicoat provided a high level of protection. One surprising finding was that the sealants did not affect the amount of blistering observed. The primers blistered to the same degree with inhibited and uninhibited sealant. The composite specimens were tested in 4 point flexure ASTM D790 at room temperature. The results are given in table 1. These results show that the flexure strength correlated with the amount of degradation observed on the surface. However, the flexure strength of the specimens which had inhibited sealant was higher than those which had uninhibited sealant. An observation of the most severely degraded samples showed that the primer had fibers embedded in it, this was evidence that the primer bonded to the surface however, due to degradation of the resin, fibers and primer were lifted from the surface.

The next set of specimens were fabricated to evaluate the effects of fiberglass surface plies, sealant and high temperature aging of the paint. The samples used for this study were 24 ply (0,90) IM-7/5250-4. The aluminum was .32 cm (.125in.) 2024-T6 sheet. The

composite and aluminum specimens were 2.5 cm X 10 cm. (1 X 4 in.). A MIL-S-85430 polysulfide sealant was applied to the faying surface and the fasteners were coated with uninhibited polysulfide sealant before installation. Two .468 cm (3/16th inch) holes were drilled one half inch from the edges of the specimens. The samples were connected using titanium 6,4 alloy bolts with an A286 alloy nut. The assembled specimen is shown in figure 5. The test matrix used in this evaluation is shown in table 2. The variables examined included the fiberglass ply, the sealant, the type of primer, and the condition of the primer. Specifically, bare and glass covered samples with and without polysulfide sealant with either a solvent based (MIL-P-23377) or a water based primer (MIL-P-85582) were evaluated. Some of the coated composite samples were heat aged at 149^{o}C (300^{o}F) for 100 hours before they were assembled. After the sealant had fully cured(1 week) the samples were exposed in a salt spray chamber. Most of the specimens were exposed for 30 days. In addition, another set of specimens which were fabricated with MIL-P-23377 primer, MIL-C-82582 and 825-009 high temperature urathene primer were exposed for 90 days. The exposure conditions for all of the salt fog specimens conform to the ASTM G-84 specification.

After 30 days, the specimens were removed from the salt spray environment and visually inspected. Each set of samples was photographed and then disassembled. After disassembly the composite samples were sectioned in half. The samples were placed in a bearing fixture and tested in compression. This specimen was chosen in order to test the area around the hole. It was expected that this would be the most vulnerable area due to the bare composite and exposed fibers in the hole.

After 30 days of exposure some of the specimens were severely blistered. Samples with water based primer and no sealant had the most severe blistering. Examples of specimens with and without glass and with and without sealant are shown in figure 6. Blisters were visible on all surfaces. The glass scrim ply on the surface had no effect on the number of blisters. The use of a faying surface sealant with water based primer had little effect on the amount of blistering. In some cases the primer flaked off the specimens during exposure and testing. The area under the primer was observed to be slightly degraded. The pH of the fluid in the blisters was measured to be in the 12 to 14 range. As was noted above, this basic solution will cause damage to the BMI resin. The solvent based primer provided better protection, however blisters occurred near the edge on several specimens. The use of a sealant on the faying surface and glass scrim reduced the number of blisters on the water based primer specimens. The edge blisters in the solvent primer samples are probably due to edge thinning of the primer as it stretched across the corner of the specimen. The samples that were heat aged for 100 hours at 149^{o}C (300^{o}F) showed no blisters for either the solvent or water based primers. In order to evaluate the amount of degradation in the hole several specimens were sectioned and microscopically evaluated. The samples exposed in salt spray all show minor amounts of degradation in the hole area. There was a qualitative correlation between the hole quality and the bearing strength of the samples.

Bearing test results are given in table 2. The data show a decrease from the control specimen strength. The average for the control was 550 MPa (80 KSI) while the coupled samples ranged from 406 MPa (58.9 KSI) for water based primer, no glass and sealant to 517 MPa (75.0 KSI) for solvent primer, temperature aged, glass surface ply samples. The results show that the glass ply had little effect on the bearing strength of the laminate. In all cases except glass with sealant the solvent borne primer specimens exhibited higher strength. Samples with sealant in the faying surface showed lower properties than the samples without sealant in every case. This result was not expected since the sealant is an added layer of protection between the composite and aluminum. It is possible that the sealant acted to concentrate any cathodic reaction on a limited area of the composite.

Specimens that were removed after 90 days showed some blistering and wrinkling of the primer. The glass, primer, sealant combinations are shown in table 3. The amount of degradation on the surface was not significantly different than the 30 day exposure samples. Bearing strength results were found to beslightly lower for the 90 day exposure specimens. The most interesting difference found was that the high temperature primed specimens with sealant had bearing strengths significantly lower than those of unsealed specimens (68.0 KSI vs 91.0 KSI). The control for this set of laminates was 86.0 KSI. This data supports the hypothesis that the sealant acts to concentrate the degradation process at the hole.

The third set of specimens prepared for exposure were open hole compression specimens. These samples consisted of 24 ply $(+45, 0, -45, 90)_{3s}$ IM-7/5250-4 connected to 2024 T6 aluminum sample of the same size with a titanium fastener in the center of the specimen. The coatings and isolation schemes used are shown in table 4. Several of the samples were scratched to simulate a flaw that may occur in the protection scheme during service. These specimens were also exposed in a salt spray environment for 30 days. After exposure, the specimens were disassembled and were tested at room temperature in an MTS test machine at a rate of .125 cm/min (.05 in/min).

These specimens showed some blistering of the primer. Scratched samples did not show any increased blistering over unscratched samples. Areas under blisters and near the fasteners showed some sign of resin damage however it was limited to the resin on the surface of the composite. Test results are shown in table 4. The data indicated that there was no significant change in the strength of the material after exposure. Non coupled control samples which were exposed for the same time had an average strength of 410 MPa (59.7 KSI) while the primed specimens which did not have a fiberglass barrier ply had a strength of 400 MPa (57.9 KSI). The use of topcoat and sealant provided a slight improvement in the strength.

The results of this testing indicate that the amount of composite that is effected by the degradation is small for this type of exposure. Specimen designs which test the mechanical integrity of the exposed surfaces are most sensitive to the degradation phenomena. The bearing strength is dependent on the quality of the material in the hole where the degradation process is concentrated. The compression strength was not affected because the small amount of degradation was insignificant in the test geometry.

Electrochemistry

In an effort to determine which variables in the process most strongly effect the rate and severity of degradation, a factorial test matrix was developed. An electrochemical cell was used to expose the BMI composite to various environments. The variables evaluated included salt concentration, oxygen concentration, pH, time, current density and temperature. Two levels of each variable were evaluated. The levels of each variable were as follows: Salt concentration .1 and 3.5%, aerated and dearated water, pH 7 and 11, 1 and 4 day exposure, temperatures of 25°C (75°F) and 83°C (180°F) and current densities of 40 and 160 micro amps per square centimeter. The specimen consisted of a 24 ply 5250-4 composite. Electrical connection was made to the composite by drilling a hole, sanding both surfaces to expose fibers, coating the hole and area around it with silver filled paint and installing a steel nut and bolt with the wire lead. The test area was then masked off and the specimens primed with epoxy primer and topcoated with urethane paint. Three samples were exposed at each condition listed in table 6. The test cell with the specimen is shown in figure 7. The composite specimen was the cathode and the platinum mesh electrode the anode. This cell allowed the duplication of the reactions in the freely corroding cell. Each test was replicated three times to eliminate extraneous results.

During exposure bubbles formed on the surface of the composite and in some specimens cracks and blisters formed as shown in (figure 8). Similar blisters were observed by Tucker and Brown (6) in graphite/vinyl ester laminates coupled to steel. After removal from the cell some of the specimens with little or no blisters were observed to have turned lighter in color. After exposure the specimens were tested in flexure. The results are given in table 5. The results showed that high current, high temperature and long times had the greatest effect on the specimen appearance and flexure strength. Many blisters and low flexure strengths were observed for specimens exposed under these conditions. Reduction of the data and determination of significant factors was performed on the flexure results. This screening showed that the variables were ranked in the following order; current density, time, temperature, oxygen concentration, pH, salt concentration. The most significant factors were current density, time and temperature. These variables had greater than .95 significance level. There was very little interaction between any of the variables. The lack of significance of the oxygen concentration is an important factor since oxygen is required for the reaction. Further study of this factor will be carried out in future studies.

Conclusion

The mechanical property testing performed indicated that bearing strength of BMI composites was most sensitive to the degradation caused by galvanic corrosion. Observation of the specimens showed that the damage to the inside of the hole was slight, however the effect on the composite bearing strength can be significant. The degradation which results from the 30 day salt spray exposure appears to only effect the exposed surface of the composite. Therefore, the bearing strength decreased but the open hole compression strength was not affected. Similarly, flexure tests on specimens exposed in the electrochemical cell showed large decreases in strength when the surface ply was blistered. However when the surface was only discolored there was only a minimal loss of strength.

The electrochemical tests point out that temperature, time and current density are important factors in the degradation process. The rate and severity of degradation are greatly effected by these factors while oxygen and salt concentration had little effect.

The Navy has dealt with corrosion and degradation in the past. Methods of preventing corrosion of metals and inspecting for corrosion are part of all aircraft production processes and maintenance manuals. Degradation of imide based composites is potentially rapid and severe. Strict attention must be paid to material selection, application and fleet inspection. Potential primary or critical application of imide composites must consider the associated risk of galvanic degradation vs alternate materials. The risk analysis must also consider the use of

corrosion resistant materials in structural components where the potential exists for a galvanic couple with imide based composites. The degradation of imide composites structures should be addressed through proper material selection, complete galvanic isolation during assembly, and inspection and maintenance in the fleet. However, the inspection rates and the repair processes required for support of these structures are unknown at this time.

Acknowledgements

The authors would like to thank D. Alley and B. Duffy for their help in specimen preparation and mechanical testing. They would also like to thank C. Hegedus, D. Hurst and B. Green for their help in selecting coatings and for painting the samples. In addition the authors acknowledge J. Boodey, V. Agerwala and J. DeLuccia for there helpful discussions on corrosion and degradation of materials.

References

1. Fischer, P. and DeLuccia, J. J., "Effects of Graphite/Epoxy Composite Materials on the Corrosion of Aircraft Alloys," Environmental Effects on Advanced Composite Materials, ASTM STP 602, ASTM, 1976, pp 50-66.
2. Thompson, S. D., White, B. L. and Snide, J.A., "Accelerated Corrosion Testing of Graphite/Epoxy Composites and Aluminum Alloy Mechanically Fastened Joints", Air Force Wright Aeronautical Laboratories Report # AFWAL-TR-84-3115, June 1985.
3. Brown, S.R. and De Luccia, J. J., "Galvanic Corrosion Fatigue Testing of 7075-T6 Aluminum Bonded With Graphite Epoxy Composite," Naval Air Development Center Report NADC-77328-60, Jan 1978.
4. Askins, D. R. "Hydrolytic Degradation of Kapton Film,"Air Force Wright Aeronautical Laboratories Report # AFWAL-TR-83-4125, Dec. 1983.
5 Wolf, C. J. and Soloman, R. S., "Ageing of Aromatic Polyimide Insulated Electrical Wire," SAMPE Jan/Feb 1984, pp16-19.
6 Tucker, W.C. and Brown, R., "Blister Formation on Graphite/Polymer Composites Galvanically Coupled with Steel in Seawater", Journal of Composite Materials, Vol 23, April 1989.

Table 1 Coating/sealant flexure test results

Coating/Sealant	Flexure Strength MPa
23377	1585
85582	1144
Koroflex	1523
Urethane	1781
23377/83430	1635
85582/83430	1583
Koroflex/83430	1648
Urethane/83438	1987
23377/81733	1741
85582/81733	1971
Koroflex/81733	1866
Urethane/81733	1756
23377/85285	2035
85582/85285	2041
Koroflex/85285	1575
Urethane/85285	1924
Unicoat	1894
Control	1753

Table 2: Bearing Results

PROTECTION SCHEME	STRENGTH (MPa) AVG	S
Water based primer, sealant	406	39.4
Solvent based primer, sealant	438	30.0
Water based primer	454	31.7
Solvent based primer	477	40.5
Water based primer, sealant, glass	436	38.6
Solvent based primer, sealant, glass	442	25.0
Water based primer, temperature aged	498	36.1
Solvent based primer, temperature aged	517	31.4
Control	550	32.1

Table 3 Three month bearing test results.

PROTECTION SCHEME	STRENGTH MPa	S
High temperature urethane	627	27
High temperature urethane, sealant, glass	469	10
Solvent based primer, sealant glass	403	21
Control	593	24

Table 4: Open Hole Compression Test Results

Protection Scheme	Strength (MPa) AVG	S
Bare / Primer / Sealant	399	16.5
Glass / Primer / Sealant	408	3.3
Bare / Primer / Topcoat	407	12.6
Bare / Primer / Topcoat / Sealant	422	15.1
Glass / Primer / Topcoat	398	14.5
Glass / Primer / Topcoat / Sealant	420	13.2
Glass / Primer / Topcoat / Sealant / Scratched	432	15.1
Control	427	18.6

Table 5 Electrochemical test results

RUN#	SALT %	OXYGEN	pH	TIME DAYS	TEMP °C	CURRENT DENSITY mA/cm2	FLEXURE STRENGTH MPa
1	.1	YES	7	1	83	40	1489
2	.1	NO	7	4	83	160	593
3	3.5	NO	11	4	25	160	855
4	.1	NO	11	4	25	40	938
5	3.5	YES	11	4	83	160	676
6	3.5	YES	7	4	25	40	1241
7	.1	NO	11	1	83	160	710
8	3.5	NO	7	4	83	40	986
9	.1	YES	11	4	83	40	1365
10	3.5	NO	7	1	25	160	1248
11	.1	YES	11	1	25	160	1152
12	3.5	YES	11	1	25	40	1420
13	3.5	NO	11	1	83	40	1055
14	.1	YES	7	4	25	160	972
15	.1	NO	7	1	25	40	1475
16	3.5	YES	7	1	83	160	882

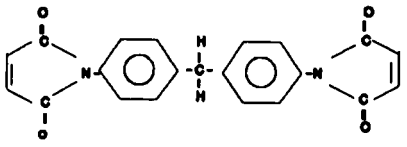

4,4 Bismaleimidodipheylmethane

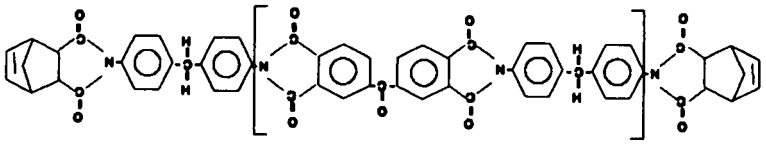

PMR-15

Figure 1 Chemical structure of bismaleimide and polyimide.

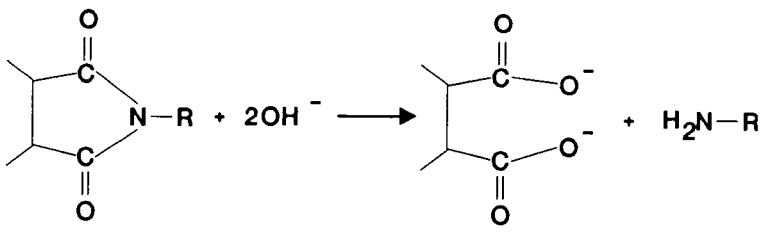

Figure 2 Imide degradation by base.

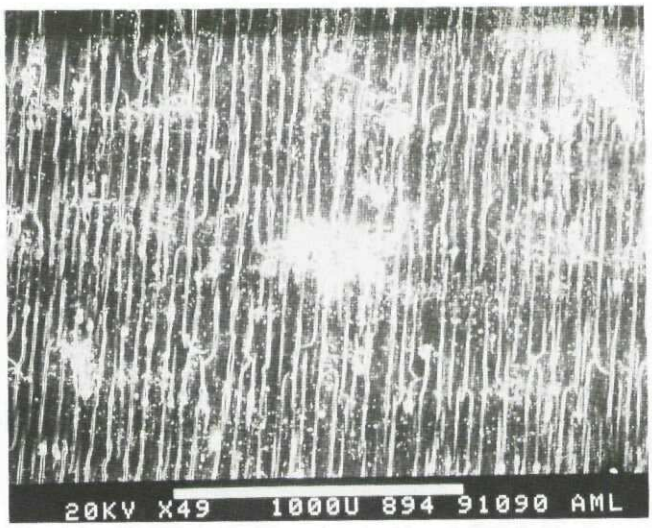

A Above degradation

B In the degraded area

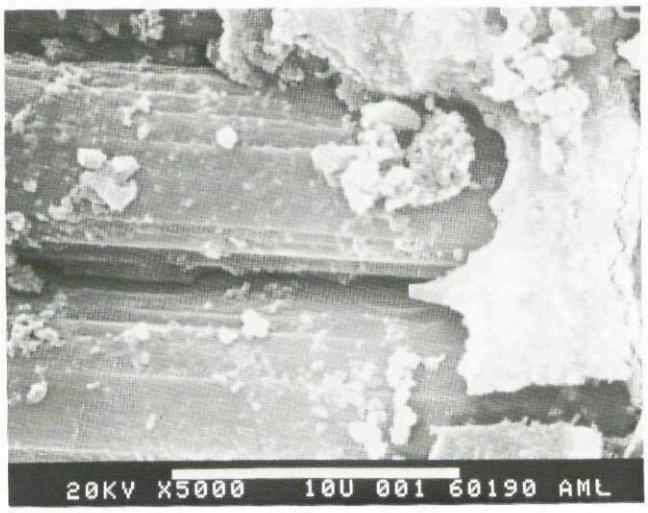

C In the degraded area

Figure 3 Electron micrographs of degraded surface

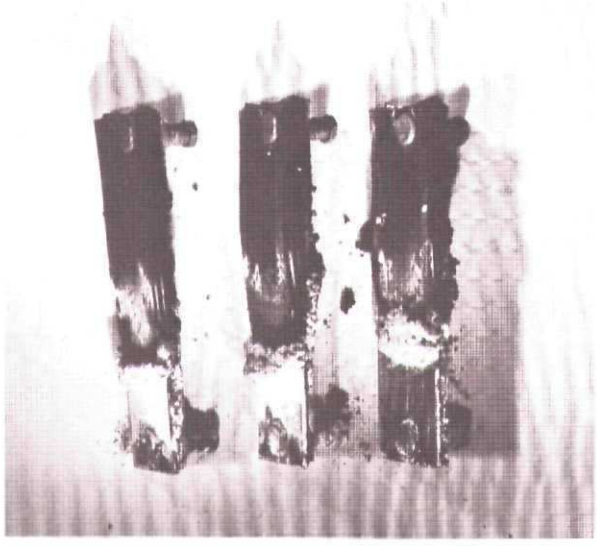

A Uncoated

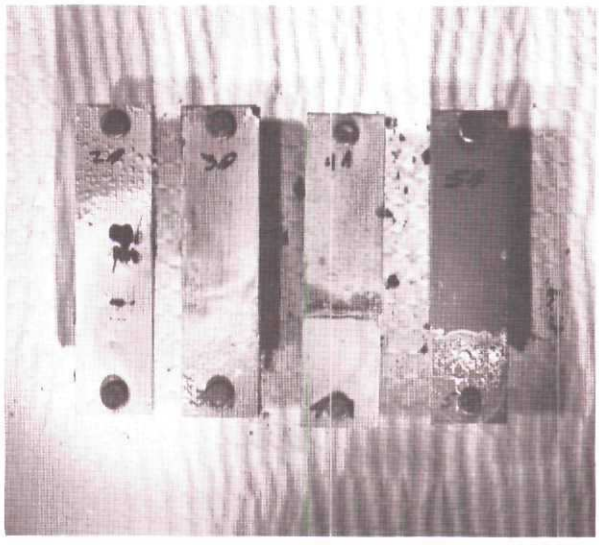

B Primer

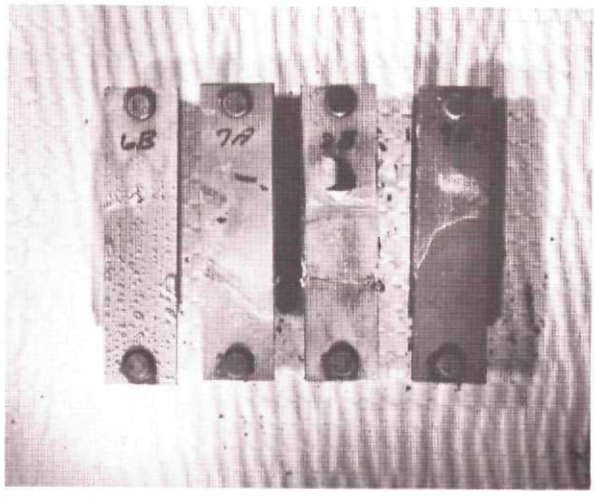

C Primer and Uninhibited sealant

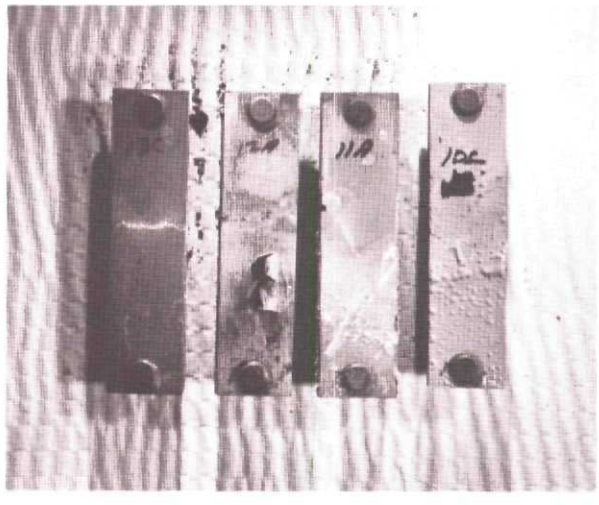

D Primer and inhibited sealant

Figure 4 Coating evaluation specimens

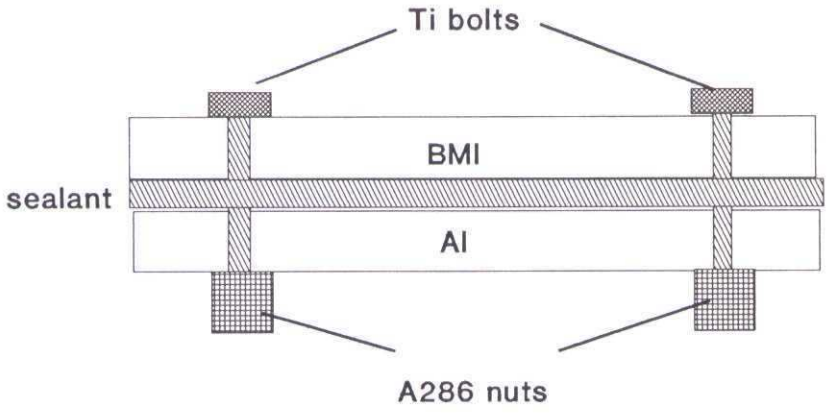

Figure 5 Salt spray exposure specimen

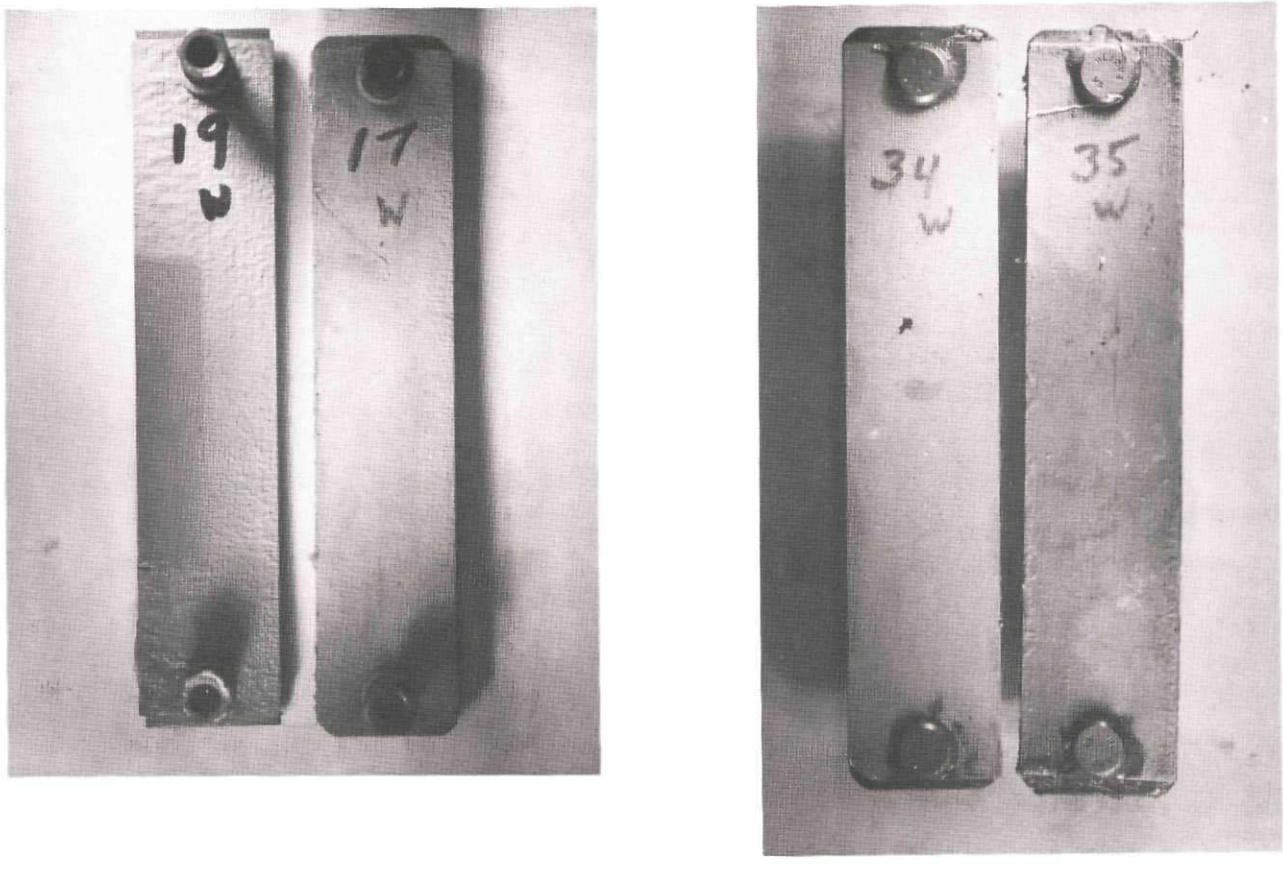

A No glass or sealant

B Glass and sealant

Figure 6 Bearing specimens after 1000 hr salt spray

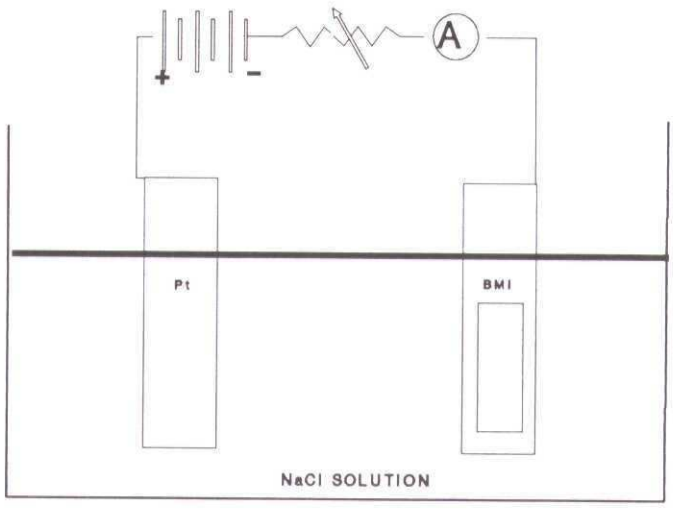

Figure 7 Electrochemical cell

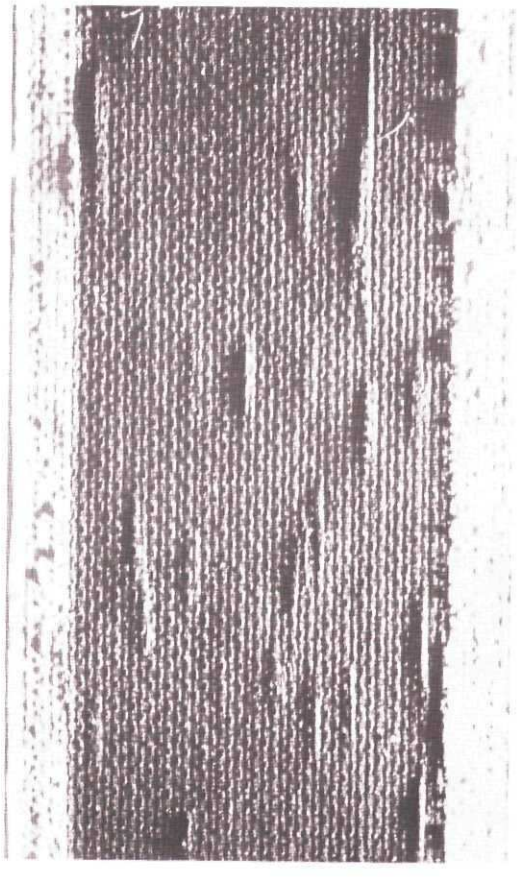

Figure 8 Surface of sample exposed in the electrochemical cell

PRISE EN COMPTE DES EFFETS DE L'ENVIRONNEMENT SUR LE COMPORTEMENT EN SERVICE DES STRUCTURES PRIMAIRES D'AVIONS EN MATERIAU COMPOSITE

HISTORIQUE ET SITUATION ACTUELLE

Jean Rouchon
Délégation Générale pour l'Armement
Centre d'essais aéronautique de Toulouse (CEAT)
31056 Toulouse cedex
France

RESUME

Lorsque furent envisagées les premières applications de matériaux composites à matrice organique dans les structures travaillantes d'avions, la préoccupation majeure des concepteurs et services officiels fut leur tenue au vieillissement. Quelques quinze années après, l'expérience acquise en service associée à de nombreux résultats de laboratoire a fortement dissipé ces craintes, tout au moins pour les structures ne faisant pas appel à un usage extensif des technologies de collage. Cela ne signifie pas que le vieillissement des composites n'existe pas, mais ses conséquences sont maintenant considérées d'une portée limitée et prévisibles, c'est à dire susceptibles d'être prises en compte au niveau de la conception, de la certification et du suivi en service des structures.
Cette publication retrace brièvement les principales étapes ayant conduit à la situation actuelle, puis analyse les différentes méthodes actuellement utilisées pour prendre en compte ces phénomènes de vieillissement, en particulier la détermination de la concentration d'eau absorbée en service par le composite. Cette analyse repose en grande partie sur la base des résultats d'un programme d'exposition naturelle aux intempéries sous charges cyclées en cours au CEAT.

1. INTRODUCTION

Le vieillissement est défini ici comme étant l'altération progressive, en cours d'exploitation de l'avion, des performances structurales. Avec les matériaux métalliques, la fatigue mécanique a été considérée pendant longtemps comme étant la cause principale de ce vieillissement, mais l'expérience récente a montré que l'importance de la corrosion avait été comparativement très sous-estimée. Fatigue mécanique et corrosion ne constituent pas à ce jour des problématiques particulières avec les structures en composite, mais par ailleurs, température et humidité se sont avérées capables d'influencer sensiblement leurs performances. L'altération des structures en composite par les dommages accidentels ne fait pas l'objet de cet article, cet aspect est largement développé dans les références [1] et [2].
Le vieillissement d'une structure en composite doit être appréhendé sous deux aspects : l'altération des propriétés mécaniques du composite proprement dit d'une part, et l'altération des fonctions d'assemblage propres aux principes constructifs utilisés (liaisons collées et/ou boulonnées) d'autre part.
L'altération des propriétés mécaniques du composite est susceptible de revêtir deux formes : la création de dommages structuraux tels qu'une fissuration interlaminaire par exemple, et la dégradation, c'est à dire la modification des propriétés intrinsèques de la matière. A l'inverse de la dégradation qui est un phénomène diffus, les dommages structuraux sont des phénomènes géométriquement définis et réputés détectables par inspection non-destructive.
Seules les liaisons collées présentent une sensibilité particulière au vieillissement. Les liaisons mécaniques pour lesquelles les phénomènes de corrosion galvanique étaient très redoutés au départ s'avèrent jusqu'à maintenant, grâce à des systèmes de protection relativement simples, d'une durabilité satisfaisante. De même que pour le composite proprement dit, l'altération de la liaison collée sera susceptible de revêtir deux formes : le dommage ou plus exactement le décollement, et la dégradation.
Le phénomène de dégradation est propre aux systèmes organiques, et relève de l'action combinée de l'humidité et de la température. Avec les composites, la dégradation ne concernera que les propriétés gouvernées par la matrice donc essentiellement la compression et le cisaillement interlaminaire. L'expérience acquise avec les époxydes, puisqu'il s'agit de l'unique famille de matériau actuellement utilisée dans les structures primaires d'avions, montre qu'admettre une relation de type univoque entre la concentration d'eau dans le composite et sa dégradation par le vieillissement, est une approximation considérée comme satisfaisante au niveau du dimensionnement des structures, ou des justifications par essais nécessaires à la certification ou homologation. Le problème se ramène donc à l'anticipation de la valeur maximale de cette concentration d'eau jusqu'au retrait de service des appareils concernés, la température extrême de la structure étant par ailleurs un paramètre beaucoup facile à déterminer.

2. EXPERIENCE ACQUISE DANS LE DOMAINE DU VIEILLISSEMENT DES STRUCTURES PRIMAIRES EN CARBONE

2.1 Expérience en service

Le tableau 1 résume l'expérience acquise en service début 1990 sur les principaux exemples d'application structurale des composites. Pour les éléments présentant une architecture conventionnelle du type structure monolithique avec fixations mécaniques, aucun problème lié à un éventuel effet du vieillissement et nécessitant des réparations structurales n'a été rapporté. Quelques problèmes ont été relevés avec les structures sandwiches, ils ont été le plus souvent le révélateur d'un problème d'assurance qualité ou d'un choix de matériau non approprié.
Un programme spécifiquement dévolu à l'étude des effets du vieillissement en service a été lancé par le STPA et l'Aérospatiale en 1980. Ce programme a consisté à monter 22 aérofreins en carbone sur certains avions du type A300B de la compagnie AIR FRANCE, à les suivre par un programme d'inspection non-destructive spécifique, puis à les prélever à des échéances prédéterminées pour mesurer leurs caractéristiques statiques résiduelles. Le tableau 2 issu de la référence [3] récapitule les résultats de ces essais, actuellement disponibles sur trois aérofreins. Pas plus ces

résultats que ceux du programme d'inspection non-destructive ne montrent d'évolution sensible de ces structures due au vieillissement. Ce programme qui doit se terminer en 1992, s'apparente à une étude lancée par la NASA en 1973 sur 108 aérofreins de B737 et dont les résultats ont été largement publiés [4].

Elément	Nombre	1° élément en service depuis	Nombre d'h. de vols accumulé
Dérive Airbus	> 200	1985	9000
Gouverne de direction Airbus	> 300	1983	20000
Voilure V10F	1	1985	3300
Ailerons Falcon 50 ou 900	280 x 2	1977	565000
Dérive et surfaces mobile M2000	>150 av. livrés	1982	120000

Tableau 1

	Type 1 nappe carbone		Type 2 tissu carbone
Durée de service effective sur avion	60 mois	51 mois	47 mois
Nombre d'atterrissages réalisés	5483	5645	4519
Résistance statique résiduelle	3,5 CL	3,3 CL	3,5 CL
Résultat essai d'un aérofrein neuf	3 CL		3,6 CL

Tableau 2

Un programme équivalent de suivi en service d'éléments en composite d'avions d'arme (ailerons F1, dérive M2000) a été lancé par le STPA et Dassault Aviation. Ce programme arrive maintenant aux premières échéances de prélèvement de pièces.

2.2 Expérience en essais accélérés

On se limitera dans ce domaine aux seuls essais où il a été tenté de simuler aussi fidèlement que possible les conditions réelles rencontrées en service, c'est à dire la combinaison de la fatigue mécanique et du cyclage thermohygrométrique. Début des années 80, le CEAT s'était équipé de quatre installations capables de la réalisation de tels programmes :
-deux installations spécialement dévolues aux essais structuraux
-deux installations adaptées aux essais de matériau et éprouvettes technologiques.
Plusieurs programmes ont été réalisés grâce à ces installations, ceux concernant des éléments de structure sont récapitulés tableau n°3.

Eléments de structure ayant subi un essai de fatigue combiné à un cyclage thermo-hygrométrique au CEAT
-Aérofrein A300B
-Aileron F50
-Aileron Mirage F1
-Caisson de flexion/torsion V10F

Tableau 3

Au niveau matériaux et éprouvettes technologiques, les principales études ont été réalisées dans le cadre de l'opération V10F et d'un programme spécifique à l'étude de l'influence d'un cyclage thermohygrométrique représentatif d'une mission d'avion de combat [5]. Le principe général de ces différentes études était de superposer un cyclage thermohygrométrique à des sollicitations de fatigue d'un niveau représentatif des sollicitations effectivement rencontrées en service (pour fixer un ordre de grandeur, environ 30% de la résistance statique). Des exemples des cycles réalisés sont représentés figures 1 et 2 . On remarquera que le cycle de la figure 2, représentatif d'une mission d'avion de combat, se différencie de celui de la figure 1, notamment par une incursion à haute température simulant une croisière à vitesse supersonique. Les effets du vieillissement étaient mesurés au travers de l'évolution des performances statiques des éprouvettes entre l'état réputé neuf et l'état vieilli, le tout assorti d'un programme d'inspection non-destructive. Les conclusions qui ont pu être tirées de ces différentes études ont été que la chute de résistance statique observée après ces vieillissements réputés représentatifs, n'était pas significativement supérieure à celle qui pouvait se déduire de la connaissance de la concentration en eau du matériau, et n'apparaissait pas influencée par l'histoire (effets de cyclage) ayant conduit à cette concentration. Des études réalisées par d'autres laboratoires européens où les cyclages thermo-hygrométriques étaient superposés à des essais classiques de fatigue à rupture (tracé d'une courbe de Wöhler) ont pu aboutir à des conclusions différentes.
De tels essais n'ont pas été reconduits dans les plus récents programmes de certification de structures primaires en composite (A320 et ATR 72).

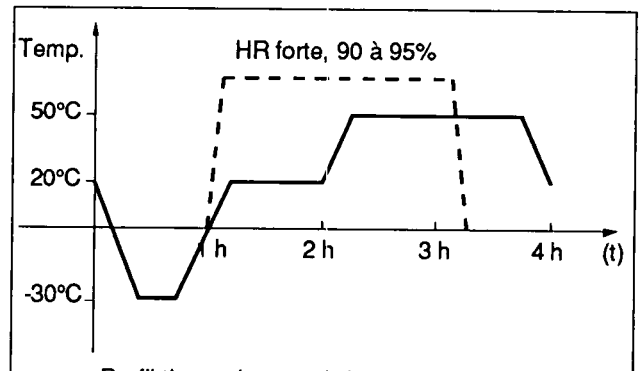

Profil thermohygrométrique type "avion de transport civil "(tiré du programme V10F)

Figure 1

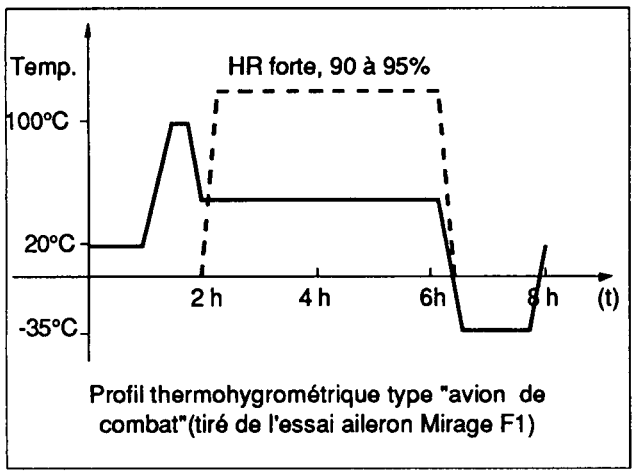

Profil thermohygrométrique type "avion de combat"(tiré de l'essai aileron Mirage F1)

Figure 2

2.3 Les essais sous exposition naturelle aux intempéries

Conscient que ces essais accélérés en laboratoire ne prenaient pas en compte l'effet de durée d'exposition et certains autres paramètres liés à l'exposition naturelle (rayonnement, facteurs biologiques), le CEAT a lancé en 1983 un programme d'étude du comportement des composites en exposition naturelle (sur le site de Toulouse) combiné, ce qui fait l'originalité de ce programme, à des sollicitations de fatigue. Les matériaux étudiés sont le T300/N5208 et le T300/914. Les éprouvettes sont représentatives de détails de dessin de structure réputés critiques (voir figure 3) : une éprouvette monolithique percée avec trou habité sollicitée en compression, et une enture à deux rangées de fixations sollicitée en traction. Ce programme a été lancé sur dix ans, et les résultats sont déjà disponibles après les prélèvements à deux ans et demi et cinq ans. Ces résultats sont rapportés dans les références [6] et [7]. La figure 4 issue de ces références montre qu'il n'a pas été observé, jusqu'à ce jour, de variation significative des performances statiques après vieillissement. Ceci confirme les conclusions provisoires de l'expérience en service, exposées § 2-1.

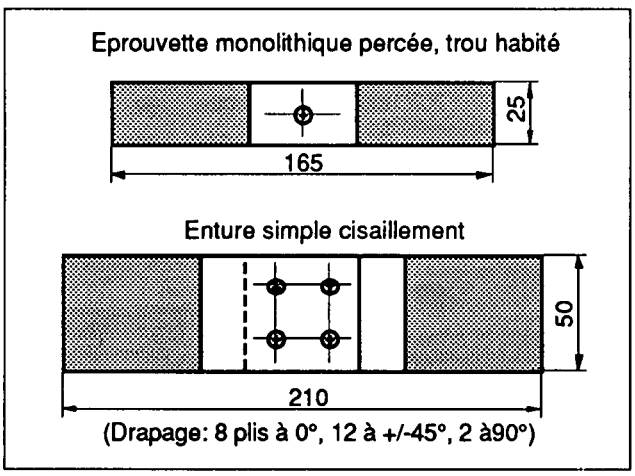

Figure 3

L'ensemble de ces résultats est encourageant, et explique l'actuelle "baisse de pression" relative à ces problèmes de vieillissement en service des composites. Il est toutefois important de noter que les premières pièces montées sur avions en service en Europe n'ont pas encore accumulé 10 années d'exploitation, alors que les problèmes importants récemment rencontrés (problèmes dits des "vieux avions") sont apparus à des échéances ultérieures. En conséquence, éluder définitivement le problème serait prématuré, prudence et humilité demeurent encore nécessaires.

3. DETERMINATION DE LA CONCENTRATION D'EAU ABSORBEE A LONG TERME PAR LES COMPOSITES

La sensibilité au vieillissement humide d'un composite, en terme de concentration en eau absorbée dans un environnement donné, est une caractéristique intrinsèque du matériau. S'il est admis que la connaissance de cette concentration constitue une approximation suffisante pour quantifier la dégradation, due aux effets de l'environnement rencontré en service, d'un matériau composite à matrice époxyde, celle-ci mérite d'être déterminée de façon rigoureuse. Lorsque la modélisation est utilisée à cet effet, les modèles doivent être validés par des résultats expérimentaux aussi représentatifs que possible des durées effectives d'exposition. Alors que les avions sont actuellement conçus pour des durées d'exploitation de 20 à 25 ans, les modèles utilisés pour déterminer l'absorption d'eau (Fick, Langmuir) ont été au mieux validés sur quelques cycles thermohygrométriques réalisés en laboratoire. Il existe donc un grand besoin d'accumuler des résultats dans ce domaine, en particulier en faisant "voler" des éprouvettes suiveuses sur des avions, ou en effectuant des mesures par dessiccation sur des échantillons prélevés dans des pièces retirées de service (exemple dans le cadre des programmes spécifiques relatés en fin de § 2-1).

3.1 Les résultats expérimentaux disponibles

La figure 5 montre l'évolution de la masse d'échantillons non peints exposés en ambiance naturelle à Toulouse pendant 5 ans. Une augmentation de la masse est observée en début d'exposition, puis ensuite les phénomènes d'érosion superficielle dépassent en importance l'accroissement de l'humidité absorbée. Cette méthode de mesure n'est donc pas valable, et peindre les échantillons ne fait que reporter le problème à l'échéance ultérieure de la dégradation de la protection. En conséquence, la méthode la plus fiable est la mesure gravimétrique par dessiccation des échantillons après prélèvement, tout en essayant de prendre en compte les phénomènes de rémanence par piégeage de l'eau susceptibles d'exister. Des résultats obtenus au CEAT suivant cette méthode seront exposés à la fin de ce paragraphe.

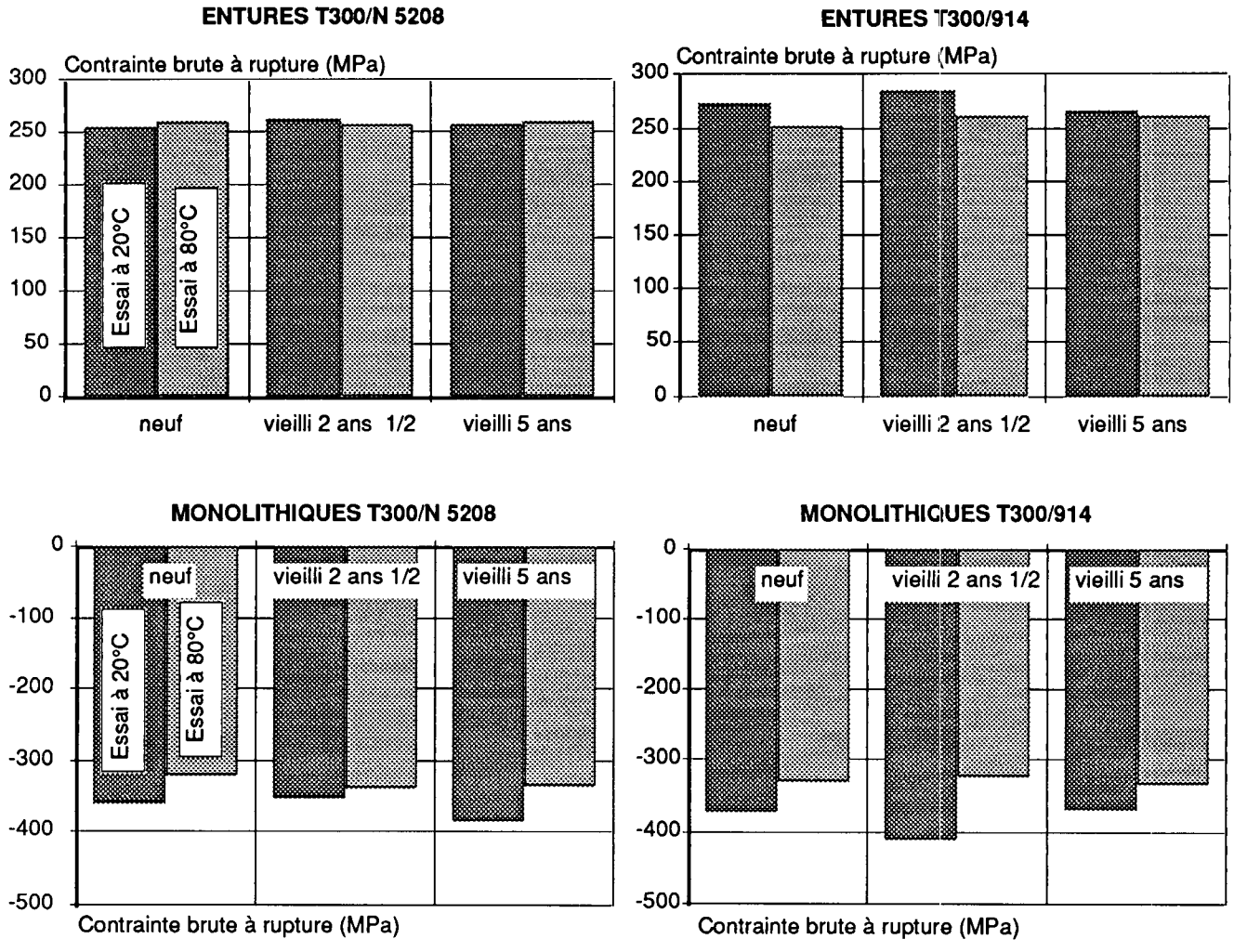

Figure 4

Les premiers résultats disponibles relatifs à des mesures d'absorption d'eau pendant des durées significatives (au moins cinq ans) sont dus à des programmes soutenus par la NASA, dont une synthèse est présentée dans la référence [8] . C'est sur le matériau T300/N 5209, dénominateur commun à plusieurs de ces programmes, que le plus de résultats sont disponibles. Des expériences réalisées par MBB-UT en RFA ont montré que la concentration maximale en eau mesurée pour ce même matériau (soit 0,8%) dans les conditions climatiques les plus sévères correspondait environ à celle absorbée à l'équilibre dans une exposition à 70°C/70% HR. Un programme d'éprouvettes suiveuses en T300/913C, attenantes à des spoilers montés sur A300 B4 exploités par Thai Airways (localisation géographique réputée sévère vis à vis de l'humidité) a donné une concentration à l'équilibre d'environ 1,1% laquelle correspond également à un conditionnement en atmosphère constante à 70°C/70% HR. Cette dernière expérience était également pilotée par MBB-UT. C'est à partir de ces observations sur deux matériaux que cette règle d'équivalence a été extrapolée à tous les matériaux composites utilisés dans l'A320, dans le cadre des justifications structurales associées à la certification de cet avion.

D'autres résultats d'essai obtenus depuis remettent en cause cette règle d'équivalence. Ces résultats sont toujours extraits de l'étude CEAT [6] [7] et concernent deux matériaux : le T300/N5208 réputé comme un des moins sensibles à l'humidité dans la catégorie des matrices époxydes, et le T300/914 réputé un des plus sensibles (du moins à l'intérieur des résines durcissant à 180°C). Les mesures ont été effectuées par dessiccation à 70°C jusqu'à équilibre d'échantillons de 50 x 30 mm prélevés dans les surlongueurs des éprouvettes d'enture dont les résultats ont été donnés § 2-3.

Les résultats de ces mesures, jusqu'à cinq ans, sont récapitulés tableau 4. Il est intéressant d'observer que pour ces matériaux considérés au départ comme très différents au niveau de leur caractère hydrophile, simultanément exposés à quelques cm l'un de l'autre, les résultats obtenus sont quasiment équivalents.

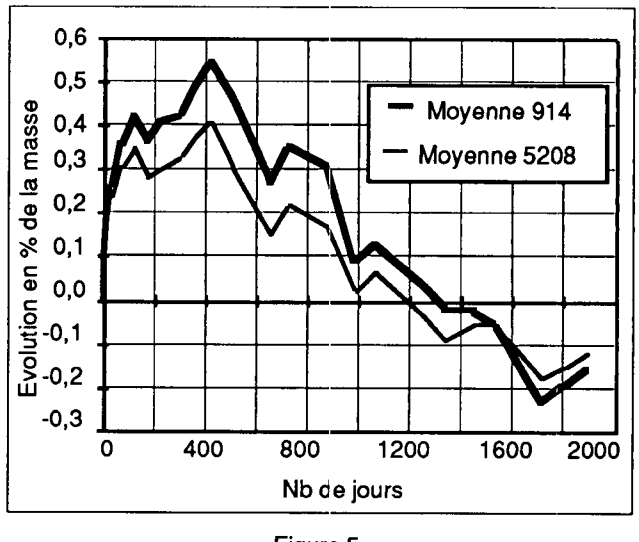

Figure 5

		Masse restituée par les échantillons après dessiccation	
		Après 2 ans 1/2	Après 5 ans
MATERIAU	T300 N5208	0,68%	0,90%
	T300 Ciba 914	0,71%	0,88%

Tableau 4

3.2 La modélisation

L'absorption de l'humidité par les composites est un processus de diffusion contrôlé qui a été modélisé à partir de la théorie de la diffusion de Fick. De nombreuses publications existent sur le sujet, avec pour point de départ les travaux de Shen et Springer [9] . Les limites de ce modèle, en particulier pour ce qui concerne certaines matrices et les températures élevées, ont été rapidement mises en évidence [10].
Un modèle plus évolué (Langmuir) prenant en compte une certaine non-réversibilité du phénomène (effet de piégeage de l'eau par fixation sur un nombre limité de sites) a été également développé. Il a fait l'objet de certains travaux en France [11] mais est néanmoins peu répandu.
Ces modèles devraient permettre, à partir des caractéristiques du matériau et de ses conditions d'exposition en termes de profils de température et d'humidité, de connaître à tout moment l'humidité contenue dans le composite. Relativement dépensiers en temps de calcul, ces modèles ne tolèrent pas une discrétisation très fine des conditions d'environnement. Pour les échantillons du tableau 4, exposés pendant cinq ans à TOULOUSE, un calcul a été effectué avec 60 segments représentant les valeurs moyennes mensuelles d'humidité relative et de température sur le site. Les résultats sont représentés figure 6.

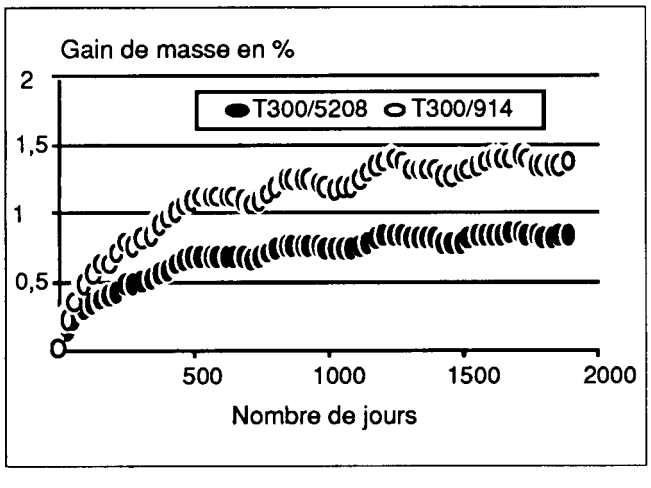

Figure 6

La simplification maximale de cette discrétisation consiste à ne considérer qu'un seul segment représentant l'humidité relative moyenne du site pendant les cinq années d'exposition (soit HR 79,7% dans ce cas précis). En lui associant la valeur de la température moyenne il est possible, à partir du même modèle, de démontrer que les échantillons précités ont atteint un état d'équilibre avant cinq ans. Cet état correspond à une humidité absorbée de 1,34% pour le T300/914 et 0,82% pour le T300/N5208 (voir figure 7 les conditions du calcul). Ces valeurs sont très proches de celles obtenues avec la discrétisation en 60 segments de la figure 6, respectivement 1,37% pour le T300/914 et 0,83% pour le T300/N5208.

	T300/N5208	T300/914
C 79,7%	0,82%	1,34%

Conditions de calcul:

$C = Cmax \left(\frac{HR}{100}\right)^b$; $b = \begin{cases} 1,316 \text{ (N5208)} \\ 1,548 \text{ (914)} \end{cases}$

C = concentration à l'équilibre, pour une HR constante donnée

Cmax=saturation (pour HR 100%)
= 1,1%(N5208)
= 1,9%(914)

Figure 7

Cette méthode de discrétisation en couples de segments associés représentant respectivement la température et l'humidité relative moyennes enregistrées pendant 1 jour, une semaine, un mois etc... est remise en cause par une étude du Royal Aircraft Establishment [12]. Il est proposé une pondération de ces valeurs pour tenir compte des corrélations naturelles existant, dans un climat donné, entre la température et l'humidité relative ambiante durant la journée.

3.3 La corrélation théorie/expérience

Dans le cas du T300/N5208, la concentration réelle en eau mesurée au bout de cinq ans est un peu plus élevée que celle prédite par l'analyse (0,90% au lieu de 0,83%) alors que pour le T300/914 elle est, par contre, très inférieure à la prédiction (0,88% au lieu de 1,37%). Un écart aussi sensible mérite une recherche des causes possibles.
La première explication à considérer serait l'existence d'une fraction rémanente d'eau, piégée par le matériau. La figure 8 illustre les résultats d'un essai de saturation (à 70°C dans de l'eau distillée) réalisé sur les échantillons qui avaient été utilisés pour mesurer, par déshydratation, la concentration en eau au bout de cinq ans. La partie droite de cette même figure illustre les résultats d'essais de saturation et de déshydratation (toujours à 70°C) réalisés simultanément sur des échantillons identiques prélevés au bout de cinq ans de vieillissement. Les valeurs montrent que la "capacité" du matériau à absorber de l'eau (1,8 - 1,9%) n'a pas été modifiée par rapport aux hypothèses de calcul, ce qui écarte donc l'hypothèse de l'existence d'une forte proportion d'eau piégée par le T300/914. La même expérience a été réalisée sur le T300/N5208 et les résultats obtenus, illustrés figure 9, montrent que pour ce matériau également, il n'y a pas lieu de considérer une part importante d'eau piégée par le matériau.

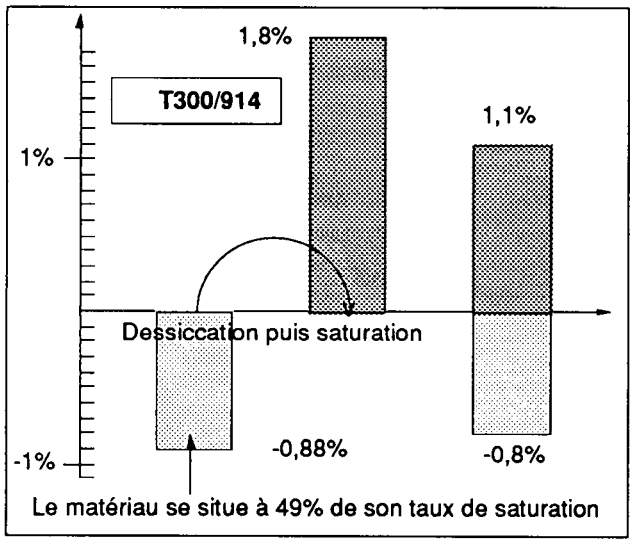

Figure 8

La figure 10 illustre des résultats d'essais de cisaillement interlaminaire réalisés à 100°C sur des échantillons prélevés dans des coupons identiques ayant subi : cinq ans de vieillissement naturel, cinq ans de vieillissement naturel plus une déshydratation, cinq ans de vieillissement naturel plus une saturation en eau à 70°C. Ces résultats sont normalisés par rapport à la valeur obtenue la plus forte (échantillons secs). La chute de caractéristiques après vieillissement seul étant identique pour les deux matériaux (≠ 10%), ceci confirmerait, comme les mesures de concentration en eau, que le T300/914 est moins sensible au vieillissement humide, s'il est exposé en ambiance naturelle réaliste, que ce que laissaient supposer les valeurs mesurées après les traditionnels conditionnements à 70°C. Une conclusion inverse, mais à un bien moindre degré, semblerait se dessiner avec le T300/N5208.
Cette constatation conduit tout naturellement à remettre en cause la mesure des paramètres nécessaires à l'application de la loi de Fick (en particulier le taux de saturation) par des conditionnements à des températures trop élevées ou plus exactement trop différentes de celles existant en service.

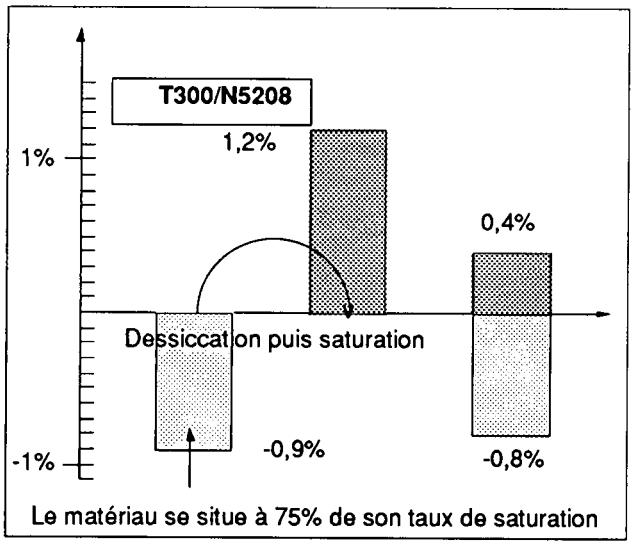

Figure 9

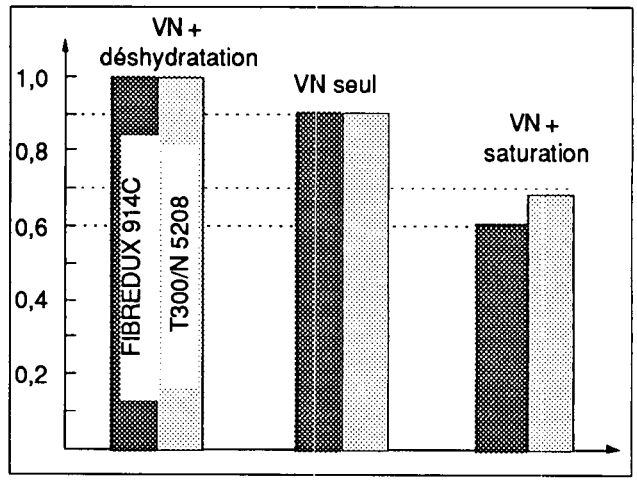

Figure 10

4. PRISE EN COMPTE DU VIEILLISSEMENT DANS LES ESSAIS DE JUSTIFICATION STRUCTURALE

Sachant que la concentration en eau d'un composite soumis à un environnement donné est dépendante de sa nature plus ou moins hydrophile, la solution la mieux appropriée consiste à définir un environnement constant, forfaitaire en terme d'humidité relative ambiante, dans lequel l'état d'équilibre du matériau correspondrait effectivement à la concentration maximale d'eau susceptible d'être atteinte en service. Des résultats présentés dans cette publication ont montré que la valeur de 70% HR qui avait été démontrée et utilisée dans le cadre des justifications structurales associées à la certification de l'A320 ne pouvait pas être étendue sans précaution à tous les autres matériaux composites. La valeur de 85% HR déjà acceptée en Europe dans le domaine des avions de combat devrait dorénavant servir également de référence dans le domaine des avions civils, à moins que des résultats d'essai en exposition représentative pendant des durées significatives ne justifient des valeurs moins conservatives.
Cette condition d'environnement, généralement associée à la température de 70°C pour les époxydes durcissant à 180°C, sera utilisée pour déterminer la concentration maximale en eau absorbée à prendre en compte pour chaque matériau composite. Cette valeur constituera par la suite l'objectif à atteindre, contrôlé par des éprouvettes suiveuses d'épaisseurs et drapages représentatifs, dans les essais structuraux destinés à mettre en évidence l'influence du vieillissement. Il est une pratique courante de réaliser ces conditionnements à une valeur plus élevée de l'humidité relative afin de raccourcir leur durée. Augmenter, aux mêmes fins, la température du conditionnement n'est pas une pratique recommandée, car il est nécessaire de rester dans un domaine où les lois de comportement du matériau, relativement à l'absorption d'humidité, sont réputées ne pas être modifiées.
L'application des règlements de navigabilité relatifs à la certification des structures, n'exige pas des essais d'ensemble systématiques avec simulation du vieillissement. Celui-ci peut être pris en compte par l'utilisation de coefficients majorateurs sur les charges ou par l'analyse à partir de résultats d'essai obtenus sur des échantillons représentatifs des caractéristiques du matériau et des principes constructifs utilisés. Une telle pratique paraît relativement peu recommandée à l'auteur dans le cas de solutions technologiques faisant largement appel au collage, où l'essai de vieillissement humide est susceptible d'être le révélateur des principaux problèmes liés à ce type de solution : choix inadéquat des matériaux, assurance qualité, etc...

5. CONCLUSION

L'expérience maintenant accumulée en service depuis l'introduction des composites dans les structures travaillantes d'aéronefs a considérablement tempéré les premières craintes quant à la susceptibilité à l'environnement de tels matériaux. Il est maintenant démontré que leur "vieillissement", exprimé en terme de dégradation des propriétés mécaniques intrinsèques de la matière, est d'une portée limitée et peut être pris en compte par l'analyse.

Admettre que ce vieillissement est l'unique effet de l'humidité absorbée par le matériau et qu'il existe une relation univoque entre la concentration d'eau dans le composite et ses performances structurales résiduelles constituent, à ce jour, une approximation suffisante pour appréhender le phénomène. A partir de là, les évaluations par essai de type cyclage thermohygrométrique (ou climatique) sur des ensembles structuraux ont perdu leur raison d'être et ont été progressivement remplacés au milieu des années 80, par des conditionnements à paramètres constants permettant d'aboutir au même résultat en terme de concentration d'eau finale dans le matériau. Il serait néanmoins imprudent d'extrapoler une telle approche démontrée avec les époxydes, à toutes les nouvelles matrices organiques, réputées à ténacité améliorée, apparaissant maintenant sur le marché, sans l'avoir redémontrée au travers d'essais sur coupons et éprouvettes technologiques élémentaires.

L'utilisation de méthodes analytiques pour déterminer cette concentration en eau, à partir des profils thermohygrométriques rencontrés par l'aéronef au sol et en vol, a montré rapidement ses limites. Ceci non seulement en raison de la nature mathématique des modèles, mais très certainement de par la dépendance des caractéristiques "matériau" qui sont nécessaires à leur application, à des paramètres tels que la géométrie, le drapage, les effets de bord, la température, le vieillissement physique, etc... Continuer à améliorer ces modèles pour les rendre plus précis, pourrait conduire à une complexité de mise en oeuvre sans aucune mesure avec l'ampleur du problème qui est à résoudre.

La définition d'un environnement constant, forfaitaire en terme d'humidité relative ambiante, dans lequel l'état d'équilibre du matériau correspondrait effectivement à la concentration maximale d'eau susceptible d'être atteinte en service est une solution préférable. Un consensus se dessine actuellement en Europe sur une telle approche avec une valeur forfaitaire de l'humidité relative égale à 85%. Ces conditions seront en effet appliquées à la certification des structures en composite du nouvel Airbus A330/340, ainsi que pour les avions d'arme français [13] en particulier l'ACT/ACM Rafale, dont la cellule comprend environ 28% de matériau composite.

Si l'altération par le vieillissement des performances structurales des matériaux composites proprement dits apparaît aujourd'hui comme un phénomène bien maîtrisé, on ne peut considérer qu'il en est de même pour les solutions d'assemblage de type liaison collée souvent utilisées avec ces matériaux. De tels principes constructifs, toujours très performants du point de vue du devis de masse, continuent à nécessiter une attention particulière au niveau de la sélection des matériaux, de l'assurance qualité, des essais de justification structurale, et du suivi en service.

REFERENCES

[1] Rouchon, J. "Certification of large airplane composite structures., recent progress and new trends in compliance philosophy" 17th ICAS congress, Stockholm 1990.

[2] "Justification en fatigue/tolérance aux dommages des structures en composite pour avions civils" Note technique CEAT n° 1/M/88, révision 1 du 30/11/88.

[3] Radondy, R. "Expérimentation des aérofreins en carbone sur A300B Air France" Rapport Aérospatiale n° 442.011/89.

[4] Coggeshall, Randy, L. "737 graphite composite spoiler flight service evaluation" 7th annual report NASA CR-165826, February 1982.

[5] "Comportement des matériaux composites soumis à un environnement thermohygrométrique cyclé, combiné à de la fatigue mécanique" PV CEAT n° M1 5383.

[6] "Etude des effets à long terme du vieillissement des composites carbone-époxy, par exposition naturelle aux intempéries sous charges cyclées" Résultats du prélèvement à 2 ans et demi, PVCEATn°M1 6413, partiel 1.

[7] "Etude des effets à long terme du vieillissement des composites carbone-époxy, par exposition naturelle aux intempéries sous charges cyclées" Résultats du prélèvement 5 ans, PV CEAT n° M1 6413, partiel 2 (à paraître).

[8] Dexter, H.B. and Baker, J.B. "Worldwide flight and ground-based exposure of composite materials" ACEE Composite structures technology, NASA Conference Publication 2321.

[9] Shen, C.-H. and Springer, G.S. "Moisture absortion and desorption of composite materials" Journal of composite materials 10 (january 1976) pp 2-20.

[10] Whitney, J.M. and Browning, C.E. "some anomalies associated with moisture diffusion in épxoy matrix composite materials" ASTM STP 658 (1978).

[11] Dewas, J. et Favre, J.P. JNC 5 (1986) Pluralis Paris.

[12] Collings T.A. "The effect of observed climatic conditions on the moisture equilibrium level of fibre reinforced plastics" Composites, 17, pp 33-41 (1986).

[13] "Conditions de justification des structures d'avion d'arme en matériaux composites" Note N° 012/90/STPA/EG3.

Fluid Effects: Thermoset and Thermoplastic Matrix Composites

D.B. Curliss
WL/MLBC
Wright-Patterson AFB, OH 45433-6533

1. SUMMARY

The sensitivity of several advanced aerospace composite materials to military jet fuel, JP-4, was investigated in this study. The following fiber/matrix prepreg materials were used in this investigation: AS-4/3501-6; IM7/8551-7A; IM7/977-2 (1377-2T); IM7/5250-4; IM8/HTA; and AS-4/PEEK(APC-2). The materials were chosen as representative state-of-the-art materials in their classes of standard epoxy, toughened epoxy, toughened BMI, and thermoplastic matrix composites respectively. The materials were processed into $[\pm 45]_{2S}$, $[0]_{12T}$, and $[90]_{12T}$ laminates using the manufacturer's recommended process cycle and standard quality assurance checks were performed on the panels. Standard geometry coupons were fabricated from the panels and divided into a control set and test set. The test coupons were immersed in JP-4 in a sealed pressure vessel at 180°F. The weight gain was recorded as a function of the square root of time and the jet fuel was exchanged each time the coupon weight was recorded. In general, the thermoset matrix composites did not pick-up significant levels of fuel in any lay-up examined; while the thermoplastics did absorb JP-4. The amount of JP-4 absorbed by the thermoplastic matrix composites was dependent on the lay-up. After 1680 hours of total exposure time the mechanical properties of the coupons were evaluated. G_{12} was determined from the $[\pm 45]_{2S}$ coupons and E_{flex} and σ_{flex} were determined for the $[0]_{12T}$ and $[90]_{12T}$ coupons. In addition, the creep compliance, $S_{12}(t)$, was determined for APC-2 with various thermal processing cycles and after exposure to JP-4. G_{12} for the thermoplastic matrix composites was markedly lower at elevated temperatures in the fuel exposed specimens than in the control specimens, due to plasticization of the matrix. The 0° and 90° thermoset matrix composites flexure specimens exposed to JP-4 had lower strengths than did the control specimens. The lower strength is attributed to degradation of the interface between the fiber and matrix. Scanning electron microscopy was used to examine the failure surfaces. The flexure modulus in the 90° flexure specimens was not affected by exposure to JP-4 while the 0° flex modulus was lower in the fuel exposed coupons than in the control coupons. The creep rate for quenched APC-2 control specimens was always greater than the standard slow cooled APC-2. After exposure to JP-4, however, the slow cooled specimens had greater creep rate than the quenched specimens exposed to JP-4. This is most likely due to greater plasticization of the matrix in the slow cooled coupons, since they absorbed a great deal more JP-4 than the quenched specimens.

2. INTRODUCTION

The issue of the interaction between organic matrix composite materials and fluids which they may be exposed to during their lifetime has been controversial. It is well understood that advanced composites utilizing thermosetting resins absorb moisture when exposed to high humidity environments. The absorption of moisture causes plasticization of the resin with concurrent swelling and lowering of the resin's glass transition temperature (Tg). This results in a reduced service temperature of the composite. This phenomena has been studied and well characterized (1,2). Composite materials are typically tested after exposure to temperature and humidity to determine the reduction in mechanical properties.

The effects of other aircraft fluids which are in contact with these materials over their lifetime has not been as well characterized. There are no current industry standards to assess possible effects. A typical exposure test may involve submersion of the materials in the fluid at room temperature for seven days. The material is then mechanically tested at room temperature. Typically no reduction in properties occurs from this type of exposure. Therefore, it is concluded that the fluids tested have no significant effect on the mechanical properties and that a "hot/wet" exposure represents the worst case environmental conditions.

Recent investigations of thermoplastic matrix composites have determined that these materials absorb some aircraft fluids (3,4). An attempt was made to correlate this data with other fluid studies. However, because there are no current industry standards for testing fluid exposure, it was impossible to compare or correlate any existing data.

An Air Force sponsored study was conducted (5) in an attempt to assess current industry practice for testing composites in fluids. The procedures employed by companies surveyed were so varied that it was extremely difficult to correlate data from one participant to another. These variations ranged from the number of plies and orientation to the choice of fluid, exposure time, and exposure conditions.

Aircraft composites may be exposed to relatively aggressive fluids, such as jet fuel at elevated temperatures, on a daily basis for as long as 20 or 30 years. Because of this it is important to gain a fundamental understanding of the effects of aircraft fluids on composite materials. Several issues have been raised relative to the sensitivity of advanced composites to aircraft fluids. These include: a) realistic temperatures and time, b) the definition of typical in-service mechanical state during exposure, c) the development or selection of a mechanical test to measure the effects of fluid exposure on composites, and d) understanding the mechanisms of interaction between the fluid and the composite.

In this study we have adopted the approach of trying to gain a better understanding of the fundamental mechanisms of interaction of the aircraft fluid with the composite. Our view is that if the fundamental mechanisms of interaction are understood then this information can be used to understand the effect of fluid interaction on the macroscopic properties of more complex composite materials. This approach includes exposure of the composite at an elevated temperature until saturation (or apparent saturation) is achieved, weight gain versus time and coupon configuration, determination of diffusion mechanisms, effects of weight gain on physical and mechanical properties, and absorption/desorption studies.

There are several aircraft fluids of concern. Hydraulic fluid, paint strippers, cleaners, and jet fuel are among those of most concern. In this study we have chosen to evaluate only the effect of jet fuel since very little is known about this and also because it is very difficult to protect the composite from this fluid.

3. EXPERIMENTAL PROCEDURES

3.1 Sample Preparation

The materials used in this study, the supplier of the material, and the cure or consolidation cycle used are given in table 1. The cure or consolidation cycles are those recommended by the supplier and in all cases were found to give quality laminates. The thermoset materials were all autoclave cured using a standard net resin bagging technique; the thermoplastic materials were all press consolidated. After processing, the panels were C-scanned to verify that they were free of porosity. Photomicrograph specimens were also made from several different sections in the laminates to verify uniform fiber distribution. Acid digestion of specimens taken from various sections of the laminates was used to obtain the fiber volume of each laminate. Differential Scanning Calorimetry, Thermogravimetric Analysis, and Thermomechanical Analysis were also used to verify that the laminates were of expected quality. Test specimens were cut from laminates using a water-cooled diamond impregnated saw and the edges were finished using a fine grit paper. All specimens were then dried in a vacuum oven and weighed and measured. The control specimens were stored in a desiccator until testing, and the exposure specimens were immediately placed in the exposure vessels.

For the APC-2 creep compliance studies at different processing cycles, quenched +/-45° specimens were prepared by cold press transfer consolidation. X-ray scattering was used to determine that the quenched specimens were amorphous.

3.2 Jet Fuel Exposure

Military jet fuel, type JP-4, was used in this study as the exposure fluid. JP-4 is an extensively used jet fuel and is a more aggressive solvent than another widely used jet fuel, JP-8. JP-8 has lower levels of low molecular weight aromatic hydrocarbons and is also less volatile than JP-4. Therefore, JP-4 was chosen as a "worst case" fluid.

Composites may be exposed to jet fuel at temperatures greater than ambient because of several factors such as aerodynamic heating of the structures and radiant heating. Fuel may even be used as a cooling medium for aircraft systems and is heated in the process. We chose 82°C as a representative temperature for exposure of the composites to fuel. Specially made vessels were used to contain the jet fuel and coupons at temperature. The vessels were constructed of stainless steel aircraft hydraulic tubing and had flare fittings with copper gaskets to assure a leakproof seal. The vessels were filled with JP-4 and the composite coupons, leaving only a minimal head space for thermal expansion. This was done to prevent differences in liquid and vapor phase compositions of the JP-4. The low molecular weight aromatic components of the jet fuel are likely to absorb into the composites to the greatest extent; therefore an effort was made to ensure that these components were of the highest possible concentration in the liquid phase. The specimens were sealed in the vessel and then the vessels were placed into a convection oven at temperature. Periodically the vessels were cooled down and the specimens were wiped off and weighed. At each weighing the fuel was exchanged with fresh fuel from the same batch. The exchange was done in an attempt to maintain the same composition in the exposure vessel. The coupons were exposed to jet fuel for a total of 1680 hrs.

3.3 Thermal Analysis

Differential Scanning Calorimetry (DSC), Thermogravimetric Analysis (TGA), and Thermomechanical Analysis (TMA) were performed on each laminate produced and on specimens after exposure to JP-4. DSC was performed with a DuPont Model 910 DSC, TGA was performed with a DuPont Model 951 TGA, and TMA was performed with a DuPont Model 943 TMA. The DuPont equipment was controlled with an Omnitherm Atvantage II IBM PS/2-60 data station.

Sample size ranged from 5 mg to 15 mg for the DSC and TGA while the TMA used 6 mm X 6 mm X laminate thickness for samples. TMA and TGA were performed under an inert atmosphere. All tests were performed at a standard heating rate of 10°C/min. In addition to standard quality assurance, TGA isothermal aging was performed on laminates after exposure to JP-4 to determine if weight change during mechanical testing at elevated temperatures would be a problem. The specimens were aged at their maximum test temperature up to 45 min. and showed no measurable weight loss due to fuel desorption.

3.4 Dynamic Mechanical Analysis

Dynamic Mechanical Analysis (DMA) was performed on both the control and fuel exposed specimens. The $[0°]_{12T}$ coupons were used in a forced torsion geometry on a Rheometrics RDS-II dynamic mechanical spectrometer. The shear storage and loss moduli were determined as a function of temperature at 1Hz ($G'(T)_{\omega=1Hz}$ and $G''(T)_{\omega=1Hz}$). The heating rate used was 10°C/min. These data were used to determine the Tg of the coupons, for a quality control check and also to determine if there is a detectable Tg depression due to the fuel absorption.

3.5 Mechanical Testing

The mechanical test matrix used to evaluate the effect of the jet fuel exposure is given in Table 2. The tests (with the exception of 90° flex and 0° four point shear) were conducted at room temperature, 82°C, and an elevated temperature indicated in Table 2. These temperatures were chosen low enough to be in the elevated temperature dry service range of the composites, but high enough to see the effect of the JP-4 on the properties. The span-to-depth ratio was 32:1 for the 0° and 90° four point flex tests and 16:1 for the 0° four-point shear.

3.5.1 *Four Point Flexure Testing*

The four-point flex testing was performed in accordance with ASTM standard D790-81 on an Instron test frame. The crosshead speed in all flex and the 0° four-point shear was 0.127cm/min. Crosshead displacement was used to calculate mechanical properties for the 0° flex and 0° shear, while the 90° flex specimens were strain gauged on their tensile surface.

3.5.2 *+/- 45° Tension Testing*

The +/- 45° tension testing was performed in accordance with ASTM standard D3518-76(82) on an MTS test frame. The samples were all strain gauged and the loading rate was 44.5N/sec. The specimens were only tested to approximately 0.3% axial strain so end-tabbing was not necessary.

Creep tests were also performed on the +/-45° strain gauged specimens. The deformations used were determined to be linear and recoverable. The MTS test frame was used to apply loads to the specimen in approximately 0.2 seconds (without overshoot or oscillation).

3.6 Scanning Electron Microscopy

The 90° flex failure surfaces and the "3-direction" surface of the 90° flex control and fuel exposed coupons were examined using a JEOL 840 scanning electron microscope. The samples were coated with Palladium-Gold and examined using 10kV. The "3-direction" surface was examined for crazing due to fuel exposure, and the failure surfaces were examined for fiber/matrix adhesion and any other characteristics of the 90° flex failure.

3.7 Desorption Analysis

A specially designed apparatus was used to extract and trap the components of jet fuel that were absorbed into the composite specimens. This apparatus is shown schematically in Figure 1. The fuel exposed coupons are loaded into the sample chamber and the entire apparatus is repeatedly purged with nitrogen to remove all air then evacuated under continuous vacuum. The chamber is heated to approximately 316°C and held for 1 hr. Any volatiles from the laminates are collected in the cold trap. The desorption process is quantitative, as the weight of the laminates after desorption is identical to their weight before exposure to JP-4. The condensate is diluted with spec grade n-pentane and collected. The samples are then analyzed using GC-MS. This technique allows for separation of the components in the mixture (GC) and their identification (MS). This technique can also be used to qualitatively determine the relative amount of each component in the mixture.

4. RESULTS AND DISCUSSION

4.1 Jet Fuel Exposure Results

The weight gain plotted versus the square root of time is shown for the thermoplastic $[+/-45°]_{2S}$ coupons in Figures 2 and 3 and for the $[0°]_{12T}$ in Figure 4. Figure 2 is the weight gain characteristics for the conventionally processed APC-2 and HTA thermoplastic matrix composites. Figure 3 shows the weight gain curves for APC-2 as a function of the processing cycles investigated. The fuel absorption of the thermoset matrix [+/-45°] coupons was identical to the thermoset matrix unidirectional coupons so it is omitted here. The weight gain trends of the $[90°]_{12T}$ coupons were identical for all materials to the $[0°]_{12T}$ specimens so that data is not presented.

The $[+/-45°]_{2S}$ thermoplastic laminates, APC-2 and the IM8/HTA, both picked up approximately 0.85 weight percent (wt%) jet fuel and reached an apparent saturation value. However, in the 0° and 90° unidirectional coupons the APC-2 did not pick up a significant amount of jet fuel and the IM8/HTA absorbed only approximately 0.35wt%. This difference may be attributed to several factors such as residual stress, crystallinity and crystal morphology (in

APC-2), fiber wicking, or microcracks. If fiber wicking were responsible for the observed difference there should be a difference between the 0° and 90° unidirectional coupons. However, these configurations have virtually identical weight gain characteristics. Thus, fiber wicking has been ruled out as a mechanism for absorption in this case. Photomicrographs of the +/-45°, 0°, and 90° coupons show no microcracking so this has been ruled out as a cause of the difference. The crystal morphology of the APC-2 may be different in the angle ply laminates and the unidirectional laminates, but this was not investigated in this study. The state of stress in a polymer has been directly related to the diffusion of solvents (6) in polymers and this is the most likely reason for the difference in absorption characteristics between the different laminate configurations.

The thermoset matrix laminates, with the exception of IM7/8551-7A, absorbed less than 0.1wt% in all laminate configurations. There was also large scatter in the measurements because of the low level of fuel absorbed and the small number of coupons exposed. The IM7/8551-7A system had a very pronounced weight gain between 48 hrs and 168 hrs, after which the weight gain remained constant within the scatter. The 8551-7A is a very complex heterogeneous resin system. The unusual absorption characteristics are attributed to the complex phase structure of the resin.

Other than demonstrating that the absorption of jet fuel into the composites is non-fickian, no attempt has been made to model the diffusion behavior of the composites from this data. Much more testing will be required to make any conclusions about the nature of the diffusion process.

4.2 Thermal Analysis Results

The thermal analysis performed on the control specimens was used primarily for quality assurance, verifying that the Tg, crystallization temperature (Tc), and endotherm peaks were all characteristic of the materials evaluated. Thermal analysis on the fuel exposed specimens was performed to detect changes in Tg and phase transitions. The thermoset matrix composites did not absorb any appreciable jet fuel, and there are no significant changes in their DSC, TMA, or TGA scans. The APC-2 DSC scan did have a larger heat of crystallization for the +/-45 laminate configuration exposed to jet fuel than for the +/-45 control coupon. TGA-MS results have indicated that there is a large volatile evolution that occurs with the crystallization transition. This could contribute to the larger heat of crystallization. The TMA scan of the APC-2 +/-45 exposed to JP-4 indicated a Tg of 106°C. This is an approximately 40°C decrease in the Tg for the fuel soaked coupons. The TMA of the IM8/HTA specimen did not yield a distinct glass transition. The thermal analysis data are presented in their entirety in a separate report (7).

4.3 Dynamic Mechanical Results

The results of the DMA are summarized in Table 3. There was very little effect of the jet fuel on AS-4/3501-6 and IM7/977-2, but all of the other materials experienced drop in their Tg, as measured by the storage and loss modulus respectively. The Tg from the storage modulus transition for APC-2 is 137°C as opposed to 106°C from the TMA measurement. This is due to the large difference in absorbed JP-4 content between the $[+/-45°]_{2S}$ (0.85wt% JP-4) coupon used for the TMA and the $[0°]_{12T}$ (0.05wt% JP-4) coupon used for the DMA measurements.

4.4 Mechanical Testing Results

The results of the test matrix (Table 2) are given in Table 4. No measurements of error or standard deviation are given because of the low number of specimens tested.

4.4.1 *0° Four-Point Flexure Results*

At room temperature all of the materials exposed to JP-4 had lower flex strength and moduli than the controls. The same trend was observed in the specimens tested at 82°C. With the exception of IM7/5250-4, the specimens tested at their respective elevated temperatures (See Table 2 for temperatures) exhibited no measurable difference in strength and modulus between the control specimens and those exposed to JP-4.

The decrease in room temperature properties could be attributed to several factors such as: a) decrease in matrix modulus due to plasticization, b) degradation of the fiber/matrix interface from the solvent absorption, or c) surface microcracks or crazing from thermal cycling or JP-4 absorption. With the exception of IM8/HTA the 0° laminates did not absorb an amount of fuel sufficient to plasticize the materials to the degree observed. In addition, crazing is usually observed in polymers exposed to very good solvents. JP-4 is not a good solvent for the matrix polymers evaluated. Degradation of the fiber/matrix interface could be a possible explanation for the observed decrease in four point flex properties. This phenomenon will be discussed further in the next section.

The elevated temperature results support the hypothesis that degradation of the interface could be occurring. The effect of temperature on the composite properties is overwhelming the effect of temperature.

4.4.2 *90° Four-Point Flexure Results*

The $[90°]_{12T}$ coupons were only tested at room temperature. There is no measurable difference in the moduli; however the strengths are dramatically lower in the coupons exposed to JP-4 than are the control coupons. The 90° flex is very sensitive to interfacial adhesion, thus this data supports the hypothesis that there is degradation of the fiber/matrix interface. The SEM photographs in Section 3.4.3 give some supporting evidence that the interface has degraded. The 90° flex is also very sensitive

to surface flaws, such as crazing. However, SEM evaluation of the surfaces showed no evidence of crazing.

4.4.3 *0° Four-Point Shear Results*

The 0° four point shear strengths of the coupons exposed to fuel were only slightly lower than the control coupons. More testing will be required to determine if the 0° four-point shear test is sensitive to the effects of fluid exposure on composites.

4.4.4 *+/- 45° Tension Results*

The +/-45° tension test is used to determine the In Plane Shear (IPS) Modulus, G_{12}. G_{12} is very sensitive to the composite matrix, and is a good measure of plasticization due to solvent absorption. The angle-ply laminates also absorb much more solvent than do the unidirectional coupons. Thus, the IPS evaluation is viewed as a litmus test for fluid exposure testing.

Table 4 shows a measurable effect of the jet fuel exposure on G_{12} for most of the materials. The largest differences between the control specimens and those exposed to JP-4 were observed in the thermoplastics. The APC-2 was tested at an elevated temperature of 121°C which is above its fuel soaked Tg of approximately 106°C. Based on this we would expect a dramatic drop in the modulus at 121°C. The APC-2 retains only 42% of the 121°C control G_{12}. The IM8/HTA also exhibits a significant drop in elevated temperature properties due to plasticization from the jet fuel. The IM8/HTA retains 84% of the 177°C control G_{12}.

Figures 5 and 6 are plots of the creep compliance, $S_{12}(t)$, at room temperature and 100°C comparing the creep after exposure to JP-4 (Figure 3.) of APC-2 that has been slow cooled from the melt state to APC-2 that has been quenched from the melt state. In both cases, contrary to our intuitive expectations, the relatively amorphous APC-2 absorbed less JP-4 than the slow cooled APC-2, and consequently had a lower creep rate.

4.5 Scanning Electron Microscopy Results

We choose IM7/8551-7a as representative of the property degradation exhibited by the thermosets. The 90° flex strength of the fuel soaked specimen was only 52% of the control specimen; while the modulus of the fuel soaked specimen was 96% that of the control. Similar results were observed for all of the thermoset matrix composites evaluated. Our hypothesis is that the mixture of hydrocarbons must degrade the interfacial adhesion between the fiber and matrix. SEM analysis supports this belief. There appear to be many more "clean" fibers in the fracture surface of the coupons exposed to JP-4.

4.6 Desorption Results

The jet fuel extracted from the APC-2 IPS sample was analyzed using GC-MS and the results are presented in Table 5. For purposes of comparison the GC-MS analysis of JP-4 used for exposure is also presented. The extracted fuel is nearly entirely composed of aliphatic substituted benzene components, while the JP-4 sample is predominantly low molecular weight paraffin and olefin hydrocarbon components. To estimate some relative measure of concentration, all component peaks were normalized to the octane peak. Only one component, 1,2-dimethylbenzene, is common to both samples, but the desorbed sample has a concentration nearly 18X greater than in the JP-4 sample. Thus, it appears that the aromatic components of JP-4 are selectively absorbed and concentrated in the APC-2 specimen. A complete analysis of the GC-MS data is presented in a separate report (7).

5. CONCLUSIONS

A technique was developed to expose composite materials to volatile and inflammable fluids at elevated temperatures. Exposure to JP-4 at elevated temperatures has been demonstrated to have a significant effect on the performance of advanced thermoplastic and thermoset matrix composite materials. The mechanism of property degradation on the thermoplastic matrix composites evaluated appears to be a plasticization of the matrix polymer. The mechanism in the thermoset matrix composites evaluated appears to be degradation of the fiber/matrix interface. Further work in this area will focus on the following topics: a) effect of the state of stress in the matrix on absorption of JP-4; b) investigation of the degradation of the fiber/matrix interface; and c) use of high pressure dilatometry to measure the glass transition temperature of exposed specimens.

6. ACKNOWLEDGEMENTS

The authors gratefully acknowledge the assistance of the University of Dayton Research Institute personnel for performing some of the material characterization and mechanical testing reported here. We would also like to thank Michael S. Arnett for his many hours in the laboratory preparing the specimens for testing and fluid absorption.

7. REFERENCES

1. C.E. Browning, G.E. Husman, and J.M. Whitney in, Composite Materials: Testing and Design (Fourth Conference), ASTM STP 617, American Society for Testing and Materials, 1977, pp. 481-496.

2. C.D. Shirrell, and J. Halpin in, Composite Materials: Testing and Design (Fourth Conference), ASTM STP 617, American Society for Testing and Materials, 1977, pp. 481-496.

3. AF Contract No. F33615-86-C-5058 "High Temperature Thermoplastic Processing"

4. AF Contract No. F33615-84-C-5029 "Exploratory Development of Thermoplastic Composite Processing"

5. C.L. Hamermesh, Proceedings of the Sixth Industry/Government Review of Thermoplastic Composites (1989).

6. S.R. Lustig, Ph.D. Thesis, Purdue University, West Lafayette, IN (1989).

7. D.B. Curliss "The Effect of Jet Fuel on Advanced Aerospace Composites I: Thermal and Chemical Analysis," WL TR-91-4017.

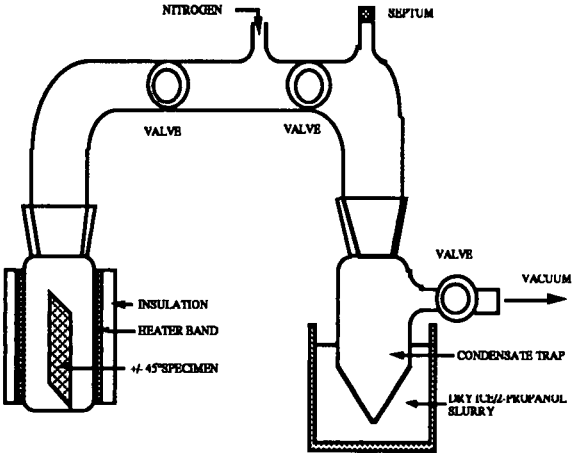

Figure 1. Schematic diagram of apparatus used to desorb JP-4 from thermoplastic matrix composite coupons.

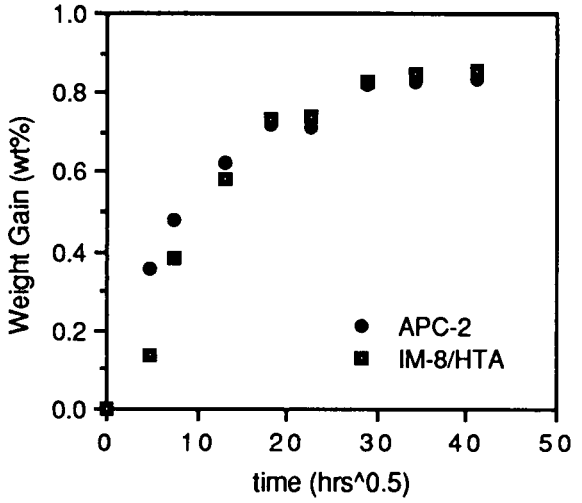

Figure 2. JP-4 weight gain characteristics for standard process (see Table 1.) APC-2 and IM8/HTA ±45° coupons.

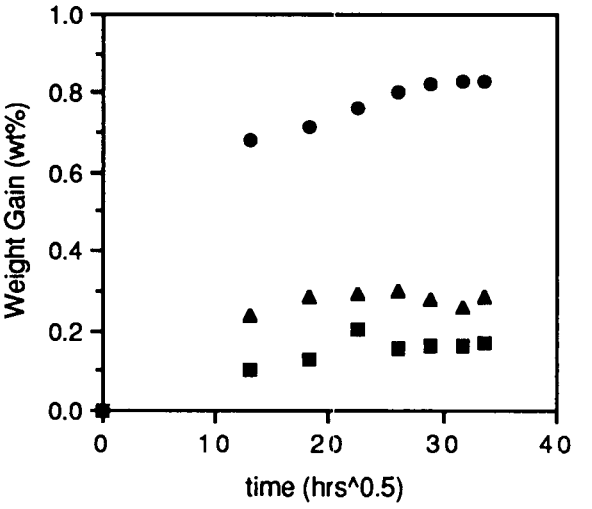

Figure 3. JP-4 weight gain for APC-2 ±45° coupons for various processing cycles. The circles are slow cooled (see Table 1.), the triangles are quenched, and the squares are quenched/annealed at 160°C.

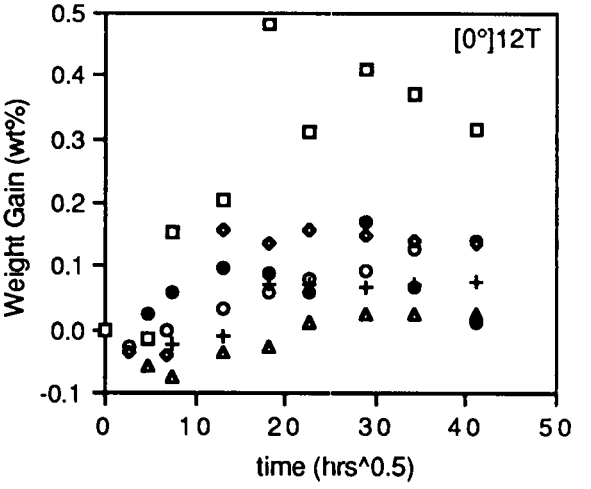

Figure 4. JP-4 weight gain for 0° laminates for materials given in Table 1. Symbol meanings are as follows: open square, IM8/HTA; diamond, IM7/8551-7A; solid circle, APC-2; open circle, AS4/3501-6; cross, IM7/977-2; and triangle, IM7/5250-4.

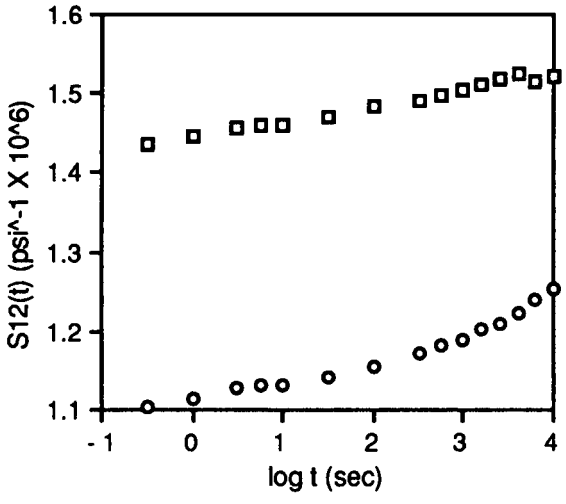

Figure 5. Creep Compliance for APC-2 ±45 after exposure JP-4, at room temperature.

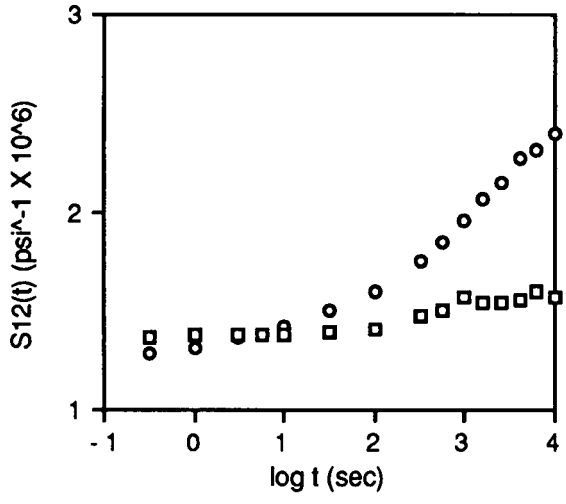

Figure 6. Creep Compliance for APC-2 ±45 after exposure JP-4, at 100°C.

Table 1. Materials and Process Conditions Used.

Material	Supplier	Cure Cycle
AS-4/3501-6	Hercules	Heat to 116°C, 60 min. @ 586 KPa. Heat to 177°C, 6 hrs. @ 655 KPa.
IM7/8551-7A	Hercules	Heat to 180°C, 250 min. @ 620 KPa.
IM7/977-2(1377-2T)	ICI/Fiberite	Heat to 99°C, 60 min. @ 690 KPa. Heat to 177°C, 3 hrs. @ 690 KPa.
IM7/5250-4	BASF/Narmco	Heat to 149°C, 45 min. @ 586 KPa. Heat to 191°C, 6 hrs. @ 586 KPa. Post-cure @ 227°C for 6 hrs.
AS-4/PEEK(APC-2)	ICI/Fiberite	Heat to 382°C, 30 min. @ 1379 KPa.
IM8/APC(HTA)	ICI/Fiberite	Heat to 357°C, 30 min. @ 1379 KPa.

Table 2. Mechanical Test Matrix for JP-4 Exposure Study

MATERIAL	CONDITION	0° 4-PT Flex*			90° 4-PT Flex	0° 4-PT Shear*	±45° Tension**		
		RT	82 °C	ET1***	RT	RT	RT	82 °C	ET1
AS-4 / 3501-6	CONTROL	3	3	3	3	3	3	3	3
	JP-4	"	"	"	"	"	"	"	"
IM-7 / 5250-4	CONTROL	3	3	3	3	3	3	3	3
	JP-4	"	"	"	"	"	"	"	"
IM-7 / 8551-7A	CONTROL	3	3	3	3	3	3	3	3
	JP-4	"	"	"	"	"	"	"	"
IM-7 / 977-2	CONTROL	3	3	3	3	3	3	3	3
	JP-4	"	"	"	"	"	"	"	"
AS-4 / PEEK (APC-2)	CONTROL	3	3	3	3	3	5	5	5
	JP-4	"	"	"	"	"	"	"	"
IM-8 / APC (HTA)	CONTROL	3	3	3	3	3	3	3	3
	JP-4	"	"	"	"	"	"	"	"

***AS-4 / 3501-6 ET1 =149 °C
IM-7 / 8551-7A 121 °C
IM-7 / 5250-4 177 °C
IM-7 / 977-2 149 °C
AS-4/PEEK (APC-2) 121 °C
IM-8/APC (HTA) 177 °C

* ASTM # D790-81
length = 6.35 cm
width = 1.14 cm
thickness = 0.16 cm

** ASTM# D3518-76(82)
length = 13.9 cm
width = 1.91 cm
thickness = 0.10 cm

Table 3. Dynamic Mechanical Analysis Results.

Material	Control, G'	JP-4, G'	Control, G"	JP-4,G"
AS-4/3501-6	181	182	205	200
IM7/8551-7A	195	181	219	206
IM7/5250-4	243 (272)	258	266 (313)	276
IM7/977-2 (1377-2)	174	178	194	193
AS-4/PEEK (APC-2)	150	137	167	157
IM8/HTA	262	253	273	264

*Temperature in °C, Heating Rate =10°C/min, Numbers in Parenthesis are Rescan

Table 4. Mechanical Test Results

MATERIAL	COND.	0° Flex* RT	0° Flex* 82 °C	ET1***	90° 4-pt Flex* RT	0° 4-pt Shear* RT	±45 Tension** RT	±45 Tension** 82 °C	ET1***
		MOD/STR (GPa/MPa)	MOD/STR (GPa/MPa)	MOD/STR (GPa/MPa)	MOD/STR (GPa/MPa)	STR (MPa)	MOD (GPa)	MOD (GPa)	MOD (GPa)
AS4/3501-6	CNTRL	118.5/1841.0	131.3/1698.0	100.7/1161.0	10.5/85.3	100.6	5.8	5.3	4.3
	JP-4	86.0/1493.0	87.9/1346.0	101.3/1162.0	9.3/39.8	93.7	6.2	5.8	3.5
IM7/5250-4	CNTRL	153.8/1772.0	170.8/1756.0	128.4/1131.0	10.4/83.4	100.4	7.0	6.8	5.9
	JP-4	111.1/1399.0	113.5/1330.0	113.3/1029.0	10.5/46.2	92.0	6.9	6.1	5.4
IM7/8551-7a	CNTRL	151.3/1671.0	157.7/1468.0	138.9/1229.0	9.6/92.8	91.2	6.4	5.6	5.1
	JP-4	115.1/1259.0	105.3/1120.0	134.4/1216.0	9.3/47.9	74.6	6.5	5.4	5.4
IM7/977-2	CNTRL	138.5/1678.0	147.9/1402.0	125.6/1048.0	10.2/107.6	96.8	5.7	5.7	4.5
	JP-4	107.1/1299.0	97.8/1116.0	122.4/1004.0	10.0/68.0	88.0	6.3	5.6	3.4
AS4/PEEK	CNTRL	141.0/1875.0	150.2/1619.0	125.7/1211.0	11.4/136.5	107.1	6.7	6.0	5.4
(APC-2)	JP-4	100.8/1515.0	102.7/1347.0	126.0/1234.0	11.2/135.8	99.2	5.9	5.4	2.3
IM8/HTA	CNTRL	169.9/1472.0	186.6/1277.0	152.8/865.0	8.8/99.2	85.0	4.9	4.8	4.0
	JP-4	122.3/1182.0	125.2/1084.0	153.0/949.0	9.0/82.6	89.5	4.7	4.1	3.4

Table 5. GC-MS Results (Octane is used as reference).

No.	Desorbed	A/Ao	JP-4	A/Ao
1	octane	1.0	2,3-dimethylpentane	2.3
2	1,2-dimethlybenzene	8.9	heptane	1.9
3	1-ethyl-3-methylbenzene	31.8	methylcyclohexane	1.4
4	1-ethyl-2-methylbenzene	9.4	octane	1.0
5	1,2,3-trimethylbenzene	34.4	2,6-dimethylheptane	0.1
6	1,2,4-trimethylbenzene	17.9	ethylcyclohexane	0.5
7	1-methyl-3-propylbenzene	8.8	2-methyloctane	0.4
8	1,4-diethylbenzene	32.2	1,2-dimethylbenzene	0.5
9	2-ethyl-1,4-dimethylbenzene	21.8	nonane	1.0
10	1,2,4,5-tetramethylbenzene	31.8	3,4,4-trimethyl-2-hexene	0.1

JET FUEL ABSORPTION AND DYNAMIC MECHANICAL ANALYSIS OF CARBON FIBRE COMPOSITES

by

S. A. Paipetis and V. Kostopoulos
Department of Mechanical Engineering
University of Patras, Patras 260 01, Greece

Abstract

Fluid absorption of carbon fibre composites, both thermosetting and thermoplastic, immersed in jet fuel under controlled conditions of time and temperature, was determined and, in the sequence, DMA studies were performed. Storage modulus, loss factor and glass transition temperature were the parameters utilized for the evaluation of the dynamic behaviour of said materials.

1. INTRODUCTION

Structural composites applied in vehicles driven by various kinds of thermal engines are subject to the influence of chemical reagents associated with the presence of a large number of fluids, among which fuels, hydraulic oils, lubricants etc. are only a few, besides humidity, salt water etc. normally existing in the environment.

The effect of water absorption on the various properties of polymeric composites has been studied extensively, see for example [1, 2], and it is well known how sensitive thermosetting matrices are, absorbing up to 5% b.w. water, as opposed to thermoplastics, by which water absorption does not exceed 2%. Very few studies exist for other important fluids, as the ones already mentioned, most of which contain substantial amounts of organic solvents.

A considerable number of the latter, even mild ones, may have a detrimental effect on polymers. For example, acetone may cause a stressed resin to craze, with a simultaneous decrease by more than 16% for both static and dynamic strength, while alcohol, ether, chlorophorm and carbon tetrachloride may have similar effects, especially with highly plasticized resins [3, 4].

In the present an attempt is made to investigate jet fuel interaction with two typical carbon fibre laminates, with a thermosetting and a thermoplastic matrix respectively.

2. EXPERIMENTAL

2.1 Materials

The following materials were tested:

(a) A 0°/90° non crimp fabric/polyetherimide thermoplastic composite (C/PEI) made of Courtauld's Apollo 43-750 12K untreated, A-size C-fibres at about 50% volume fraction manufactured by Brochier, France. Hot forming took place at 10 *bar* pressure and 380° *C* temperature. The FIT consists of fibre rovings which are spread out and impregnated with unmelted polymeric powder. Then they are put into a polymer sheath, the polymer used being the same as that of the original powder resin. The product has the advantage to remain flexible and, when woven, gives a fabric preimpregnated to the core.

Specimen dimensions were 40x10x2.4 mm.

(b) A unidirectional thermosetting 8-layer laminate, at about 55% volume fraction manufactured from a prepreg type SIGRI UD tape CE 1007/150/36 with Toho fibres HTA7.

The curing temperature was 125° *C* and the curing process was a controlled heating/cooling 2-hour cycle, leading to a practically stress-free laminate at ambient temperature. Specimen dimensions were 40x12x1.2 mm.

The main properties of both types of laminates appear in Table 1.

TABLE 1.

Properties / Materials	E_1 *GPa*	E_2 *GPa*	G_{12} *GPa*	ν_{12}	α_1 $\times 10^{-6}\,°C^{-1}$	α_2 $\times 10^{-6}\,°C^{-1}$	Tg °*C*
SIGRI CE 1007	145	8.5	4.8	0.335	-0.55	30	147
C/PEI	60.5 (warp)	58.5 (weft)	--	0.07	15	15	215

Specimens were immersed for several hours in JP-8 jet fuel [5] at two different temperatures, namely 25° *C* and 75° *C*.

2.2 DMA tests

After immersion specimens were tested on a DuPont Dynamic Mechanical Analyzer (DMA) at both fixed and resonant frequency modes, to determine complex moduli as well as glass transition temperatures over a temperature range from -70 to 200° *C*.

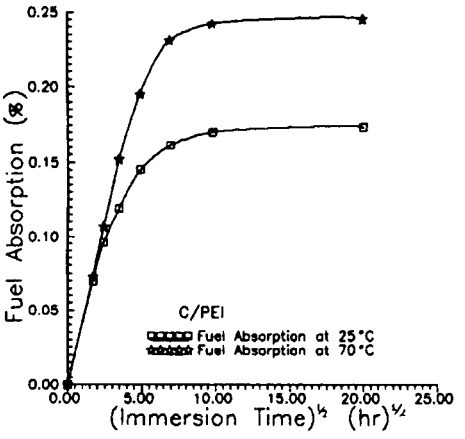

Figure 1. Fuel absorption curves for C/PEI specimens at two different temperatures.

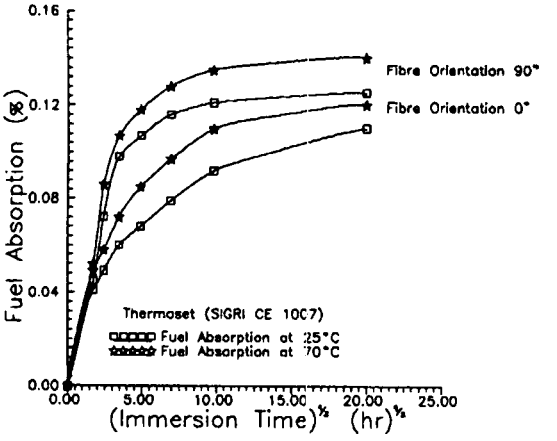

Figure 2. Fuel absorption curves of SIGRI CE 1007 thermosetting specimens at 0° and 90° fibre orientation, and at two different temperatures.

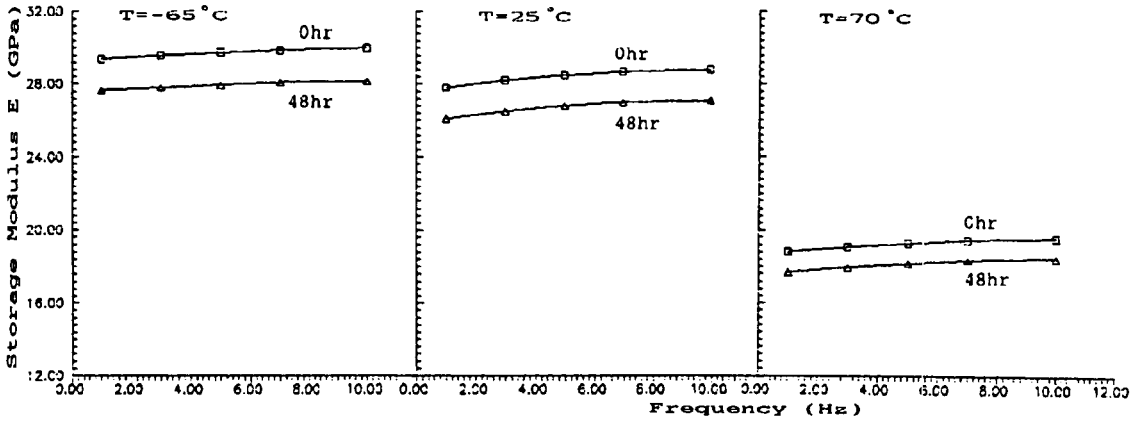

Figure 3. Storage modulus of virgin and 48 hr - immersed C/PEI specimens, at three different temperatures, against frequency.

3. RESULTS AND DISCUSSION

3.1 Fuel absorption

Fuel absorption against time for both laminates (a) and (b) is presented in Figures 1 and 2 respectively. On both occasions absorption is low as compared with water absorption. However, with the thermoplastic laminate (Fig. 1), by which a state of saturation is reached in 48 hours, temperature seems to be important, since a difference in saturation values of over 30% appears. With the thermosetting laminate (Fig. 2), the temperature is less important, the latter value is less than 13%, and absorption is substantially lower. As expected, a difference appears with fibre orientations, which, however, does not exceed 10%.

3.2 Dynamic measurements

The complex E-modulus was determined by means of the storage modulus E' and the loss factor tan.

With the fixed frequency mode both parameters were measured at three different temperatures, namely, -65, 25 and 70° C, as functions of frequency in the range from 0 to 10 Hz both for virgin and for 48-hour immersed specimens.

The results for the thermoplastic laminate appear in Figs. 3 and 4: The detrimental effect of fuel immersion is of the order of 6% for the storage modulus, while the loss factor increases by around 25%. The effect of frequency is much more pronounced for the loss factor.

The results for the thermosetting laminate for fibre orientations 0° and 90° appear in Figs. 5 and 6 and 7 and 8 respectively: Values for the storage modulus are reduced by 11-12% on both occasions, while for the loss factor they seem to increase by 45%.

With the resonant frequency mode, storage modulus and loss factor were plotted as functions of temperature in the range from -100 to 200° C, out of which values for storage modulus, loss factor and glass transition temperature against immersion time at a given temperature and at the respective resonant frequency can be determined.

With the thermoplastic laminate the storage modulus drops, as expected, by nearly 6% within 48 hours of immersion (Fig. 9), while the loss factor first drops by 6.5%, assumes a minimum value at 6 hours of immersion and then increases rapidly (Fig. 10). This effect appears to be the same as with moisture absorption, by which the water diffused is at first filling the voids and acts as a lubricant, while in the sequence it causes plasticization of the polymeric matrix.

In Fig. 11 both the first and the second transition temperatures are presented. In the first case the variation was of the order of 10%, while in the second it did not exceed 4%.

With the thermosetting laminate the results appear in Figs. 12, 13 and 14 and analogous phenomena appear. A remarkable difference lies in the variation of glass transition temperature, which for both fibre orientations is of the order of 12.5%.

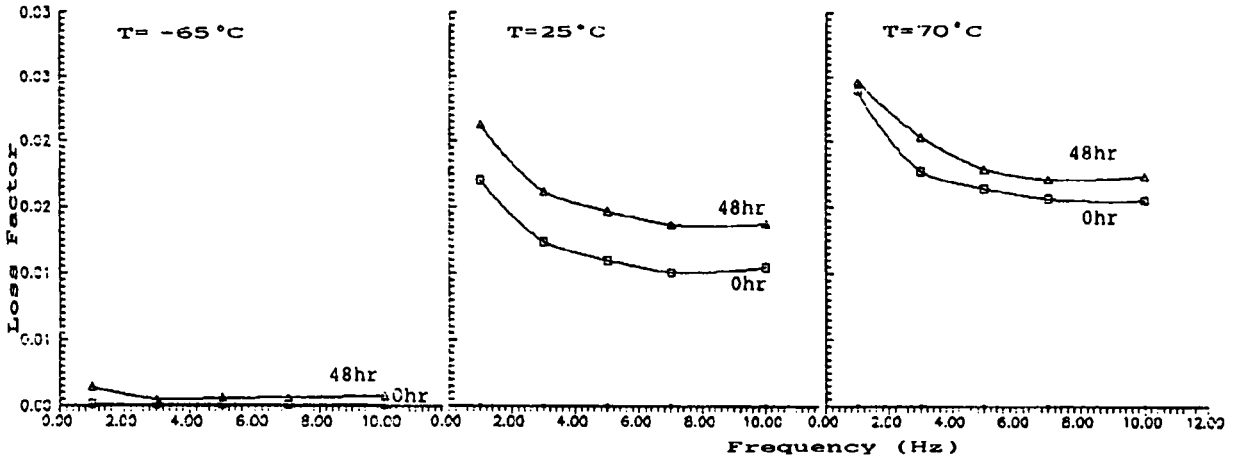

Figure 4. Loss factor of virgin and 48 hr - immersed C/PEI specimens, at three different temperatures, against frequency.

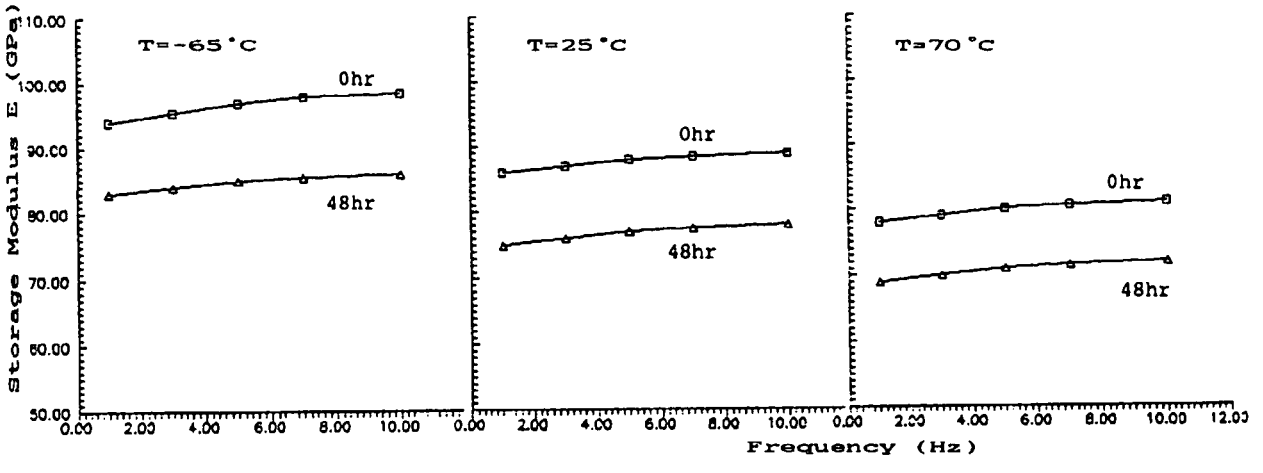

Figure 5. Storage modulus of virgin and 48 hr - immersed SIGRI CE 1007 specimens 0° fibre orientation, and at three different temperatures, against frequency.

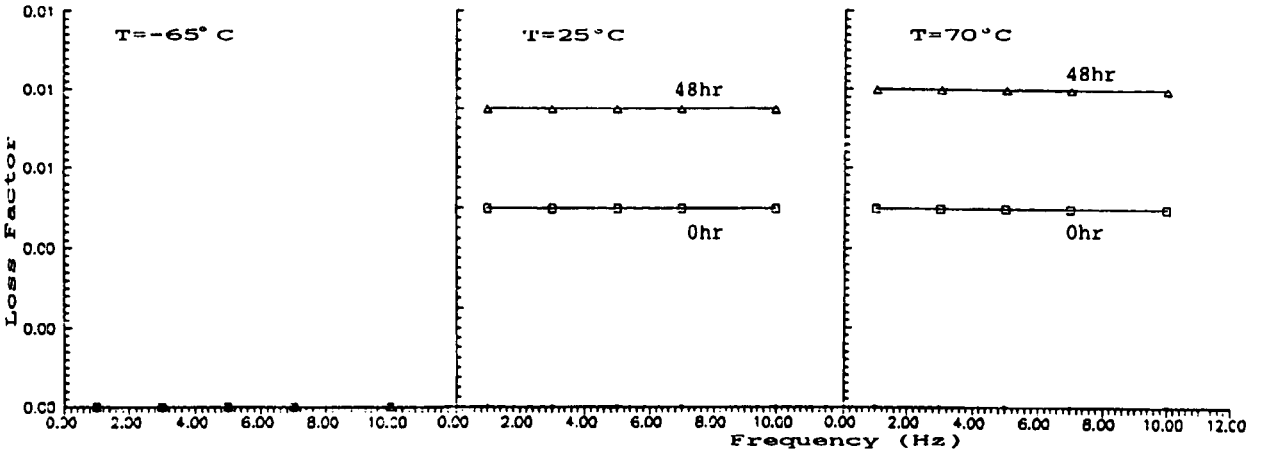

Figure 6. Loss factor of virgin and 48 hr - immersed SIGRI CE 1007 specimens for 0° fibre orientation, at three different temperatures, against frequency.

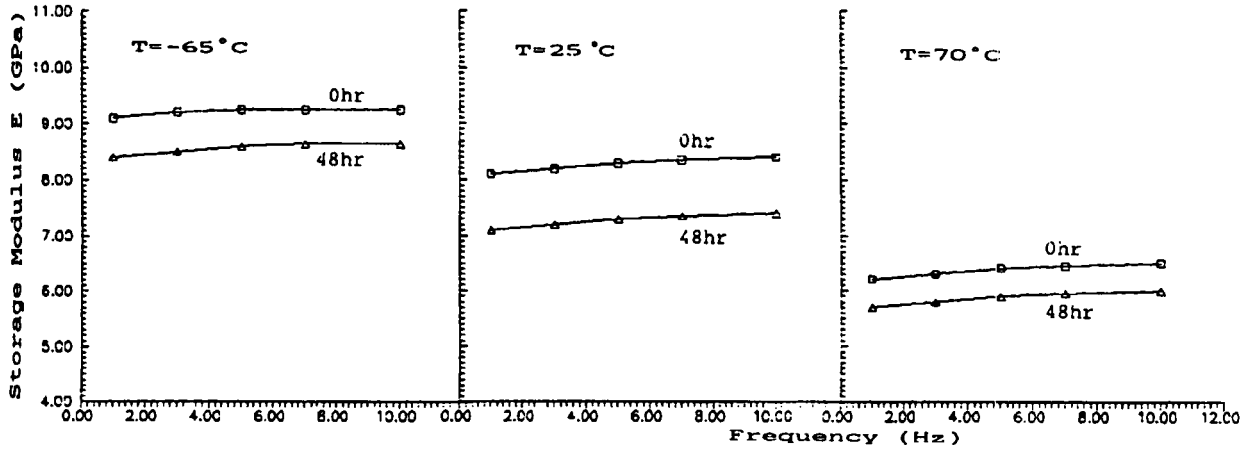

Figure 7. Storage modulus of virgin and 48 hr - immersed SIGRI CE 1007 specimens for 90° fibre orientation, at three different temperatures, against frequency.

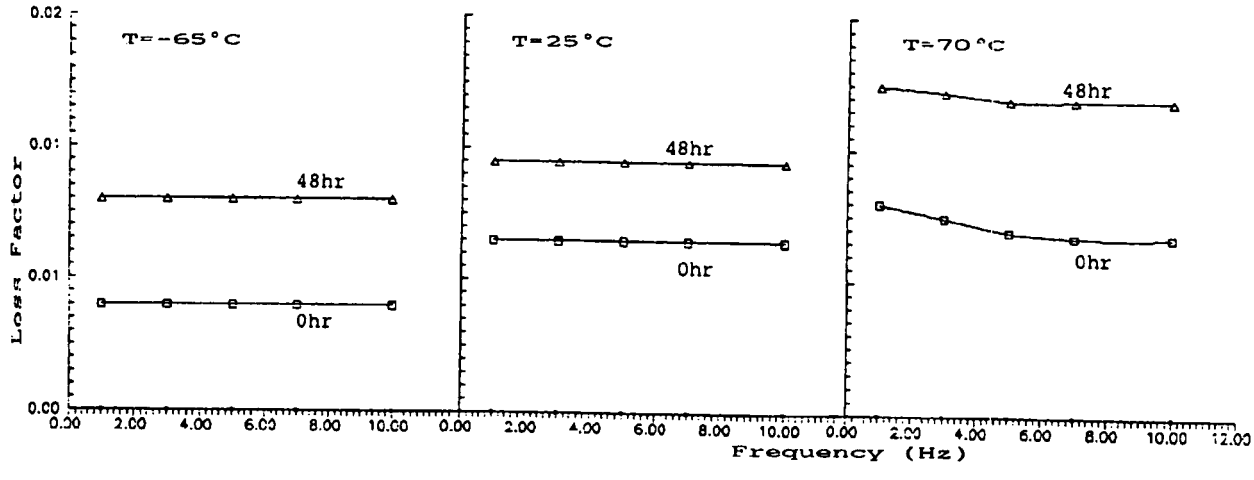

Figure 8. Loss factor of virgin and 48 hr - immersed SIGRI CE 1007 specimens for 90° fibre orientation, at three different temperatures, against frequency.

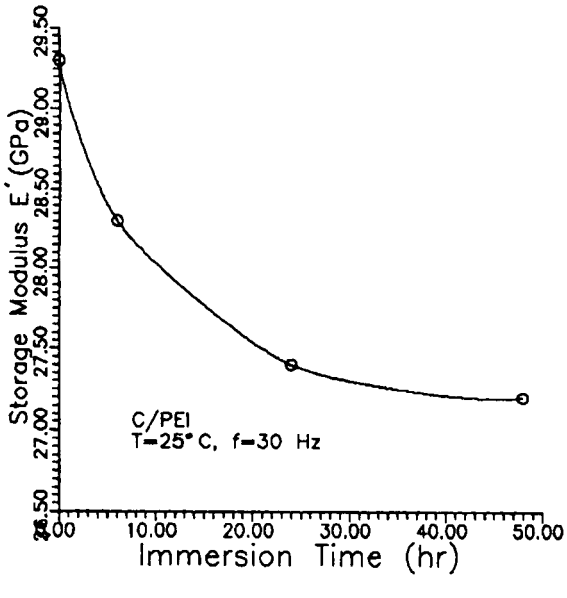

Figure 9. Storage modulus of C/PEI specimens against immersion time at $T = 25° C$ and $f = 30$ Hz.

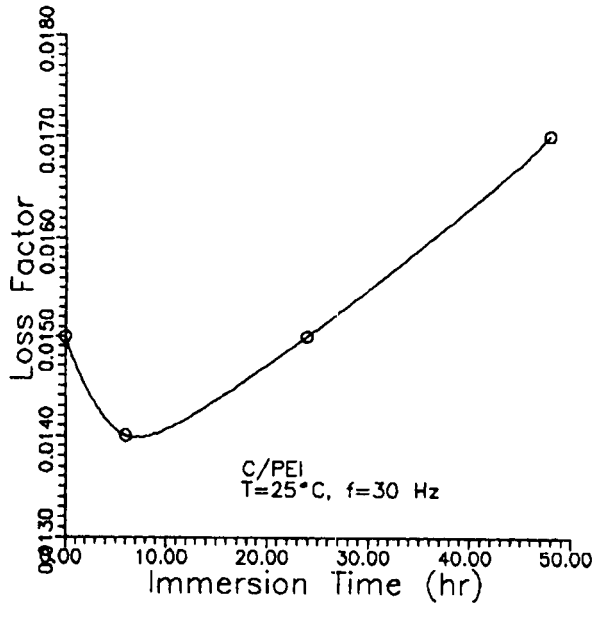

Figure 10. Loss factor of C/PEI specimens against immersion time at $T = 25° C$ and $f = 30$ Hz.

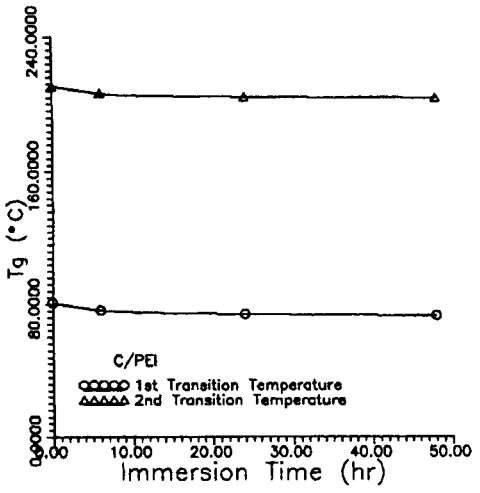

Figure 11. 1st and 2nd glass transition temperatures of C/PEI specimens against immersion time.

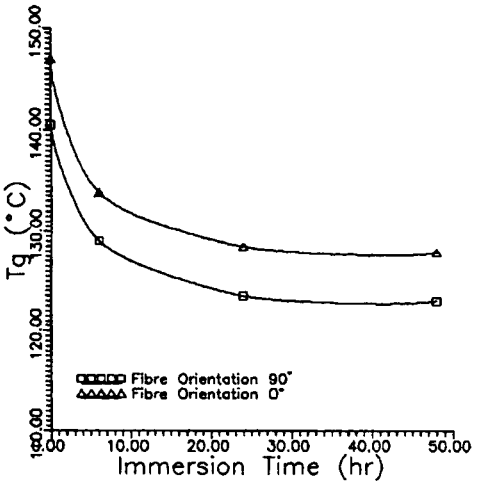

Figure 12. Storage modulus of SIGRI CE 1007 specimens for both 0° and 90° fibre orientation, against immersion time.

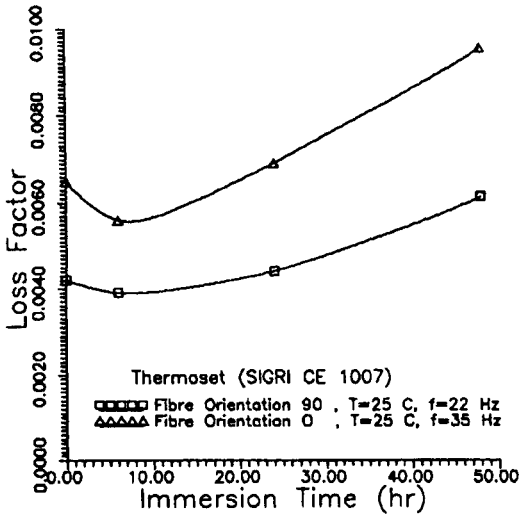

Figure 13. Loss factor of SIGRI CE 1007 specimens for both 0° and 90° fibre orientation, against immersion time.

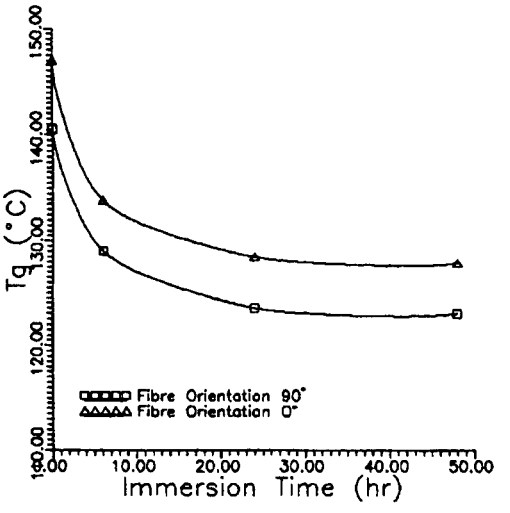

Figure 14. Glass transition temperature of SIGRI CE 1007 specimens for both 0° and 90° fibre orientation, against immersion time.

Figure 15. Surface photomicrograph (x200) of a C/PEI specimen immersed for 24 days in jet fuel.

3.3 Microscopic observations

A number of specimens were subjected to microscopic examination, and interesting effects in the form of rather deep pits appeared with thermoplastic laminate immersed in jet fuel for over 24 days (Fig. 15), a fact which, if confirmed, indicates action of organic solvents within an otherwise inert fluid.

4. CONCLUSIONS

With both types of laminates fuel absorption is low in comparison to moisture absorption, although thermoplastic specimens absorb higher amounts - a tendency quite opposite than with moisture absorption. Despite that, the effect on the properties investigated is much more pronounced with thermosetting laminates. Fuel temperature during immersion, although important for the amount of fuel absorbed, has no statistically significant effect on the respective properties - probably due to the fact that, when the specimen is heated up during measurements, the fuel is partially rejected and the material resumes its previous state. This fact, together with the variation of loss factor with immersion time, as illustrated in Figs. 10 and 13, indicates that fuel absorption is based on more or less the same mechanisms as moisture absorption, despite the differences in quantitative results, due to the individual properties of the respective materials. At this point, it is interesting to stress the importance of loss factor in the determination of the variation of properties, as a parameter far more sensitive to changes than glass transition temperature.

The additional action of organic solvents, especially with thermoplastic matrices, must be further examined, not only from the point of view of improving the operating conditions of materials working in adverse environments, but also as a problem of environmental protection, associated with disposal and perhaps recycling of such materials, now produced in vast quantities..

References

1. C. H. Shen and G. S. Springer, *Moisture absorption and desorption in composite materials*, in "Environmental Effects in Composite Materials", 1, G. S. Springer, Editor, Technomic Publishing Co Inc, 1988, 15-33.

2. C. H. Shen and G. S. Springer, *Environmental effects on the elastic moduli of composite materials*, ibid, 94-107.

3. P. S. Theocaris and S. A. Paipetis, *Thermal crazing of hot-setting plasticized epoxy polymers*, Fibre Science and Technology, 7, 1974, 33-44.

4. P. S. Theocaris, S. A. Paipetis and J. M. Tsangaris, Thermal crazing phenomena in epoxy resins, *Polymer*, **15**, 1974 441-445.

5. Turbine fuels, Aviation, Kerosene Types NATO F-34 (JP-8) and NATO F-35, MIL-T-83133C, Amendment 1, 22 March 1990.

Fracture Surface Characteristics of Compressive Failures in Carbon Fibre Reinforced Epoxy Laminate Subjected to Hot/Wet Conditioning

S. Lee, P.C. Gaudert and R.F. Scott
Structures and Materials Laboratory
Institute For Aerospace Research
National Research Council
Montreal Road, Ottawa
Canada K1A 0R6

SUMMARY

This paper presents the results of an investigation into the effect of environmental exposure on the compressive fracture surface characteristics of carbon/epoxy composite material (Hercules AS4/3501-6). The effects of temperature and absorbed moisture on laminates are explored. Specimens were preconditioned in either ambient laboratory humidity or in water at 64 °C for 4 or 7 weeks. The fractures were produced at room temperature and 93 °C. The observed fracture features (Scanning Electron Microscope) of the specimens with different preconditioning and test environments are presented. These results illustrated differences in the amount of fibre/ matrix separation, fibre fracture and resin fracture with increasing temperature and absorbed moisture. The reduction in compressive strength of laminates due to hygrothermal effects is also discussed.

1 INTRODUCTION

The use of composite materials in military aircraft structures is common, and in service they are exposed to a wide range of environmental conditions. It is well recognized that epoxy resins utilized in high-performance structural composites absorb moisture in humid environments (Ref 1). The absorption of moisture causes a slight swelling and lowers the resin's glass transition temperature. Composite properties which are matrix dominated such as compression strength, can also be adversely affected by moisture uptake and this can reduce the maximum permissible service temperature.

2 EXPERIMENT

2.1 Development of a New Test Fixture

For the evaluation of combined moisture-temperature effects on the matrix performance of composites, American Cyanamid Corporation's " hot-wet compression test" (Ref 2) which utilized the test fixture of ASTM Test Method D 695 (Ref 3) had been used in a recent material characterization of newly developed toughened resin composites at IAR (Ref 4). During the testing, there were occasional occurrences of specimen end-brooming in the ASTM D 695 test fixture. The end-brooming occurred in the specimen portion which extended 2 mm beyond the jig, see Figure 1 . This end-brooming led to a partial load transfer through the test fixture of an unknown magnitude. The end-brooming problem was particularly serious for the specimens which were affected by high moisture uptake and high temperature test conditions. The specimen end-brooming and frictional load uncertainties are inherent shortcomings of continuous rigid support jigs. As part of the current study, an improved compression fixture has been developed to overcome the problem of end-brooming of the specimen (Ref 5), as well as to eliminate frictional load transfer to the fixture during compression loading. This new fixture is capable of maintaining alignment and resisting lateral motion. The test specimen is secured in the fixture with clamping plates which also contribute to load transfer to the specimen through shear forces and to prevent end crushing, see Figure 2.

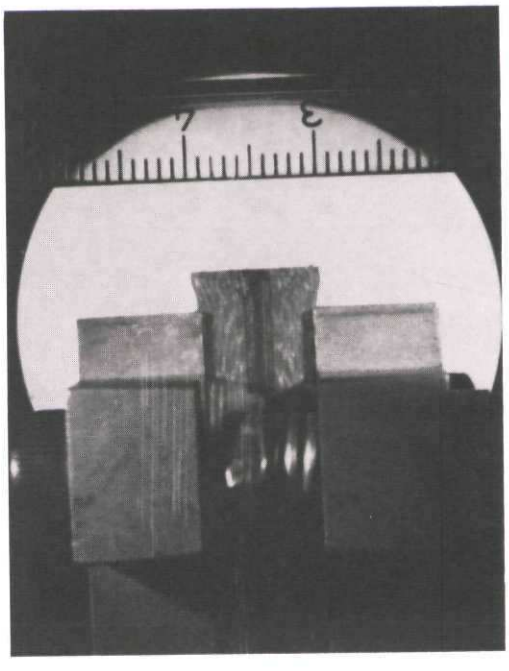

Figure 1. Brooming of Specimen Outside the ASTM D 695 Support Jig

2.2 Specimen

The material used in this study was Hercules AS4/3501-6 carbon/epoxy unidirectional preimpregnated tape supplied in 300 mm-wide rolls and stored at temperatures below -18 °C. The prepreg was cut and laid up with the use of templates to assure proper fibre angles from ply to ply. The material was cured in an autoclave in accordance with the prepreg manufacturer's instructions. After cure, the panels were examined in the IAR ultrasonic inspection facility using a pulse echo technique and they were found to be free of detectable defects.

The stacking sequence of the 16 ply symmetric laminate and the specimen configuration are presented in Figure 3. Individual specimens were cut from the panels using a diamond impregnated saw. Each specimen was then ground on the edges and the ends to a tolerance of +/- 0.05 mm.

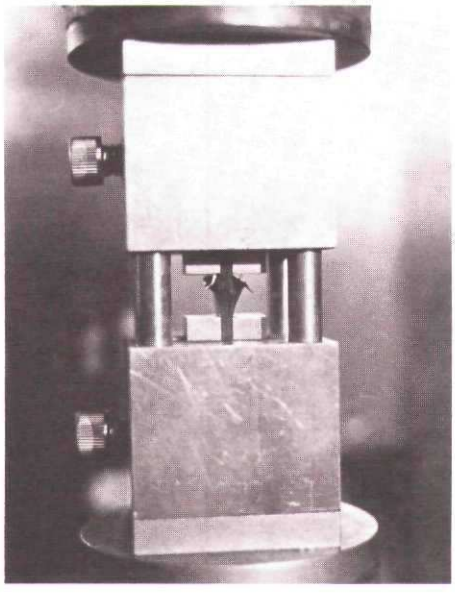

Figure 2. New Test Fixture

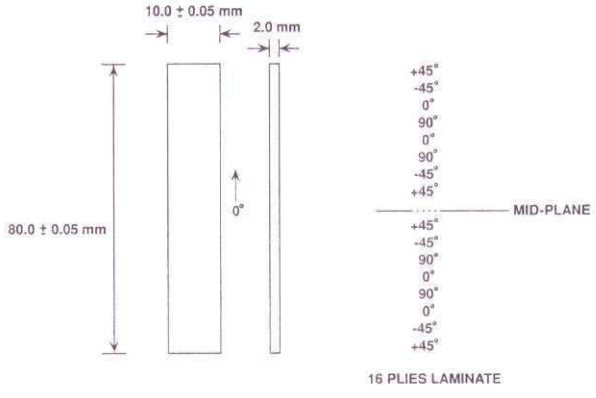

Figure 3. Configuration and Stacking Sequence of Specimen

2.3 Conditioning

In order to investigate the effects of different environmental and test parameters on the fracture surfaces and the compression strength of the laminate, the specimens were conditioned at two moisture contents for different durations and tested at two temperatures to provide 7 combinations. The details and codes are listed in the following:

1. DR, "dry" (conditioned in room air) and tested at room temperature. These specimens would provide a baseline for determining the heat and moisture effects on the compression strength.

2. M4R, "moist" conditioned: 4 weeks in 64 °C water and tested at room temperature to reveal the moisture effect on the compression strength.

3. M7R, "moist" conditioned: 7 weeks in 64 °C water and tested at room temperature to reveal the effect of any additional moisture adsorption on the compression strength.

4. DH, "dry" as in (1) but tested "hot" at 93 °C to reveal the effect of heat on the compression strength.

5. DWH, "dry" as in (1) but clamped into a warm jig, brought to the test temperature in 93 °C water and tested " hot" at 93 °C.

6. MH, " moist" conditioned 4 weeks in 64 °C water and tested "hot" at 93 °C (hot-wet compression).

7. MRR, " moist" conditioned 4 weeks in 64 °C water, exposed to 93 °C for 15 minutes, subsequently dried for 2 days at 80 °C in a vacuum oven and tested at room temperature.

The moisture contents of the conditioned specimens were determined by weight gain measurements. The weight gains and test temperatures for the seven conditions of specimens are presented in Table 1. As shown in the table, the moisture gain between 4 and 7 weeks of water immersion at 64 °C is very small, and this suggests an equilibrium of moisture content of 1.7 % at 64 °C for the Hercules AS4/3501-6 material.

Table 1. Effects of heat and moisture on compressive strength of AS4/3501-6 laminate

Condition Code	Conditioning state	Moisture content %	Test temperature °C	Test Results: Ultimate compression strength MPa	Test Results: *C.V. %	Test Results: Retention %
DR	Dry as made (conditioned in ambient room air)	0.3	22	704	5.1	100
MR4	Moist (conditioned in water at 64° for 4 weeks)	1.44	22	658	3.4	93.5
MR7	Moist (conditioned in water at 64°C for 7 weeks)	1.64	22	660	3	93.7
DH	Dry (conditioned in ambient room air)	0.3	93	604	5.4	85.8
DWH	Dry (surface-wetted in a pre-heat bath)	0.4	93	593	5.2	84.2
MH	Moist (conditioned in water at 64° for 4 weeks)	1.44	93	428	6.1	60.8
MRR	Moist and dried	0.6	22	688	1.7	97.7

*C.V. = coefficient of variation

2.4 Test Procedures

Compression tests were conducted in an environmental chamber in the load frame of the Instron 1125 testing machine, see Figure 4. The loading rate was 0.5 mm/min. and the chart recorder speed was 20 mm/min..

The mounting of the specimen in the jig required proper clamping as described in (Ref 5). The DWH and MH specimens were clamped in the support jig and pre-heated in a water bath that was maintained at 93 °C, whereas the clamped DH specimens were pre-heated in the chamber. The test temperature was monitored with a thermocouple.

2.5 Strength Test Results

The average compression strengths of the various conditioned laminates are given in Table 1. Each value is the mean of 14 tests. The coefficients of variation are generally low and do not exceed 6 %. For comparison purposes, the strength values

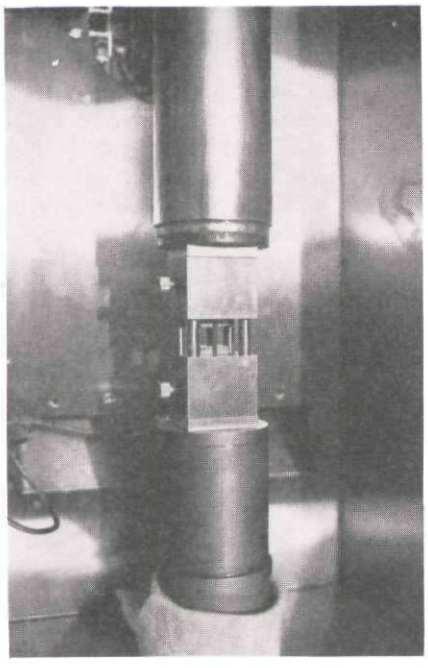

Figure 4. A Typical Set-Up for Hot-Wet Compression Test

expressed as a percentage of the average value of the dry room temperature specimens (DR) are also presented in Table 1. It is apparent that the application of combined heat and moisture produced a large decrease (39 %) in the compression strength of the laminate. For the dry conditioned specimens, the application of heat alone, such as DH and DWH, had moderate effects, which reduced the compression strength of the laminate up to 16 %, while moisture conditioned specimens, such as M4R and M7R, had little reduction in strength (approximately 6 %) at room temperature. The relatively small amount of moisture increase of 0.2 % between 4 and 7 weeks of immersion had no significant effect on strength. The strength of MRR specimens was only slightly reduced and this indicated that specimens immersed in 64 °C water for 4 weeks did not suffer any significant damage.

3 MACROGRAPHIC OBSERVATIONS

Macroscopically, the fractures produced under compression loading exhibited gross buckling, extensive delamination, cracks and over-running of the delamination planes. Since there was a significant difference in the compressive strength between the DR and the MH specimens , macrographic observations were conducted mainly on these specimens.

Preliminary visual examination of the failed specimens revealed significant differences in the overall appearance of the fractures of the DR and MH specimens, shown as edge views in Figure 5a and 5b respectively. Compression failure modes in MH specimens are predominately shear crippling as defined in (Ref 6) accompanied by delamination. In general, cracks in outer plies are oriented at an angle of approximately 45° to the longitudinal axis of the specimen, whereas in the central ply regions, the cracks are generally oriented at an acute angle of approximately 10° to the longitudinal axis of the specimen. For the DR specimens, compression failures are characterized by extensive delamination and many cracks propagated through the thickness of the laminate at an angle of approximately 45 degree to the longitudinal axis.

Compression micro-buckling appears to be the primary failure mechanism for these specimens; it involves local buckling of

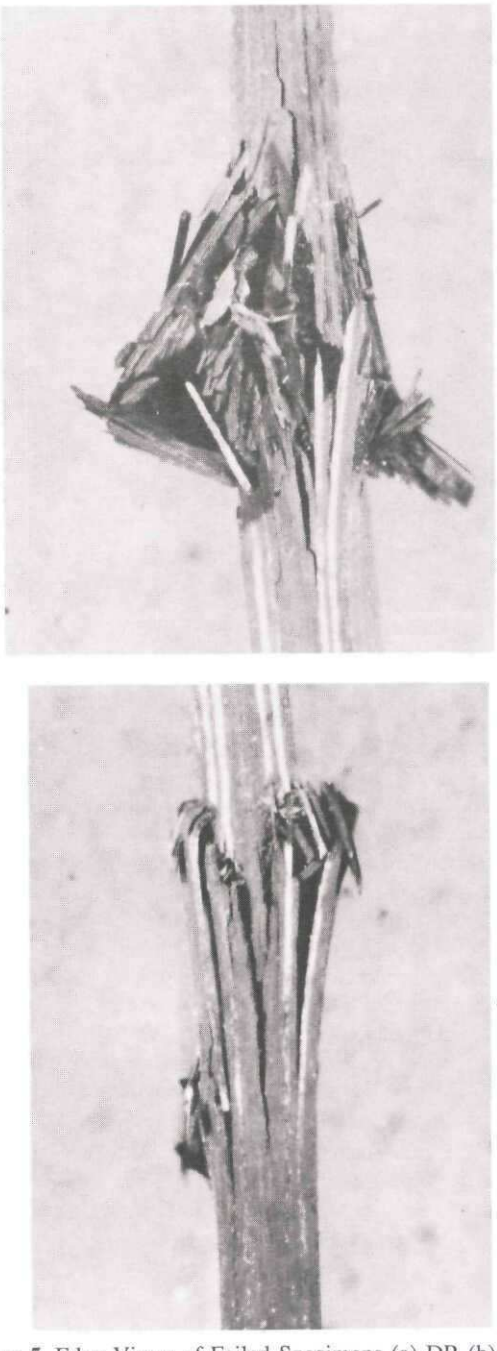

(a)

(b)

Figure 5. Edge Views of Failed Specimens (a) DR (b) MH (x25)

individual fibres at a point where a localized instability exists. When the fibres are supported by a rigid matrix , failure usually occurs at high stress with considerable delamination. The DR specimens exhibited this failure pattern, see Figure 5a. Low modulus resins offer less support to the fibres, hence the fibres may kink and lead to shear crippling and thus failure may occur at a lower load. The MH specimens failed in this fashion, see Figure 5b.

Closer examination of the failure surface (exposed by carefully pulling the laminates apart in the laboratory) reveals significant differences in the fracture features of DR and MH specimens as shown in Figure 6. The fracture of DR specimens are predominately oriented 45° to the loading direction and the fracture surfaces exhibit a mix of intra-, inter- and trans-laminar failures. The fracture surfaces are very

irregular since the dominating feature of trans-laminar fracture is broken fibre bundles. Overall, the test of the DR specimen produced a large failure surface area which was a result of failure at high stress.

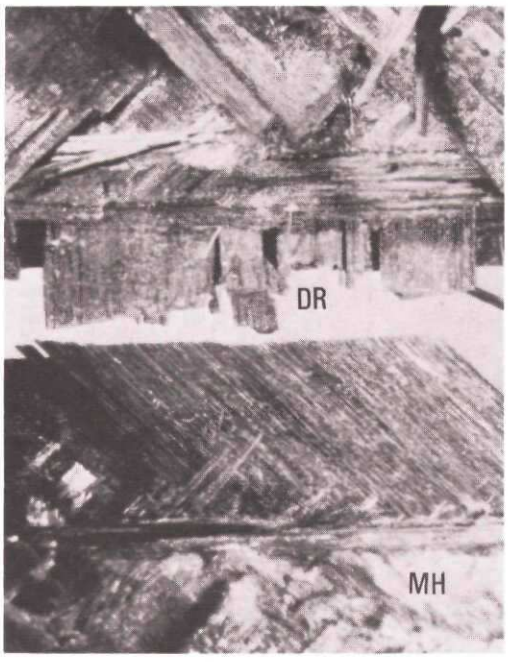

Figure 6. Failure Surfaces of DR and MH Specimens

The MH specimens exhibit fractures that are normal to the loading direction. The fracture surfaces in the X-Y planes are mainly ±45° degree plies which are terminated in the transverse direction. The ±45° degree plies in the laminate appear to be predominately in the 45 degree fracture mode while the 0° and 90° plies are in the transverse fracture mode. Since the dominant failure mode for the MH specimens is shear crippling within the laminate, the fractures through the 0°, 90°,0°, 90° degree ply groups in the laminate are confined to small multiple steps at the ends of the fracture surface. The relatively planar fracture surfaces of the MH specimens are dominated with inter-laminar fracture surfaces which are significantly smaller than those of the DR specimens.

3.1 Process of Failure in Laminates

DR specimens:

In an analysis of this failure process, it was known that the specimen had been subjected to a compressive load with monotonic increasing applied strain at any given cross section. Based on the ultimate strains reported in (Ref 7) for ±45° , 90° and 0° degree orientations, it appears that during compressive loading of the specimen, when the applied strain value reached a critical value for the 0° degree plies, failure would initiate in a region leading to a gradual loss of stiffness. As the applied compressive strain was further increased to the critical value for ±45° plies, these plies started yielding. When the applied compressive strain approached the ultimate failure strain value for the 90° plies, the laminate failed by buckling and delaminating.

MH specimens:

Grimes (Ref 8) reported that both shear and transverse strains could be affected significantly by elevated temperature testing of high moisture content material and their ultimate strains could be reduced up to 50% of the room temperature value. Again, based on the reported ultimate strain values (Ref 7) for ±45° , 90° , 0° orientations, as soon as the applied compressive strain was close to the ultimate failure strain values, the ±45° and 90° plies lost stiffness and caused the remaining 0° plies to buckle. At this point, possibly a small elastic buckle occurred because of softening of the matrix due to the elevated temperature. As a consequence, the matrix was no longer capable of supporting the fibres, resulting in shear crippling prior to fracture across the entire cross section.

In general, the inter-laminar fractures of the ±45° plies in the MH specimens are very prominent and this is probably due to the low shear strain of the matrix which has been degraded by a combined effect of the elevated temperature and high moisture.

4 DISCUSSION ON FRACTOGRAPHIC OBSERVATIONS

Scanning electron microscopic (SEM) examinations were carried out on the failed specimens to (a) characterize and compare the fracture surface topography of the differently conditioned specimens and (b) to establish whether specific morphology could be correlated to the ultimate compressive strengths of specimens subjected to hot/wet conditioning. SEM is a very useful technique for the detailed examination of the fracture surfaces.

±45° Ply Fractures: Figures 7a and 7b show delamination between and within the ±45° plies for the DR and MH specimens, respectively. Typical fractures generated in the DR specimens exhibit combined features of cohesive matrix failure and limited fibre pull-out. The fibre surfaces appear to be coated with a layer of matrix material. This implies that a satisfactory interfacial fibre/matrix bond existed. The fracture surfaces of the MH specimens typically exhibit a rougher topography with large areas of fibre/matrix separation and de-bonded fibres. In general, these observations are in agreement with published literature (Ref 8,9,10) and they indicate a degradation in the "fibre-to-matrix" interfacial region that tends to occur under elevated temperature and high absorbed moisture conditions.

0° and 90° Cross-Ply Fractures: The fracture topography of delamination produced between cross plies is illustrated in Figure 8a and 8b for the DR and MH specimens respectively. Matrix fracture appears to be the dominant fracture feature for the DR specimens. The coherent fracture surface reveals good interfacial bonding as evidenced by resin matrix adherence to the fibre surface, and numerous hackles (H) are also exhibited. On the MH fracture surface matrix fracture, fibre/matrix separation and fibre breakage can be observed in Figure 8b. Again, this indicates that the interfacial strength has been degraded due to the elevated temperature and high moisture content in the materials. There is an increased amount of fibre/matrix separation for the MH specimens as compared to the DR specimens and the fracture planes tended to occur within or adjacent to closely packed fibres within the ply, resulting in fibre fracture, fibre imprints and local regions of resin fractures.

As shown in Figure 9, an examination of the fracture surface of the DH specimen reveals little fibre and matrix

fragmentation. Most of the fibres appear to be coated with matrix. In contrast to the DR specimens, the DH interfacial fracture surfaces show significant reduction in the size of the hackles. The reduced fracture surface area may relate to the moderate strength loss of the DH specimens.

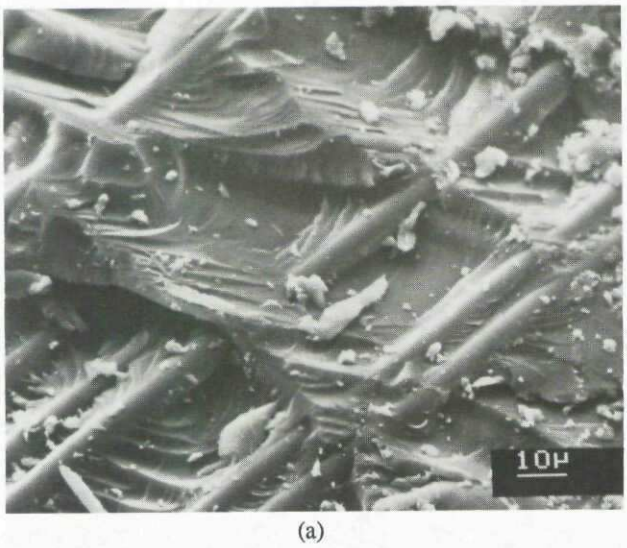

(a)

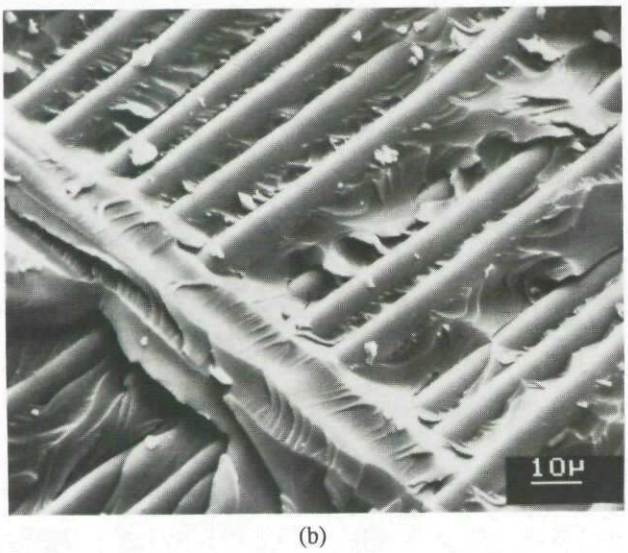

(b)

Figure 7. Fracture Surfaces Between and Within ±45° Plies of Specimens (a) DR (b) MH

90° Ply Fractures: As shown in Figure 10a, the fracture surfaces of the 90 degree ply of the DR specimen exhibit many hackles of various sizes. The small hackles appear to be more of an integral part of the matrix than the deeply cleaved large ones. The fracture surfaces of the MR specimen show coarse hackles and other hackles appear to have separated leaving a scalloped appearance, see Figure 10b. In Figure 10c, the DH specimen exhibits intra-laminar (within the ply) fracture surfaces with small hackles and broken fibres. A crack (C) can be observed that appears to be approximately normal to the fracture surface. It is difficult to assess the degree of debonding on this surface. The fracture surface of the 90° ply of the MH specimen, see Figure 10d, shows extensive matrix disintegration and fibre breakage.

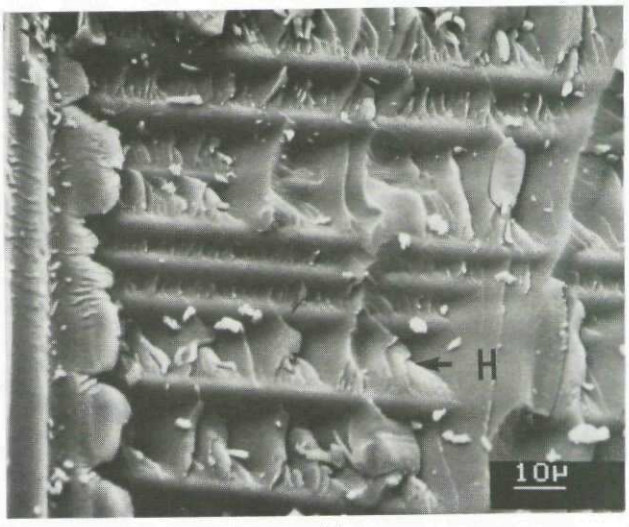

(a)

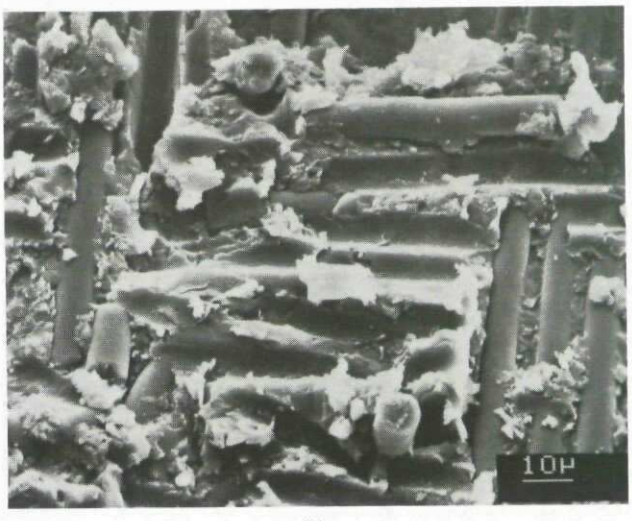

(b)

Figure 8. Fracture Surfaces Between 0° and 90° Cross-ply of Specimens (a) DR (b) MH

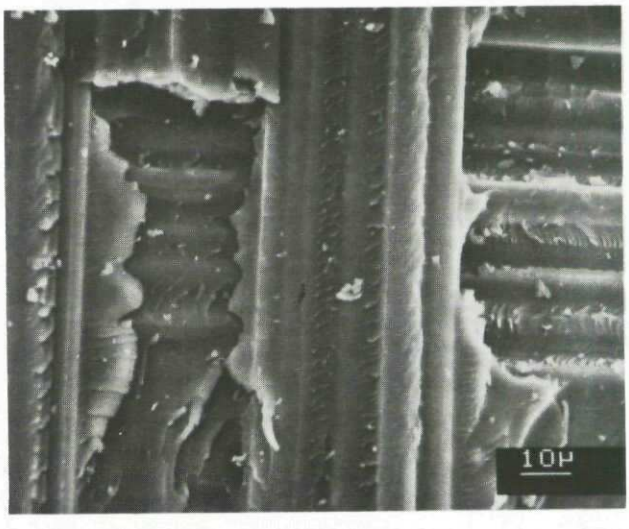

Figure 9. Fracture Surfaces of DH Specimen Between 0° and 90° Cross-ply

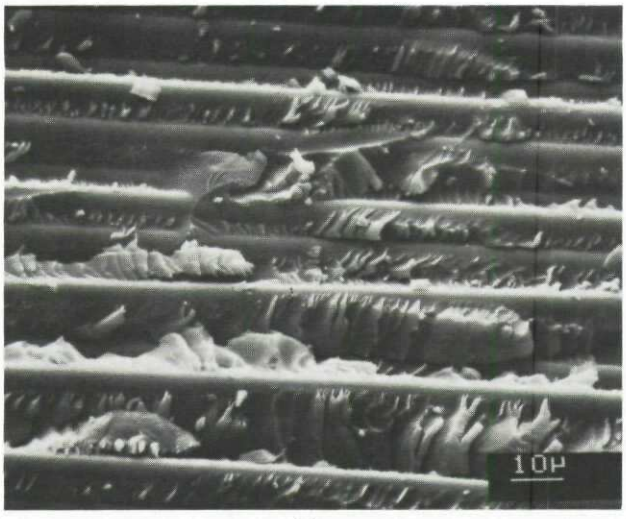

(a)

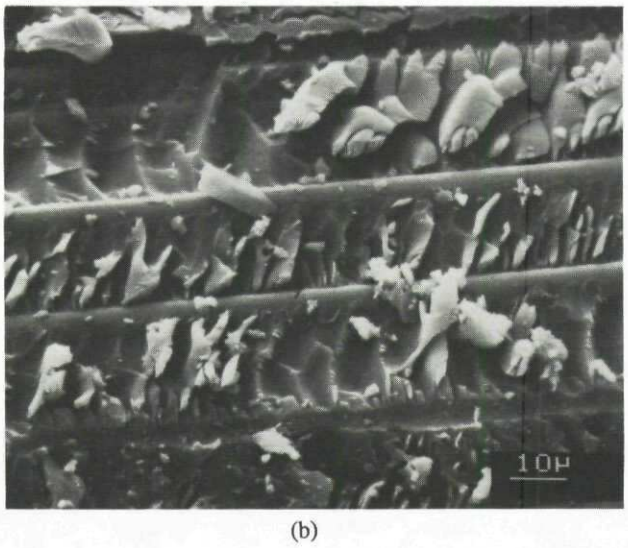

(b)

Figure 10. Fracture Surfaces in 90° Ply of Specimens (a) DR (b) MR

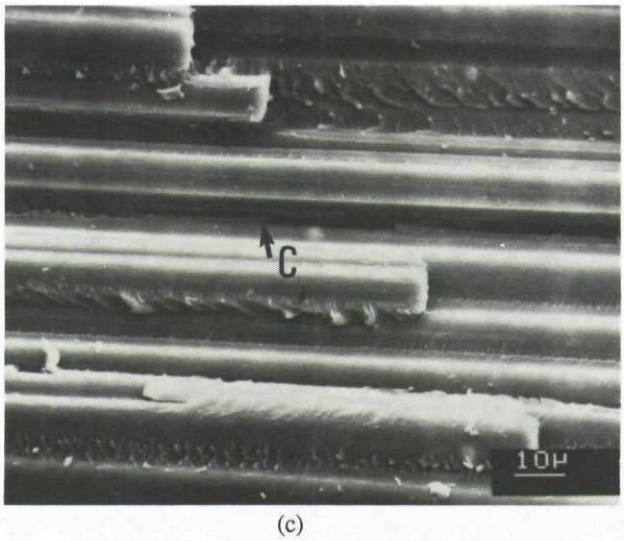

(c)

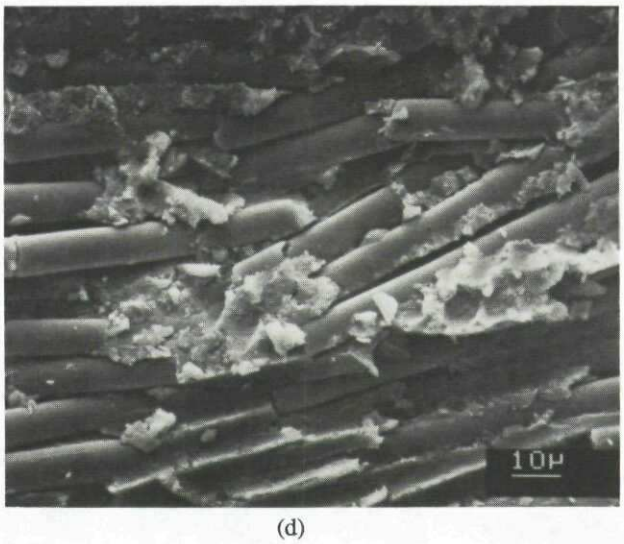

(d)

Figure 10. Fracture Surfaces in 90° Ply of Specimens (c) DH (d) MH

The hackle markings were usually formed on the fracture surface with fibres at 90° to the load and the hackles were between the fibres. Grove and Smith (9) suggested that hackle formation initiates between the fibres provided that the interfacial strength is reasonably high. For the DR and MR specimens, see Figure 10a and 10b respectively, examination of the fibres appears to reveal good interfacial bonding as evidenced by resin matrix adherence to the fibre surfaces. Hence, the hackle marking is a predominant feature on the fracture surfaces of both specimens. The fracture surface of the DH specimen exhibits a few shallow hackles, see Figure 10c, and this suggests that the softening of matrix due to the elevated temperature may reduce the size and number of hackles. The relatively clean fibre surfaces of the MH specimen, see Figure 10d, suggests a weaker fibre/ matrix interfacial region which may prevent the formation of hackles in the matrix between fibres as there is no evidence of hackles in the MH specimen.

0° Ply Fractures: In Figure 11a, the fracture surface of the DR specimen does not exhibit any micro-buckling. The integrity of the matrix appears to be intact below the fracture surface. The fracture features consist mainly of hackles.

In contrast with the DR specimen, the DH, MR, and MH fracture surfaces in Figure 11 (b, c and d) indicate micro-buckling (short fibre lengths) and breakup of the composite. Figure 11c and d show an increase in matrix/fibre separation. For the MH specimen, the fibre surface is almost devoid of adhering matrix while on the DH and MR specimens some matrix remained as ridges on the fibre fragments.

5 CONCLUSIONS

Hercules AS4/3501-6 laminate specimens conditioned to a moisture content of about 1.5 % and tested in compression at 93 °C showed a strength reduction of 39.2 % as compared to a dry laminate with a moisture content of 0.3 % tested at room temperature.

Macrographic observations indicated that specimens that had sustained high failure loads appeared to exhibit larger fracture areas than lower strength specimens. The general trend for the fracture areas of the different conditioned specimens are in decreasing order DR, MR, DH and MH and this trend agrees very well with their respective strengths.

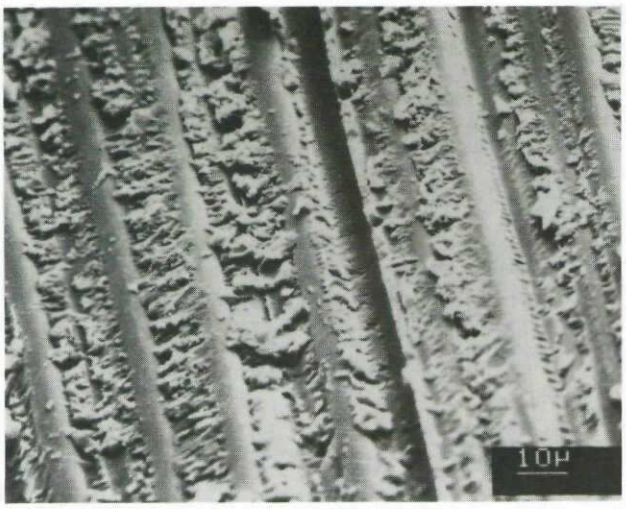

(a)

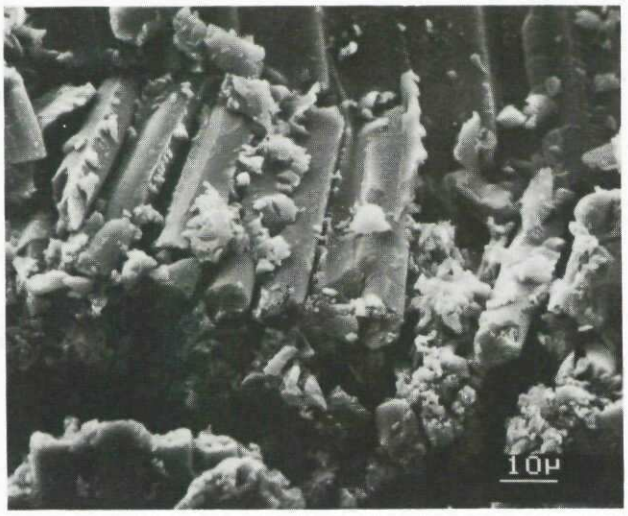

(b)

Figure 11. Fracture Surfaces in 0° Ply of Specimens (a) DR (b) MR

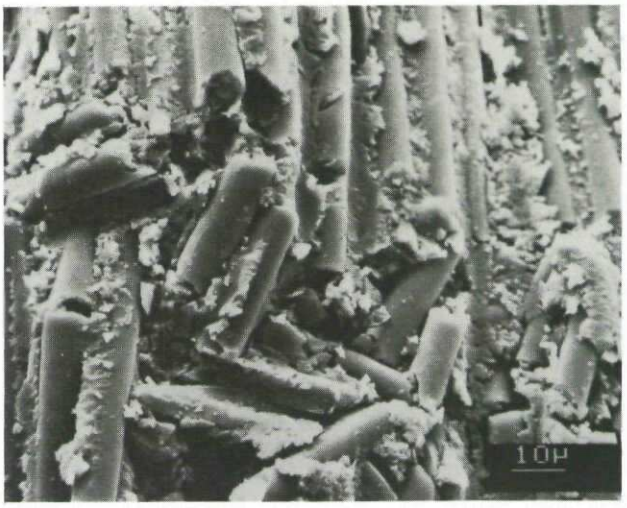

(c)

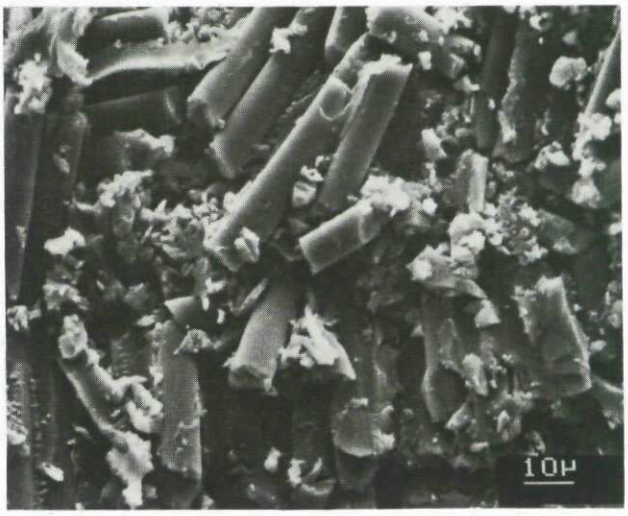

(d)

Figure 11. Fracture Surfaces in 0° Ply of Specimens (c) DH (d) MH

The predominant failure mode for laminates under compression loading was micro-buckling of the fibres. It appeared that micro-buckling was very sensitive to matrix support. The combination of a weak fibre/matrix interfacial region and a lower modulus matrix is expected to promote fibre micro-buckling and hence poor compression performance.

The specimens that were moisture conditioned and tested at 93° C appear to have failed in the fibre-matrix interface region.

ACKNOWLEDGEMENTS

This work has been supported financially by the Department of National Defence of Canada under Technology Base- Air Vehicles, Defence Research Establishment Pacific, and by the National Research Council Canada under IAR-SML Project JHB-00. The support of both organizations is gratefully acknowledged.

REFERENCES

1. C.E. Browning, G.E. Husman and J.M. Whitney, " Moisture Effects in Epoxy Matrix Composites", ASTM STP 617 ,481-498 (1977).

2. R. B. Krieger, " The Relation between Graphite Composite Toughness and Matrix Shear Stress-Strain Properties", 29th National SAMPE Symposium, 3-5 April, 1984.

3. "Compressive Properties of Rigid Plastics", ASTM Standard D 695-85.

4. S,Lee, R.F.Scott, P.C. Gaudert, W.H.Ubbink and C. Poon, " Characterization and Toughened Resin Testing of New Generation Carbon Fibre/Epoxy Systems", NAE Laboratory Technical Report, LTR-ST-1638, National Research Council Canada, Ottawa, 1987.

5. P.C. Gaudert, R.F. Scott and S. Lee, " Improved Specimen Support Jig For Hot-Wet Compression Testing ", IAR Laboratory Technical Report, LTR-ST-1790, National Research Council Canada, Ottawa, September, 1990.

6. H.T. Hahn and J. G. Williams, "Compression Failure Mechanism in Unidirectional Composites", ASTM STP 893 , 115-139 (1984).

7. Hercules Magnamite AS4/3501-6 Graphite Prepreg Tape and Fabric Module Data Package, July 1987.

8. G. C. Grimes, " Experimental Study of Compression-Compression Fatigue of Graphite/Epoxy Composites", ASTM 734, 281-337 (1979).

9. R. Grove and B. Smith, " Compendium of Post-Failure Analysis Techniques For Composite Materials", AFWAL-TR-86-4137, (1987).

10. A. J. Barker and V. Balasundaram, " Compression Testing of Carbon Fibre Reinforced Plastics Exposed to Humid Environments", Composites 18,3, 217-226 (1987).

THE EFFECT OF HEAT TREATMENT ON THE PROPERTIES OF PEEK AND APC-2

by

A. Ankara and **G. Kalay**
Middle East Technical University
06531 Ankara
Turkey

M.J. Folkes
Department of Materials Technology
Brunel University
United Kingdom

SUMMARY

This paper examines the effect of certain heat treatments on the properties of PEEK and carbon fibre reinforced PEEK. Differential scanning calorimetry, wide angle X-ray diffraction, dynamic mechanical testing, flexture testing and microscopy were done to study the changes in the amount of crystallinity and to observe the effect this crystallinity change on the other properties.

DSC thermograms showed that although there is no considerable change in crystalline melting point of the composite specimens depending on the heat treatment applied there is a change in PEEK. It was confirmed by both DSC and WAXD data that it is possible to control crystallinity of PEEK and APC-2 easily by applying simple heat treatments. The glass transition temperatures of as-received PEEK and APC-2 obtained from dynamic mechanical spectrum are 165.9° and 160.9° C respectively. More higher glass transition temperatures were also observed for high % crystalline composite specimens. In the literature 143° C is stated as Tg of these materials. The frequency effect on dynamic mechanical spectrum was also determined. It is concluded that as the frequency decreases the dynamic mechanical spectrum shifts to lower temperatures and loss tangent (tan δ) increases in value.

Flexture testing results shows that the flexture properties are independent of crystallinity. Fracture surface examination was confirmed the debonding in quenched APC-2 samples. It was also observed strong adhesion for crystallized samples. This research clarifies the use and applicability of heat treatment for commercial processing.

1. INTRODUCTION

Thermoplastic matrix composites have become an important material for the aerospace industry. The recent developments in thermoplastics made possible the production of high strength and enviromental resistant composites. As mentioned by Heym et al [1] and Clemans and Hartness [2] various thermoplastic polymers with high glass transition and crystalline melting temperatures are commercially available in the market.

The tougness and enviromental resistance are primarily important porperties of PEEK/carbon fibre composites. High glass transition (Tg) and melting temperature (Tm) are also quite attractive where high temperature applications are necessary. APC-2 has also superiority against traditional thermosetting composites from production point of view since the materials chemistry is determined before the impregration stage and no need for prolonged curing stages. It has also low moisture absorption [3] and improved repairability.

Undoubtedly, the fibre-matrix interface and the crystallinity have the main role in determining most of the composites' mechanical properties. In APC-2 fibre-polymer interface acts as nucleating sites for spherulites. So the heat treatment applied to APC-2 may change fibre-matrix interface characteristics and spherulite morphology which in turn affect the mechanical response of the material. Blundell et al [4] enlightened the nucleation behavior of spherulites in APC-2 and determined how spherulitic morphology changes with the preparation conditions of the composite. Talbott et al [5] determined that both fracture toughness and fracture energies depend mainly on the amount of crystallinity for APC-2 and both of these decrease with increasing the amount of crystallinity.

The purpose of this research is to find out the effect of certain heat treatments on the amount of crystallinity which also affects dynamic mechanical behavior, flexural properties and fibre-matrix interface characteristics. This research provides an understanding of the physical properties of APC-2 which also determines the mechanical characteristics. Additionally the possibility of heat treatment with PEEK and APC-2 clarifies since the heat treatment has an importance in commercial processing.

2. EXPERIMENTAL DETAILS

2.1 Materials and Heat Treatments

For this research, PEET (450 G grade) supplied by ICI (UK) and carbon fibre reinforced PEEK (APC-2) supplied by MBB (Germany) were used. The composite was unidirectionally reinforced and was composed of 32 weight % PEEK and 68 weight % IM-6 carbon fibres.

Four different heat treatments were done to PEEK and the composite. The temperature of 330° C were chosen to increase the amount of crystallinity of the specimens since this temperature is below the crystalline melting point of the materials. The temperatures 335° C, which is around the T_m of the materials, and 345° C which is above the T_m of the materials were chosen to decrease the crystallinity of the materials by quenching from these temperatures. These heat treatments were as follows:

i) The specimens were heat treated at 330° C for 10 minutes and furnace-cooled.

ii) The specimens were heat treated at 330° C for 10 minutes then taken and put in a furnace at 240° C and slow-cooled.

iii) The specimens were quenced in liquid nitrogen after heat treating an hour in a furnace at 335° C.

iv) The specimens were quenched in liquid nitrogen after heat treating an hour in a furnace at 345°C.

Furnace cooled samples are denoted by FC and quenched samples are denoted by Q. For example, APC-2 specimens heat treated at 330° C and furnace cooled will be shown by APC2-FC(330), and PEEK specimens quenched from 345° C will be shown by PEEK-Q(345). Additionally, as received specimens will be called APC2 and PEEK, respectively for the composite and the polymer.

2.2. Differential Scanning Calorimetry (DSC)

In order to obtain DSC thermograms by which crystallinity, and crystal melting point (T_m) were found, Perkin Elmer DSC-2 were used, 10-15 mg samples were cut from both APC2 and PEEK samples and sealed in alumimum pans. The heating rate of 20.0 deg/min and the cooling rate of 320 deg/min were applied.

The heat of fusions (ΔH_f) of the materials were found from the area of the melting peaks. By accepting the heat of fusion of fully crystalline sample as 130 J/g [6,7] the crystallinities of the PEEK samples were calculated. For APC2 samples similar calculations were done by correcting the ΔH_f data for pure PEEK since the composite contains 68 weight % carbon fibers.

2.3. Wide Angle X-Ray Differaction (WAXD)

Cu Kα radiation was used. Diffraction profiles were recorded by scanning at a rate of 0.02° 2θ /sec over an angular range 8°<2 <38°. For PEEK samples, the crystallinity calculation was done by using the following equation [8]

$$\text{Crystallinity} = \frac{\text{Area of Crystalline Fraction}}{\text{Area of Crystalline Fraction} + \text{Area of Amorphorous Fraction}} \quad (1)$$

The shape of non-crystalline background was estimated by referring to the data by Blundell [6]. Figure 1 shows the typical diffraction profile for PEEK samples.

The crystalline determination for the composite specimens was done by referring the calibration curve drawn by Blundell et al [9]. More precisely, h_{110}/h_c ratios were found and corresponding crystallinities were datermined from the mentioned calibration curve.

2.4. Dynamic Mechanical Evaluation

The Rheometrics RSA2 Solids Analyzer was used to determine tan δ vs temperature, E' (storage modulus) vs temperature, and E" (loss modulus) vs temperature curves. E' is the real part of the complex modulus. E*, and E" is the imaginary part of E*. E* is defined as

$$E^* = E' + iE'' \quad (2)$$

Unclamped three point bending test at a frequency of 62.8 rad/sec was done. In order to determine the frequency effect on the glass transition temperature and tan δ additional tests were also done at different frequencies.

2.5. Flexture Testing

Flexural three point bending tests were done by using an Instron 4206 materials testing machine. The specimen dimensions were (1mmx16mmx60mm) and (3.25mmx16mmx60mm) for APC2 and PEEK specimens, respectively. The span was 40mm. The crosshead speed of 2.667 mm/min and 1.6mm/min were applied for APC2 and PEEK samples, respectively.

The flexture modulus, E, was calculated using the equation:

$$E = \frac{mL^3}{4bh^3} \quad (3)$$

where b is the beam width and m is the value of the applied load divided by the crosshead movement of the testing machine. L is the span.

The flexural strength, σ, was calculated using the equation:

$$\sigma = \frac{3PL}{2bh^2} \quad (4)$$

where P is the maximum load applied. The load applied was perpendicular to fibre direction.

The fracture surfaces of the tested specimens were examined under scanning electron microscope. Primarily, the fracture surfaces were mounted on stubs and coated with Au-Pd.

3. RESULTS AND DISCUSSION

3.1. DSC Results and Crystal Melting Points

For as-received PEEK and APC2 the melting points were determined as 338.5° and 341.9° C respectively. Additionally the glass transition temperatures were determined as 168° and 163.7° C for PEEK and APC2, respectively. The melting points are in agreement with the tabulated data but T_g values are 20-25° C higher than the usually reported values for these materials in the literature. The DSC results for the heat treated samples show slight change in melting points for the composite specimens. However, the samples which were crystallized at 240° C shows approximately 10° C increase in the melting point of the composite specimen. This is attributed to the change in spherulic crystal structure, both in terms of spherulite diameter and lamellae thickness. On the other hand PEEK specimens show approximately 10° C increase in melting points after each heat treatment except the one which was quenched in liquid nitrogen from 335° C.

The melting point increase in PEEK samples may be due to lack of reinforcements which means the spherulite shape can change more easily without any impingement by carbon fibres and without any nucleation effect due to carbon fibres. Tables 1 and 2 show the melting points of PEEK and APC2 samples respectively.

3.2. Dynamic Mechanical Spectrums and Glass Transition Temperatures

The T_g of PEEK and APC2 from the DSC data and from the dynamics spectrums are in close agreement. The dynamic spectrum gave 165.9° and 160.9° C as T_g of PEEK and APC2, respectively. The T_g of the composite samples show changes depending on the heat treatment done. While the T_g of APC2 and APC2-Q(345) are almost same there is 10° C increase in T_g for APC2-FC(330), 15° C for APC2-FC(240), and approximately 5° C increased for APC2-Q(335). Therefore a question arises if the glass transition temperatures are not only dependent on the amorphous phase but on crystalline phase as well. This means degree and perfection of crystallinity. It is imposible to answer this question at this moment without further investigation. Attributing these changes to the changing molecular weight of the sample is diffucult because it is known that even though the molecular weights of three commercial grade polyethoretherketone polymers, namely 150P, 380P and 450P grades, are different they have the same glass transition temperatures. If the change in glass transition temperatures does not depend on crystallinity in addition to amorphous phase it may be thought that the entanglement of the polymer chains somehow changes so that they loose their mobility. The chain mobility also decreases by the presence of carbon fibres. On the other hand glass transition temperatures of PEEK samples are more or less same. There is no distinct change in Tg of these samples. Tables 3 and 4 show the Tg values of PEEK and APC2 samples respectively.

Figures 2 and 3 show the dynamic mechanical specturms of PEEK and APC2, respectively, in the temperature range 100° -240° C.

It was further determined if there is frequency effect on the dynamic mechanical spectrums. For this purpose 1 rad/sec and 0.1 rad/sec frequencies were applied. It was concluded that there is a considerable frequency effect on the spectrums especially at low frequency value of 0.1 rad/sec. The results of these experiments were shown in terms of Tg and tan δ in Tables 5 and 6.

Even when the frequency was decreased to 0.1 rad/sec the Tg obtained was greater than the usually reported value of 143° C. Partridge et al (10) have also reported T_g of PEEK as 160° C. The results show that Tg of PEEK in literature is also lower than the Tg of APC2 tested which is also an indication for the difference of the matrix of APC2 than of usual matrix material PEEK.

It was also seen that tan δ value measured at Tg for less crystalline composite material is the largest. This may be an indication of debonding the fibre and the matrix. As the debonding increases it becomes possible for the material to dissipate more of the input energies due to inter-fibre friction. The decrease in adhesion in quenched samples was also cofirmed by fracture surface analysis which is discussed below.

3.3. Crystallinity of the Specimens

As mentioned above, the crystallinity of the specimens was determined by using two methods. First, it was determined by using the heat of fusion values obtained from DSC thermograms. Second, wide angle X-ray diffraction was used to calculate the crystallinities. Table 7 shows the heat of fusion values and corresponding crystallinities for PEEK samples. Table 8 shows the heat of fusion values for APC2 specimens, corrected heat of fusions for the matrix and corresponding crystallinities of APC2 samples. The crystallinities determined by using WAXD are shown in Tables 9 and 10.

It is seen that both DSC data and WAXD data gave more or less same figures. The difference, especially for the APC2 samples between the crystallinities of the samples obtained by two different methods is undoubtedly due to the method difference and neither the DSC crystallinities nor WAXD crystallinities are the absolute crystallinities of the materials. The only exeption which is contradictory is data obtained for PEEK-Q(345). All the crystallinities of PEEK samples were estimated by drawing an hypothetical background reflection due to amorphous phase. This high crystallinity of PEEK-Q(345) is probably a wrong estimation. Nevertheless, it is concluded that the percent crystallinity can be changed to a certain extent by heat treatment which may facilitate a change in mechanical properties if it is desired. It is obvious from the results that both slow cooling from 330° C and first heating to 330° C followed by slow cooling from 240° C increases the crystallinity as expected. Although the difference in crystallinities obtained as a result of these two heat treatments is not significant for the composite samples, 10% difference is seen in the case of PEEK specimens. Quenching in liquid nitrogen from 335° C changes crystallinity but since already existing crystals could not melt at this temperature for PEEK-Q(335) this heat treatment only increased crystallinity for this specimen as if it was annealed and final quenching changed nothing. However same heat treatment for APC2-Q(335) shows a considerable decrease in crystallinity. This means that the former crystallites of APC2-Q(335) melted to a certain extent and further crystallization was suppressed by quenching. The reason why the melting of spherulites occur below 341.9° C, which is the determined crystal melting point, is that some spherulites may have different morphology which in turn means that they may have somewhat lower crystal melting point. Some of the DSC thermograms show double peaks as crystal melting occurs (Figure 4). This is probably due to recrystallization which occured as a result of the heat treatment applied.

When both PEEK and APC2 were quenched in liquid nitrogen from 345° C they showed a considerable decrease in crystallinity.

It is also worth mentioning that although the obtained diffraction patterns for APC2 specimens are in agreement with the patterns appeared in the literature there is a difference between the diffraction pattern obtained and that in the literature for PEEK. The obtained peaks appear at 18.7°, 20.7°, 22.5° and 28.7° which are in agreement with the reported figures but the peak at 18.7° is not the strongest intensity peak in the results but it is the strongest peak in the literature on PEEK [5,9]. The strongest intensity peak appears at 22.5° (Figure 1). Additionally there is no preferred orientation in the PEEK tested is it was expected.

3.4. Flexure Testing Results and Fracture Surfaces

Flexture tests were done to determine the effect of the heat treatment on flexural properties. The results of flexure tests are shown in Tables 11 and 12.

As mentioned above the load applied was perpendicular to the fibre direction. As far as the results are concerned there is no direct relationship between flexure modulus or strength and crystallinity. Therefore it seems that flexural properties develop independent of crystallinity at least in the crystallinity range tested which is 21.45-41.13% for PEEK samples and 18.61-34.42% for APC2 samples according to DSC data. For the case the load parallel to fibre direction the behaviour of the composite may be different.

Finally fractographic examination was done under scanning electron microscope. In these micrographs it is clearly seen that apart from tension and compression failures buckling and delamination also occured. Figures 5 and 6 show the whole thickness of the fracture surfaces of APC2-FC(330) and APC2-Q(335). If the crystallized APC2-FC(330) is compared with the quenched APC2-Q(335) it will be clearly seen that the fibre-matrix adhesion in the quenched sample is lower than the crystallized one. The fibre surfaces in the quenched sample is more clean. Fibre pull-out from the matrix in the tension area is quite obvious. Figure 7 shows the fibre-matrix interfaces in tension area of APC2-FC(330). This micrograph also shows good fibre-matrix adhesion in a crystallized sample. Figure 8 shows the compressive fibre failure and ductile tensile failure of matrix of APC2-FC(330). Figure 9 shows fibre-matrix interfaces in tension area and fibre tips in compression area of APC2-FC(330). Good fibre-matrix adhesion can also be seen for the crystallized sample in these figures. However, fracture surface from compression area of APC2-Q(345) shows fibre-matrix debonding as a results of quenching as shown in Figure 10. Figure 11 shows compression and tension surfaces on a single fibre tip and fibre-matrix debonding of the specimen APC2-Q(345).

Table1. The melting points of PEEK specimens.

	PEEK	PEEK-FC(330)	PEEK-FC(240)	PEEK-Q(335)	PEEK-Q(345)
Tm (°C)	338.5	350.2	346.2	337.6	345.2

Table 2. The melting points of APC2 specimens.

	APC2	APC2-FC(330)	APC2-FC(240)	APC2-Q(335)	APC2-Q(345)
Tm (°C)	341.9	344.8	349.6	342.11	342.5

Table 3. The glass transition temperatures of PEEK specimens.

	PEEK	PEEK-FC(330)	PEEK-FC(240)	PEEK-Q(335)	PEEK-Q(345)
Tg (°C)	165.9	170.8	170.8	164.9	170.1

Table 4. The frequency effect on Tg in dynamic mechanical spectrum.

	APC2	APC2-FC(330)	APC2-FC(240)	APC2-Q(335)	APC2-Q(345)
Tg (°C)	160.9	171	176	165.2	160.3

Table 5. The frequency effect on Tg in dynamic mechanical spectrum.

	FREQUENCY		
	62.8 rad/sec	1 rad/sec	0.1 rad/sec
Tg (°C) [APC2]	160.9	159.6	154.7
Tg (°C) [PEEK]	165.9	159.7	154.8

Table 6. The frequency effect on tan in dynamic spectrum.

	FREQUENCY		
	62.8 rad/sec	1 rad/sec	0.1 rad/sec
tan (at Tg) [APC2]	6.0x10-3	7.05x10-3	1.56x10-2
tan (at Tg) [PEEK]	1.69x10-1	2.72x10-1	2.26x10-1

Table 7. The heat of fusion data and corresponding crystallinities for PEEK specimens.

	PEEK	PEEK-FC(330)	PEEK-FC(240)	PEEK-Q(335)
ΔHm PEEK (J/g)	38.96	53.47	40.93	43.33
% Crystallinity	29.97	41.13	31.48	33.33

Table 8. Heat of fusion data and corresponding crystallinities for APC2 specimens.

	APC2	APC2-FC(330)	APC2-FC(240)	APC2-Q(335)
ΔHm composite (J/g	10.81	13.15	12.02	7.74
ΔHm matrix (J/g)	33.78	41.09	37.56	24.19
% Crystallinity	25.99	31.61	28.89	18.61

Table 9. Crystallinities of PEEK specimens from WAXD data.

	PEEK	PEEK-FC(330)	PEEK-Q(335)	PEEK-Q(345)
% Crystallinity	28.61	36.08	36.03	32.1

Table 10. The crystallinities of APC2 specimens from WAXD data.

	APC2	APC2-FC(330)	APC2-Q(335)	APC2-Q(345)
% Crystallinity	18.33	24.72	18.33	17.7

Table 11. Flexture testing results of PEEK specimens.

	PEEK	PEEK-FC(330)	PEEK-FC(240)	PEEK-Q(335)	PEEK-Q(345)
(MPa)	191.75	184.67	174.48	173.46	173.72
E (MPa)	2976.77	3421.53	3418.56	3201.89	3234.58

Table 12. Flexture testing results of APC2 specimens.

	APC2	APC2-FC(330)	APC2-FC(240)	APC2-Q(335)	APC2-Q(345)
(MPa)	1789.13	1887.13	1799.91	1788.16	1835.7
E (MPa)	152224	151204	147497	151466	156796

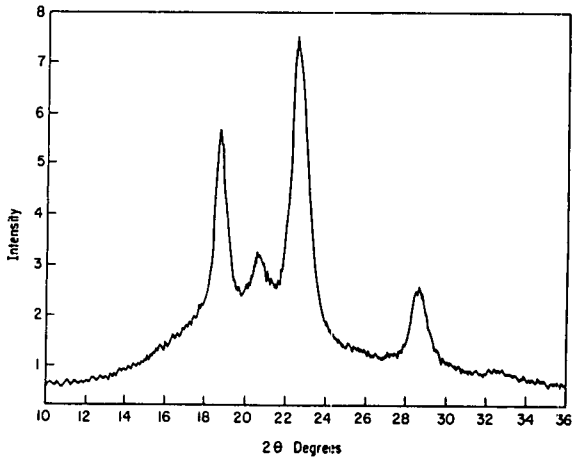

Figure 1. A typical X-ray diffraction scan of PEEK specimens.

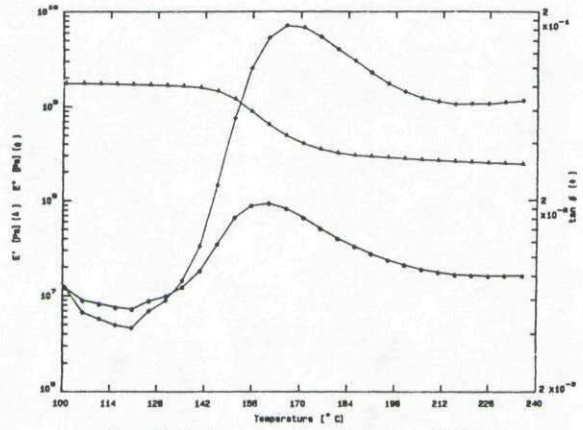

Figure 2. The dynamic mechanical spectrum of PEEK.

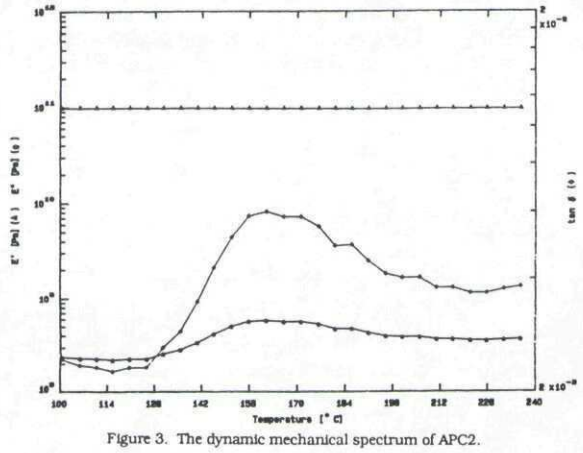

Figure 3. The dynamic mechanical spectrum of APC2.

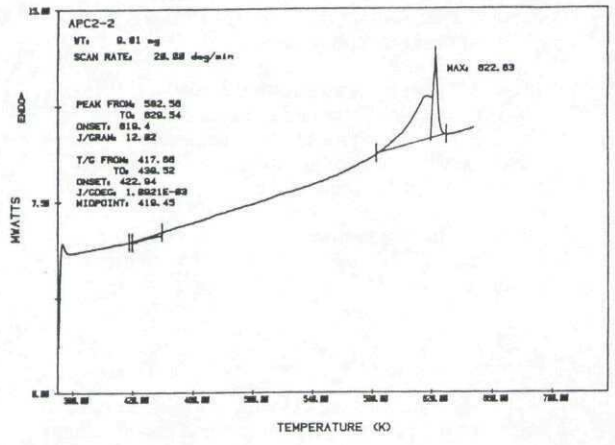

Figure 4. DSC thermogram of APC2-FC(240).

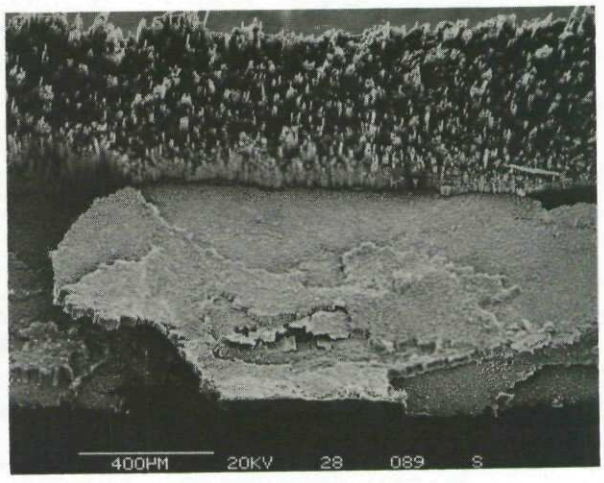

Figure 5. Flexural failure of APC2-FC(330) where whole specimen thickness is shown.

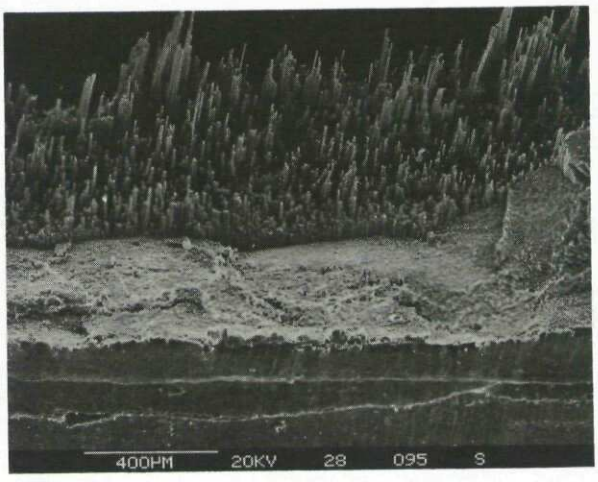

Figure 6. Flexural failure of APC2-Q(335) where whole specimen thickness is shown.

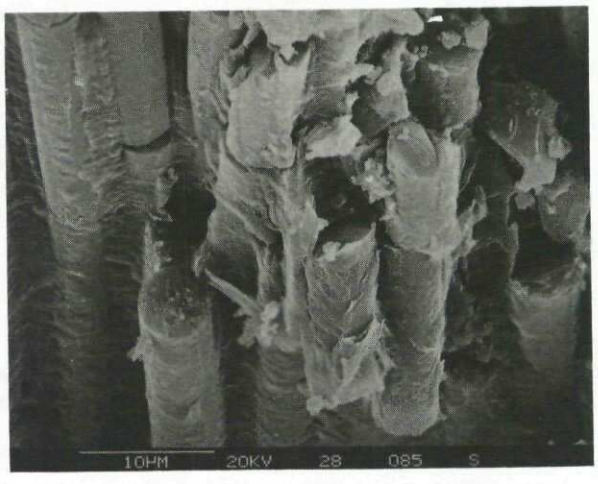

Figure 7. Fibre-matrix interfaces in tension area of APC2-FC(330).

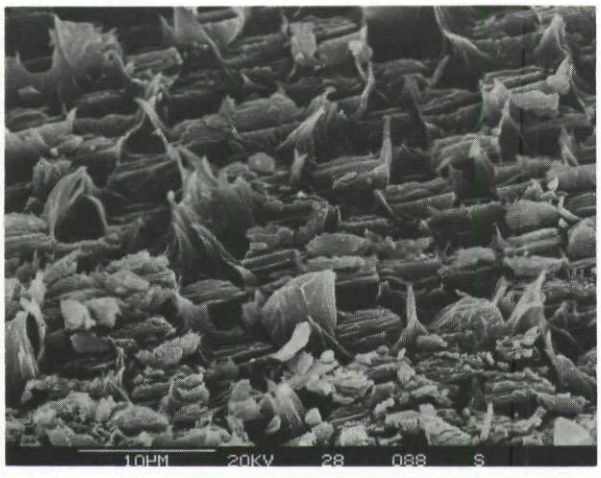

Figure 8. Compressive fibre failure and ductile tensile failure of the matrix of APC2-FC(330).

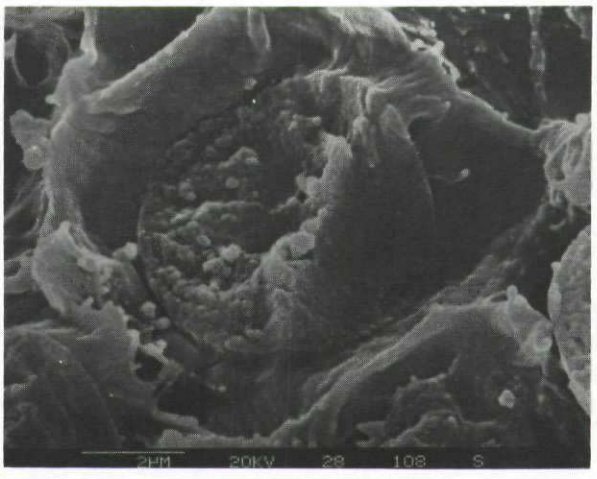

Figure 11. Compression and tension surfaces on a single fibre tip and fibre-matrix debonding (APC2-Q(345)).

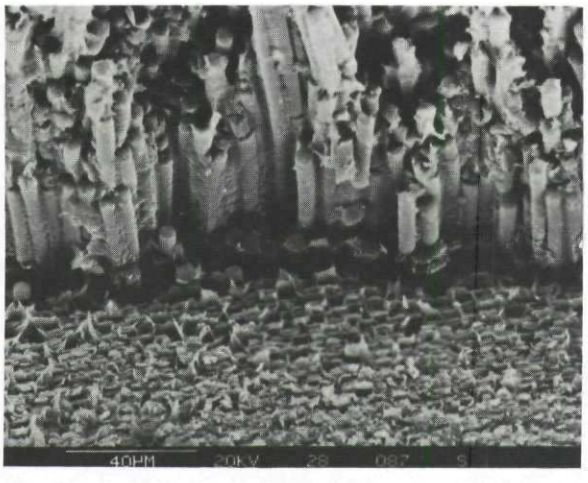

Figure 9. Fibre-matrix interfaces in tension area and fibre tips in compression area (APC2-FC(330)).

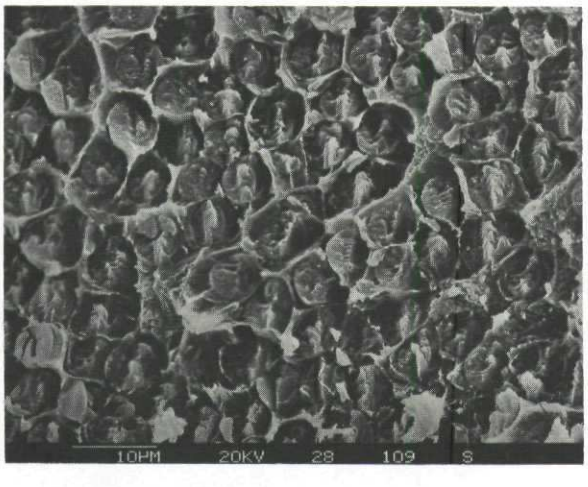

Figure 10. Fracture surface from compression area of APC2-Q(345).

4. CONCLUSIONS

The conclusions of this resarch are:

1. It is possible to control crystallinity of PEEK and APC2 by a suitable heat treatment. Quenching the materials around their crystal melting points can decrease the crystallinity to a certain extent. Annealing below the glass transition temperature and slow cooling increases crystallinity.

2. Both PEEK and APC2 have glass transition temperatures higher than usually reported 143°C. Moreover the diffraction pattern of PEEK is slightly different than the reported one.

3. There is no relationship between the flexural properties of both materials and the heat treatments applied. This in turn means that flexural properties of the composite does not depend on the crystallinity for the case the load perpendicular to the fibre direction.

4. Fracture surface studies show that the quenched APC2 looses its fibre-matrix adhesion to certain extent.

ACNOWLEDGEMENT

The authors wish to thank ICI (UK) and MBB (Germany) for the material supply and encouraging discussions. Part of the work was supported by NATO under the SMP Programme Project T.41 which is greatly acknowledged.

REFERENCES

1. Haym, M., Western, E.D., and Winkler, M., "New Material Forms for Manufacture of Thermoplastic Composites", Proc. PRI Conf., "Automated Composites '88", Leeuwenhorst 3/1-3/12, (1988).

2. Clemans, S., and Hartness, T., "Thermoplastic Prepreg Technology for High Performance Composites", SAMPE Quartley, 38-42, July 1989.

3. Cogswell, F.N., and Hopprich, M., "Enviromental Resistance of Carbon Fibre-Reinforced Polyetheretherketone", Composites, Vol.14, 251-253, (1983).

4. Blendell, D.J., Crick, R.A., Fife, B., Peacock, J., Keller, A., and Waddon, A., "The Spherulitic Morphology of the Matrix of Thermoplastic PEEK/Carbon Fibre Aromatic Polymer Composites", Journal of Materials Science, Vol.24, 2057-2064, (1989).

5. Talbott, M.F., Springer, G.S., and Berglund, L.A., "The Effect of Crystallinity on the Mechanial Properties of PEEK Polymer and Graphite Fiber Reinforced PEEK", Journal of Composite Materials, Vol.21, 1056-1081, (1987).

6. Blundell, D.J., and Osborn, B.N., "The Morphology of Poly (aryl-ether-ether-kentone)", Polymer, Vol.24, 953-958, (1983).

7. Mijovic, J., and Gsell, T.C., "Calorimetric Study of Polyetheretherketone (PEEK) and Its Carbon Fiber Composite", SAMPE Quartely, 42-46, January 1990.

8. "Handbook of X-Rays, For Diffraction, Emission, Absorption, and Microscopy", Edited by E.F. Kaelble, McGraw-Hill, (1967).

9. Blundell, D.J., Chalmers, J.M., Mackenzie, M.W., and Gaskin, W.F., "Crystalline Morphology of the Matrix of PEEK-Carbon Fibre Aromatic Polymer Composites: I. Assessment of Crystallinity", SAMPE Quarterly, Vol.16, 22-30, (1985).

10. Partidge, I.K., Davies, P., Parker, D.S., and Yee, A.F., "Yield and Fracture in PES and PEEK Matrix Polymers and Their Composites", PRI Polymer for Composites Conference, Paper 5, (1987).

11. Kalay, G., "The Effect of Heat Treatment on the Properties of PEEK and Its Carbon Fibre Composite", M.Sc. Thesis, Middle East Technical University, Ankara, (1990)

Environmental Resistance of Amorphous Bonded Thermoplastic Joints

C. Voto
M. Iannone
Alenia S.p.A.
Zona ASI Incoronata
71100 Foggia, Italy

1. SUMMARY

Amorphous bonding appears to be a promising method of joining thermoplastic matrix advanced composites.

The temperature to bond, lower than for fusion bonding, and the limited dimension of the melted zone, allow significant cost reduction and guarantee good mechanical characteristics.

On the other hand a potential problem exists, due to lower resistance to aeronautical solvents and service fluids, because of the amorphous nature of the bonding layers.

The basic resistance to environmental degradation of the resins used for bonding, and the chemical stability of their blends with the semicrystalline matrices of the adherends, have been investigated.

2. INTRODUCTION

Thermoplastic resins show several characteristics very interesting for their use as composite matrix in aeronautical applications. In fact, their molecular structure makes them tougher than thermosettings, because of their higher plasticity; this property gives them also a higher impact resistance. When heated above the glass transition temperature (Tg) or, for semicrystalline thermoplastics, above the melting temperature (Tm), the thermoplastic composites can be molded. They can be indefinitely stored at room temperature and can be potentially reprocessed. Several of the thermoplastic resins used as composite matrix show high service temperature and good resistance to the environment and the aeronautical fluids. Finally, welding is a joining technique applicable to thermoplastics, with high potentiality for cost reduction.

On the other hand, the major drawbacks affecting thermoplastic application for aeronautics are the high cost of raw materials and the incomplete availability of processing techniques and facilities.

Two of the thermoplastic resins more widely investigated are PEEK (Poly-Ether-Ether-Ketone) and PPS (Poly-Phenilen-Sulfide). They are semicrystalline, i.e. in their molecular structure an amorphous phase is merged with a crystalline one. This latter phase gives higher resistance to the environment. Furthermore, being the melting temperature of the crystalline phase always higher than the glass transition temperature of the amorphous one (an approximate ratio of 3/2 of the two temperature expressed as Kelvin Degrees does usually exist), the high temperature properties of the material are strongly increased when a crystalline phase is included.

One of the most interesting composite with a semicrystalline thermoplastic matrix is APC-2, tradename of a composite developed and supplied by ICI Fiberite, with PEEK matrix and Hercules AS-4 carbon fiber reinforcement. Poly-Ether-Ether-Ketone (PEEK), as reported before, is a semicrystalline polymer, with a melting temperature of 343°C and glass transition temperature of 143°C (1-2).

Relative amount and morphology of the crystalline phase depend on processing; a very important processing parameter is cooling rate from melt. In fact, it has been found that a very high crystallinity level (about 40%) is obtained by cooling the melt at very low cooling rates (1°C/min). At cooling rates ranging from 10 to 80°C the final crystallinity reached by the polymer is nearly constant, showing a value of about 30%. Quenching the melt polymer at higher cooling rates a lower crystallinity content is obtained, until a complete quenching, giving fully amorphous material, is observed at cooling rates higher than 1000°C/min.

The mechanical and physical properties of the PEEK resin, as well as those of PEEK based composite, have been found nearly constant in the cooling rate range from 10 to 80°C/min, in spite of the different sizes of the formed spherulites correspondent to the different cooling rates. That means that the above mentioned range can be considered as a processing window giving properties nearly constant; furthermore this "intermediate crystallinity" condition is the best compromise between the condition with higher crystallinity, which improves the environmental properties decreasing the toughness, and the one with lower crystallinity with higher toughness and poorer environmental strength.

In practical applications the cooling rate of the processed parts obviously depends on

the fabrication technique. When PEEK, or PEEK based composite, is processed in thicknesses above 0.5 mm, it has been proved that, also for very fast cooling of the external surface of the processed part, cooling rate of most of the parts falls in the "optimum processing window" described above. So, for the techniques in which PEEK is processed as laminate, amorphization can affect only the surface zone. Some problems can arise, for this way of processing, only by too slow cooling rates. This is a potential problem for techniques like autoclaving, where a cooling rate not lower than 10°C/min must be obtained to prevent a too high crystallinity content. When the material is processed in thin plies, as in the case of automated techniques like automated tape lay-up or filament winding, the problem of amorphization by quick cooling exists.

Processing of the PEEK in the amorphous state has been investigated (3). The interest on this issue arises mainly by the possibility to process it above Tg, instead than above Tm, with a strong process simplification; that is infact potentially possible because, when the crystalline phase is absent, the material can flow above Tg, and can be potentially molded. The analysis carried out in the reference paper by DMA coupled with Thermal Analysis confirmed that this way of processing is potentially possible, but at the same time pointed out that crystallization from amorphous phase is too fast to allow a practical application of this technique.

Another investigated issue was the nature of the crystalline phase obtained by amorphous state (cold crystallization). It was found that crystallinity generated from amorphous state can reach, annealing for sufficient times at adequate temperatures, a satisfactory quantitative level, but morphology is quite different from the spherulitic one generated from melt, and this structure has been found to be more brittle. This consideration is then discouraging about this way of processing PEEK, and suggests to control, as carefully as possible, cooling rate from melt.

3. GENERAL ASPECTS OF THERMOPLASTIC WELDING

The knowledge of crystallization and amorphization mechanisms is very important for welding, which is a joining technique peculiar, among the polymers, of thermoplastics. Fusion welding consists of melting (this term is appropriate for semicrystalline thermoplastics, less for the amorphous ones, where Tg is not a melting, but a transition point) the facing zones (and eventual inserts) and joining the parts by cooling under pressure.

Different fusion welding techniques exist, depending on the heat generation source: vibration welding, where the heat is generated by friction of the contacting parts; ultrasonic welding, where heat is generated by ultrasounds; hot plate welding, where melting of the facing surfaces is obtained by contact with a heated plate; induction welding, where heating is obtained by the Foucauld's currents generated by a variable electromagnetic field; resistance welding, where heating is obtained by Joule effect.

Among the listed techniques resistance welding appears to be potentially suitable for industrial applications, namely when it is performed using an insert.

The set-up for resistance welding of APC-2 performed with a prepreg insert is shown in fig.1. Heating is obtained by Joule effect, by applying electric power to a prepreg, from the ends of which the resin has been removed to improve the contact. Additional layers of neat PEEK resin are provided to prevent the current to pass through the APC-2 parts.

The current intensity must be optimized as function of time in order to:

a. reach a temperature high enough to melt the overall zone of the insert and the surface zone of the parts to be melted, but at the same time not so high to induce polymer degradation;

b. obtain a cooling history which gives a right crystallinity content and morphology in the melted part. In fact, being the conductive heat flow very high and the heated zone very small, amorphization by quenching of the welded areas can easily happen, unless the power is not adequately applied during the time.

A theoretical model has been used for the optimization of these parameters (4). Amorphization of the welding zones is not a problem for the "short term" mechanical properties of the joints; in fact, the shear strength of the joints with amorphous welding zone is not lower than that of the joints where semicrystalline morphology has been kept through appropriate cooling; major concerns arise from environmental stability of amorphous PEEK. In fact, as previously mentioned, amorphous PEEK is less resistant to temperature and solvents than the semicrystalline one. Furthermore, it quickly crystallizes above Tg, giving imperfect crystalline structures, which are unwanted by a toughness point of view. This cold crystallization could happen also, for longer times, at temperatures below Tg; the crystallization kinetics increase when plasticization effects are induced by solvents.

4. AMORPHOUS WELDING

One of the major technological difficulties for thermoplastic welding, as well as for other processing techniques, is the need to reach a very high temperature. As previously described the possibility to work the composite in the amorphous state in order to reduce that temperature is, for APC-2, rather theoretical than practical. Another method to reduce processing temperature for semycristalline thermoplastics is based on addition of a different amorphous polymer, having a Tg lower than the Tm of the semicrystalline one. Further than decreasing the welding temperature, the use of an amorphous layer gives the additional advantage to operate with a welding zone "lower melting" than the rest of composite; consequently, it is possible to weld the parts minimizing disturbance of the zones

not involved in the welding. Thus, the use of the amorphous layer allows to perform more easily, and with lower disturbance of the joining parts, all the fusion welding techniques previously mentioned.

Furthermore, it is possible to use some techniques like autoclaving, operating with not too complicate tools. Amorphous welding by autoclave is similar, by tooling point of view, to thermoset secondary bonding, because the parts keep their shape during bonding, like the precured parts. A meaningful difference is given by processing time, which for amorphous bonding is much lower, because the resin is already polymerized and does not need any cure.

To be successfully applied to APC-2 amorphous bonding, which has been patented by ICI-Fiberite with the name of "Thermabond", an amorphous polymer (presently Poly-Ether-Immide PEI Ultem has been found to be the most suitable) needs to be consolidated on the surface of the parts to be joined. PEI and PEEK have been found to form a blend, and the adhesion of the parts depend on compenetration by molecular diffusion of the two phases.

The nature of the PEEK-PEI blends has been investigated by thermal analysis (5). For blends PEEK-PEI with different PEI content a single glass transition temperature has been observed, and its value can be satisfactorily evaluated by a theoretical equation. The effect of the amorphous PEI on the PEEK crystallinity is of simple dilution; the heat of fusion of the blends, in fact, is proportional to the PEEK content.

The evaluation of crystallinity of PEEK-PEI blends cooled at different cooling rates showed a processability window narrower than the one observed for neat PEEK. In fact amorphization of the blend by quenching is observed for cooling rates (above 100°C/min) lower than the ones needed to amorphize neat PEEK.

5. EVALUATION OF AMORPHOUS BONDED JOINTS

A program aimed to evaluate mechanical strength of amorphous joints exposed to aeronautical fluids has been performed.

The joints have been fabricated by overlap of two panels obtained laying up 16 plies of APC-2 with a quasi isotropic configuration; on the surface PEI plies have been added during consolidation of the composite panel. The overlap geometry is showed in fig.2.

Different process parameters have been evaluated to found the optimum conditions, both for panel consolidation and joint bonding. The evaluated consolidation variables are: consolidation apparatus (press or autoclave), pressure, thermal history (temperature vs. time), thickness of the additional PEI layer; the evaluated joining variables have been: method to give pressure and temperature (by press or by autoclave), pressure, thermal history (temperature vs. time), thickness of PEI insert.

Optimum parameters have been established on the basis of shear strength tests, performed on single lap joint shear specimens obtained from the joints showed in fig. 2 and tested per ASTM D1002. This experimental analysis allowed the detection of the best processing conditions and indicated that there is a wide processability window in which the shear strength of the joint is satisfactory.

Several lap joints were then fabricated with the processing conditions found to be optimum. From each joint five single lap shear specimens were obtained and were exposed to different environments, to evaluate the effect of aging. At the end of the exposure period shear strength of the specimens was tested, and the values were compared with the strength of the unexposed specimens.

The exposition conditions were the following:

30 days in Aviation Fuel Jet A at R.T.

30 days in Skydrol at R.T.

30 days in Methilene Cloride at R.T.

30 days in ambient at R.H. 95%, T=70°C (tests both at R.T. and 93°C)

30 days in Methil-Ethil-Keton (MEK) at R.T.

The individual and average shear strengths are reported in table 1, compared with the strength of specimens tested in "dry" conditions.

The results agree with the available data on the environmental resistance of PEEK and PEI. In fact, PEEK demonstrates a very good strength to all the evaluated aggressive environments, but PEI dissolves completely in Methilene Chloride and is weakened by skydrol.

As listed before, all the tests have been performed after one month of exposition; so, by the service performance point of view, the sensitivity to methilene cloride, which is used only for paint stripping, should be evaluated in less severe conditions.

Sensitivity to skydrol must be more deeply evaluated, but also in this case one month of immersion can be considered a very severe condition.

The anomaly of the hot wet properties better than the room temperature dry ones can be explained in terms of toughening by sligth plasticization.

6. CONCLUSIONS

The environmental strength of APC-2 panels amorphous bonded by PEI has been evaluated. The behaviour has been found generally good, except for resistance to methilene-chloride and skydrol. Some additional investigations are required on the following points:

- Effect of short term exposure in solvents (less than one month of immersion).

- Long term crystallization of PEEK-PEI blends.
- Reciprocal molecular diffusion of PEI-PEEK.
- Possibility to use different amorphous layer material (e.g. PAS, PES, etc.) to bond PEEK matrix composite.

REFERENCES

1. D.J. Blundell and B.N. Osborn, Polymer, 24, 953 (1983)

2. D.J. Blundell, J.M. Chalmers, M.W. Mackenzie and W.F. Gaskin, SAMPE Quarterly, 16(4), 22 (1985)

3. J. Kenny, A. D'Amore, L. Nicolais, M. Iannone and B. Scatteia, SAMPE Journal, 25 (4), (1989)

4. A. Maffezzoli, J.M. Kenny and L. Nicolais, SAMPE J., 25(4), 35 (1989)

5. L. Torre and J.M. Kenny, "Characterization of blends of semi-crystalline and amorphous matrices for high performance composites", Proceedings of the 49th ANTEC Conference, p. 2108, 1991

Table 1

Lap Shear Strength of amorphous bonded joints exposed to different environments

	Exposure Condition						
	DRY	WET	HOT WET (1)	JET FUEL	SKYDROL	MEK	METHILEN CHLORIDE
INDIVIDUAL	27.2	24.3	36.1	25.0	9.6	29.9	(2)
	28.6	25.3	38.5	24.8	9.0	31.9	(2)
	28.3	25.9	35.8	24.3	7.9	30.7	(2)
	27.6	26.9	36.1	25.9	8.5	32.5	(2)
	28.2	27.2	33.9	25.8	7.6	31.3	(2)
MEAN	28.0	25.9	36.1	25.2	8.5	31.3	(2)

(1) Exposed 30 days 95% R.H., T= 70°C, tested at 93°C.

(2) Joints dissolved during exposition.

RESISTANCE WELDING SETUP

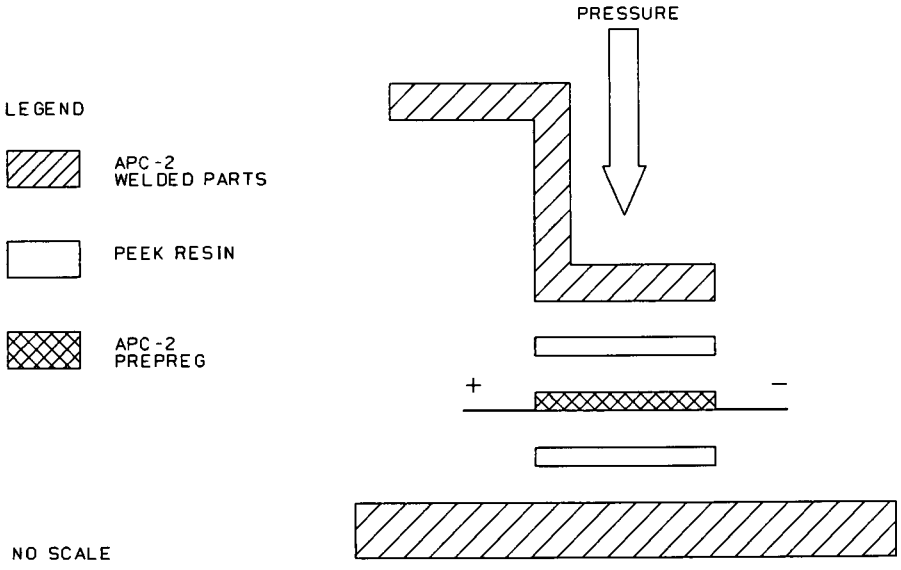

FIG. 1

LAP JOINT SHEAR SPECIMEN CONFIGURATION

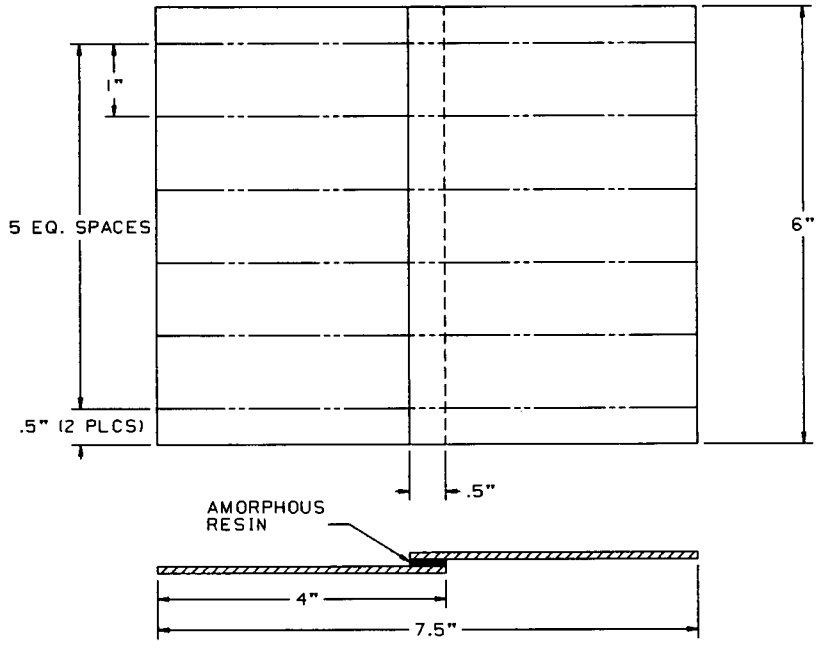

FIG. 2

FLIGHT SERVICE ENVIRONMENTAL EFFECTS ON COMPOSITE MATERIALS AND STRUCTURES

H. Benson Dexter
NASA Langley Research Center
Hampton, VA USA 23665-5225

and

Donald J. Baker
U.S. Army Aviation Research and Technology Activity (AVSCOM)
Aerostructures Directorate
NASA Langley Research Center
Hampton, VA USA 23665-5225

SUMMARY

NASA Langley and the U.S. Army have jointly sponsored programs to assess the effects of realistic flight environments and ground-based exposure on advanced composite materials and structures. Composite secondary structural components were initially installed on commercial transport aircraft in 1973; secondary and primary structural components were installed on commercial helicopters in 1979; and primary structural components were installed on commercial aircraft in the mid-to-late 1980's. Over 5.3 million total component flight hours have been accumulated on 350 composite components since 1973. Service performance, maintenance characteristics, and residual strength of numerous composite components are reported. In addition to data on flight components; 10-year ground-based exposure test results on material coupons are reported. Comparisons between flight and ground-based environmental effects for several composite material systems are also presented. Test results indicate excellent in-service performance with the composite components during the 15 year evaluation period. Good correlation between ground-based material performance and operational structural performance has been achieved.

INTRODUCTION

The influence of operational and ground-based environments on the long-term durability of advanced composite materials and aircraft components fabricated from them is an ongoing concern of aircraft manufacturers and airline operators. Some of the uncertainties include the effects of moisture absorption, temperature cycling, ultraviolet radiation, lightning strikes, and long-term sustained stress. As a result of these concerns, NASA Langley and the U.S. Army initiated flight and ground-based environmental effects programs to assess the performance of composite materials and structures when subjected to normal operational environments. Secondary and primary structural composite components have been in service on transport aircraft and helicopters since the early 1970's. Service performance has been documented and residual strength tests were performed to assess the effects of flight environments on structural performance. Since most aircraft spend a considerable portion of their service life on the ground, a series of coupon tests were performed to assess the effects of ground-based environments on several composite material systems. Residual strength, stiffness, and moisture absorption as a function of exposure time were determined and the results are compared with tests on composite structural components removed from service. The purpose of this paper is to summarize the results of 10 years of environmental exposure of composite materials and to discuss results for 15 years of flight service of composite components on transport aircraft and helicopters.

FLIGHT SERVICE EVALUATION OF COMPOSITE COMPONENTS

In 1973 the NASA Langley Research Center initiated a series of programs to evaluate the effects of realistic flight environments on composite components. The objective was to establish confidence in the long-term durability of advanced composites through flight service of numerous composite components on transport aircraft. Emphasis was on commercial aircraft because of their high utilization rates, exposure to worldwide environmental conditions, and systematic maintenance. The experimental composite components allowed the airlines to develop inspection and repair procedures prior to making production commitments. In 1979 NASA Langley and the U.S. Army initiated joint programs to evaluate composite components on commercial and military helicopters. Although helicopters accumulate fewer flight hours than transport aircraft, in many instances the environments and fatigue loading are more severe for the helicopter components. Primary emphasis for the helicopter components is to establish the effects of realistic operating service environments on the strength of primary and secondary composite components. These environmental factors can then be applied with more confidence and less conservatism in the future design of composite components.

Component Description

The transport aircraft that are flying composite components in the NASA Langley service evaluation program are shown in figure 1. Eighteen Kevlar-49/epoxy fairings have been in service on Lockheed L-1011 aircraft since 1973. In 1982, eight graphite/epoxy ailerons were installed on four L-1011 aircraft for service evaluation. One hundred and eight B737 graphite/epoxy spoilers have been in service on seven different commercial airlines in worldwide service since 1973. Ten B737 graphite/epoxy horizontal stabilizers have been installed on five aircraft for commercial service. Fifteen graphite/epoxy DC-10 upper aft rudders have been in service on twelve commercial airlines and three boron/aluminum aft pylon skin panels were installed on DC-10 aircraft in 1975. One graphite/epoxy vertical stabilizer was installed on a DC-10 aircraft in 1987. Ten graphite/epoxy elevators have been in service on B727 aircraft since 1980. In addition to the commercial aircraft components indicated in figure 1, two boron/epoxy reinforced aluminum center-wing boxes have been in service on U.S. Air Force C-130 transport aircraft since 1974. Details of the structural design concept and manufacturing procedures used for each component can be found in reference 1. The transport airlines/operators participating in the NASA Langley flight service program are listed in figure 2. The airlines were selected to represent diverse climatic conditions and route structures.

The helicopters that are flying composite components in the NASA Langley/U.S. Army service evaluation program are shown in figure 3. Forty shipsets of Kevlar-49/epoxy doors and fairings and graphite/epoxy vertical fins have been installed on Bell 206L commercial helicopters for 10 years of service evaluation. The helicopters are operating in diverse environments in Alaska, Canada, U.S. Gulf Coast, Northeast U.S., and Southwest U.S. Selected components are periodically removed from service for residual strength testing. Details on the design, fabrication, and test of the Bell 206L composite components can be found in reference 2.

Ten graphite/epoxy tail rotors and four hybrid Kevlar-49-graphite/epoxy horizontal stabilizers were removed periodically from Sikorsky S-76 production helicopters to determine the effects of realistic operational service environments. Static and fatigue tests were conducted on the components removed from service, and the results were compared with baseline certification test results. Details on the design, fabrication, and test of the S-76 composite components are reported in reference 3.

A Kevlar-49/epoxy cargo ramp skin is installed on a U.S. Marine Corps CH-53D helicopter for service evaluation. Details of the design, fabrication, and installation of the cargo ramp skin are reported in reference 4. The helicopter airlines/operators participating in the NASA Langley/U.S. Army flight service program are listed in figure 4.

As indicated in figure 5, the NASA Langley flight service program that was initiated in 1973 included a total of 350 composite components. As of June 1991, 139 components were still in service; more than 5.3 million component flight hours had been accumulated, with the high-time aircraft having more than 58,000 flight hours. Some components were removed from service for residual-strength testing, and others were retired due to damage or other service-related problems that are discussed herein.

MAINTENANCE, REPAIR, AND STRUCTURAL PERFORMANCE

Transport Components

For the first several years of the flight service evaluation program, the composite components were tracked and inspected by aircraft manufacturer engineering personnel. Later in the program, maintenance and repair data were obtained from the airline maintenance personnel. Overall, the composite components have performed better than conventional metallic structures because of reduced corrosion and fatigue problems. However, some operational maintenance concerns surfaced with the composite components during the 15 year service evaluation. Some of the concerns were considered to be minor, whereas some of the components may require design changes before the aircraft manufacturers are ready to commit to production of composite components. One area that needs more attention in future designs is improved lightning protection schemes.

L-1011 Kevlar-49/Epoxy Fairings

The photographs shown in figure 6 indicate various types of damage incurred by the L-1011 Kevlar-49/epoxy fairings in service. Minor impact damage from equipment and foreign objects has been noted on several fairings, primarily the honeycomb sandwich wing-to-body fairings. Surface cracks and indentations have been repaired with filler epoxy and, in general, the cracks have not propagated with continued service. Paint adherence has been a minor problem, particularly for parts that have been in contact with hydraulic fluid. Frayed fastener holes have been noted in several fairings, primarily due to nonoptimum drilling procedures and improper fit. Elongated holes have been noted, primarily due to improper fit and nonuniform fastener load distribution. There have been no moisture intrusion problems with the Kevlar-49/epoxy fairings, and they have performed similar to production fiberglass/epoxy fairings. The fairings are still in service, and the three participating airlines are monitoring their performance during normal maintenance inspections. Additional details on the design, fabrication, and service evaluation of the Kevlar-49/epoxy fairings are presented in references 5 and 6.

B737 Graphite/Epoxy Spoilers

The B737 spoiler skins were fabricated with three different graphite/epoxy systems: T300/5209, T300/2544, and AS/3501. Aluminum honeycomb substructure and aluminum fittings were similar to those used in production aluminum spoilers. During the 15 year service evaluation period, several types of in-service damage were encountered. Over 75 percent of the damage incidents were related to design details. The most prevalent damage was caused by actuator rod interference with the graphite/epoxy skin. This problem was resolved by redesigning the actuator rod ends. The second most frequent damage was caused by moisture intrusion and corrosion at the splice between the center hinge fitting and spar. This damage could be prevented by redesigning the splice to prevent disbonds between the skin and spar cap. Miscellaneous cuts and dents related to airline usage were also encountered. Damage due to hailstone, bird strike, and ground handling equipment was noted on several spoilers. Minor repairs were performed by the airlines after proper instruction by Boeing repair personnel. Because of the expense involved, spoilers with major damage were removed from service.

A typical corrosion damage scenario for a splice between the center hinge fitting and spar is shown in figure 7. The corrosion damage can be characterized by three phases of development. Phase 1 involves corrosion initiation at an aluminum fitting or at the aluminum spar splice. The corrosion initiates due to moisture intrusion through cracked paint and sealant material. If the corrosion products are not removed and new sealant applied, the damage progresses to phase 2 where moisture penetrates under the graphite/epoxy skin along the aluminum C-channel front spar. Normal service loads combined with moisture contribute to crack growth and subsequent corrosion. If the phase 2 corrosion is not repaired, the damage progresses to phase 3 where extensive skin-to-spar separation takes place. Phase 3 corrosion can result in significant strength and stiffness loss. It takes about 2 years for the corrosion to progress from phase 1 to phase 3. Design changes and improved sealing methods could prevent corrosion damage in composite-metal interfaces.

Residual strength tests were conducted on 37 graphite/epoxy spoilers to establish the effects of service environments. The spoilers were tested with compression load pads on the upper surface to simulate airloads. Trailing edge tip deflection was measured as a function of applied load for each spoiler tested. The test results are compared with the strength of 16 new spoilers in figure 8. The strength for each spoiler through 6 years of service generally falls within the strength scatter band for the baseline spoilers. However, spoilers with significant corrosion damage which were tested after 7 and 8 years of service, respectively, indicated a 35 percent strength reduction. An additional T300/2544 spoiler with no corrosion damage was tested after 7-1/2 years of service, which verified that the 7 year strength reduction was related to corrosion damage. Three spoilers tested after 9 years of service with little or no corrosion damage exhibited strengths equal to the strength of the baseline spoilers. An AS/3501 spoiler with 10 years of service and known corrosion damage failed at 78 percent of the average strength of the baseline spoilers. Two other spoilers with 10 years of service with no corrosion damage failed within the baseline strength scatter band. Spoilers tested after 12 years of service failed at or above the average strength of the baseline spoilers. One spoiler that had known corrosion damage after 15 years of service failed at about 75 percent of the strength of baseline spoilers.

Load-deflection response of spoilers with 10 years and 15 years of service time are compared with the response of baseline spoilers in figure 9. The 10 year spoiler with known corrosion damage failed at about 78 percent of the baseline strength. However, the 15 year spoiler with almost 38,000 flight hours failed at about 8 percent above the baseline strength. Additional details of service experience with the spoilers can be found in reference 7.

DC-10 Boron/Aluminum Aft Pylon Skins

One of the three boron/aluminum skin panels on the DC-10 aircraft was removed from service after 7 years because of corrosion damage. The photograph shown in figure 10 indicates that the outer layer of boron filaments on the inside of the panel was almost completely exposed. The panel contained a light residue of ester oil similar to engine oil; however the specific corrodent was not identified. A second panel also had some corrosion damage and a small crack, but the panel is still in service and is being monitored closely to check for crack growth and further corrosion damage. The crack in the panel was probably caused by exterior mechanical damage during removal and reinstallation of the panel during inspection. It has been concluded that the method of corrosion protection used was inadequate. In general, the boron/aluminum panels have not performed as well as similar production titanium panels. Additional details on the DC-10 boron/aluminum skin panels are presented in reference 8.

DC-10 Graphite/Epoxy Rudders

There have been several incidents which required rudder repairs. The damage sustained by the rudders included minor disbonds, rib damage due to ground handling, and skin damage due to lightning strike. Figure 11 shows minor in-service lightning strike damage to the trailing edge of a rudder and rib damage that occurred while a rudder was off the aircraft for other maintenance. The lightning strike damage was limited to the outer four layers of graphite/epoxy and a room temperature repair was performed in accordance with procedures established at the time the rudders were certified by the FAA. The rib damage was more extensive and a portion of a rib was removed and rebuilt. A detailed discussion of the repair procedure is given in reference 9.

More extensive lightning damage was sustained on another graphite/epoxy rudder as shown in figure 12. Upon inspection of the rudder, it was discovered that the lightning protection strap was inadvertently left off after the previous maintenance check. The skin in the damaged area is eight plies thick over an 8-ply spar cap. Fiber damage and resin vaporization extended through the skin forward of the spar, and the skin and spar cap aft of the rear spar were completely destroyed. Details of the repair procedures are given in reference 10.

A graphite/epoxy rudder was removed from service for residual strength testing after 5.7 years and 22,265 flight hours on Air New Zealand. The load-deflection response shown in figure 13 indicates that the 5.7-year rudder had an initial stiffness higher than the baseline rudder, but the overall response is similar for the two rudders. The baseline and the 5.7-year tests were stopped at approximately 400 percent limit load because of an instability of the loading apparatus. Although the rudders are designed by stiffness considerations and only one residual strength test has been conducted, the overall response of the rudder indicates that no degradation has occurred as a result of over 22,000 flight hours.

B727 Graphite/Epoxy Elevators

Since initiation of flight service of 10 elevators in 1980, there have been four B727 graphite/epoxy elevators damaged by minor lightning strikes and two elevators damaged during ground handling. Damage from lightning strikes ranged in severity from scorched paint to skin delamination. Figure 14 shows typical lightning damage to the trailing edge of an elevator and trailing edge fracture of another elevator caused by impact from a deicing apparatus. The most severe damage to an elevator occurred when the static discharge probe of one B727 penetrated the elevator of another B727 during ground handling. Skin panels were punctured, four holes in the lower surface and one hole in the upper surface, and the lower horizontal flange at the front spar was cut inboard of the outboard hinge. All the elevator repairs were performed by airline maintenance personnel.

The lightning damage was repaired with epoxy filler and milled glass fibers. The skin punctures were repaired with T300/5208 prepreg fabric and Nomex honeycomb core plugs. The front spar was repaired with a machined titanium doubler, which was mechanically fastened to the lower skin flange of the spar chord. The repaired graphite/epoxy elevators are in storage and can be reinstalled for continued service. Details of the design and fabrication of the graphite/epoxy elevators are given in reference 11.

L-1011 Graphite/Epoxy Ailerons

During the 9 year service evaluation period there have been no damage incidents or major maintenance actions required. Minor paint touch-up has been performed periodically and loose fibers around one fastener hole on the Lockheed company aircraft were rebonded with epoxy. Details of the flight service evaluation program are reported in reference 12.

B737 Graphite/Epoxy Horizontal Stabilizers

There have been three reported damage incidents on the B737 horizontal stabilizers. De-icer impact damage was induced on the upper surface panel of both stabilizers on one aircraft. These impacts were minor and damage was limited to the skin, not affecting the stiffener elements. The third stabilizer was damaged when a broken fan blade penetrated the lower surface of the stabilizer. The penetration missed the stiffener elements and damage was limited to a small area of the skin panel. All three of the stabilizers were repaired on the aircraft using wet lay-up cure techniques per specifications developed by Boeing. Figure 15 shows details of the in-service repair process.

One of the B737 aircraft with composite stabilizers crashed in Alaska in June 1990. The graphite/epoxy stabilizers were returned to Boeing for inspection, teardown, and testing. Figure 16 shows a photograph of one of the stabilizers. No "non-crash" induced delaminations were found and there was no corrosion of metal-composite interfaces. These results indicate the effectiveness of the fiberglass isolation system that was used to prevent galvanic corrosion between graphite and metal parts. Boeing plans to conduct residual strength tests on material coupons machined from skin panels and compare results with baseline tests. Details on the development of the graphite/epoxy horizontal stabilizers are reported in reference 13.

DC-10 Graphite/Epoxy Vertical Stabilizer

One graphite/epoxy vertical stabilizer has been in service on a DC-10 aircraft since January 1987. Three inspections have been performed by Douglas engineering personnel and no defects have been found. The graphite/epoxy Nomex honeycomb skin panels have been x-rayed and no moisture has been found in the core. Ultrasonic inspections of solid laminates have been conducted annually and no disbonds or other defects have been indicated.

C-130 Boron/Epoxy Reinforced Wing Box

Two boron/epoxy reinforced wing boxes have been in service on U.S. Air Force C-130 aircraft since 1974. The wing boxes have been inspected regularly by U.S. Air Force personnel and no damage or defects have been found. These wing boxes provide significant improvement in fatigue life compared to conventional aluminum boxes.

Helicopter Components

The helicopter components involved in the NASA/U.S. Army flight service evaluation program have been installed on Sikorsky S-76 and Bell 206L commercial helicopters. The S-76 graphite/epoxy tail rotor spars and the hybrid graphite-Kevlar/epoxy horizontal stabilizers are production parts. These parts are subjected to normal maintenance inspection for damage every 100 flight hours and an inspection for structural damage annually or after 1000 flight hours. The Bell 206L Kevlar/epoxy fairings and doors and the graphite/epoxy vertical fins are inspected annually or after 1200 hours of service for evidence of damage, repair, excessive wear, or weathering. Except for Kevlar/epoxy baggage doors on the 206L, the composite components have demonstrated good service performance. Because of poor bonding between facesheets and honeycomb core, the 206L baggage doors were removed from the service evaluation program.

Sikorsky S-76 Composite Components

Four horizontal stabilizers and 11 tail rotor spars have been removed from aircraft and tested over a 9 year evaluation period. The components were inspected prior to residual strength testing and no significant service-induced defects or damage were found. Figure 17 shows predicted and measured moisture absorption data and strength retention of AS1/6350 tail rotor spars. All the spars were removed from helicopters operating in the Louisiana Gulf Coast region. Weather data from Lake Charles, LA were used in predicting the moisture absorption profile. Measured moisture absorption values shown in figure 17 are below the prediction by 0.05 to 0.15 percent for service times up to 40 months and are above the predicted values by 0.1 to 0.30 percent for service times beyond 70 months. During the development of design allowables and FAA certification testing, Sikorsky conducted accelerated conditioning at 87 percent relative humidity and 88°C on material coupons. The predicted moisture saturation level for AS1/6350 graphite/epoxy was 1.1 percent. After 9 years of service, the moisture level in the AS1/6350 tail rotor spars was slightly below 1.0 percent. Cyclic shear stress as a function of cycles to failure for the flight service tail rotor spars is shown in figure 17, along with data for baseline dry spars tested at room temperature for FAA certification. The shape of the curves was based on interlaminar shear fatigue tests. The results in figure 17 indicate a 95 percent strength retention for the service exposed spars compared to the baseline strength data used for certification.

Structural response of the S-76 composite horizontal stabilizers is shown in figure 18. Proof load deflection data for the four stabilizers returned from service indicate deflections below the maximum allowable deflection of 0.41 cm, indicating no significant stiffness loss. The maximum moisture content for the stabilizers, 0.49 percent, occurred after 91 months of service and 5846 flight hours. Full moisture saturation has not yet been reached. Vibratory roll moment as a function of cycles to failure is plotted in figure 18. The three stabilizers with 56, 66, and 91 months of service were fatigue tested at applied loads exceeding loads used for FAA certification. The average vibratory roll moment at failure for the service exposed stabilizers was approximately 2 percent higher than the corresponding roll moment for the baseline stabilizers used for certification. The shape of the curves was established by evaluating graphite/epoxy and Kevlar/epoxy coupons in the laboratory. The same shape was assumed to apply to full scale components. Additional details on the S-76 flight service program can be found in reference 14.

Bell 206L Composite Components

A total of 78 composite components have been removed from service for structural testing. The exposure times range from 12 to 84 months and flight times range from 386 to 6750 hours. Moisture absorption and strength retention data for T300/E-788 vertical fins are shown in figure 19. The moisture content was determined by drying plugs removed from the fins. The plugs included painted graphite/epoxy skins, adhesive, and honeycomb core material. The average moisture content measured for the fins is approximatley 1.1 percent by weight. The fins operating in the humid Gulf of Mexico had moisture contents slightly higher than those for fins operating in other exposure locations. The residual strengths for 15 fins removed from service exceeded the design ultimate strength requirement. Failure loads for 12 of the fins fall within the baseline scatter band for five fins selected at random. One of the fins operating in the northeast USA and Canada was struck by lightning. This fin was damaged at the top but no apparent damage was inflicted on the structural box. This damaged fin failed below the baseline scatter band, but well above the design ultimate requirement.

Moisture absorption and strength retention data for Kevlar-49/F-185 litter doors are shown in figure 20. Average moisture content for the litter doors is approximately 2.0 percent. This high moisture content was expected since laboratory tests and other outdoor exposure tests indicated that Kevlar/epoxy composites absorb about twice the moisture of graphite/epoxy composites. There is considerable scatter in the strength data for the 15 litter doors that were removed from service and tested. All the litter doors exceeded the design ultimate strength requirement. Seven litter doors failed above the baseline scatter band and five litter doors failed below the baseline scatter band. The large scatter is expected since some of the failures were a result of metal hinge failures and latch pins slipping from the test fixture.

Since the baggage doors had manufacturing defects and were removed from service, test results are not discussed herein. The forward fairings were designed by stiffness requirements and are considered to be secondary load-carrying components. All the fairings failed at loads at least a factor of nine above the design ultimate strength requirement. Additional details on the Bell 206L flight service evaluation program can be found in reference 15.

CH-53D Kevlar/Epoxy Cargo Ramp Skin

A Kevlar/epoxy composite skin was installed on the aft end of a CH-53D Cargo ramp for U.S. Marine Corps service evaluation in 1981. The panel has been inspected annually since installation and no damage or service related problems have been reported by the U.S. Marine Corps.

FLIGHT AND GROUND-BASED ENVIRONMENTAL EXPOSURE EFFECTS ON COMPOSITE COUPONS

In conjunction with the flight service evaluation program, NASA Langley and the U.S. Army initiated four flight and ground-based environmental exposure programs. The objectives of these programs were to supplement component data with less expensive coupon data, correlate ground exposure data with flight exposure data, and to assess the requirement for future flight service programs. The four programs are outlined in Figure 21. The first program, 10 year worldwide ground exposure, was structured to supplement flight data obtained through service evaluation of B737 spoilers, DC-10 rudders and L-1011 fairings. Since the largest number of components were installed on B737 aircraft, ground-based exposure locations were selected where B-737 aircraft with graphite/epoxy spoilers would be operating. The following exposure locations were selected: Hampton, VA; San Diego, CA; Honolulu, HI; Frankfurt, F.R.G.; Wellington, New Zealand; and São Paulo, Brazil. The materials selected for exposure were the B737 spoiler materials: T300/5209, T300/2544, AS/3501; the DC-10 rudder material: T300/5208; and the L-1011 fairing materials: Kevlar-49/F155 and Kevlar-49/F161. Compression and short beam shear test coupons were selected to represent matrix dominant failure modes; whereas flexure coupons were selected to represent a fiber dominant failure mode.

The second program, 10 year ground and flight exposure, was structured to compare ground and flight exposure data, compare the effects of solar versus nonsolar (partially shielded) exposure, compare the effects of aircraft interior and exterior exposure, and to assess the effects of long-term sustained stress. The exposure sites chosen were: Edwards AFB, CA; Dallas, TX; Honolulu, HI; and Wellington, New Zealand. These sites offered diverse climates with significant variations in temperature and humidity conditions. In addition to ground exposure, composite coupons were installed on top and bottom surfaces of B737 flap-track fairing tail cones and in the nonpressurized interior of the aircraft behind the aft pressure bulkhead. The objectives of these exposure locations were to compare the effects of direct solar and nonsolar exposure and to compare the effects of interior and exterior aircraft exposure. One additional material, T300/934, and an additional matrix dominate test: $(+45/-45)_{2s}$ tension coupon were added to the list of materials and test coupons discussed previously.

The third program, 10 year Bell 206L ground exposure, was structured to support the Bell 206L helicopter flight service program. The composite materials used to fabricate the flight service components were used in the ground exposure program and are listed in figure 21. The ground exposure coupons were installed on racks in Hampton, VA; Cameron, LA; on a U.S. Gulf oil platform; Toronto, Canada; and Fort Greely, AK. The test coupons were configured for compression, short beam shear, and tension testing.

The fourth program, 9 year Sikorsky S-76 ground exposure, was structured to compare ground and flight data for two composite materials that were in production on S-76 commercial helicopters. The exposure locations selected were Stratford, CT and West Palm Beach, FL. The two exposure materials discussed previously for the flight components included AS1/6350 and Kevlar/5143. Compression, short beam shear, flexure, and tension coupons were exposed for moisture absorption determination and residual strength.

Geographic location of all the ground-based exposure racks is shown in figure 22. Coupons were removed from exposure racks at specified intervals ranging from 1–10 years of exposure. Selected coupons were dried and weighed to determine moisture content and the remainder of the coupons were subjected to residual strength testing. Most coupons were tested at room temperature, however some tests were conducted at 82°C.

10 Year Worldwide Ground Exposure

Triplicate unpainted coupons were mounted in exposure racks and placed on rooftops to receive maximum exposure to the environment. The average residual properties (moisture content, strength, and modulus of elasticity) were compared to average baseline properties. Test coupons were removed from the racks for evaluation after 1, 3, 5, 7, and 10 years of exposure. The objectives of the test in this exposure program were to establish the effects of various realtime outdoor environments on the moisture absorption and strength of composite materials and to compare the results with results obtained from flight service components.

The amount of moisture that composite materials absorb is a function of matrix and fiber type, temperature, relative humidity, and exposure conditions. Average moisture absorption (as a fraction of composite coupon weight) is plotted as a function of exposure time in figure 23 for the following exposure locations: Hampton, VA; San Diego, CA; Honolulu, HI; Frankfurt, F.R.G.; Wellington, New Zealand; and São Paulo, Brazil. The T300/5208 and T300/5209 graphite epoxy materials absorbed the least amount of moisture after the 10 year exposure period, about 0.7 percent. The AS/3501 graphite/epoxy absorbed slightly over 1.0 percent moisture during the 10 year exposure period. The T300/2544 graphite/epoxy suffered significant surface degradation due to ultraviolet radiation and absorbed about 2.0 percent moisture during the 10 years of exposure. The two Kevlar-49/epoxy materials absorbed approximately 2.5 percent moisture during the 10 year exposure period. These results are expected since the Kevlar fibers also absorb moisture. The Brazil and New Zealand exposures resulted in the highest moisture absorption for all the materials. These results are expected since the average annual humidity in São Paulo, Brazil and Wellington, New Zealand is about 75 to 80 percent. Specific moisture data for each exposure site can be found in reference 1.

Moisture absorption for material coupons is compared with moisture absorption data for plugs removed from B737 graphite/epoxy spoilers in figure 24. The coupon data are for three unpainted graphite/epoxy materials exposed at San Diego, CA and São Paulo, Brazil for 10 years. The spoiler data are for painted honeycomb sandwich plugs removed from spoilers that had flown for 10 years on Frontier and VASP airlines. The results indicate that the unpainted ground exposed coupons absorbed significantly more moisture than the painted flight spoilers. Although the spoilers spend a significant portion of time on the ground, it is expected that the flight profile would tend to dry out the outer surface of the material.

The average room temperature residual strengths (flexure, short beam shear, and compression) of six composite materials for 10 years of outdoor exposure at the six exposure sites discussed previously are plotted in figure 25. The graphite/epoxy coupons were fabricated with 0-degree tape and the Kevlar/epoxy coupons were fabricated with (0/90) fabric. Three-point flexure tests were conducted to assess the effects of outdoor environments on surface fiber strength. The coupons were tested with the exposed surface in compression; in general, however, failure occurred in tension at mid-span of the coupons. After 10 years of exposure, the Kevlar-49/F155 material indicated the largest flexural strength loss, about 20 percent. The T300/2544 material, which had significant surface degradation in the resin, failed at about 13 percent below the average baseline strength. The matrix dominant compression coupons indicated a similar strength loss, 15 to 20 percent, during the 10 year exposure.

The maximum strength loss for the matrix dominant short beam shear coupons was about 23 percent. Strengths of the Kevlar-49/F155 and T300/2544 materials were consistently below the baseline scatter band between 3 and 10 years of exposure. The two Kevlar/epoxy materials also indicated a loss in modulus ranging from 20 to 28 percent during the 10 year exposure. These results, along with detailed data plots for each exposure site, are reported in reference 1.

Ten year compression strength data for material coupons are compared with B737 graphite/epoxy spoiler strength data in figure 26. The strength data are for coupons and spoilers with the same exposure conditions that were discussed for the moisture comparison of figure 24. Except for one spoiler with known corrosion damage, the spoilers exhibited residual strengths that were slightly higher than the coupon residual strengths. As discussed previously, the spoiler corrosion damage is a design related problem and could be prevented through design changes. These results indicate excellent strength correlation between ground exposed coupons and flight exposed spoilers.

10 Year Ground and Flight Exposure

Coupon exposure locations for the flight portion of this program are shown in figure 27. Short beam shear, flexure, and tension coupons were mounted on the upper (solar) and lower (nonsolar) surface of B737 flap-track fairing tailcones to represent exterior aircraft exposure. Short beam shear, flexure, compression, stressed tension, and unstressed tension coupons were mounted inside the unpressurized tailcone area of the aircraft. The sustained stress tension coupons were stressed at 20 percent of baseline failure loads with the aid of a calibrated torqued bolt/Bellville spring washer load system. The ground exposure coupons are shown in figure 28. One side of the

exposure rack has coupons mounted for direct solar radiation and one side is shielded to prevent direct solar radiation. A phenolic honeycomb core was mounted above the coupons to prevent direct ultraviolet radiation impingement, however, the core allowed adequate air circulation and allowed precipitation to drain down the individual cells and onto the coupons.

The effect of ground exposure on compression strength of T300/5208, T300/5209, and T300/934 graphite/epoxy materials is shown in figure 29. The results are for coupons exposed on the shielded nonsolar side of the exposure rack at Dallas, TX. Tests were conducted at room temperature and at 82°C. However results are shown for the room temperature tests only since extensive grip failures were evident at 82°C. Results indicate that most coupons failed at or above the baseline failure strengths. The maximum compression strength loss was about 15 percent for the T300/934 material after 10 years of exposure.

The effects of flight and ground exposure on short beam shear strength of three graphite/epoxy materials is shown in figure 30. The results are for coupons exposed on the upper (solar) surface of B737 flap-track fairing tailcones on Aloha Airlines and for solar exposed material coupons at Honolulu, HI. The coupons were tested at 82°C and are compared to baseline coupons that were also tested at 82°C. An unexplained trend is evident; a significant strength loss after 2 to 3 years of exposure with an increase in strength thereafter. A maximum short beam shear strength loss of 40 percent was evident for the T300/5209 material after 2 years of exposure on Aloha Airlines. However, after 10 years of exposure, strength losses of only 13 to 25 percent occurred. The T300/934 material cures at 177°C, compared to 121°C for the T300/5209 material, however the T300/934 material performed only slightly better in the 82°C test. The coupons exposed at Honolulu, HI performed the same or slightly better than the coupons exposed on the Aloha Airlines aircraft. The results of these tests indicate that the less expensive ground-based tests could be used to assess material performance for future evaluations.

A comparison between interior and exterior aircraft exposure effects on flexure strength of three graphite/epoxy materials is shown in figure 31. The results are for coupons exposed on the upper (solar) surface and lower (nonsolar) surface of B737 flap-track fairing tailcones and in the interior of Southwest Airlines aircraft. The coupons were tested at 82°C and compared to baseline coupons tested at 82°C. A maximum strength reduction of 20 percent occurred for the T300/5209 material exposed on the upper surface of the flap-track fairing tail cone. Considering test data scatter, there is no discernible difference between the effects of solar exterior, nonsolar exterior or aircraft interior exposure.

The effects of sustained stress on tensile strength of three graphite/epoxy materials exposed outdoors at the NASA Dryden Research Center in Edwards Air Force Base, CA, are shown in figure 32. The unstressed coupons are compared with coupons that were continuously stressed at 20 percent of the baseline failure stress. The tensile coupons were tested at 82°C. The test results indicate no discernible difference between the stressed and unstressed coupon data. Small variations above and below baseline values are indicated during the 10 year evaluation period. Additional details on the ground and flight exposure program are reported in reference 16.

10 Year Bell 206L Ground Exposure

Moisture absorption data for three Kevlar/epoxy fabrics and one graphite/epoxy tape material are shown in figure 33. The painted T300/E-788 graphite/epoxy material absorbed about 0.7 percent moisture, whereas the painted Kevlar/epoxy materials absorbed about 2.5 percent moisture, as expected. The average residual strengths for four Bell 206L composite materials after outdoor exposure at five exposure sites discussed previously are shown in figure 34. In the summer of 1985 the exposure racks located at Cameron, LA and on the offshore oil platform were destroyed by hurricanes. Therefore, the data for 5, 7, and 10 years of exposure are from racks located in Hampton, VA, Toronto, Canada, and Fort Greely, AK. Six replicates for each exposure site were tested for each exposure period. The residual compression strength varies between 88 and 101 percent of the baseline strength. The short beam shear strength varies between 89 and 104 percent of the baseline strength. The Kevlar-49/LRF-277 material exhibited the largest compression and shear strength reductions and the T300/E-788 exhibited no strength reduction. The residual tension strengths for all four materials were within the baseline scatter band for all exposure periods up to 10 years.

Figure 35 compares strength retention and moisture absorption data for T300/E-788 composite coupons with corresponding data from Bell 206L vertical fins after 5 years of flight service. The vertical fins absorbed about 1.1 percent moisture, whereas the 5 year ground exposed coupons absorbed about 0.7 percent moisture. The fin moisture content includes moisture absorbed by paint, sealer, primer, graphite/epoxy skins, and honeycomb core. Strength retention for compression coupons and vertical fins was near 100 percent. These results indicate that ground-based coupon strength data are representative of strength retention results expected from flight service components. Additional details on the test program and test results are reported in reference 15.

Nine Year Sikorsky S-76 Ground Exposure

As discussed previously, Sikorsky conducted accelerated laboratory conditioning tests to develop environmental factors that account for anticipated strength reduction as a function of absorbed moisture. These tests were conducted at 87 percent relative humidity and 88°C. To establish a correlation between realtime outdoor exposure and accelerated laboratory exposure, composite panels were exposed for 9 years in outdoor racks located at Stratford, CT and West Palm Beach, FL. Results for 6-ply AS1/6350 short beam shear and flexure coupons machined from the panels are shown in figure 36. Residual strength is plotted as a function of absorbed moisture and the results indicate that the matrix dependent short beam shear strength is affected more than the fiber dependent flexure strength. The accelerated laboratory conditioning tests indicated moisture saturation for the 6-ply laminates at about 1.1 percent. The panels exposed at Stratford, CT absorbed a maximum of 1.13 percent moisture, however, the panels exposed at West Palm Beach, FL absorbed a maximum of 1.40 percent moisture. The results are inconsistent in that the 5 year panels absorbed the most moisture, whereas the 9 year panels absorbed the least amount of moisture. These results are probably affected by local weather conditions at the time of panel removal.

Strength retention trends parallel the accelerated laboratory test data. The residual flexure strengths for exposed laminates exceed 95 percent of the baseline room temperature dry strength and also meet or exceed the strength of the accelerated conditioned specimens. Residual short beam shear strengths for exposed laminates vary between 70 and 90 percent of the baseline strength and are within 1 percent of the strength of the accelerated conditioned specimens. Additional details of the ground exposure test program can be found in reference 14.

CONCLUDING REMARKS

The influence of ground-based and aircraft operational environments on the long-term durability of several advanced composite materials and structural components has been studied. Results of 10 years of outdoor exposure indicate that Kevlar/epoxy material systems were more affected by the various environments than were graphite/epoxy material systems. Residual strength tests were conducted to establish the effects of various environments on composite materials. Differences

in the effects of solar versus nonsolar exposure, aircraft interior exposure versus aircraft exterior exposure, and sustained stress versus unstressed exposure were not discernible. Some of the differences that might be expected were masked by data scatter.

Numerous aircraft and helicopter composite components have been in service for more than 15 years and excellent operational performance has been achieved. Normal maintenance and in-service related damage such as ground handling damage, foreign object damage, and lightning strikes have occurred. Design related corrosion damage was experienced on aluminum fittings and splices on some graphite/epoxy reinforced spoilers. Excellent service and residual strengths have been achieved with composite horizontal and vertical stabilizers and tail rotor spars during 9 years of helicopter service.

Good performance correlations between ground exposed material coupons and flight service components indicate that ground-based exposure data should be sufficient to predict long-term behavior of composite aircraft structures. It is important to note that at the coupon level, nothing was learned from exposing materials on the aircraft that could not be learned from ground-based exposure. A significant cost saving during aircraft design development would be a major benefit.

Lessons learned in the NASA Langley/U.S. Army program indicate that additional research is needed to select better material test methods that result in less data scatter. The environmental exposure programs described in this report would have benefited if more baseline and post exposure replicates had been planned. Future exposure programs should consider exposing larger panels that are more representative of aircraft structure. The logistics of tracking materials would be lessened and more flexibility in selecting test coupons would be available.

The results of this program indicate that composite materials can be applied to the next generation of aircraft with a high degree of confidence. With proper design on the part of the aircraft manufacturer, the airlines and operators of future aircraft should expect reduced corrosion and fatigue concerns compared to conventional metallic structures.

REFERENCES

1. Dexter, H. B., "Long-Term Environmental Effects and Flight Service Evaluation of Composite Materials," NASA TM 89067, January 1987.
2. Zinberg, H., "Flight Service Evaluation of Composite Components on the Bell Model 206L: Design, Fabrication, and Testing," NASA CR 166002, November 1982.
3. Rich, M. J. and Lowry, D. W., "Flight Service Evaluation of Composite Helicopter Components—First Annual Report," NASA CR 165952, June 1982.
4. Lowry, D. W. and Rich, M. J., "Design, Fabrication, Installation, and Flight Service Evaluation of a Composite Cargo Ramp Skin on a Model CH-53 Helicopter," NASA CR 172126, April 1983.
5. Wooley, J. H., Paschal, D. R., and Crilly, E. R., "Flight Service Evaluation of PRD-49/Epoxy Composite Panels in Wide-Bodied Commercial Transport Aircraft." NASA CR 112250, March 1973.
6. Stone, R. H., "Flight Service Evaluation of Kevlar-49/Epoxy Composite Panels in Wide Bodied Commercial Transport Aircraft—Tenth and Final Annual Flight Service Report," NASA CR 172344, June 1984.
7. Coggeshall, R. L., "Boeing/NASA Composite Components Flight Service Evaluation," NASA CR 181898, November 1989.
8. Fox, B. R., "Flight-Service Evaluation of an Advanced Metal Matrix Aircraft Structural Component—Flight Service Final Report," MDC Report J3827, August 1985.
9. Lehman, G. M., "Flight-Service Program for Advanced Composite Rudders on Transport Aircraft-Sixth Annual Summary Report." MDC Report J6574, August 1982.
10. Fox, B. R., "Flight-Service Program for Advanced Composite Rudders on Transport Aircraft—Ninth Annual Summary Report." MDC Report J-3871, September 1985.
11. Chovil, D. V. et al., "Advanced Composite Elevator for Boeing 727 Aircraft—Volume 2 Final Report." NASA CR 15958, November 1980.
12. Stone, R. H., "Flight Service Evaluation of Advanced Composite Ailerons on the L-1011 Transport Aircraft—Fifth Annual Flight Service Report." NASA CR 17832, June 1987.
13. McCarty, J. E. and Wilson, D. R., "Advanced Composite Stabilizer for Boeing 737 Aircraft," in "Sixth Conference on Fibrous Composites in Structural Design," AMMRC MS 83-2, November 1983.
14. Mardoian, G. H. and Ezzo, M. B., "Flight Service Evaluation of Composite Helicopter Components," NASA CR 182063, November 1990.
15. Baker, D. J., "Evaluation of Composite Components on the Bell 206L and Sikorsky S-76 Helicopters," NASA TM 4195, August 1990.
16. Hoffman, D. J. and Bielawski, W. J., "Environmental Exposure Effects on Composite Materials for Commercial Aircraft," NASA CR 187478, April 1991.

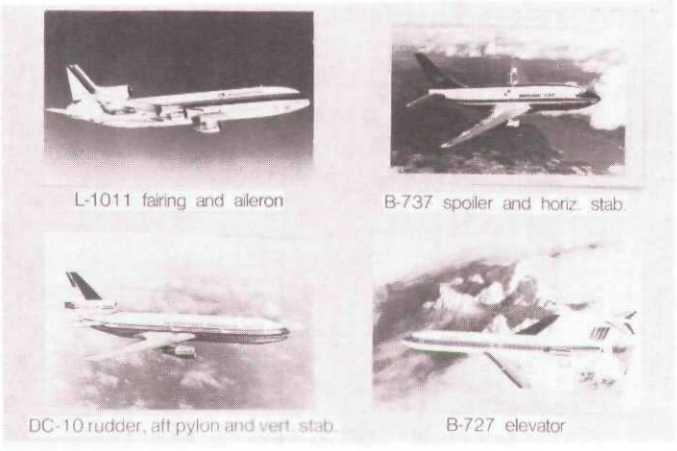

Figure 1. Flight service composite components on transport aircraft.

L-1011 K/E Fairings
- Eastern
- Air Canada
- TWA

C-130 B/E Reinforced Wing Boxes
- U.S. Air Force

DC-10 B/Al Aft Pylon Skins
- United

DC-10 G/E Rudders
- Korean
- Swiss Air
- Federal Express
- Mozambique
- Western
- Lan Chile
- Air Siam
- Continental
- Trans-International
- Finn Air
- Air New Zealand
- Trans-America

B-727 G/E Elevators
- United

B-737 G/E Spoilers
- Air New Zealand
- Lufthansa
- Piedmont
- Frontier
- VASP
- PSA
- Aloha

L-1011 G/E Ailerons
- Delta
- TWA

B-737 G/E Horizontal Stabilizer
- Delta
- Mark Air

DC-10 G/E Veritical Stabilizer
- Finn Air

Figure 2. Airlines and operators participating in composite flight service program for transport aircraft.

Figure 3. Flight service composite components on helicopters.

Bell 206L Composite Components
- Island Helicopter
- ERA Helicopters
- Trans Quebec Helicopters
- Royal Canadian Mounted Police
- Heli-Voyageur
- Commercial Helicopters
- Pumpkin Air
- Air Logistics
- Petroleum Helicopters, Inc.
- Houston Helicopters
- Clearwater Foods
- Air Services International
- Viking Helicopters
- Canadian Dept. of Transportation

Sikorsky S-76 Composite Components
- Air Logistics

CH-53 K/E Cargo Ramp Skin
- U. S. Marine Corps

Figure 4. Airlines and operators participating in composites flight service program for helicopters.

Aircraft Component	Total Components		Start of Flight Service	Cumulative Flight Hours	
				High Time Aircraft	Total Component
L-1011 Fairing panels	18	(15)	January 1973	52,610	742,630
737 Spoiler	108	(33)	July 1973	45,260	2,747,760
C-130 Center wing box	2	(2)	October 1974	10,920	21,520
DC-10 Aft pylon skin	3	(2)	August 1975	45,640	107,840
DC-10 Upper aft rudder	15	(10)	April 1976	58,340	519,430
727 Elevator	10	(8)	March 1980	40,930	336,610
L-1011 Aileron	8	(8)	March 1982	31,720	249,480
737 Horizontal stabilizer	10	(8)	March 1984	19,620	189,800
DC-10 Vertical stabilizer	1	(1)	January 1987	17,580	17,580
S-76 Tail rotors and horizontal stabilizer	14	(0)	February 1979	5,860	53,150
206L Fairing, doors, and vertical fin	160	(51)	March 1981	11,325	440,000
CH-53 Cargo ramp skin	1	(1)	May 1981	5,000	5,000
Grand total	350	(139)			5,377,650

( ) Still in service

June 1991

Figure 5. NASA composite structures flight service summary.

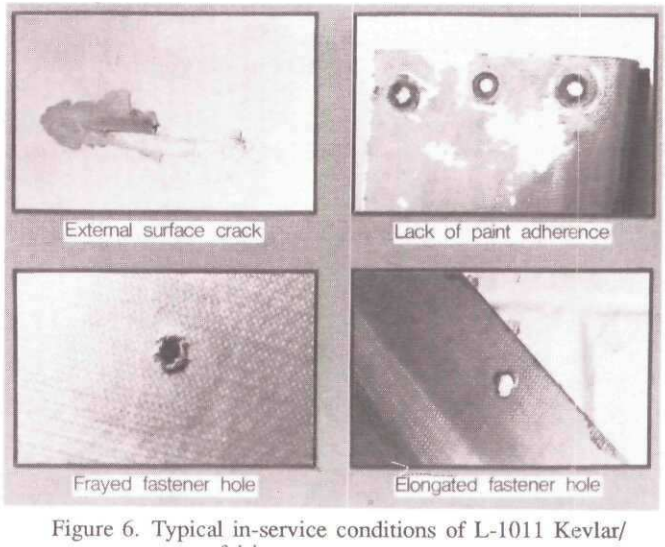

Figure 6. Typical in-service conditions of L-1011 Kevlar/epoxy fairings.

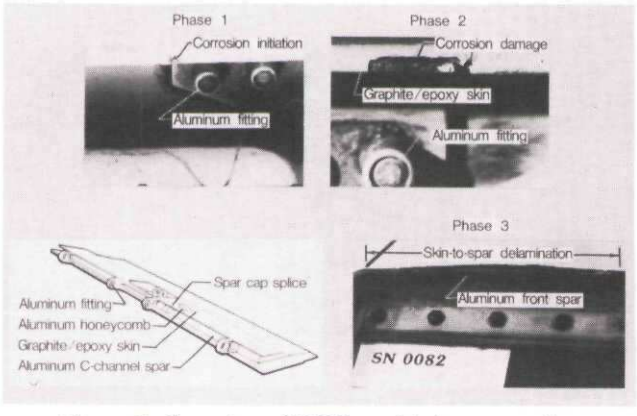

Figure 7. Corrosion of B737 graphite/epoxy spoilers.

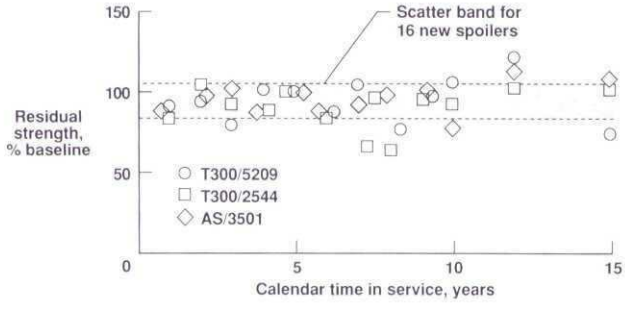

Figure 8. Residual strength of B737 graphite/epoxy spoilers.

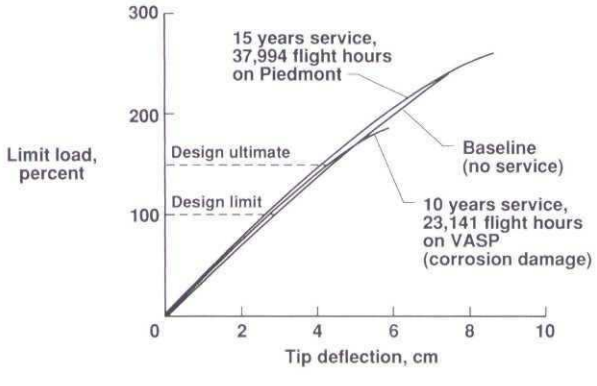

Figure 9. Load-deflection response of AS/3501 graphite/epoxy spoilers for B737 aircraft.

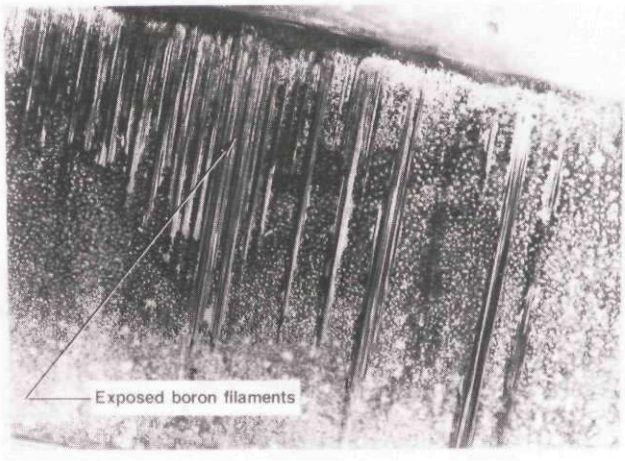

Figure 10. Corrosion damage to DC-10 boron/aluminum aft pylon skin panel.

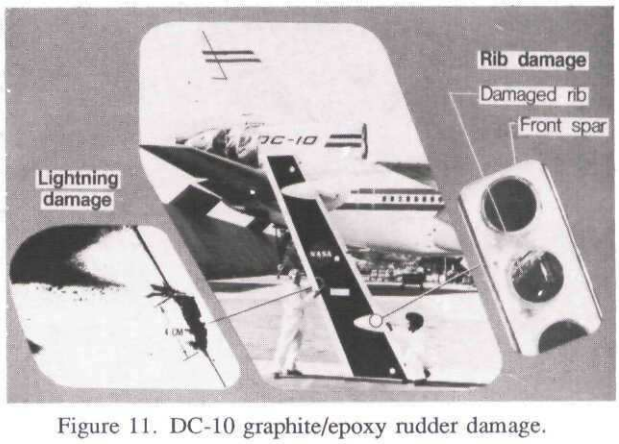

Figure 11. DC-10 graphite/epoxy rudder damage.

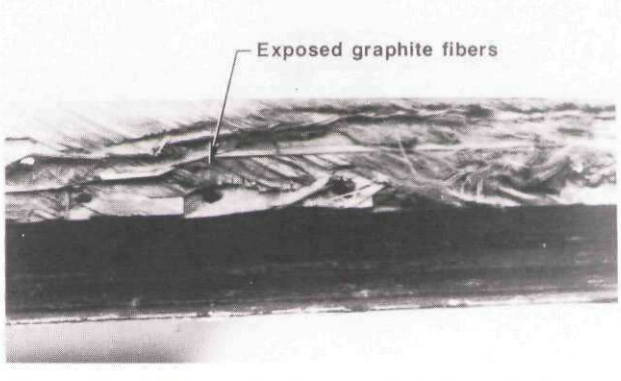

Figure 12. Lightning strike damage to DC-10 graphite/epoxy rudder trailing edge.

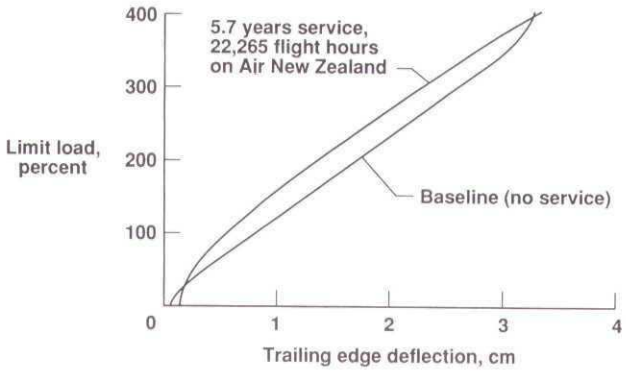

Figure 13. Load-deflection response of T300/5208 graphite/epoxy rudders for DC-10 aircraft.

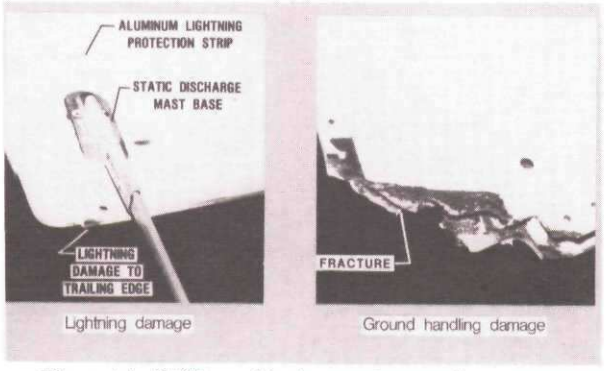

Figure 14. B727 graphite/epoxy elevator damage.

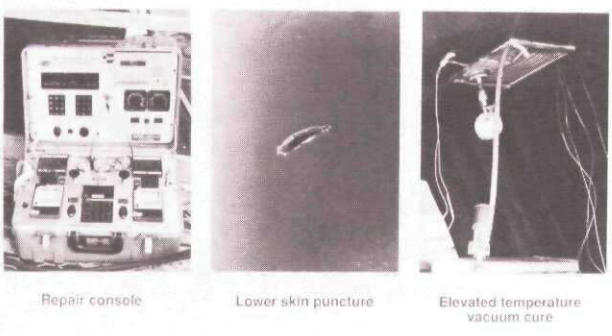

Figure 15. In-service repair of B737 graphite/epoxy horizontal stabilizer.

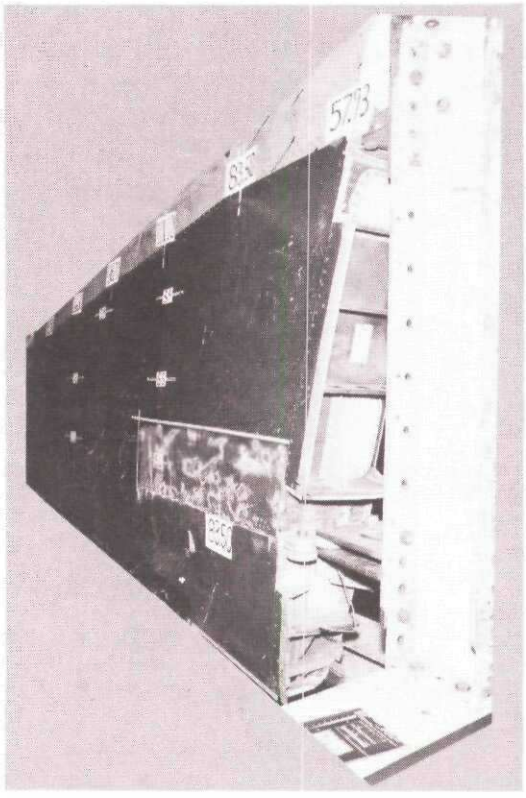

Figure 16. B737 graphite/epoxy horizontal stabilizer recovered from Markair crash.

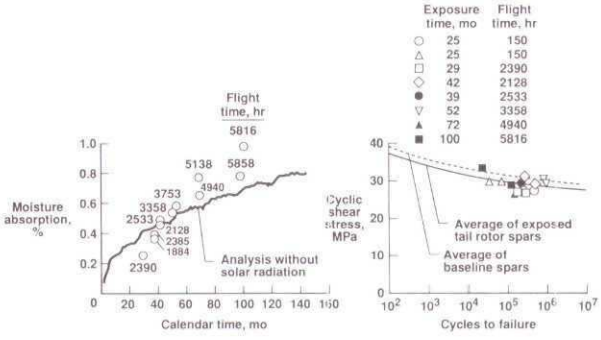

Figure 17. Moisture absorption and strength retention of AS1/6350 Sikorsky S-76 tail rotor spars.

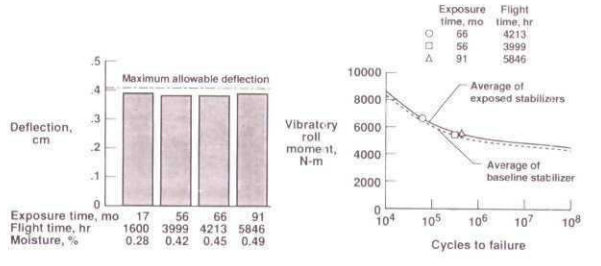

Figure 18. Structural response of Sikorsky S-76 composite horizontal stabilizers.

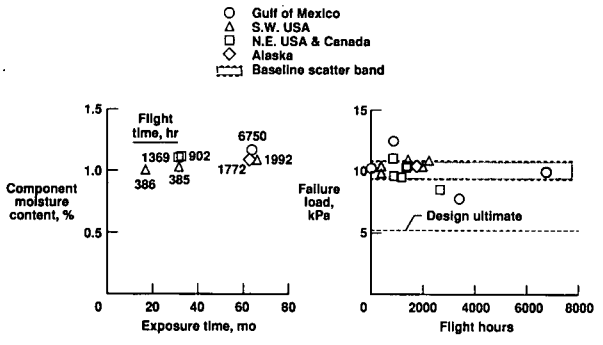

Figure 19. Moisture absorption and strength retention of T300/E-788 Bell 206L vertical fins.

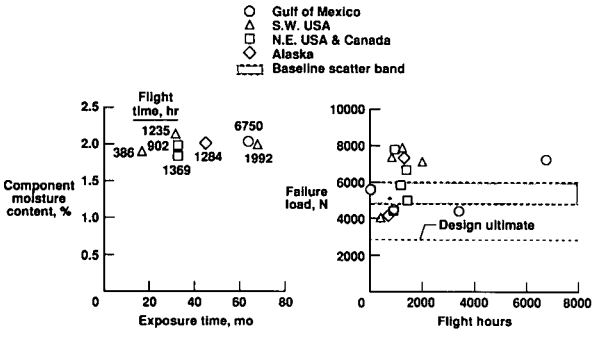

Figure 20. Moisture absorption and strength retention of Kevlar-49/F-185 Bell 206L litter doors.

- 10 yr Worldwide Ground Exposure -		- 10 yr Ground and Flight Exposure -	
Exposure Locations	**Materials**	**Exposure Locations**	**Materials**
• Hampton, VA	• T300/5209	• Edwards AFB, CA	• T300/5209
• San Diego, CA	• T300/2544	• Dallas, TX	• T300/5208
• Honolulu, HI	• T300/5208	• Honolulu, HI	• T300/934
• Frankfurt, F.R.G.	• AS/3501	• Wellington, NZ	
• Wellington, NZ	• Kevlar/F155	• B737 interior	
• São Paulo, Brazil	• Kevlar/F161	• B737 exterior	
Test Coupons		**Test Coupons**	
• Compression		• Compression	
• Short beam shear		• Short beam shear	
• Flexure		• Flexure	
		• Tension	
- 10 yr Bell 206L Ground Exposure -		**- 9 yr S-76 Ground Exposure -**	
Exposure Locations	**Materials**	**Exposure Locations**	**Materials**
• Hampton, VA	• T300/E-788	• Stratford, CT	• AS1/6350
• Cameron, LA	• Kevlar/CE-306	• West Palm Beach, FL	• Kevlar/5143
• U.S. Gulf oil platform	• Kevlar/LRF-277	**Test Coupons**	
• Toronto, Canada	• Kevlar/F-185	• Compression	
• Fort Greely, AK		• Short beam shear	
Test Coupons		• Flexure	
• Compression		• Tension	
• Short beam shear			
• Tension			

Figure 21. Environmental exposure of composite coupons.

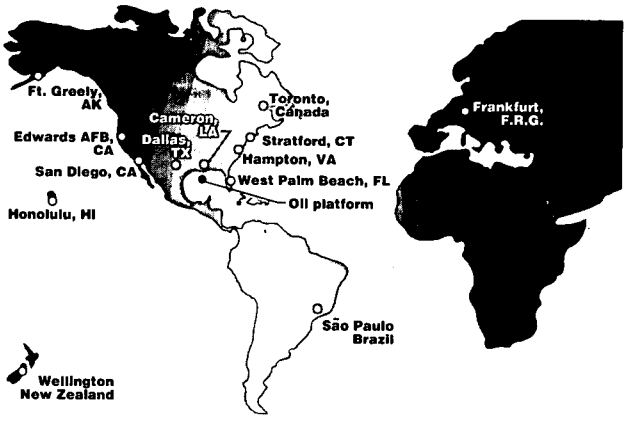

Figure 22. Geographic location of ground-based exposure racks.

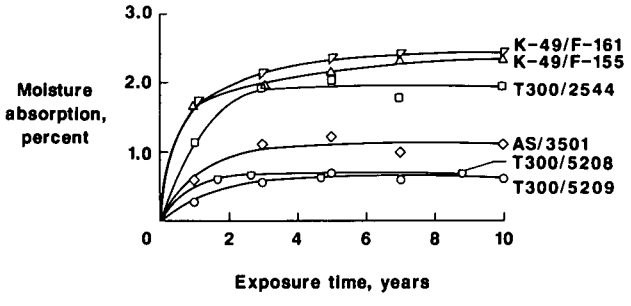

Figure 23. Moisture absorption of unpainted composite materials after worldwide outdoor exposure.

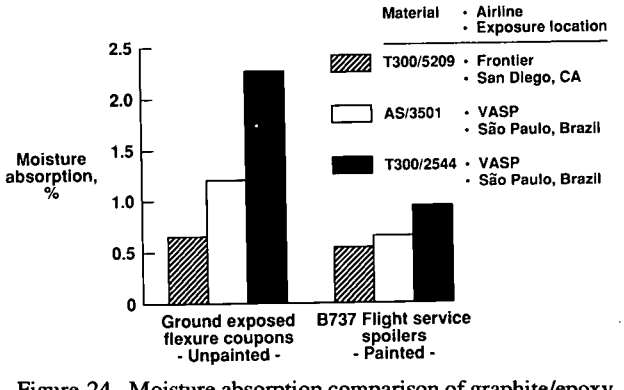

Figure 24. Moisture absorption comparison of graphite/epoxy materials after 10 years of ground and flight exposure.

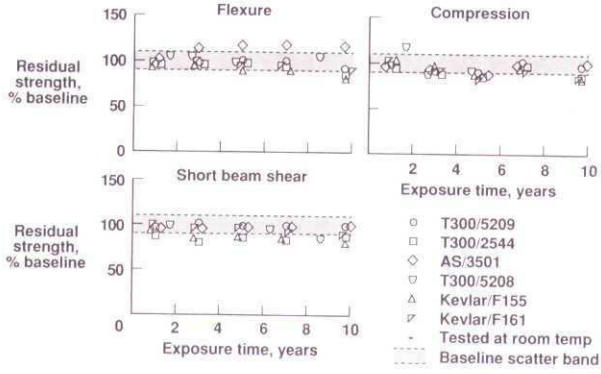

Figure 25. Residual strength of unpainted composite materials after worldwide outdoor exposure.

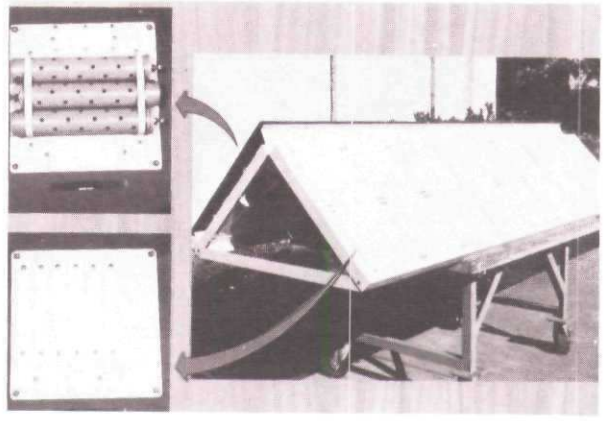

Figure 28. Boeing outdoor environmental exposure rack.

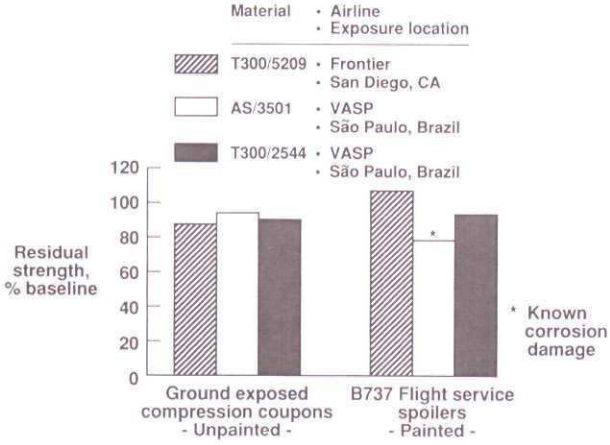

Figure 26. Strength comparison of graphite/epoxy materials after 10 years of ground and flight exposure.

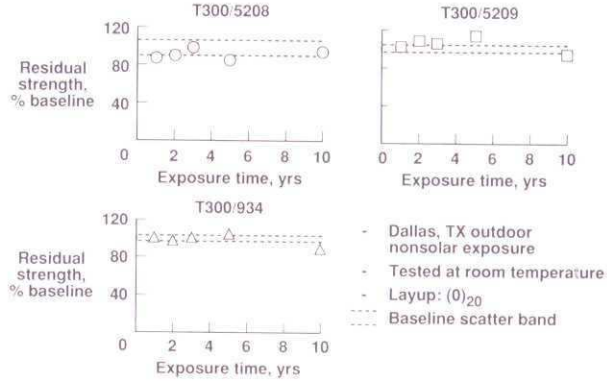

Figure 29. Effect of ground-based exposure on compression strength of painted graphite/epoxy materials.

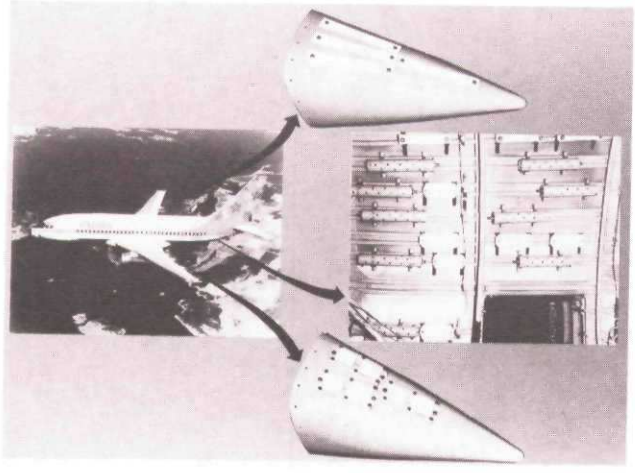

Figure 27. Boeing 737 flight environmental exposure.

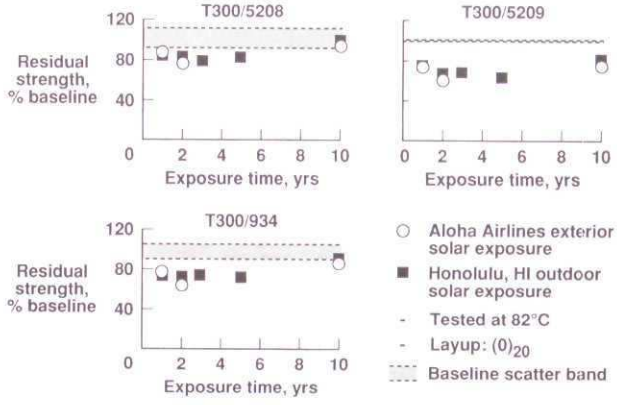

Figure 30. Effect of flight and ground-based exposure on short beam shear strength of painted graphite/epoxy materials.

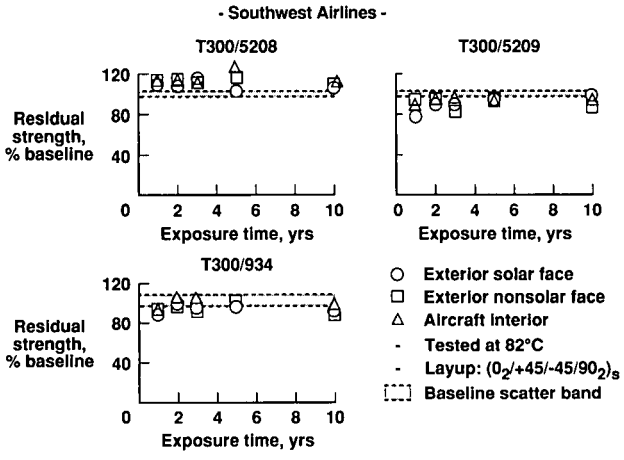

Figure 31. Effect of interior and exterior aircraft exposure on flexure strength of painted graphite/epoxy materials.

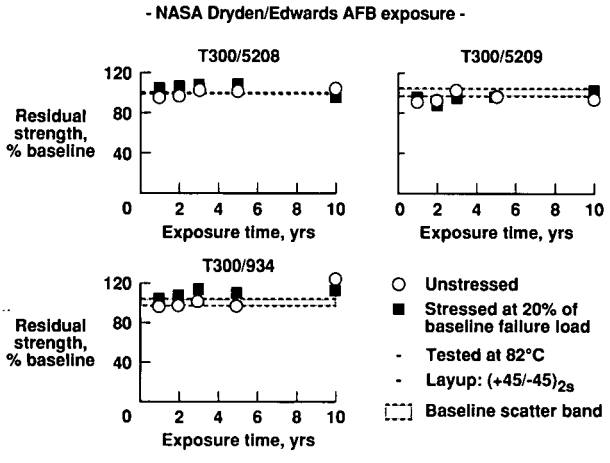

Figure 32. Effect of sustained stress on tensile strength of painted graphite/epoxy materials after outdoor exposure.

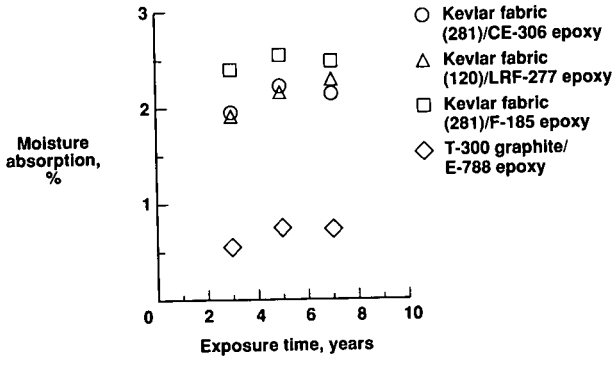

Figure 33. Moisture absorption of Bell 206L painted composite materials after outdoor exposure.

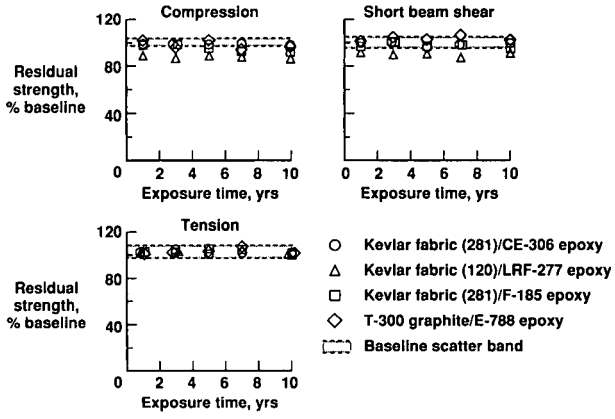

Figure 34. Residual strength of Bell 206L painted composite materials after outdoor exposure.

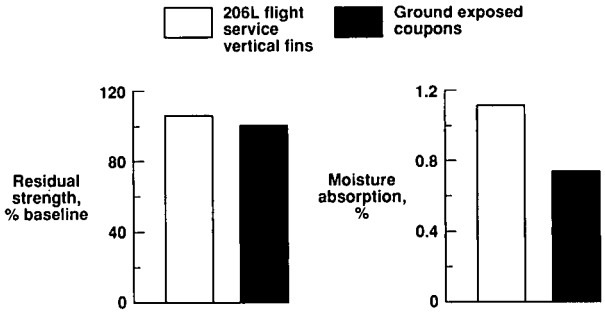

Figure 35. Strength retention and moisture absorption of T300/E-788 after 5 years of ground and flight exposure.

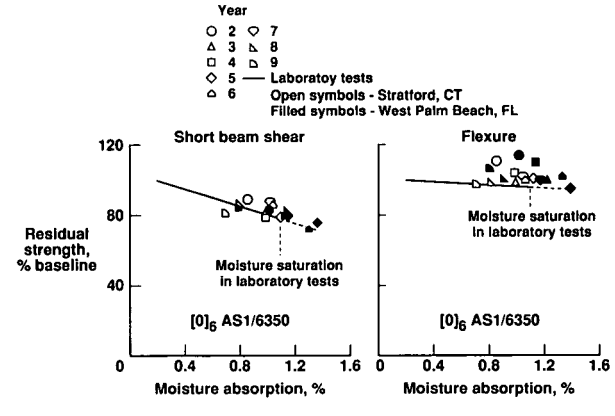

Figure 36. Effect of moisture on the residual strength of Sikorsky S-76 graphite/epoxy laminates.

REPORT DOCUMENTATION PAGE

1. Recipient's Reference	2. Originator's Reference	3. Further Reference	4. Security Classification of Document
	AGARD-R-785	ISBN 92-835-0666-9	UNCLASSIFIED

5. Originator The Utilization of Advanced Composites in Military Aircraft
North Atlantic Treaty Organization
7 Rue Ancelle, 92200 Neuilly sur Seine, France

6. Title THE UTILIZATION OF ADVANCED COMPOSITES IN MILITARY AIRCRAFT

7. Presented at the 73rd Meeting of the AGARD Structures and Materials Panel, held in San Diego, CA, United States, 7th—11th October 1991.

8. Author(s)/Editor(s)	9. Date
Various	April 1992
10. Author's/Editor's Address	**11. Pages**
Various	200

12. Distribution Statement This document is distributed in accordance with AGARD policies and regulations, which are outlined on the back covers of all AGARD publications.

13. Keywords/Descriptors

Military aircraft
Composite materials
Compression tests
Compressive properties
Failure
Degradation
Fluids

14. Abstract

The purpose of this Workshop was to identify the current state-of-the-art in key issues related to compression loading and fluid effects in composite materials.

Papers presented revealed some areas of common concern. In the area of compression loading there was considerable concern over the quite different results obtained from various test methods. It was agreed that the failure modes produced by the various test methods along with a better fundamental understanding of compression failure were key issues in the development of compression test methods. In the area of fluid effects, a lack of a comprehensive data base hampers identification of key mechanisms leading to fluid degradation. This is further complicated by the fact that interactions depend on the fluid and the composite under consideration.

It is hoped that the Workshop, bringing together the various experiences of industry, government, and universities, has served in achieving the goal of identifying key issues related to compression loading and fluid effects in composite materials.

This Workshop was sponsored by the Structures and Materials Panel of AGARD.

AGARD Report 785 Advisory Group for Aerospace Research and Development, NATO THE UTILIZATION OF ADVANCED COMPOSITES IN MILITARY AIRCRAFT Published April 1992 200 pages The purpose of this Workshop was to identify the current state-of-the-art in key issues related to compression loading and fluid effects in composite materials. Papers presented revealed some areas of common concern. In the area of compression loading there was considerable concern over the quite different results obtained from various test methods. It was agreed that the failure modes produced by the various test methods along P.T.O	AGARD-R-785 Military aircraft Composite materials Compression tests Compressive properties Failure Degradation Fluids	AGARD Report 785 Advisory Group for Aerospace Research and Development, NATO THE UTILIZATION OF ADVANCED COMPOSITES IN MILITARY AIRCRAFT Published April 1992 200 pages The purpose of this Workshop was to identify the current state-of-the-art in key issues related to compression loading and fluid effects in composite materials. Papers presented revealed some areas of common concern. In the area of compression loading there was considerable concern over the quite different results obtained from various test methods. It was agreed that the failure modes produced by the various test methods along P.T.O	AGARD-R-785 Military aircraft Composite materials Compression tests Compressive properties Failure Degradation Fluids
AGARD Report 785 Advisory Group for Aerospace Research and Development, NATO THE UTILIZATION OF ADVANCED COMPOSITES IN MILITARY AIRCRAFT Published April 1992 200 pages The purpose of this Workshop was to identify the current state-of-the-art in key issues related to compression loading and fluid effects in composite materials. Papers presented revealed some areas of common concern. In the area of compression loading there was considerable concern over the quite different results obtained from various test methods. It was agreed that the failure modes produced by the various test methods along P.T.O	AGARD-R-785 Military aircraft Composite materials Compression tests Compressive properties Failure Degradation Fluids	AGARD Report 785 Advisory Group for Aerospace Research and Development, NATO THE UTILIZATION OF ADVANCED COMPOSITES IN MILITARY AIRCRAFT Published April 1992 200 pages The purpose of this Workshop was to identify the current state-of-the-art in key issues related to compression loading and fluid effects in composite materials. Papers presented revealed some areas of common concern. In the area of compression loading there was considerable concern over the quite different results obtained from various test methods. It was agreed that the failure modes produced by the various test methods along P.T.O	AGARD-R-785 Military aircraft Composite materials Compression tests Compressive properties Failure Degradation Fluids

with a better fundamental understanding of compression failure were key issues in the development of compression test methods. In the area of fluid effects, a lack of a comprehensive data base hampers identification of key mechanisms leading to fluid degradation. This is further complicated by the fact that interactions depend on the fluid and the composite under consideration.

It is hoped that the Workshop, bringing together the various experiences of industry, government, and universities, has served in achieving the goal of identifying key issues related to compression loading and fluid effects in composite materials.

This Workshop was sponsored by the Structures and Materials Panel of AGARD.

ISBN 92-835-0666-9

with a better fundamental understanding of compression failure were key issues in the development of compression test methods. In the area of fluid effects, a lack of a comprehensive data base hampers identification of key mechanisms leading to fluid degradation. This is further complicated by the fact that interactions depend on the fluid and the composite under consideration.

It is hoped that the Workshop, bringing together the various experiences of industry, government, and universities, has served in achieving the goal of identifying key issues related to compression loading and fluid effects in composite materials.

This Workshop was sponsored by the Structures and Materials Panel of AGARD.

ISBN 92-835-0666-9

with a better fundamental understanding of compression failure were key issues in the development of compression test methods. In the area of fluid effects, a lack of a comprehensive data base hampers identification of key mechanisms leading to fluid degradation. This is further complicated by the fact that interactions depend on the fluid and the composite under consideration.

It is hoped that the Workshop, bringing together the various experiences of industry, government, and universities, has served in achieving the goal of identifying key issues related to compression loading and fluid effects in composite materials.

This Workshop was sponsored by the Structures and Materials Panel of AGARD.

ISBN 92-835-0666-9

with a better fundamental understanding of compression failure were key issues in the development of compression test methods. In the area of fluid effects, a lack of a comprehensive data base hampers identification of key mechanisms leading to fluid degradation. This is further complicated by the fact that interactions depend on the fluid and the composite under consideration.

It is hoped that the Workshop, bringing together the various experiences of industry, government, and universities, has served in achieving the goal of identifying key issues related to compression loading and fluid effects in composite materials.

This Workshop was sponsored by the Structures and Materials Panel of AGARD.

ISBN 92-835-0666-9

AGARD
NATO OTAN
7 RUE ANCELLE · 92200 NEUILLY-SUR-SEINE
FRANCE
Téléphone (1)47.38.57.00 · Télex 610 176
Télécopie (1)47.38.57.99

DIFFUSION DES PUBLICATIONS AGARD NON CLASSIFIEES

L'AGARD ne détient pas de stocks de ses publications, dans un but de distribution générale à l'adresse ci-dessus. La diffusion initiale des publications de l'AGARD est effectuée auprès des pays membres de cette organisation par l'intermédiaire des Centres Nationaux de Distribution suivants. A l'exception des Etats-Unis, ces centres disposent parfois d'exemplaires additionnels; dans les cas contraire, on peut se procurer ces exemplaires sous forme de microfiches ou de microcopies auprès des Agences de Vente dont la liste suite.

CENTRES DE DIFFUSION NATIONAUX

ALLEMAGNE
Fachinformationszentrum,
Karlsruhe
D-7514 Eggenstein-Leopoldshafen 2

BELGIQUE
Coordonnateur AGARD-VSL
Etat-Major de la Force Aérienne
Quartier Reine Elisabeth
Rue d'Evere, 1140 Bruxelles

CANADA
Directeur du Service des Renseignements Scientifiques
Ministère de la Défense Nationale
Ottawa, Ontario K1A 0K2

DANEMARK
Danish Defence Research Board
Ved Idraetsparken 4
2100 Copenhagen Ø

ESPAGNE
INTA (AGARD Publications)
Pintor Rosales 34
28008 Madrid

ETATS-UNIS
National Aeronautics and Space Administration
Langley Research Center
M/S 180
Hampton, Virginia 23665

FRANCE
O.N.E.R.A. (Direction)
29, Avenue de la Division Leclerc
92322 Châtillon Cedex

GRECE
Hellenic Air Force
Air War College
Scientific and Technical Library
Dekelia Air Force Base
Dekelia, Athens TGA 1010

ISLANDE
Director of Aviation
c/o Flugrad
Reykjavik

ITALIE
Aeronautica Militare
Ufficio del Delegato Nazionale all'AGARD
Aeroporto Pratica di Mare
00040 Pomezia (Roma)

LUXEMBOURG
Voir Belgique

NORVEGE
Norwegian Defence Research Establishment
Attn: Biblioteket
P.O. Box 25
N-2007 Kjeller

PAYS-BAS
Netherlands Delegation to AGARD
National Aerospace Laboratory NLR
Kluyverweg 1
2629 HS Delft

PORTUGAL
Portuguese National Coordinator to AGARD
Gabinete de Estudos e Programas
CLAFA
Base de Alfragide
Alfragide
2700 Amadora

ROYAUME UNI
Defence Research Information Centre
Kentigern House
65 Brown Street
Glasgow G2 8EX

TURQUIE
Millî Savunma Başkanlığı (MSB)
ARGE Daire Başkanlığı (ARGE)
Ankara

LE CENTRE NATIONAL DE DISTRIBUTION DES ETATS-UNIS (NASA) NE DETIENT PAS DE STOCKS DES PUBLICATIONS AGARD ET LES DEMANDES D'EXEMPLAIRES DOIVENT ETRE ADRESSEES DIRECTEMENT AU SERVICE NATIONAL TECHNIQUE DE L'INFORMATION (NTIS) DONT L'ADRESSE SUIT.

AGENCES DE VENTE

National Technical Information Service
(NTIS)
5285 Port Royal Road
Springfield, Virginia 22161
Etats-Unis

ESA/Information Retrieval Service
European Space Agency
10, rue Mario Nikis
75015 Paris
France

The British Library
Document Supply Division
Boston Spa, Wetherby
West Yorkshire LS23 7BQ
Royaume Uni

Les demandes de microfiches ou de photocopies de documents AGARD (y compris les demandes faites auprès du NTIS) doivent comporter la dénomination AGARD, ainsi que le numéro de série de l'AGARD (par exemple AGARD-AG-315). Des informations analogues, telles que le titre et la date de publication sont souhaitables. Veuiller noter qu'il y a lieu de spécifier AGARD-R-nnn et AGARD-AR-nnn lors de la commande de rapports AGARD et des rapports consultatifs AGARD respectivement. Des références bibliographiques complètes ainsi que des résumés des publications AGARD figurent dans les journaux suivants:

Scientifique and Technical Aerospace Reports (STAR)
publié par la NASA Scientific and Technical
Information Division
NASA Headquarters (NTT)
Washington D.C. 20546
Etats-Unis

Government Reports Announcements and Index (GRA&I)
publié par le National Technical Information Service
Springfield
Virginia 22161
Etats-Unis

(accessible également en mode interactif dans la base de données bibliographiques en ligne du NTIS, et sur CD-ROM)

Imprimé par Specialised Printing Services Limited
40 Chigwell Lane, Loughton, Essex IG10 3TZ

1960

AGARD

NATO OTAN

7 RUE ANCELLE · 92200 NEUILLY-SUR-SEINE

FRANCE

Telephone (1)47.38.57.00 · Telex 610 176
Telefax (1)47.38.57.99

DISTRIBUTION OF UNCLASSIFIED AGARD PUBLICATIONS

AGARD does NOT hold stocks of AGARD publications at the above address for general distribution. Initial distribution of AGARD publications is made to AGARD Member Nations through the following National Distribution Centres. Further copies are sometimes available from these Centres (except in the United States), but if not may be purchased in Microfiche or Photocopy form from the Sales Agencies listed below.

NATIONAL DISTRIBUTION CENTRES

BELGIUM
Coordonnateur AGARD — VSL
Etat-Major de la Force Aérienne
Quartier Reine Elisabeth
Rue d'Evere, 1140 Bruxelles

CANADA
Director Scientific Information Services
Dept of National Defence
Ottawa, Ontario K1A 0K2

DENMARK
Danish Defence Research Board
Ved Idraetsparken 4
2100 Copenhagen Ø

FRANCE
O.N.E.R.A. (Direction)
29 Avenue de la Division Leclerc
92322 Châtillon Cedex

GERMANY
Fachinformationszentrum
Karlsruhe
D-7514 Eggenstein-Leopoldshafen 2

GREECE
Hellenic Air Force
Air War College
Scientific and Technical Library
Dekelia Air Force Base
Dekelia, Athens TGA 1010

ICELAND
Director of Aviation
c/o Flugrad
Reykjavik

ITALY
Aeronautica Militare
Ufficio del Delegato Nazionale all'AGARD
Aeroporto Pratica di Mare
00040 Pomezia (Roma)

LUXEMBOURG
See Belgium

NETHERLANDS
Netherlands Delegation to AGARD
National Aerospace Laboratory, NLR
Kluyverweg 1
2629 HS Delft

NORWAY
Norwegian Defence Research Establishment
Attn: Biblioteket
P.O. Box 25
N-2007 Kjeller

PORTUGAL
Portuguese National Coordinator to AGARD
Gabinete de Estudos e Programas
CLAFA
Base de Alfragide
Alfragide
2700 Amadora

SPAIN
INTA (AGARD Publications)
Pintor Rosales 34
28008 Madrid

TURKEY
Milli Savunma Başkanlığı (MSB)
ARGE Daire Başkanlığı (ARGE)
Ankara

UNITED KINGDOM
Defence Research Information Centre
Kentigern House
65 Brown Street
Glasgow G2 8EX

UNITED STATES
National Aeronautics and Space Administration (NASA)
Langley Research Center
M/S 180
Hampton, Virginia 23665

THE UNITED STATES NATIONAL DISTRIBUTION CENTRE (NASA) DOES NOT HOLD STOCKS OF AGARD PUBLICATIONS, AND APPLICATIONS FOR COPIES SHOULD BE MADE DIRECT TO THE NATIONAL TECHNICAL INFORMATION SERVICE (NTIS) AT THE ADDRESS BELOW.

SALES AGENCIES

National Technical
Information Service (NTIS)
5285 Port Royal Road
Springfield, Virginia 22161
United States

ESA/Information Retrieval Service
European Space Agency
10, rue Mario Nikis
75015 Paris
France

The British Library
Document Supply Centre
Boston Spa, Wetherby
West Yorkshire LS23 7BQ
United Kingdom

Requests for microfiches or photocopies of AGARD documents (including requests to NTIS) should include the word 'AGARD' and the AGARD serial number (for example AGARD-AG-315). Collateral information such as title and publication date is desirable. Note that AGARD Reports and Advisory Reports should be specified as AGARD-R-nnn and AGARD-AR-nnn, respectively. Full bibliographical references and abstracts of AGARD publications are given in the following journals:

Scientific ar
published b
Informatior
NASA Hea
Washington
United Stat

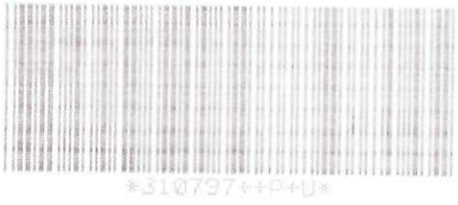

Printed by Specialised Printing Services Limited
40 Chigwell Lane, Loughton, Essex IG10 3TZ